COMSAT
Technical Review

COMSAT TECHNICAL REVIEW
Volume 8 Number 2, Fall 1978

Tunnel diodes in satellite communications

A. G. Revesz and P. L. Fleming

(Manuscript received May 4, 1978)

Abstract

Tunnel diodes, which are widely used in the amplifiers of communications satellites, are unique in terms of fabrication, technology, limited production, and failure mechanism. For example, germanium (Ge) tunnel diodes are subject to an internal mechanical stress that depends on subtle variations in the fabrication process and may significantly vary from one device to another. This stress may initiate plastic deformation (creep) in the germanium, resulting in the eventual deterioration of the diode characteristics.

An understanding of the failure mechanism has led to the introduction of a completely new screening technique. In addition, the match of the thermal expansion coefficients of the device components has been improved. Therefore, tunnel diodes are very reliable and are, at present, the most prevalent active microwave solid-state devices in communications satellites: 102 diodes have been used in 15 INTELSAT satellites for a total operational time of about 2×10^6 device-hours. No failure has occurred during their operation. Tunnel diodes are also used in at least 20 other communications satellites.

Introduction

Germanium tunnel diodes, which are extensively used as first stage amplifiers in the transponders of various communications satellites, have achieved the longest lifetime in space without failure of any active solid-

state microwave device. This accomplishment is significant considering the several unique and potentially adverse features of this device. This paper emphasizes the importance of this device in satellite communications.

Background

The invention of the tunnel diode and its early phases have been described by Esaki [1]. The device consists of such a narrow junction between heavily doped (degenerate) p and n regions (p^+/n^+ junction) that the electrons can easily penetrate via tunneling the potential barrier across the junction. When the forward bias is gradually increased, the electrons tunnel from the n^+ region into an increasing density of empty states in the valence band of the p^+-type material, followed by a decreasing density of states as the conduction band in the n^+-type side rises over the valence band in the p^+-type side. Correspondingly, the current first increases and then decreases with voltage. With further increases in the forward voltage, the normal diffusion current (as in the case of the usual p-n diode) dominates, and the current increases again. The result is the well-known current-voltage characteristic shown in Figure 1. The negative differential resistance portion of the I-V characteristic is employed in the tunnel diode amplifier (TDA).

In contrast to the usual diodes and transistors, no speed limiting factors due to minority carrier lifetime or thermal processes are involved in tunnel diode operation. Hence, the application of tunnel diodes to microwave and high-speed switching circuits appeared promising. Also, because of the very high doping density, the tunnel diode is insensitive to environmental conditions; other Ge devices had been plagued by surface instability effects when the tunnel diode emerged in the late fifties. At that time the most widely used semiconductor material was germanium, and p-n junctions were usually fabricated by alloying techniques.

However, the situation changed dramatically following the successful surface passivation of silicon by a thermally grown SiO_2 film that could also be used as a selective mask during the gaseous diffusion of dopants. These two discoveries led to the evolution of silicon planar technology as the mainstay of semiconductor device technology. Thus, the role of germanium as a semiconductor material has been greatly reduced, and alloying as a technique for fabricating p-n junctions has practically disappeared.

The evolution of the semiconductor device technology has essentially bypassed that of tunnel diodes. This is reflected in the recent market
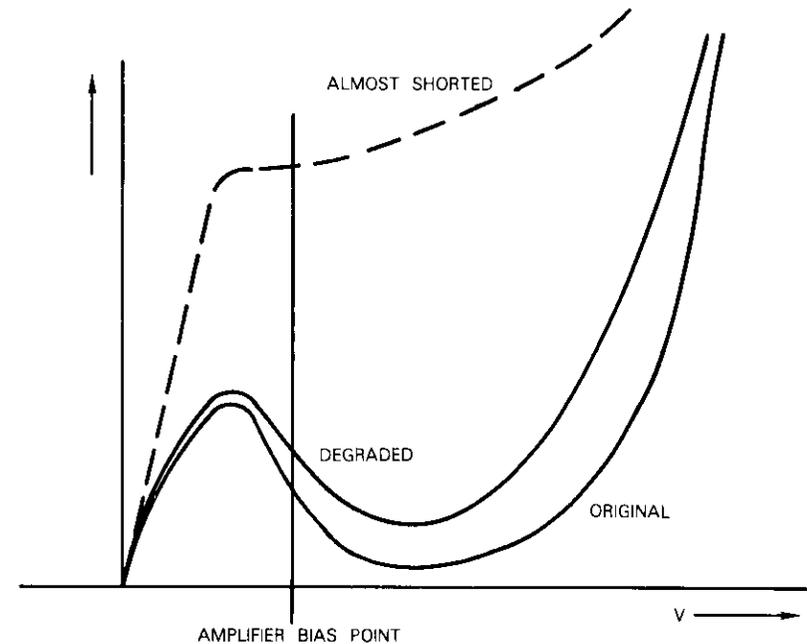
Figure 1. *Qualitative Tunnel Diode Current-Voltage Characteristics (Scales are arbitrary)*

trends: Total semiconductor device production has increased from \$2.04 $\times$ 10^9 in 1975 to \$3.2 $\times$ 10^9 in 1977; however, the tunnel diode market has declined from \$2 $\times$ 10^6 to \$1.6 $\times$ 10^6 [2], which represents only 0.05 percent of the total semiconductor device market. Because of the very small production volume, R&D activity on tunnel diodes has been much less vigorous than that on other semiconductor devices. Consequently, the technology has not significantly changed since the late fifties.

Tunnel diodes in communications satellites

Regardless of their declining market and unsophisticated fabrication technology, tunnel diodes have been very important in microwave circuits, particularly in the transponders of communications satellites. In this application, their wideband negative resistance is utilized in a microwave reflection amplifier. Figure 2 shows the basic AC equivalent circuit of a
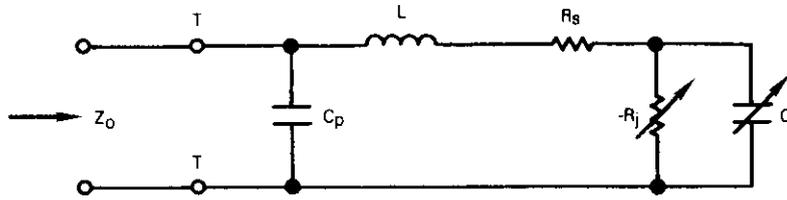
Figure 2. *Equivalent Circuit of a Microwave Tunnel Diode (C_p = package capacitance, L = series inductance, R_s = series resistance, $-R_j$ = voltage variable negative resistance of the p/n junction, C_j = voltage variable junction capacitance, and Z_o = characteristic impedance)*

microwave tunnel diode mounted in a transmission line. The negative resistance presented by the diode at the reference plane TT will reflect an incident wave with gain if

$$|R_{TT}| > Z \qquad . \qquad (1)$$

The companion developments of the ferrite junction circulator and the tunnel diode proved a natural combination for application to satellite front ends. A typical configuration utilized in INTELSAT III, IV, and IV-A communications satellites is illustrated in Figure 3. The application of
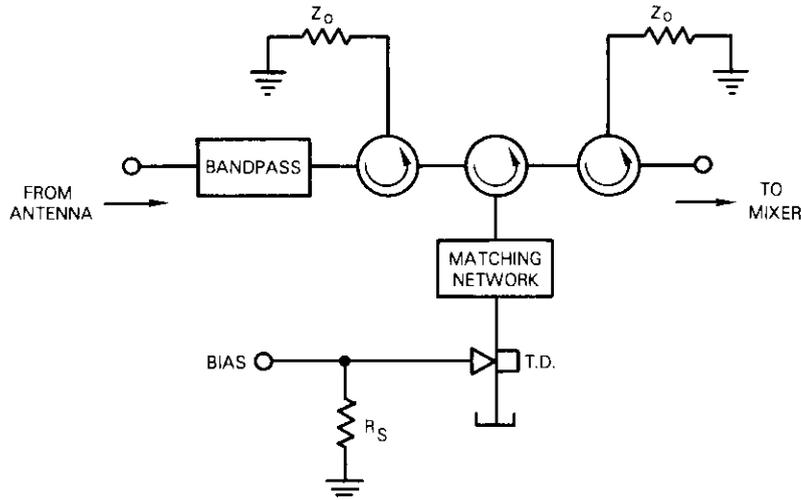
Figure 3. *Schematic of a Tunnel Diode Amplifier Circuit*

the 5-port circulator provides high isolation between the output and input, thus overcoming the limitations of coupling with a 2-terminal device.

A typical Ge diode at 6 GHz can provide 12- to 13-dB gain with an associated noise figure (NF) of about 5 dB. This is adequate for application in the receiver front end of communications satellites. The INTELSAT V satellites (planned for launch beginning in 1980) will use Ge tunnel diodes to provide a 6-dB noise figure at 14 GHz.

In addition to the low noise figure, another attractive feature of the device is its low-power drain. A diode with a peak current of 2.0 mA biased at the low-noise operating point dissipates only about 150 μW. The wideband stabilizing resistor (typically 25Ω) at the bias terminal will draw significantly more supply power. At the power levels received (typically -50 dBm), the tunnel diode is sufficiently linear so that intermodulation distortion of a multicarrier signal is not a problem.

Because of the aforementioned characteristics, the tunnel diode has been indispensable in satellite communications receivers. A companion paper [3] in this issue discusses a detailed design and study of a TDA suitable for use in the 14-GHz receiver in INTELSAT V.

Fabrication and construction of tunnel diodes

The technology of tunnel diodes is summarized to provide an understanding of the principal failure mode and the reliability aspects of Ge tunnel diodes. Figure 4 is a schematic of a tunnel diode structure. The
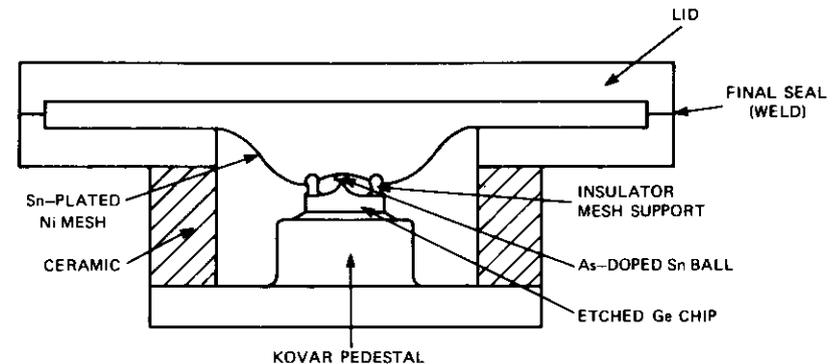
Figure 4. *Cross-Section of a Ball Alloy Ge Tunnel Diode [4]*

arsenic (As) in the As-doped tin ball forms the n^+ region on the surface

of the p^+ Ge chip during recrystallization following alloying at a tempera-
ture exceeding the Ge-Sn eutectic point (232°C). The tin ball ($\sim$25- to
$\sim$50-μm diameter) is attached to a wire mesh which is separated from the
Ge chip by two insulator supports. After alloying, the Ge chip is etched
so that the diameter of the resulting pinnacle is about 2.5 μm for a 6-GHz
device and even less for higher frequency devices. The height of the pin-
nacle or neck is usually larger than $\sim$20 μm. Figure 5 is an SEM photo-
graph of the structure (excluding the insulator support).
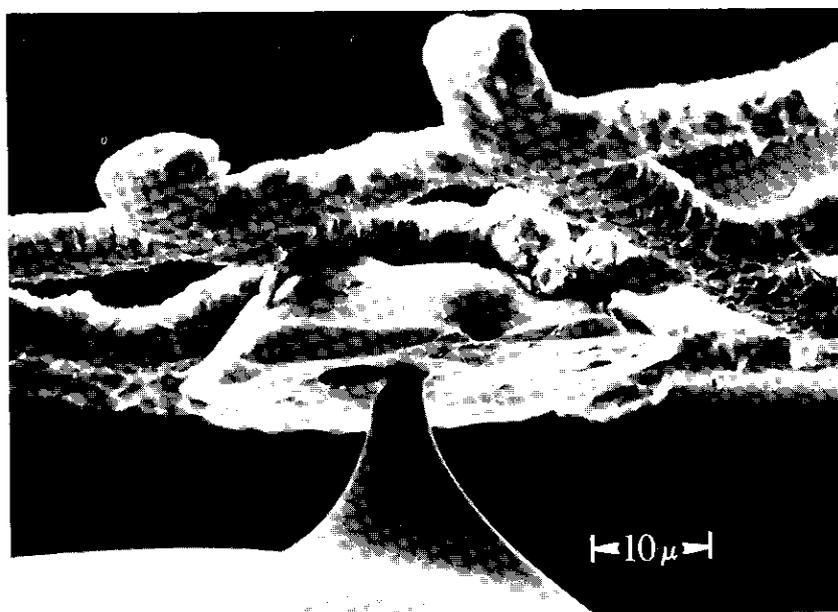
Figure 5. *SEM Photograph of a 6-GHz Tunnel Diode showing the Neck
in Ball and Mesh (Courtesy T. Kirkendall)*

A study by Varadi and Kirkendall [4] has revealed that there are large
variations in the shape of the pinnacle and the position of the tin ball,
as well as in the soldering of the mesh electrode to the tin ball. These results
confirmed earlier ideas about the importance of internal stress [5]. Virk [6]
has demonstrated that the mesh should be as symmetrical as possible to
ensure minimum stress. However, even relatively minor deviations from the
mechanically ideal structure may result in significant stress, since the

junction area is very small. Hence, these devices are characterized by a
built-in stress of varying magnitude that is important in terms of the
failure mechanism of tunnel diodes.

Another important feature of the tunnel diode structure, particularly
with respect to the temperature cycling behavior of the device [6], is the
insulator support. It has been shown [7] that the median temperatures of
failure are 175°C and 160°C for tunnel diodes with glass and epoxy sup-
port rods, respectively. This difference is attributed to the better match
in the thermal expansion coefficient of glass as opposed to that of ger-
manium. Presently, only tunnel diodes with glass mesh supports are used
in communications satellites.

In addition to the previously described ball alloy tunnel diodes, planar
diodes have been fabricated on an experimental basis. In these devices,
the junction area is defined by masking the Ge surface with a chemically
deposited SiO_2 film [8]. With respect to mechanical stress, planar diodes
are much better than ball alloy diodes. However, the properties of the
Ge/SiO_2 interface have not been optimized, and this interface is a source
of excessive noise [9]. Planar tunnel diodes have never been employed in
communications satellites.

Failure mechanism of Ge tunnel diodes

The erratic behavior of the TDA in an INTELSAT III communications
satellite* in 1969 prompted an intensive study of the failure mechanism
of Ge tunnel diodes at COMSAT Laboratories. It has been established [5]
that the principal failure mode of ball alloy diodes is the increase in the
valley current, I_v, as shown in Figure 1. As a result, the peak-to-valley
current ratio, I_p/I_v, and the negative differential conductance decrease.
Consequently, the operation of the diode in the amplifier is impaired.
In the extreme case, the negative differential conductance regime may
completely disappear.

The valley current increases because, in addition to the electron tunneling
from the conduction to the valence band, tunneling involving electronic
states in the forbidden band of the germanium crystal also occurs. These
states arise from defects in the crystal and are responsible for the excess
(*i.e.*, non-zero) valley current of varying magnitude observed in every
tunnel diode.

*The failure of the TDA was attributed to a tunnel diode. However, because
the amplifier recovered, the cause of failure was unrelated to the diode.

It has been shown that the I_v of a ball alloy tunnel diode increases (and consequently I_p/I_v decreases) during heat treatments (temperature stress) [5]. The behavior of the diodes exhibited considerable scatter as shown in Figure 6. Apparently, defects are generated during the heat
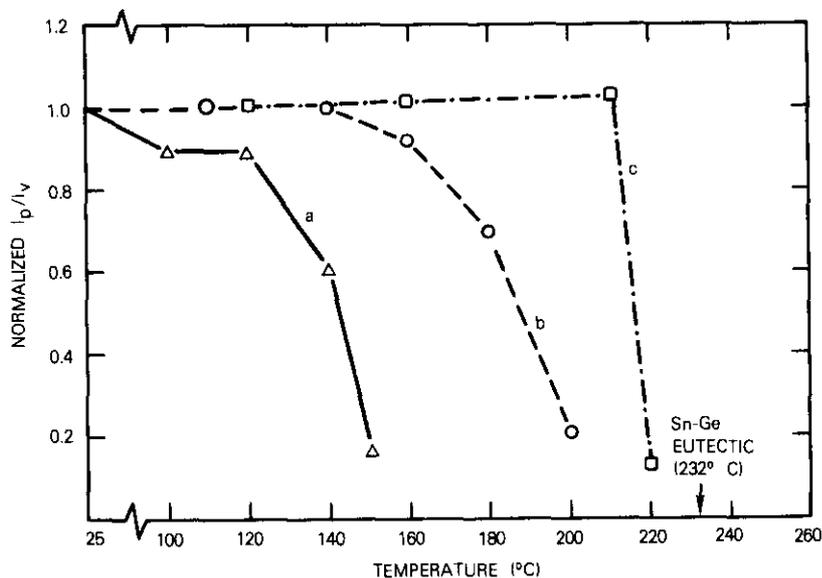
Figure 6. *Behavior of Ge Tunnel Diodes During Isochronal (1 hr) Heat Treatment at 10°C Increments* [5]

treatment. It has been suggested that mechanical creep is responsible for the generation of defects and the ensuing increase in the valley current. Creep is the initial phase of plastic deformation during which defects are generated. Creep is thermally activated and time-dependent. Under constant stress there is an incubation time, t_i. Before t_i the introduced strain and defect density are very small; after t_i the strain increases linearly with time, which greatly increases the defect density. This incubation time depends exponentially on temperature and stress [10]:

$$t_i = \text{cd} \exp \frac{Q - a\sigma}{kT} \qquad (2)$$

where c and a are constants, d is the diameter of the p-n junction, Q is an

activation energy, and σ is the stress. Published values for c, a, and Q [10] have been used to calculate t_i for $d = 2.5 \ \mu$m, and the results are shown in Figure 7. This figure demonstrates that a relatively small change in stress from 0.8×10^9 to 1.2×10^9 dyne/cm^2 results in a change of five
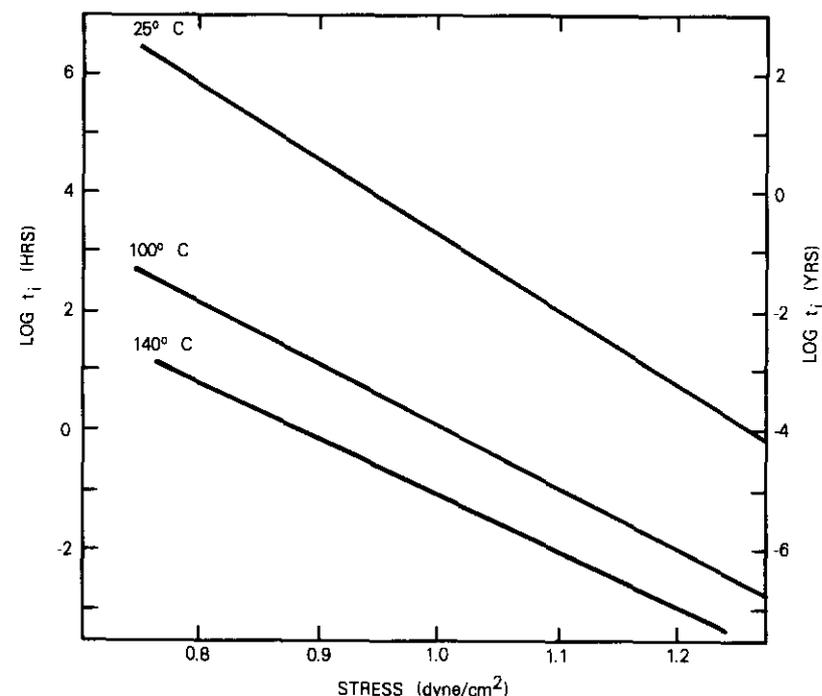
Figure 7. *Incubation Time of Creep as a Function of Stress*

orders of magnitude in the incubation time. Since the junction area in microwave tunnel diodes is of the order of 10^{-7} cm^2 (or even less), a slight variation around a force of 10^2 dyne (corresponding to $\sim$0.1 g weight) at the junction is associated with a critical variation (from tens of years to fractions of a year) in the incubation time at 25°C (the operating temperature in the satellite).

Since the structural details of tunnel diodes vary considerably, the internal stress can also vary greatly even though their initial characteristics may be very similar. Their sensitivity to creep, as manifested in the incuba-

tion time, reflects the variation in the built-in stress; therefore, Ge tunnel diodes during heat treatment behave as shown in Figure 5.

Because of their different construction, planar tunnel diodes do not have a high internal stress, and the I_v does not degrade during heat treatment [5].* Unmounted ball alloy diodes behave similarly to planar diodes [7]. These observations further emphasize that the internal stress in Ge tunnel diodes is determined by their mechanical structure.

For mounted tunnel diodes used in practical applications, the combination of internal stress, time, and temperature determines the incubation time of creep and thus degradation behavior. The results showed that degradation occurs even at temperatures below 100°C but at a slower degradation rate [5]. Defects generated during plastic deformation can be annealed out, and a degraded diode may partially recover. The degradation and recovery processes are affected by changes in the internal stress. If the stress is relieved (e.g., by a slight change in the position of the mesh), the defects may be completely annealed out, resulting in diode recovery [5].

A negative capacitance component in the RF equivalent circuit (Figure 8)
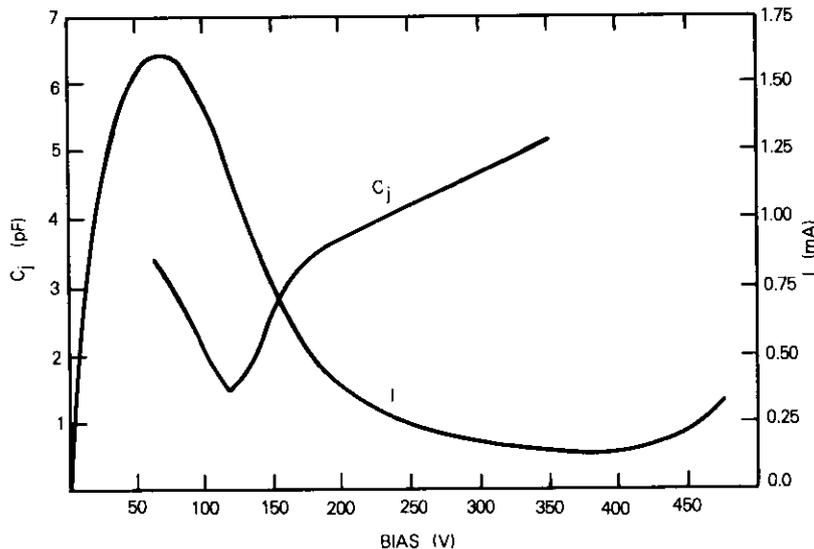
Figure 8. *Current (I) and Junction Capacitance (C_j) as a Function of Bias for a Typical 6-GHz Tunnel Diode*

---

*However, an injection-recombination current during forward biasing beyond the valley voltage degrades the planar diode [5].

may be another indicator of diode stress [7]. This component was not predicted in the development of tunneling theory and is probably related to stress-generated defects and possible associated trapping effects. The characteristic time (τ) associated with the effect is sufficiently short so that the negative capacitance component should be included in the RF equivalent circuit [11]. As a test indicator for creep, this represents a complexity which is not warranted in a simple screening technique.

Reliability

At the outset of the INTELSAT III program, very few data were available on tunnel diode lifetime. Analysis of supporting life tests indicated that about 20 percent of the diodes in use were of questionable status [12]. Simple burn-in of diodes at room temperature was not sufficient to ensure adequate satellite lifetime. It was suggested [5] that an efficient screening technique should be based on understanding the physics of failure of Ge tunnel diodes rather than on the phenomonological-statistical approach which was essentially the basis of the life tests and burn-in processes. The suggested screening technique should utilize the temperature behavior of the incubation time to effectively screen out high-stress diodes indicated by the change in I_v.

Based on this suggestion, a program was undertaken to determine prescreening criteria and to verify the results with a suitable life test [7]. This was performed electronically to avoid manual handling during the test. (This feature was not incorporated into the tests described in Reference 12.) The program was successfully completed by utilizing a screening procedure of 140°C for 1.0 hour and monitoring room temperature valley current changes. This combination of temperature and time corresponds to 0.88×10^9 dyne/cm² as the maximum tolerable stress at 25°C for the 7-year mission of a communications satellite [7] as shown in Figure 7. The screening criterion employed involved the rejection of all diodes ($\sim$13 percent) exhibiting a 10-percent or larger increase in I_v. The life test of 24 diodes has reached 55,000 hours. No failures have been experienced in the screened group while a failure rate of approximately 10 percent was experienced in the unscreened group.

The diodes for this life test were also screened by the manufacturer using a so-called process conditioning involving a heat treatment at 100°C for 48 hours. According to Figure 7, this treatment eliminates diodes with an internal stress higher than $\sim$0.85 $\times$ 10^9 dyne/cm². The significant difference between the process conditioning and the screening at 140°C is

that the change in I_v is not monitored in the former case; it is a static go/no go test. However, the change in I_v at 140°C is a sensitive indicator of a possible future degradation at 25°C even if the diode characteristics after the test are still within the acceptance limits; in other words, this is a dynamic test. The diodes analyzed in Reference 12 were not subjected to process conditioning. The lack of this step was probably one of the reasons for their poor performance. The screening at 140°C [7] has been incorporated into the ATS-F transponder program at COMSAT Labs, the INTELSAT IV-A program at Hughes Aircraft Company, and the INTELSAT V program at Ford Aerospace Communications Corporation.

Since 14-GHz tunnel diodes are being employed in the INTELSAT V program, it is important to realize that the effects of slight deviations from the mechanically perfect structure become more harmful as the operating frequency increases. Thus, the increase in the operating frequency from 6 to 14 GHz is achieved by increasing the speed index, S, ($S = I_p/C_j$, where I_p is the peak current and C_j is the junction capacitance) from 5.71 to 7.15 mA/pF. This is mainly due to a decrease in C_j, since I_p increases only by 7.5 percent. Thus, the junction area decreases by a factor of 1.25. Hence, a force of 43 dyne ($\sim$0.04 g weight), which results in an internal stress of 0.88 $\times$ 10^9 dyne/cm^2 for the 6-GHz diode, causes a stress of 1.1 $\times$ 10^9 dyne/cm^2 in the 14-GHz diode. This increase in stress and decrease in d in equation (1) reduce the incubation time of creep from 6.13 $\times$ 10^4 hours (7 years) to 9.1 $\times$ 10^1 hours (1.3 $\times$ 10^{-2} years) at 25°C. Conversely, the internal force would have to be reduced to 34 dyne/cm^2 ($\sim$0.03 g weight) to ensure the same reliability using the same screening procedure. Obviously, the demands on the mechanical perfection of the device construction increase with the operating frequency.

Performance of tunnel diodes in space

The performance of Ge tunnel diodes in space can be illustrated by the 15 satellites of the INTELSAT III, IV, and IV-A series. Five satellites of the III series carried two tunnel diodes, seven satellites of the IV series employ eight tunnel diodes, and three satellites of the IV-A series (as of year end 1977) employ 12 tunnel diodes; the total number of diodes is 102. Figure 9 is a histogram of the diodes operated for a given length of time without failure. (Standby and lease operations are not included in the operation time.) The INTELSAT III satellites, which were launched between December 1968 and May 1970 and have not been used for about 5 to 6 years, were retested in May 1977; the tunnel diodes were still operational [13].
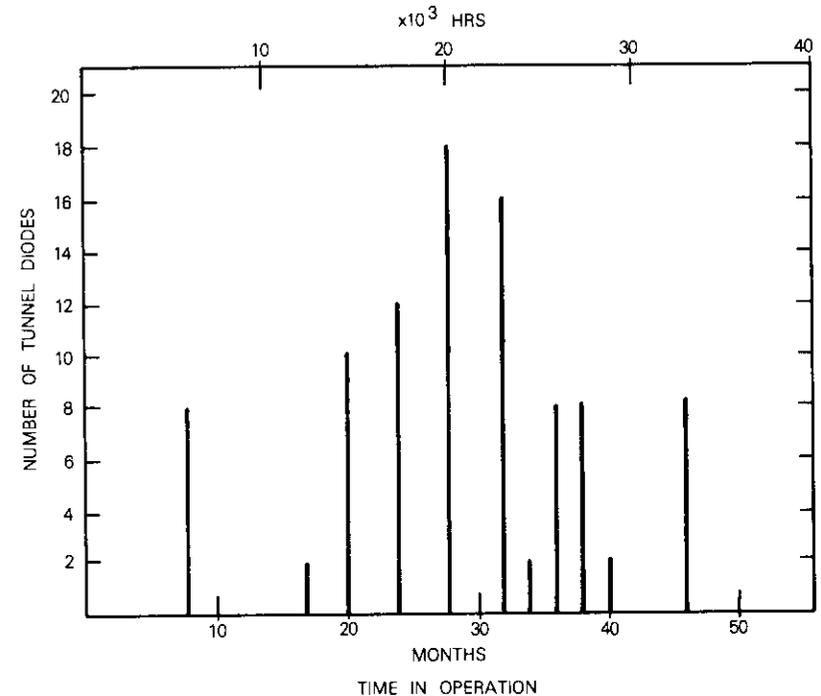
Figure 9. *Histogram of Tunnel Diodes Operated for Various Lengths of Time in INTELSAT III, IV, and IV-A Communications Satellites* [13]

Figure 9 evidences that the longest operational time is 46 months (3.32 $\times$ 10^4 hours) corresponding to 2.66 $\times$ 10^5 device-hours. The total operational time is about 2 $\times$ 10^6 device-hours, and the average operational time per device is about 2 $\times$ 10^4 hours. These data and the life test data of screened tunnel diodes (5.5 $\times$ 10^5 hours of operation for 12 devices without failure) demonstrate the very high reliability of properly screened Ge tunnel diodes.

In addition to the 15 INTELSAT satellites represented in Figure 9, at least 20 other communications satellites (*e.g.*, COMSTAR, Anik, and WESTAR) employ Ge tunnel diodes. Also, several future communications satellites (*e.g.*, the INTELSAT V series) will utilize these devices.

Conclusion

Despite the many potentially adverse features, Ge tunnel diodes have performed well in communications satellites. In fact, the Ge tunnel diode has accumulated by far the longest operating time in space without failure of any active solid-state microwave device. This achievement is due to the careful fabrication of these devices and in particular to the understanding of their unique failure mode that served as the basis of a screening technique significantly different from the conventional burn-in process.

Acknowledgment

Thanks are due to E. Colety and S. Virk (both of Aertech Corporation) and I. Dostis (Satellite Business Systems), as well as to W. Morgan and R. Strauss for helpful discussions. E. S. Rittner's comments and suggestions on the manuscript are greatly appreciated.

References

[1] L. Esaki, "Discovery of the Tunnel Diode," *IEEE Transactions on Electronic Devices*, 1976, pp. 644.

[2] "U.S. Market Forecasts," *Electronics*, January 6, 1977, p. 90; *Electronics*, January 5, 1978, p. 134.

[3] R. C. Mott, "INTELSAT V 14-GHz Tunnel Diode Noise Figure Study," *COMSAT Technical Review*, Vol. 8, No. 2, Fall 1978, pp. 487-507.

[4] P. F. Varadi and T. D. Kirkendall, "Physical and Chemical Analysis of Germanium Tunnel Diodes," *COMSAT Technical Review*, Vol. 3, No. 1, Spring 1973, p. 35.

[5] A. G. Revesz, J. Reynolds, and J. Lindmayer, "New Aspects of Failure Mechanism in Germanium Tunnel Diodes," *Solid State Electronics*, Vol. 14, 1971, p. 1137.

[6] S. Virk, "The State of Tunnel Diode Technology," *Electronic Products*, November 1969, p. 30.

[7] P. L. Fleming, "Prescreening Techniques for Flight Germanium Tunnel Diodes," *COMSAT Technical Review*, Vol. 4, No. 2, Fall 1974, p. 449.

[8] W. Schultz, "Planar Tunnel Diode Process Development," Final Report, Contract No. AF 19-(628)-5467 (1969).

[9] S. Virk, Private Communication.

[10] H. G. Van Bueren, *Imperfections in Crystals*, Chapter 30, North Holland, Amsterdam, 1961.

[11] P. L. Fleming and L. E. Foltzer, "Measurement of Negative Capacitance Component in Microwave Tunnel Diodes," *IEEE-GMTT International Symposium*, Washington, D.C., May 16-19, 1970.

[12] E. P. Moyer, Private Communication.

[13] R. Strauss and J. R. Owens, "Design Factors Affecting Communications Satellite Lifetime," *28th Congress of the International Astronautical Federation*, Prague, 28 September-1 October 1977.
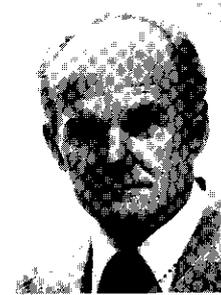
A. G. Revesz received Diploma of Engineering and Ph.D. degrees from the Technical University of Budapest, Hungary. As Senior Staff Scientist in the Applied Sciences Division at COMSAT Laboratories, he has been the principal investigator in identifying the failure mechanism of tunnel diodes and devising a better selection procedure for these devices. His work on semiconductor-insulator interfaces and noncrystalline oxides has resulted in a new antireflection film essential for the development of silicon solar cells of increased efficiency. Prior to joining COMSAT, he was with RCA David Sarnoff Research Center, where he received an Outstanding Achievement Award for his work on the Si-SiO_2 interface. He is a member of the editorial board of the COMSAT TECHNICAL REVIEW and a Fellow of the American Institute of Chemists.

Paul Fleming is Manager of the Device Physics Department at COMSAT Laboratories. He received a B.S.E.E. from the City College of New York in 1957 and an M.S.E.E. from Columbia University in 1960. He previously served as a VHF radio specialist with the Marines in South Korea. He spent 10 years with the IBM Corporation, where he received an Invention Achievement award. His work has included microwave memories, microwave modulation of light, digital microwave, 12-GHz propagation, bulk effect devices and, more recently, transmission line devices in III-V compounds. He is a member of Eta Kappa Nu, the Electron Devices Group, and a Senior Member of the IEEE.
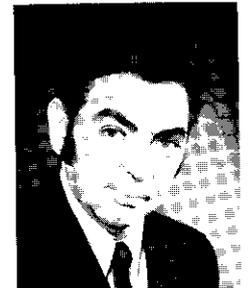
Fixed-point, parallel arithmetic digital signal processors

Z. M. ALI

Abstract

This paper presents the hardware implementation of three basic elements of digital signal processors which use fixed-point, two's complement, parallel arithmetic: a general purpose arithmetic structure for digital filtering, a high-speed computational element for implementing a fast Fourier transform, and a digital frequency synthesizer. These processors, which were designed and tested in the laboratory, have been built around a 16-bit parallel multiplier and configured in modular form. The modularity approach not only simplifies application to different forms of digital signal processing but it also enhances maintainability.

As an example of the application of these processors, an FDM/TDM transmultiplexer is described which provides a direct interface between analog FDM transmission systems and digital TDM systems.

Introduction

General purpose computers offer flexibility in terms of algorithms, data formats, and communications interface; hence, their cost can be absorbed by many applications. High-speed requirements (sampling frequency in the 0.5- to 1-MHz range), the strong desire to standardize design efforts, and the availability of large-scale integrated circuits (LSIs) for digital signal processing have led to new forms of implementing special purpose computing modules. The LSI circuits have resulted in the economic realization

273

of real-time signal analysis, previously accomplished either by analog systems or off-line computer simulations. The increasing need for digital signal processing in modern communications systems has made the new approach more attractive and cost competitive.

Analog systems, which generally require close matching of components and impose tight tolerances on the electronic devices used in their implementation, are also heavily affected by the environment. Digital processing eliminates the need for strict device parameters and provides greater noise immunity. Digital calculations enable the maintenance of n-bit accuracy throughout the processing, thus producing stable and repeatable operations. The simplicity with which a fast device may be time-shared for a number of slower operations and the ease of functional reconfiguration by electrical means may enable, for instance, a complete band of analog filters to be replaced with a single time-shared digital filter.

A digital processing facility can be exploited to implement efficient algorithms as modules or subsystems which can form larger systems, based upon software structured programming techniques. That is, smaller modules or subsystems can be designed and used separately or combined and used simultaneously, depending upon the requirements of the analysis.

The digital signal processors described in this paper employ special high-speed computing elements. These arithmetic subsystems combine high speed and low hardware cost with timing and control simplicity of parallel arithmetic. Parallel arithmetic uses parallel multipliers and adders instead of serial arithmetic units described elsewhere [1]–[4]. These arithmetic structures use random access memories (RAMs) instead of shift registers for intermediate storage and can be controlled by programmable read-only memories (PROMs). The PROMs enable microprogrammability and a looping facility for efficient utilization of the structures; for example, the multiplexing of N filters with M biquad sections, each on a single high-speed digital filter. Flexibility is further enhanced by designing structures around a tri-state bus for easy data manipulation, thereby eliminating the need for multiplexers.

Three processors are described: a parallel arithmetic structure for digital filtering, a 2-point elemental transform processor (butterfly) for fast Fourier transform (FFT), and a digital frequency synthesizer.

General purpose arithmetic structure

One of the general structures of a parallel digital signal processor designed around a tri-state bus is shown in Figure 1. The structure is com-
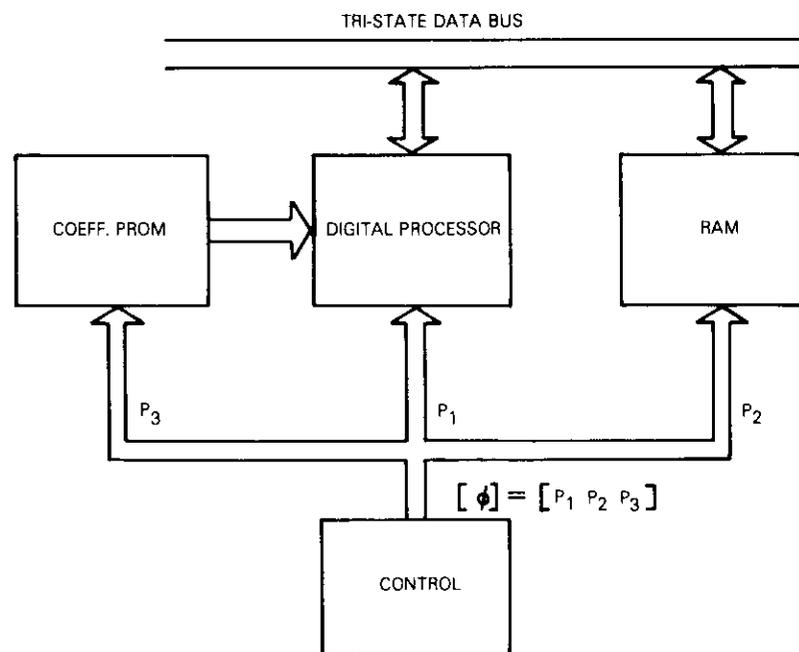
Figure 1. *Block Diagram of a Digital Signal Processor*

posed of four major blocks:

a. The coefficient PROM which contains the weights to be used for processing (for example, the FFT coefficients).

b. The high-speed arithmetic processor capable of performing special functions, such as elemental 2-point transformation of an FFT or a biquad section of a recursive filter.

c. The memory, which is usually a RAM used for storing intermediate results. This memory should not be confused with the scratch-pad memories which will be mentioned subsequently.

d. Indexing and controls in which each arithmetic structure can be viewed as a special purpose microprocessor, controlled to perform the desired function via a control vector or microinstruction [Φ]. The microinstruction has P elements which are divided into three fields, P_1, P_2, and P_3. P_1 provides various controls for the arithmetic unit, P_2 provides the necessary address and control for RAM, and P_3 provides the address for coefficient PROM. The vector [Φ], which can be

represented as $[\Phi] = [P_1 P_2 P_3]$, may be the output of a PROM, which is then termed a control PROM or microsequencer. A set of such vectors constitutes a control program to accomplish a specific function.

If the processor is multiplexed over N processes, each performing M_k functions ($k = 1, 2, 3, \ldots$) with n_i operations ($i = 1, 2, 3, \ldots$), then the required length L of the PROM is given by

$$L = \sum_{j=1}^{N} n_i M_k, \qquad i = 1, 2, \ldots, \qquad k = 1, 2, \ldots \qquad (1)$$

A control PROM and a divide-by-L counter will be sufficient to control the entire operation. This control circuit is shown in Figure 2. Variations in implementation of the control circuits are also possible [5], such as looping the program within a loop.
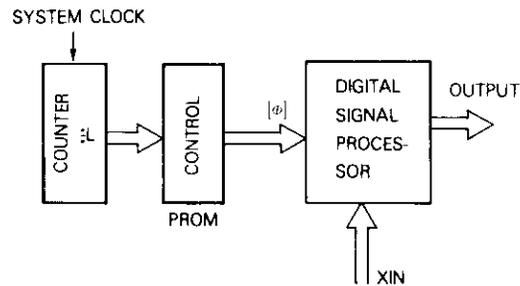
Figure 2. *Control Circuit for Digital Signal Processor*

The length and width of the control PROM can be reduced by localizing the controls with each block within the system. This function is achieved by providing small control PROMs which generate fields P_1, P_2, and P_3 separately.

Serial arithmetic structures process signals one bit at a time; therefore, they constrain the internal computational word length and hence enforce a tradeoff between word length and processing speed. Parallel arithmetic structures are independent of word length in terms of processing time, but are constrained by the size of the hardware; hence, a tradeoff between word length and size of the hardware is encountered. Parallel processors have a definite advantage over serial processors in terms of simplicity in timing and control (fewer events per sample and availability of complete results at a particular time).

Effects of finite register length in computation

The finite word length constraint requires that the input analog signal be quantized to a finite number of possible values. Even for data representable by a finite word length, the result of processing will naturally lead to numbers requiring additional bits for their representation. For example, a b-bit data sample multiplied by a b-bit coefficient results in a product $2b - 1$ bits long which will require a representation b bits longer than the previous stage. This expansion of word length can be limited by truncation, depending upon the type of arithmetic used (fixed point or floating point).

For fixed-point representation the register is considered to represent a fixed-point fraction whereby the product of two numbers remains a fraction and the limited register length is maintained by truncating or rounding the least significant bits (LSBs). This representation does not require truncating or rounding for addition processes. However, the magnitude of the resulting sum can exceed unity. This effect, which is commonly referred to as overflow, can be avoided by requiring sufficiently small input data.

Truncations

The fixed-point number is represented as $(b + 1)$-bit binary fractions, with the binary point to the right of the most significant bit (MSB). The numerical value (for positive numbers) of a 1 in the LSB is 2^{-b}, a quantity referred to as the width of quantization. For positive numbers, the one's and two's complement number representations are identical. If b_1 is the number of binary bits before truncation, and b the number of bits after truncation with $b < b_1$, the effect of truncation is to discard $(b_1 - b)$ LSBs. Consequently, the magnitude of the number after truncation is less than or equal to the magnitude before truncation. If the numbers before and after truncation are denoted as x and $Q[x]$, respectively, the truncation error, E_T, is

$$E_T = Q[x] - x \quad .$$

The largest error occurs when all discarded bits are unity, *i.e.*,

$$-(2^{-b} - 2^{-b_1}) \leq E_T \leq 0 \quad .$$

For negative numbers the truncation error depends on the number sys-

tem used. With sign and magnitude representation, the value after truncation minus the value before truncation is positive; hence,

$$0 \leq E_T \leq (2^{-b} - 2^{-b_1}) \quad .$$

For a two's complement negative number the magnitude is

$$A_1 = 2.0 - x_1$$

where

$$x_1 = 1 + \sum_{i=1}^{b_1} a_i 2^{-i}$$

and a_i assumes two values, 0 or 1. For the truncated number x_2, the magnitude is

$$A_2 = 2.0 - x_2$$

where

$$x_2 = 1 + \sum_{i=1}^{b} a_i 2^{-i} \quad ,$$

Thus,

$$\Delta A = A_2 - A_1 = \sum_{i=b+1}^{b_1} a_i 2^{-i}$$

and

$$0 \leq \Delta A \leq (2^{-b} - 2^{-b_1}) \quad .$$

Hence, the effect of truncation for a two's complement negative number is to increase the magnitude of the negative number; the truncation error is negative:

$$-(2^{-b} - 2^{-b_1}) \leq E_T \leq 0 \quad .$$

It should be noted that for two's complement numbers the range of error is the same as that for positive and negative numbers, which makes this representation very attractive for implementation.

Rounding

The numbers can be rounded off to fit into a finite length register. (Rounding is choosing the closest quantization level.) Again, b denotes the number of bits to the right of the binary point after rounding. The values are quantized in steps of 2^{-b}; that is, the smallest nonzero difference between two numbers is 2^{-b}. Thus, the maximum error has a magnitude of $2^{-b}/2$; i.e., the rounding error, E_R, is in the range

$$-\frac{1}{2}(2^{-b} - 2^{-b_1}) < E_R \leq \frac{1}{2}(2^{-b} - 2^{-b_1}) \quad .$$

The error is independent of the representation of the negative numbers. Generally, $2^{-b_1} \ll 2^{-b}$ and consequently the term 2^{-b_1} can be neglected with these approximations. The above results can be summarized as follows. For truncation,

$$-2^{-b} < E_T \leq 0 \qquad \text{(positive numbers)}$$

$$0 \leq E_T < 2^{-b} \qquad \text{(sign magnitude negative numbers)}$$

and for rounding,

$$-\frac{1}{2} 2^{-b} < E_R \leq \frac{1}{2} 2^{-b} \quad .$$

Figure 3 illustrates these results.
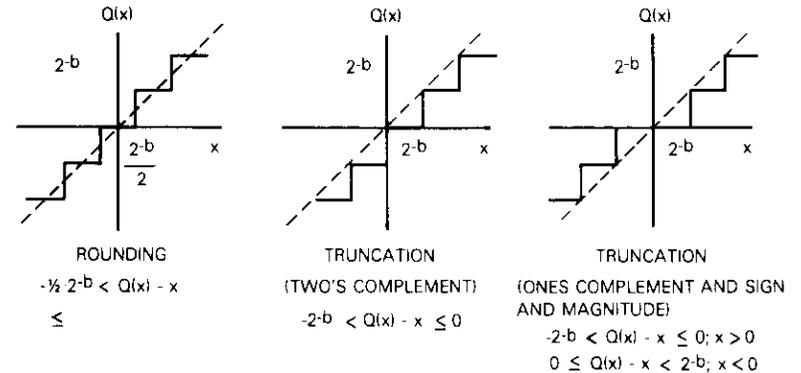
Figure 3. *Rounding and Truncation Error Representation*

Quantization in sampling analog signals

To ensure that the unquantized samples are within the range of the $(b + 1)$-bit number, it must be assumed that the analog waveform is normalized so that the sampled signal $x_a(nT)$ falls within the range

$$\left(-1 + \frac{2^{-b}}{2}\right) < x_a(nT) < \left(1 - \frac{2^{-b}}{2}\right) \quad .$$

If the input sample value falls outside this range, additional distortion results. As indicated in Figure 4, for $b = 2$ the quantized value $1 - 2^{-b}$
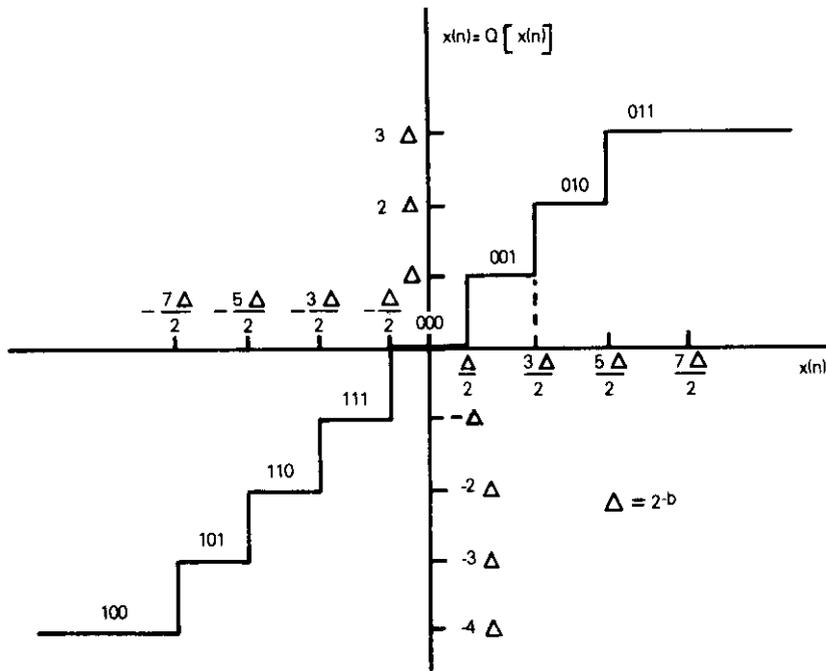
Figure 4. *Quantization in Two Bits (± 4 levels)*

is assigned to all samples exceeding $1 - 2^{-b}$ and the quantized value -1 is assigned to all samples less than $-[1 + (2^{-b}/2)]$. This clipping is undesirable and must be avoided by reducing the amplitude of the input signal.

With reference to Figure 5, the quantization process can be expressed by

$$\hat{x}(n) = Q[x(n)] = x(n) + e(n)$$

where $x(n)$ is the exact sample value, $e(n)$ the quantization, and $\hat{x}(n)$ or $Q[x(n)]$ the quantized sample value error,

$$-\frac{\Delta}{2} < e(n) \leq \frac{\Delta}{2}$$
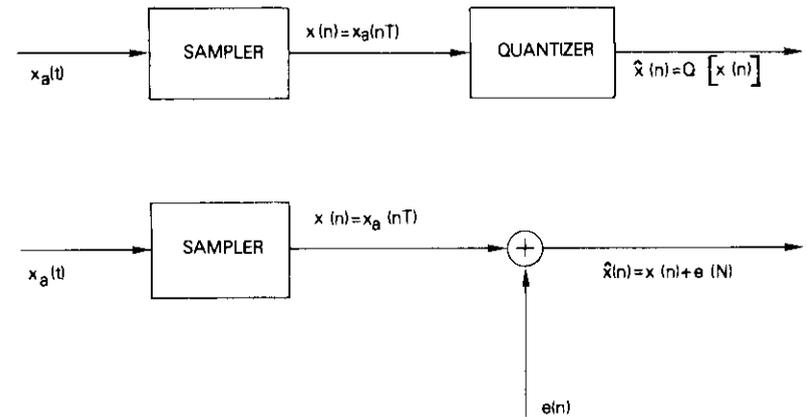
Figure 5. *Statistical Model for Quantization Noise*

where Δ is the quantization width, $\Delta = 2^{-b}$. The following assumptions [6] are usually applied to the quantization error $e(n)$:

a. The error sequence $e(n)$ is a sample sequence of a stationary random process, and is uncorrelated with the sequence of the exact sample $x(n)$.

b. The random variables of the error process are uncorrelated; hence, the error is a white noise process.

c. The probability distribution of the error process is uniform over the quantization interval.

The probability distribution of the quantization error is shown in Figure 6a. Similarly, for two's complement truncation the probability distribution is assumed to be uniform over the range of possible quantization errors in Figure 6b. Furthermore, it is assumed that error is independent of the signal. This assumption is clearly invalid for sign-magnitude truncation, since the sign of the error is always the opposite of the sign of the signal. The mean, m_e, and variance, σ_e^2, of quantization noise [6] for the two's complement system are as follows:

	m_e	σ_e^2
Truncation	$-\dfrac{2^{-b}}{2}$	$\dfrac{2^{-2b}}{12}$
Rounding	0	$\dfrac{2^{-2b}}{12}$
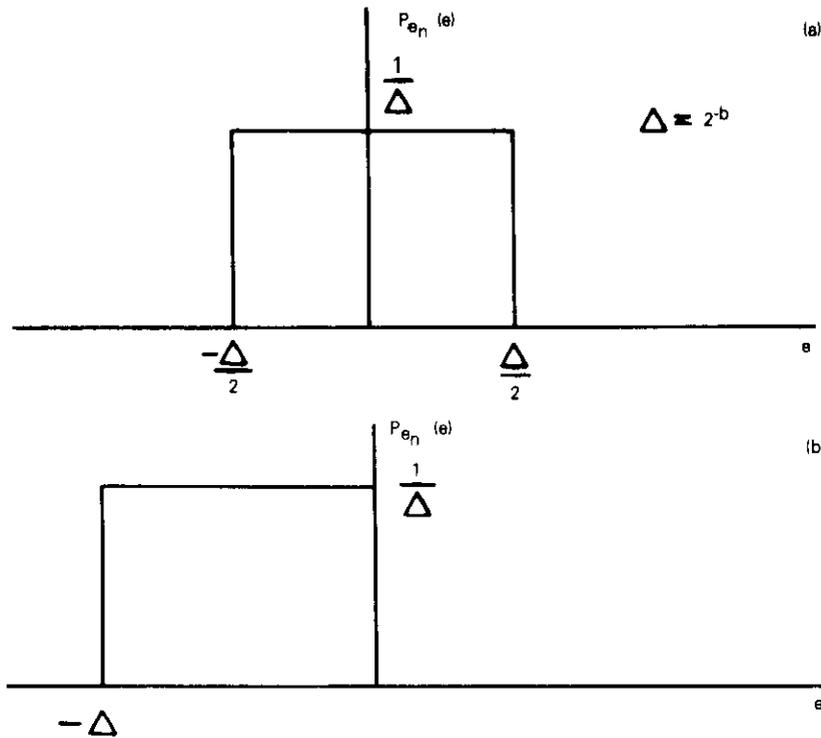
Figure 6. *Probability Distribution (a. rounding; b. truncation)*

The ratio of signal power to quantization noise power is

$$S/N = \frac{\sigma_x^2}{\sigma_e^2} = \frac{\sigma_x^2}{2^{-2b}/12} = (12)(2^{2b})\,\sigma_x^2$$

or

$$S/N = 10\log_{10}\left(\frac{\sigma_x^2}{\sigma_e^2}\right) = 6b + 10.8 + 10\log_{10}(\sigma_x^2) \quad .$$

The amplitude can be reduced by $A(0 < A < 1)$ to avoid clipping. Since the variance of $Ax(n)$ is $A^2\sigma_x^2$,

$$S/N = 6b + 10.8 + 10\log_{10}(\sigma_x^2) + 20\log_{10}A \quad .$$

Thus, S/N decreases with reduction of input. For signals whose probability distribution peaks around zero and falls off rapidly with increasing amplitude, the probability that the magnitude of a given sample will exceed three or four times the root-mean-square (rms) value of the signal is very low. Thus, if A is set at $\sigma_x/4$, S/N is given by

$$S/N = 6b - 1.24 \text{ dB} \quad .$$

Overflow

The overflow is detected in real time for parallel processors since all the bits in the addends are available at the same time. The overflow in the two's complement number system can be detected by the Boolean expression

$$\text{OVFL} = Z_S \cdot \bar{X}_S \cdot \bar{Y}_S + \bar{Z}_S \cdot X_S \cdot Y_S \tag{2}$$

where X_S and Y_S are the signs of addends and Z_S is the sign of the result. The first term is true for an overflow resulting from the addition of two large positive numbers, while the second term is true for the addition of two large negative numbers. To retain the modulo wraparound of the adder, a maximum allowable positive or negative number is loaded into the accumulator for the first or second term being true, respectively.

LSI n- × n-bit parallel multipliers

The most time-consuming operation in digital signal processing is multiplication. This section describes a parallel binary multiplication operation. The product of two n-bit fractional numbers X and Y represented in two's complement form can be written as

$$P = X_0 Y_0 - X_0 - Y_0 + X_0 \sum_{k=1}^{n} \bar{Y}_k 2^{-k} + X_0 2^{-n}$$

$$+ Y_0 \sum_{j=1}^{n} \bar{X}_j 2^{-j} + Y_0 2^{-n} + \sum_{j=1}^{n} \sum_{k=1}^{n} X_j Y_k 2^{-(j+k)}$$

where X_0 and Y_0 are the sign bits, and X_j and Y_j represent the jth bit of the corresponding numbers. The process is realized by arranging the X and Y lines perpendicularly to form a grid. At each grid intersection, an $X_j Y_k$-bit product is formed, which is then added to the sum of a similar unit in the bit column to the left and a carryout bit from the unit imme-

diately above. The results are a new sum and carryout bits. The carryout bits are passed down to the next position in this column, while the sum is fed right to an element in the column of next least significance. The array is shown in Figure 7a.

The commercially available parallel multipliers MPY-LSI series was used to implement these structures [7]. These multipliers are arranged as a 3-port device, shown in Figure 7b. The chip can operate from either a single bus or through three separate n-bit ports, where n is 8, 12, or 16. A single "round-off" pin is also available, which adds 2^{-n} to the product. Four input registers, XM, YM, ZM_L, and ZM_H, each n bits wide, are included in the LSI for holding X, Y, and low and high significant bits of the product, respectively. MPY-8 and -12 can deliver all $2n$ bits of the product simultaneously, while MPY-16 shares the Y-input leads with ZM_L. The product sign bit is supplied with both product outputs. The output is controlled by TRIL and TRIM for low and high significant products,
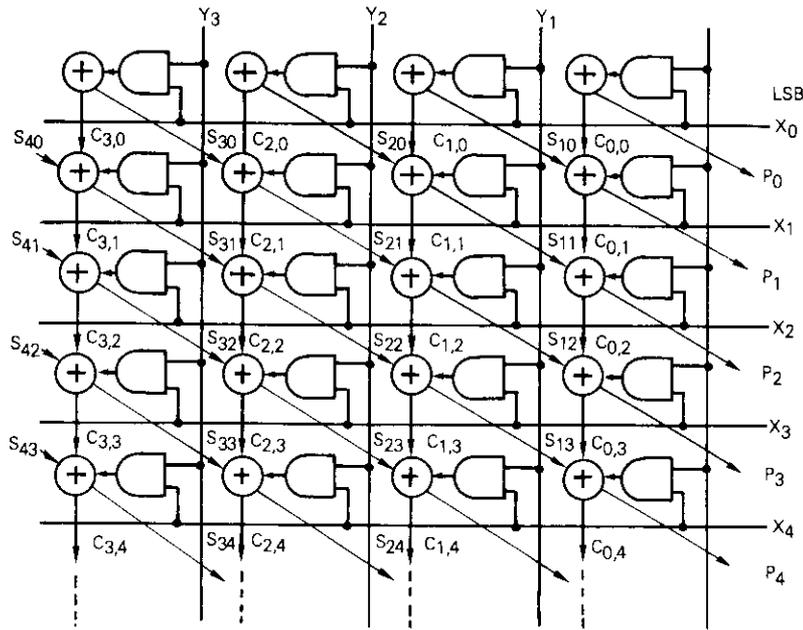
Figure 7a. *Array Multiplier*
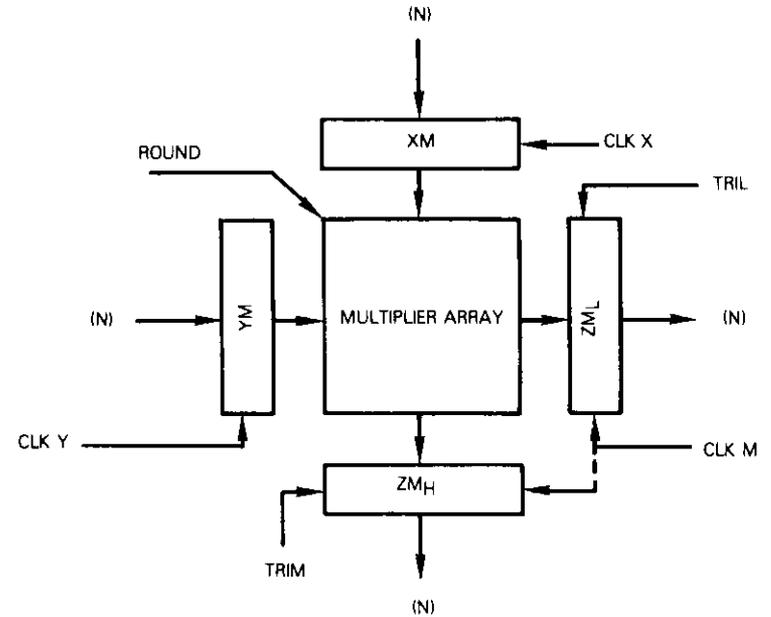
Figure 7b. *TRW's MPY Series Multipliers*

while CLKX, CLKY, CLKL, and CLKM control the loading of XM, YM, ZM_L, and ZM_H, respectively.

As soon as the XM and YM registers are loaded, computation of the product begins. After multiplication is complete, the product is latched into the output registers by CLKL and CLKM. Typical multiplication time is 130, 175, and 200 ns maximum for MPY-8, -12, and -16, respectively.

Digital filters

The transfer functions of a digital filter can be expressed as a ratio of polynomials in Z^{-1}

$$H(Z) = \frac{\sum_{i=0}^{N} a_i Z^{-i}}{1 + \sum_{i=1}^{N} b_i Z^{-i}} \tag{3}$$

where Z^{-i} represents i units of delay, and a_i and b_i are the coefficients [8].

Two major categories of filters can be derived from equation (3): recursive or infinite impulse response (IIR) filters in which the output depends on the current and past input and past output; and transversal or finite impulse response (FIR) filters in which the output depends only upon current and past input; that is, the coefficients b_i are all zeros.

IIR filters

The direct realization of equation (3) is avoided due to the severe coefficient accuracy requirements [8]. However, two types of realization are presented. The first form corresponds to a factorization of the numerator and denominator polynomials of equation (3) to produce an $H(Z)$ of the form

$$H(Z) = a_0 \prod_{i=1}^{M} \frac{\alpha_{2i}Z^{-2} + \alpha_{1i}Z^{-1} + 1}{\beta_{2i}Z^{-2} + \beta_{1i}Z^{-1} + 1}$$

where M is the integer part of $(n + 1)/2$. This is the cascade form of the digital filter; its realization is shown in Figure 8a. The second-order
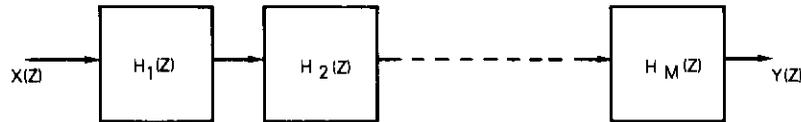
Figure 8a. *Cascade Form of Digital Filter Realization*

factors with real coefficients are usually chosen for implementation simplicity. The second-order sections are termed biquads.

The second canonical form is the parallel form in Figure 8b, which results from a partial fraction expansion of equation (1) to produce

$$H(Z) = \lambda_0 + \sum_{i=1}^{M} \frac{\lambda_{1i}Z^{-1} + \lambda_{0i}}{\beta_{2i}Z^{-2} + \beta_{1i}Z^{-1} + 1}$$

where $\lambda_0 = a_n/b_n$.

Biquad section

The transfer function of a biquad section in the Z domain is

$$H(Z) = \frac{1 + a_1Z^{-1} + a_2Z^{-2}}{1 - b_1Z^{-1} - b_2Z^{-2}} \cdot \qquad (4)$$
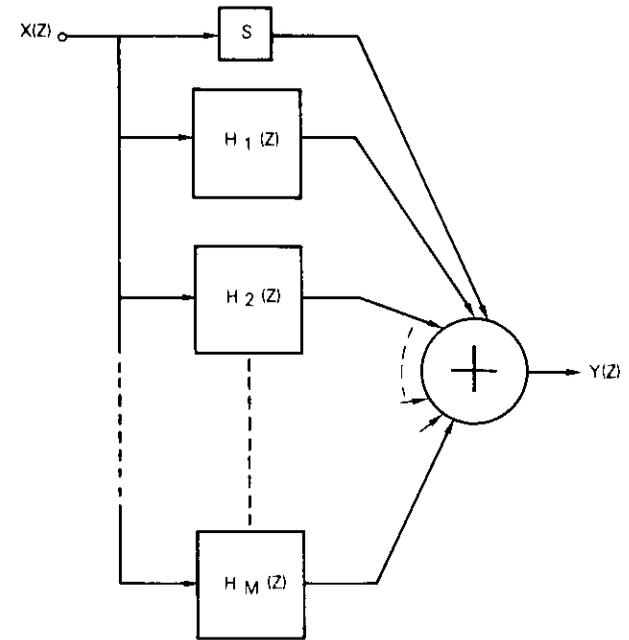
Figure 8b. *Parallel Form of Digital Filter Realization*

The following set of difference equations describes a biquad section derived from equation (4):

$$W_k = X_k + b_1W_{k-1} + b_2W_{k-2} \qquad (5a)$$

$$Y_k = W_k + a_1W_{k-1} + a_2W_{k-2} \qquad (5b)$$

where X_k is the input, Y_k is the output, and W_k is the intermediate result. This biquad section is shown in Figure 8c. From the computational point of view, the set of equation (5) can be represented as

$$\theta = \sum_{i=1}^{6} C_i\psi_i \qquad (6)$$

where C_i are the coefficients, ψ_i are the data, and θ is the result.
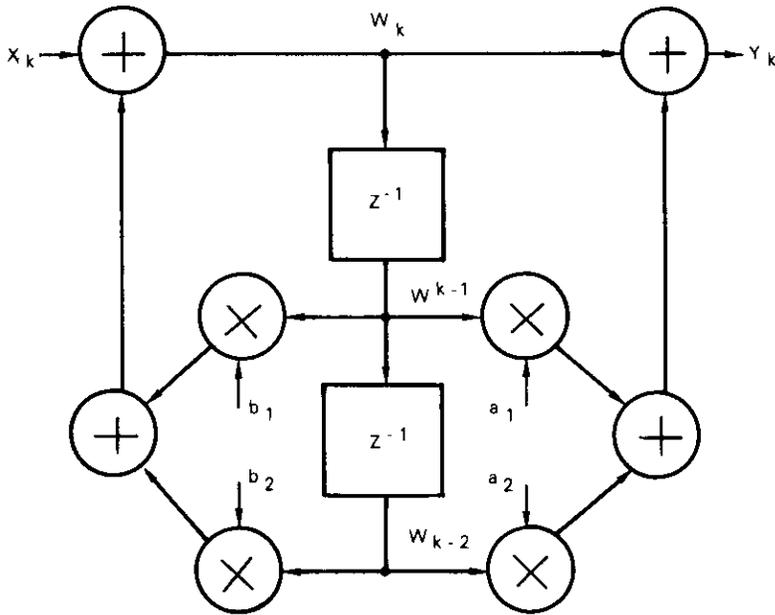
Figure 8c. *A Biquad Section*

FIR filters

The transfer function of FIR filters is given by

$$H(Z) = \sum_{i=0}^{N} a_i Z^{-i} \quad . \qquad (7)$$

Since equation (7) is essentially the same as equation (6), it may be computed by using the simple multiplying accumulator (Figure 8d).
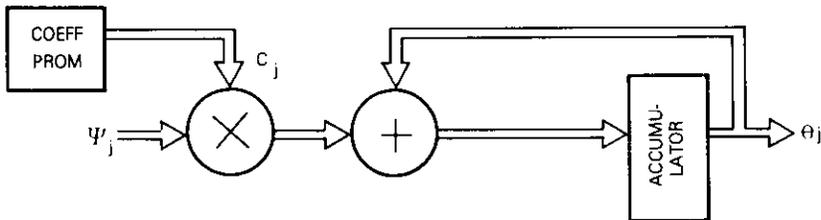
Figure 8d. *Multiply-Accumulator Structure*

Parallel arithmetic structure for digital filtering

Figure 9a is a block diagram of a general purpose arithmetic structure used for performing high-speed digital filtering [5]. This structure, which was realized on a multilayered printed circuit (PC) board (Figure 9b),
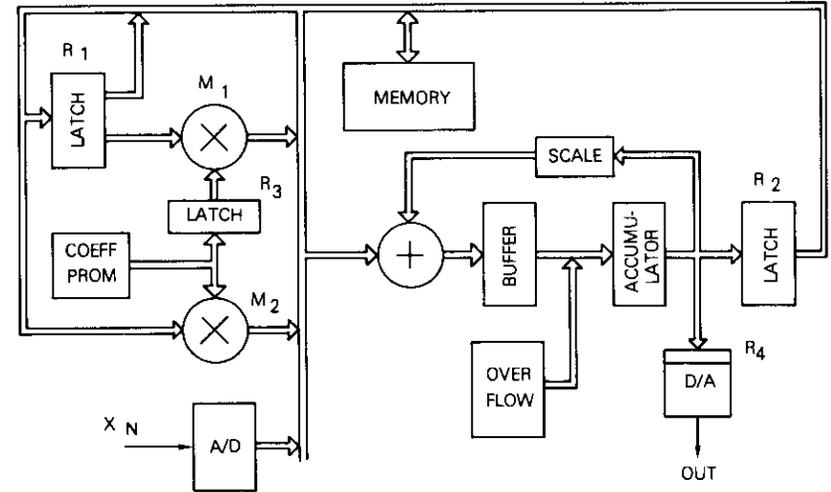
Figure 9a. *Block Diagram of the Arithmetic Processor*

uses two high-speed 16 x 16 parallel multipliers MPY16AJ, a 16-bit adder, and an accumulator with a binary scalar in the feedback loop. Four scratch-pad registers, R_1 through R_4, and an overflow detection and correction circuit are also used. The structure is designed around a tri-state bus, and a 512 x 16 RAM for intermediate storage is included on the PC board, which measures 13.5 x 19 cm. Table 1 provides the chip-power count for the structure. Forty-two chips are used, consuming 17 W of power. Four 26-pin connectors are provided for input and output data, control vectors, and memory addresses. The control is provided by the user.

Latch R_1, which has a dual output (*i.e.*, tri-state and normal) is used for loading multiplier $M1$. Latch R_3 is used to load coefficients in multiplier $M2$. This provision allows the use of a single coefficient PROM for both multipliers. Latch R_2 acts as a buffer between the accumulator and the memory and accelerates data manipulation. Latch R_4 outputs the data.
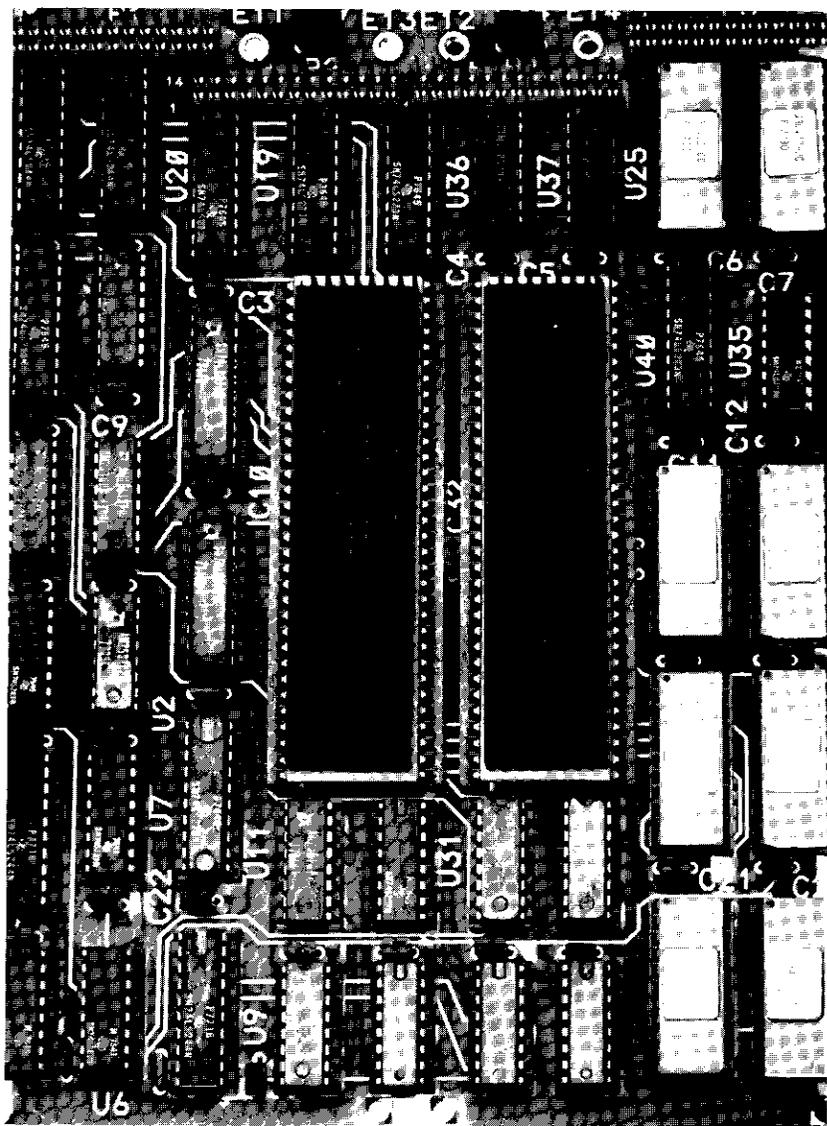
Figure 9b. *Photograph of the Arithmetic Structure*

TABLE 1. BIQUAD STRUCTURE CHIP-POWER COUNT

Component	No. of LSIs	Power (W)
Multipliers MPY16AJ	2	7.0
Address (74S283 or equivalent)	4	2.0
Latches/Buffers	22	3.0
Coefficient PROM (HM7603)	2	1.0
Scalar Circuits (AMD25S10)	4	1.0
RAM (256 × 4 organization)	8	3.0
Total	42	17.0

The overflow circuit is realized by using three tri-state buffers before the accumulator register: one contains the maximum positive number, the second contains the maximum negative number, and the third is at the output of the adder. One of these three buffers is enabled according to the condition realized by equation (2).

The binary scalar is used to limit the signal between sections and also to scale the direct accumulation when the coefficient is unity, as in the case of an elliptic filter. Since the data can be scaled in steps of 1/2 to a maximum of 1/8, two control leads are required. Control elements required for the operation of this circuit are listed in Table 2.

TABLE 2. ELEMENTS OF THE CONTROL VECTOR

Name	Function
ACLKX	Load clock for XM1
ACLKY	Load clock for YM1
ACLKZ	Load clock for ZM1
ATRIM	Output enable ZM1
BCLKX	Load clock for XM2
BCLKY	Load clock for YM2
BCLKZ	Load clock for ZM2
BTRIM	Output enable for ZM2
STROBE	Clock for loading output register
LOAD R1	Clock for loading R1
OE R1	Output enable R1
LOAD Acc.	Accumulator load clock
CLEAR Acc.	Accumulator clear signal
LOAD R2	Load clock for R2
OE R2	Output enable R2
CARRY-IN	Carry-in for the adder (for twos complement addition)
OE BUFFER	Output enable buffer in front of adder

TABLE 2. ELEMENTS OF THE CONTROL VECTOR (Continued)

OE OV	Output enable overflow circuit
SEL OV	Select maximum positive or negative numbers
XSGN	Sign for addend
YSGN	Sign for augend
ZSGN	Sign for the sum
COEF CLK	Clock for coefficient counter
CLR COEF	Clear control for coefficient counter
STACK CONTROL	Stack control for coefficient PROM
X_{in} EN	Enable input buffer
OE MEM	Output enable memory
WE MEM	Write enable memory
S_0 $\}$	
S_1	Scalar control

Simulation of a single biquad section IIR filter

For applications requiring very high speed (2-MHz sampling rate) and moderate filtering requirements, a single biquad section [equation (4)] of an IIR filter may be simulated with the arithmetic structure and the program given in Table 3 in the control memory. Multiple operations can be performed simultaneously.

TABLE 3. PROGRAM FOR SIMULATING A SINGLE BIQUAD
SECTION OF AN IIR FILTER

Operation*	Interpretation
1. $0 \rightarrow Acc$, $b_2 \rightarrow R_3$	Clear accumulator and load coefficient b_2 in register R_3.
2. $X_K + [Acc] \rightarrow Acc$ $[R_1] \rightarrow XM1$, $[R_2] \rightarrow XM2$ $[R_3] \rightarrow YM1$; $b_1 \rightarrow YM2$	Load input and load multipliers.
3. $[Acc] + [ZM1] \rightarrow Acc$ $a_2 \rightarrow R_3$ 4. $[Acc] + [ZM2] \rightarrow Acc$ $[R_3] \rightarrow YM1$, $a_1 \rightarrow YM2$	Calculate W_k [equation (5a)].
5. $[Acc] \rightarrow R_2$; $[R_2] \rightarrow R_1$	$W_k \rightarrow W_{k-1}$; $W_{k-1} \rightarrow W_{k-2}$
6. $[Acc] + [ZM1] \rightarrow Acc$ 7. $[Acc] + [ZM2] \rightarrow Acc$	Calculate feedforward loop [equation (5b)]
8. $[Acc] \rightarrow R_4$	Output sample.

*[ ] indicates the content of the register.

In this case, eight clock periods are required to compute one output sample Y_k. Thus, the system clock rate will be eight times the sampling frequency. Since the hardware operation is limited to 16 MHz, a sampling frequency of 2 MHz is possible. During the first clock period, the accumulator is cleared and coefficient b_2 is loaded into register R_3 from the coefficient memory. Operations 2 through 4 compute equation (5a). During the second clock period the input X_k is loaded into the accumulator, and at the same time, the contents of registers R_1 and R_2 are loaded into XM registers of multipliers $M1$ and $M2$, respectively. Also, the contents of R_3 are loaded into $YM2$ (YM register of multiplier $M2$) and coefficient b_1 is loaded into $YM2$ (YM register of multiplier $M2$) from the coefficient PROM. In the steady state, register R_1 will contain W_{k-2} and register R_2 will contain W_{k-1}; thus, the two multiplications required by equation (5a) are initiated in this step.

In the third clock period, the contents of the accumulator (which are X_k at this time) are added to the output of the multiplier $M1$, and the result is loaded into the accumulator. Step 4 adds the output of multiplier 2 to the contents of the accumulator. At the same time, two new multiplications are started via loading R_3 into $YM1$ and coefficient a_1 into $YM2$. The contents of the XM registers are held, as previously indicated.

In step 5 the contents of the accumulator are moved to R_2 and the contents of R_2 are moved to R_1, thereby accomplishing a unit delay for the intermediate results W_k. Steps 6 and 7 compute equation (5b) by accumulating the results of the second multiplication initiated in step 4. In step 8, the result Y_k is read out in register R_4.

In this case, the control circuit will consist of a divide-by-8 counter and a PROM with $[\Phi] = 16$ wide. Figure 10 is a typical timing diagram. It should be noted that all of the control elements shown in Table 1 are not utilized.

Multiplexing over N filters

The single biquad section described in the previous section can be multiplexed over N filters by utilizing the memory on the PC board. Two memory locations are assigned per filter. An efficient program for computing a biquad is designed and looped around N times. This looping is counted by a counter whose output is given by q. The program for this filter operation is given in Table 4.

Again, steps 2 through 8 perform a biquad section, while steps 1 and 9 provide the facility for looping. The only difference in the program is that the intermediate results are stored in and retrieved from a RAM instead of registers. The looping counter can also provide the memory
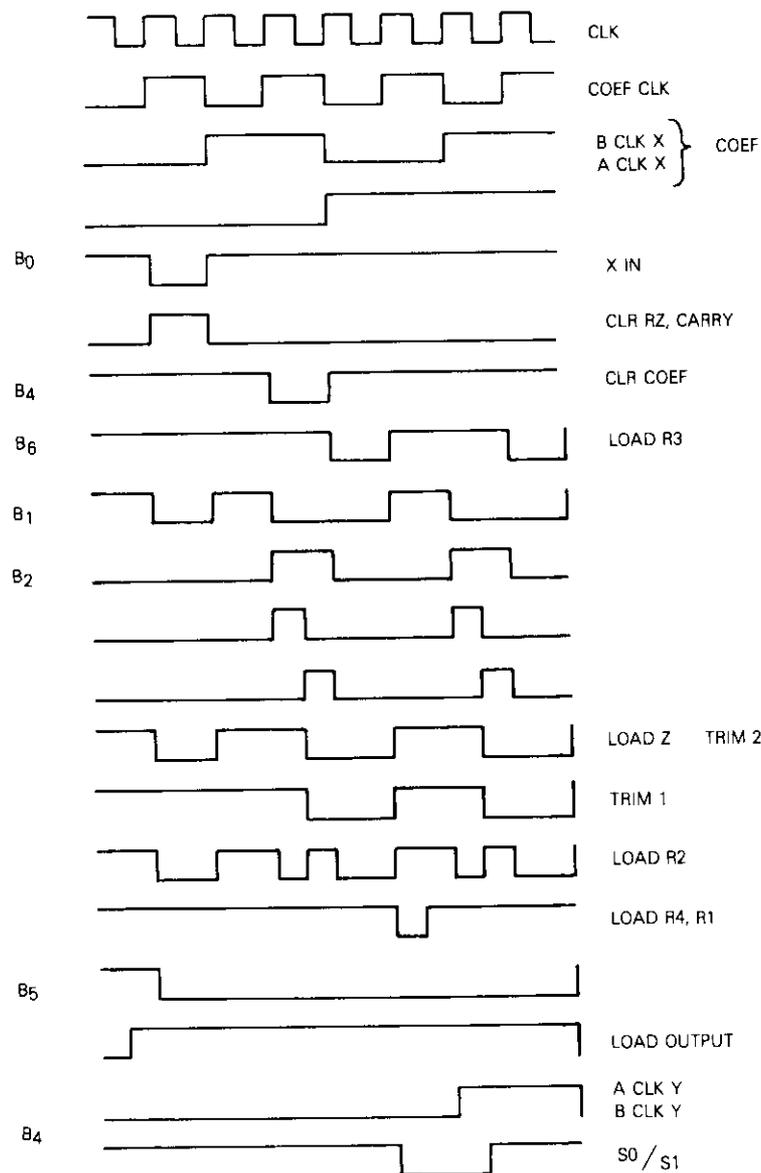
Figure 10. *Timing Diagram of Control PROM for Single Biquad Section Filter*

TABLE 4. PROGRAM FOR COMPUTING A BIQUAD TO ACCOMMODATE W_k AND W_{k-1}

Operation	Interpretation
1. $q = 0$	Initialize.
2. $0 \rightarrow Acc$	Clear accumulator and load.
$\quad M[W_{k-1}^q] \rightarrow R_1; b_1 \rightarrow R_3$	Load R_1 and R_3.
3. $X_K + [Acc] \rightarrow Acc$	
$\quad M[W_{k-2}^q] \rightarrow XM2; [R_1] \rightarrow XM1$	Load input and the multiplier.
$\quad [R_3] \rightarrow YM1; b_2 \rightarrow YM2$	
4. $[ZM1] + [Acc] \rightarrow Acc$	⎫
$\quad a_1 \rightarrow R_3; [R_1] \rightarrow M[W_{k-2}^q]$	⎬ Calculate W_k; $W_{k-1} \rightarrow W_{k-2}$.
5. $[ZM2] + [Acc] \rightarrow Acc$	⎪
$\quad [R_3] \rightarrow YM1; a_2 \rightarrow YM2$	⎭
6. $[Acc] \rightarrow R_2$	⎫
$\quad [ZM1] + [Acc] \rightarrow Acc$	⎪ Calculate feedforward loop $W_k \rightarrow W_{k-1}$ for
7. $[R_2] \rightarrow M[W_{k-1}^q]$	⎬ next cycle.
$\quad [ZM2] + [Acc2] \rightarrow Acc$	⎭
8. $[Acc] \rightarrow R_4$	⎫ Output result.
$\quad q + 1 = q$	⎭
9. Repeat steps 2–9 until $q = N$.	

*$M[W_{k-1}^q]$ are the contents of memory location addressed by W_{k-1}^q.

address. In this case the control circuit is shown in Figure 11. The system clock drives a counter whose output provides the address for the control PROM. One control PROM output updates the channel counter. Each channel is allocated two memory locations for storing W_k and W_{k-1}; therefore,
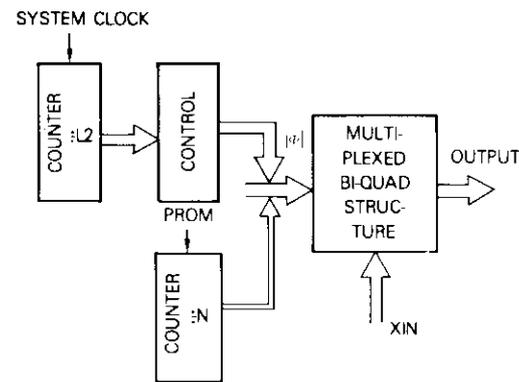
Figure 11. *Block Diagram for Multiplexed Filter*

a control element for this selection is also needed and provided as an LSB for the memory address.

Multisection IIR filter

The preceding program can be applied to multisection IIR filters with a change in looping instructions. Cascade filter realization (Figure 4a) requires the scaled output of previous sections to become the input for the next section. This is accomplished by retaining the contents of the accumulator and disabling the accumulation for the new input X_k. New coefficients for each section are also needed; these coefficients are obtained by either increasing the program length to include M sections or looping over the same program but changing the coefficients and memory address for intermediate results.

Parallel realization (Figure 4b) requires holding the input for M sections and retaining the contents of the accumulator between sections. This is accomplished by modifying the program according to the requirements.

Transversal filter

The transfer function for the FIR filter is realized by eliminating the feedback loop in the arithmetic structure. This is accomplished by disabling the loading of the R_2 register while the input X_k is loaded directly into the multiplier and stored in the memory. A simple program can be written to perform two multiplications simultaneously, and the symmetrical nature of transversal filter impulse response can be utilized for simplicity of addressing. For example, the new input may always be written at memory location $(N - K)$, $K = 0, 1, \ldots, N$, after the original content of $M[N - K]$ has been read into the multiplier.

A practical example

A single sixth-order (3-biquad-section) elliptic filter was designed with the bilinear transformation method [8] to be used in the FDM/TDM transmultiplexer [1]. A computer-simulated frequency response is shown in Figure 12a, with a pole-zero configuration in Figure 12b and an impulse response in Figure 12c. The filter has a cutoff at 0.22 F_s, where F_s is the sampling frequency. The out-of-band rejection is 49 dB. (These responses were obtained without truncating the intermediate results.) The system requires 60 channels to be multiplexed over this filter with $F_s = 8$ kHz. The coefficient PROM organization is 32 × 8 to accommodate 12 coefficients,

a. frequency response

b. pole-zero configuration on Z plane
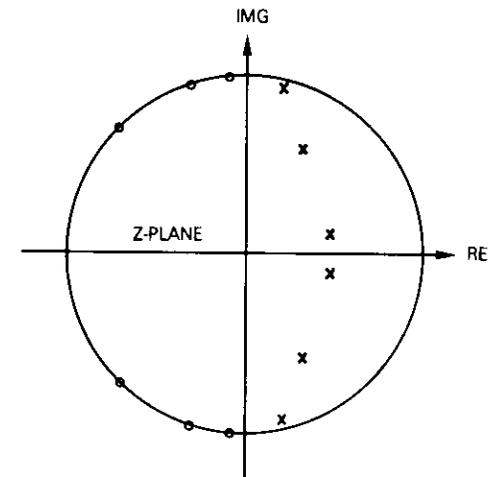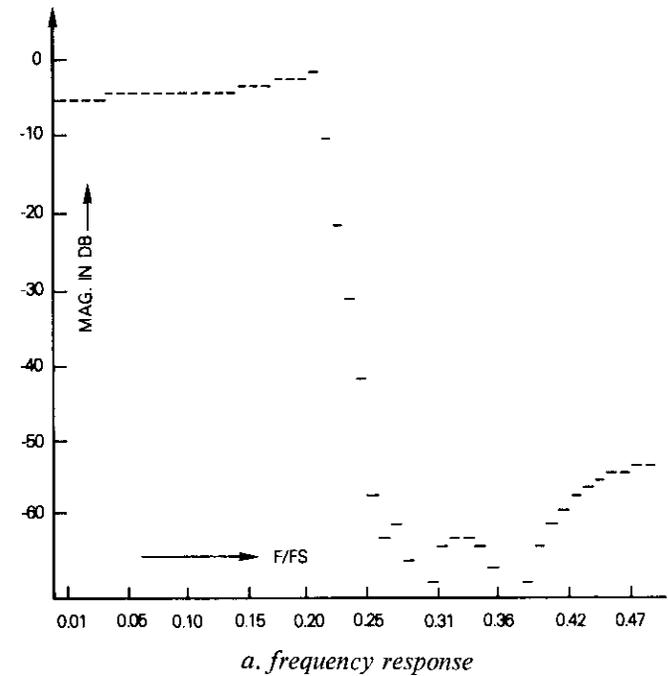
Figure 12. *Simulated Characteristics of a Low-Pass Filter*
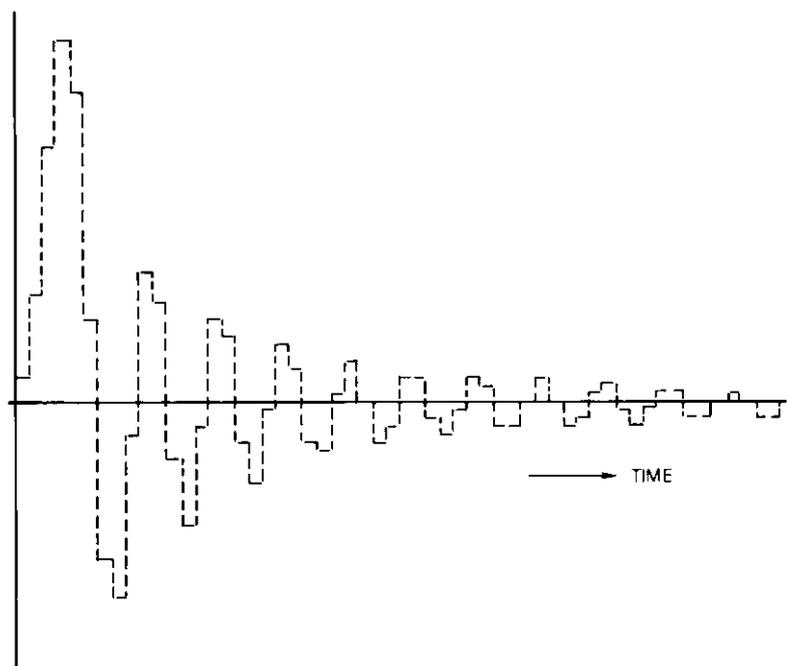
c. impulse response

Figure 12 *(continued) Simulated characteristics of a Low-Pass Filter*

which are listed in Table 5. The control PROM organization is 32×16, providing a $[\Phi]$ vector with 16 elements. The internal computation is rounded off to 16 bits with saturating overflow [5]. The number system used is two's complement, fixed-point, 16-bit.

In terms of simplicity in controls, all three biquad sections are treated as a single filter. Therefore, a new program requiring 32 clock periods or steps may be written. (The number 32 was selected primarily because of its binary nature.) A division by two was also implemented between sections to limit the amplitude. Although this program is not optimum, it constitutes a meaningful practical example. The composite program (three sections) was multiplexed over 64 (again, binary) channels. A control circuit similar to Figure 11 was used, in which counter A was divide-by-32, while counter B was divide-by-64 to accommodate the above multiplexing. Again, six memory locations (two per section) were assigned per filter. Thus, three LSBs for memory addresses representing these loca-

TABLE 5. LIST OF COEFFICIENTS

	Decimal	Binary	
		MSB	LSB
Section I			
B1	+0.96875	0 0.1 1 1 1 1 0 0	
B2	−0.34375	1 1.1 0 1 0 1 0 0	
A1	+1.4375	0 1.0 1 1 1 0 0 0	
A2	+1.0	0 1.0 0 0 0 0 0 0	
Section II			
B1	+0.671875	0 0.1 0 1 0 1 1 0	
B2	−0.6875	1 1.0 1 0 1 0 0 0	
A1	+0.625	0 0.1 0 1 0 0 0 0	
A2	+1.0	0 1.0 0 0 0 0 0 0	
Section III			
B1	+0.453125	0 0.0 1 1 1 0 1 0	
B2	−0.921875	1 1.0 0 0 1 0 1 0	
A1	+0.1875	0 0.0 0 1 1 0 0 0	
A2	+1.0	0 1.0 0 0 0 0 0 0	

tions were generated by the control PROM. Figure 13 shows a complete program in the form of a timing diagram. Table 6 represents the chip-

TABLE 6. CHIP-POWER COUNT FOR THE CONTROL CIRCUIT

	Chips	Power (W)
Buffers and drivers	4	1.0
Control PROM	3	2.0
Latches	3	1.0
Gates, etc.	2	0.5
Total	12	4.5

power count for implementing the control function; twelve chips are used, consuming 4.5 W.

For demonstration, an analog-to-digital (A/D) converter and digital-to-analog (D/A) converters are also added, along with channel selection logic. The entire control function has been implemented on a wire-wrap board. The complete filter, along with A/D and D/A converters, is shown in Figure 14. Figure 15 comprises the oscilloscope photograph for impulse

	FUNCTION
	LSB0
	LSB1
	LSB2
	LOAD R1
	LOAD Y
	COEFF CLOCK
	LOAD R3
	LOAD X
	LOAD Z
	TRIM 2
	TRIM
	LOAD R4
	RESET COEFF COUNTER
	OUTPUT EN R1
	OUTPUT EN R4
	OUTPUT EN REC MEM
	WRITE EN REC MEM
	OUTPUT ENABLE
	X BUFFER
	BYPASS FILTER
	D/A CLOCK
	CLEAR ACC
	LOAD ACC
	SCALING CONTROLS
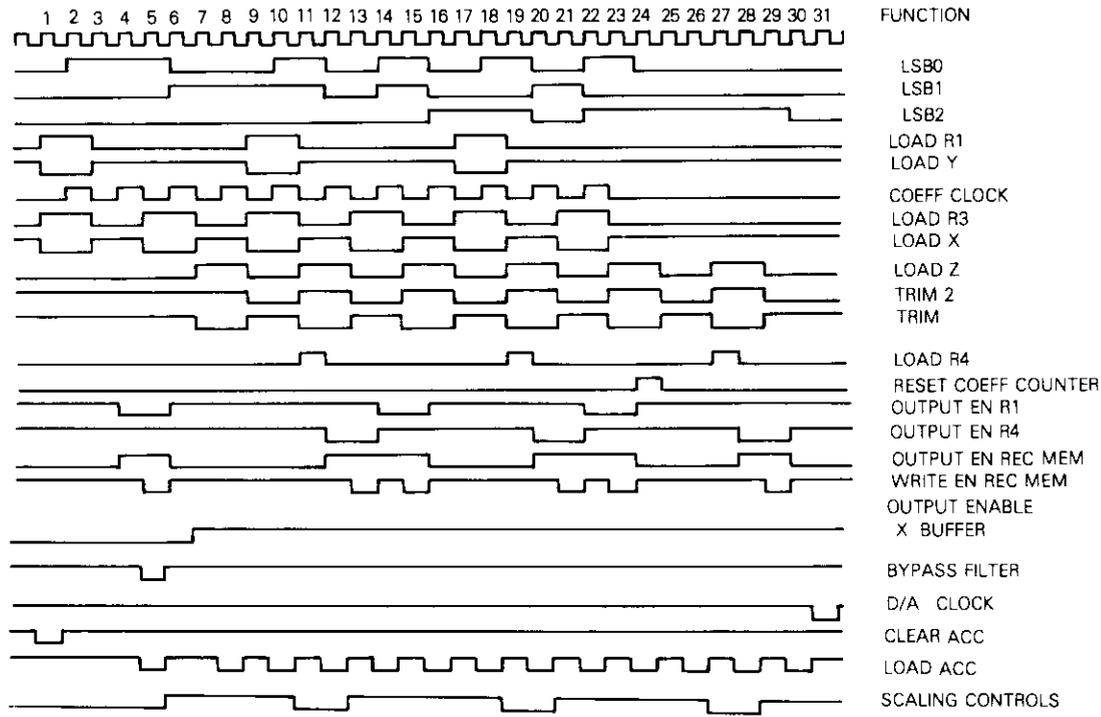
Figure 13. *Timing Diagram of a Composite 3-Biquad-Section Filter*
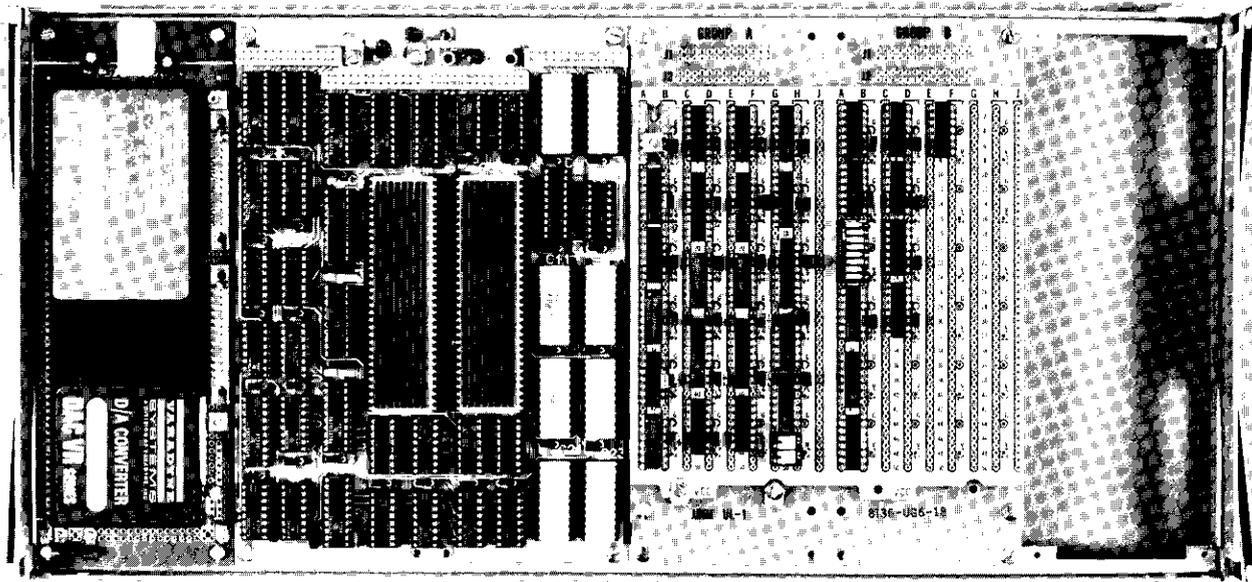
Figure 14. *3-Biquad-Section Filter*
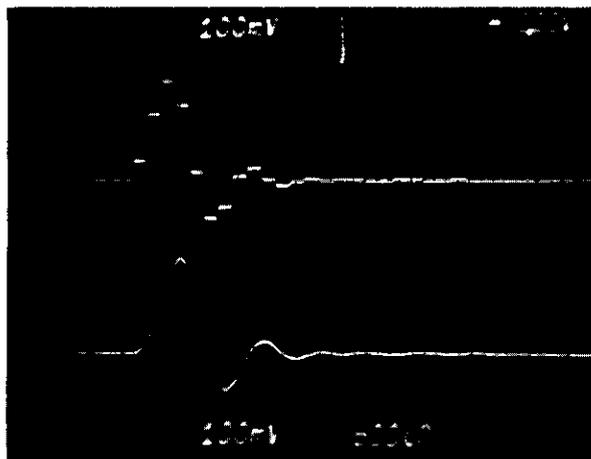
a. impulse response
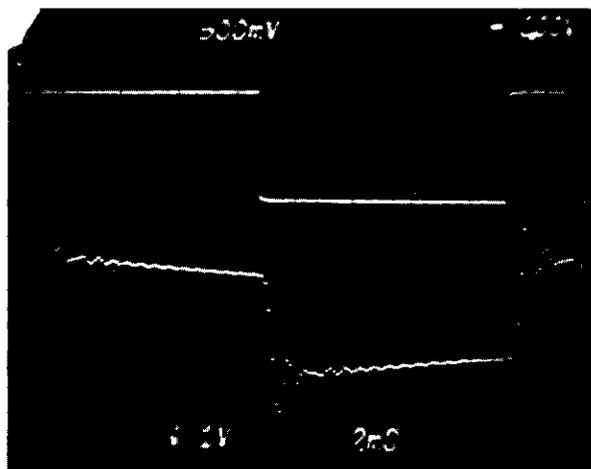
b. square wave response

Figure 15. *Low-Pass Filter Responses*
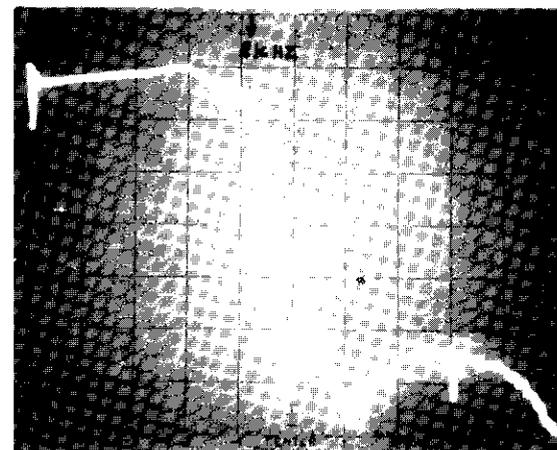
c. frequency response (vertical scale: 10 dB/div, horizontal scale:
500 Hz/div, $F_s = 8$ kHz)

Figure 15. (continued) *Low-Pass Filter Responses*

response, square wave response, and frequency response. The results correspond to the simulated results.

Background and description of the FFT process

Discrete Fourier transform

A Fourier representation of a finite-length sequence, corresponding to samples of the Fourier transform of this signal equally spaced in frequency, is defined as a discrete Fourier transform (DFT) of the sequence.

In a periodic sequence $X(n)$ with period N such that $X(n + KN) = X(n)$ for any integer value of K, $X(n)$ can be represented by a complex exponential sequence with frequencies that are integer multiples of the fundamental frequency $2\pi/N$. Thus,

$$X(n) = \frac{1}{N} \sum_{k=0}^{N-1} X(K) \, W_N^{-nk} \tag{8a}$$

with $n = 0, 1, \ldots, N - 1$ and $W_N = e^{-j2\pi/N}$. The coefficients $X(K)$ are obtained by the relationship

$$X(K) = \sum_{n=0}^{N-1} X(n) \, W_N^{nk} \quad , \qquad K = 0, 1, \ldots, N-1 \quad . \qquad (8b)$$

Fast Fourier transform

Equation (8) shows that, for an N-point DFT, $(N-1)^2$ complex multiplications and $N(N-1)$ complex additions are required. The principle of the fast Fourier transform (FFT) is to divide the original N-point sequence into shorter sequences whose DFTs can be combined to give the original N-point sequence. For a general case, it can be assumed that N is a composite integer $(N = \gamma_1 \times \gamma_2 \times \gamma_3, \ldots, \gamma_4)$, where γ_i is a set of factors which are not necessarily prime factors of N. It can be shown that the number of computational operations is proportional to

$$\sum_{i=1}^{k=\mu} \gamma_i \quad .$$

(The proportionality considers that $W^0 = 1$ such that complex multiplication involving W^0 reduces to complex additions.) If the factors of N are equal to γ, the algorithm for computing the DFT is called a radix-γ algorithm. When factors are different, the algorithm is called a mixed radix algorithm. A special case in which $i = 2$ for all i is called a radix-2 algorithm, such that

$$N \sum_{i=1}^{\mu} \gamma_i \rightarrow N \log_2 N \quad .$$

The algorithm described above is called decimation in time (DIT), since at each stage of the process the input sequence (*i.e.*, time sequence) is divided into smaller sequences. For a radix-2 form of the DIT algorithm, the most fundamental operation (butterfly) is

$$X = A + W^k B \quad , \qquad Y = A - W^k B \qquad (9a)$$

in which the two input points, A and B, are combined to give two output points, X and Y. Another form of butterfly is obtained by solving equation (9a) for A and B in terms of X and Y and by eliminating 0.5 and replacing W^{-k} by W^k such that

$$A = X + Y \quad , \qquad B = (X - Y) \, W^k \quad . \qquad (9b)$$

This process of computing the FFT is known as decimation in frequency (DIF).

Any of the basic forms can be implemented so that each computed result can be stored in the memory which contained input data that are no longer needed. This implementation, which is termed an in-place algorithm, is shown in Figure 16a. Another form of algorithm shown in Figure 16b
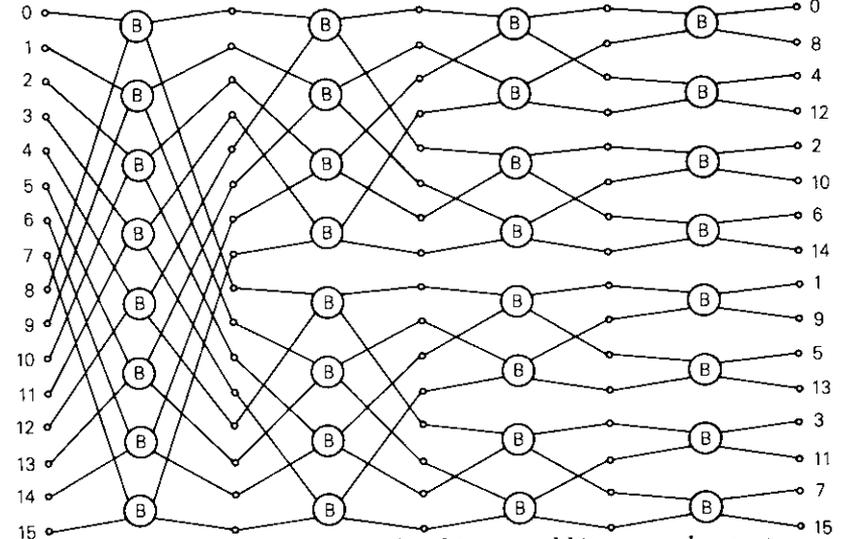
a. 16-point in-place FFT, ordered input and bit-reversed output
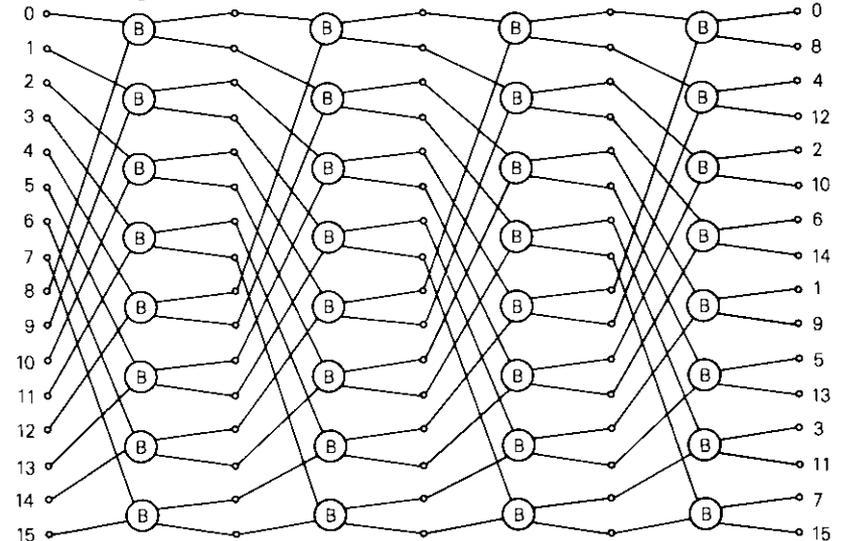
b. 16-point constant geometry FFT, ordered input and bit-reversed output

Figure 16. *Two Basic Geometries of FFT*

uses constant indexing; however, the butterfly results are not stored at the locations formerly occupied by the input data. This algorithm, generally known as the constant or fixed-geometry algorithm, uses twice the memory of the in-place algorithm. Unfortunately, any of the above FFT computations produces scrambled data. For radix-2, this scrambling can be corrected by bit reversing the index. Also, it should be noted that the ordered input data will be bit reversed, while bit-reversed input data will provide an ordered output. Bit-reversed indices are shown in Table 7. A

TABLE 7. BIT-REVERSED INDICES

Index	Binary Representation	Bit-Reversed Binary	Bit-Reversed Index
0	000	000	0
1	001	100	4
2	010	010	2
3	011	110	6
4	100	001	1
5	101	101	5
6	110	011	3
7	111	111	7

radix-2 N-point (where N is a binary number) FFT will require m iterations or passes, where $m = \log_2 N$. The frequency resolution of the spectrum is given by $\Delta f = F_s/N$, where F_s is the sampling frequency and N is the number of input data points. The sampling interval is $\Delta T = 1/F_s$. The time required to supply the FFT with N samples is $T = N \times \Delta T$.

A high-speed, low-power FFT processor may be implemented around a single high-speed butterfly (HSB). The algorithm for the FFT is chosen as radix-2, DIF and fixed- or in-place geometry. A detailed description of the FFT is provided in Reference 9. DIF computation involves six additions and four multiplications. The additions are performed prior to multiplications, and the multiplier delay is used for storing the data in the memory. The DIF butterfly is characterized by the following set of equations:

$$P' = \tfrac{1}{2}(P + Q) \tag{10a}$$

$$Q' = \tfrac{1}{2}(P - Q) \times W \tag{10b}$$

where P' and Q' are two complex points generated by the arithmetic process and W is a complex coefficient given by equation (8). The con-

stant $1/2$ is included to prevent the overflow in the addition process.

These two new points are stored sequentially in the memory, and $N/2$ such operations are performed to produce a complete new array of N points. This process is termed a pass. The new array is processed again until $\log_2 (N)$ passes are completed. The output array thus produced is the DFT of the input data. Twice the memory capacity is required for reading and storing intermediate results. In a design where $N = 128$, sixty-four butterflies are performed and seven passes are required. During pass 1, input data are supplied by the input buffer and the results are stored in the FFT memory. Passes 2 through 6 utilize the FFT memory for reading data and storing results. During pass 7, data are read from the FFT memory and results are stored in the output buffer. Figure 17 is a block diagram of the complete processing cycle.

High-speed butterfly

The high-speed butterfly performs the complex arithmetic operation described by equation (10), which can be divided into its real and imaginary parts as follows:

$$Re(P') = \frac{Re(P)}{2} + \frac{Re(Q)}{2} \tag{11a}$$

$$IMG(P') = \frac{IMG(P)}{2} + \frac{IMG(Q)}{2} \tag{11b}$$

$$LC = \frac{Re(P)}{2} - \frac{Re(Q)}{2} \tag{11c}$$

$$LD = \frac{IMG(P)}{2} - \frac{IMG(Q)}{2} \tag{11d}$$

$$Re(Q') = LC \times Re(W) + LD \times [\mp IMG(W)] \tag{11e}$$

$$IMG(Q') = LC \times [\pm IMG(W)] + LD \times Re(W) \tag{11f}$$

where $\pm$ in equations (11e) and (11f) represents forward and inverse transforms, respectively. Addition and multiplication are performed simultaneously, and the delay of the multiplication process is utilized for storing and retrieving intermediate results.

Figure 18 is a block diagram of the high-speed butterfly. It is composed
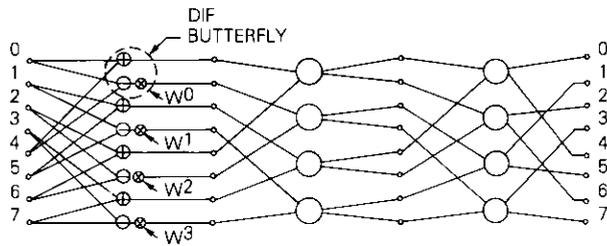
a. 8-point constant geometry FFT flow diagram
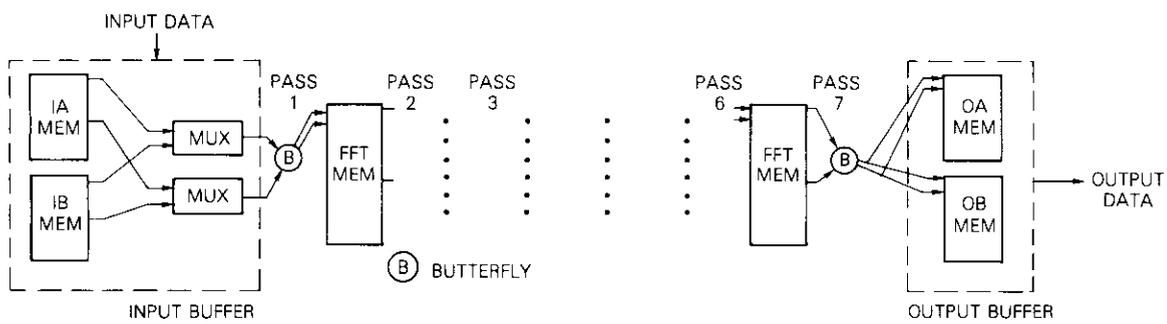
b. implementation of FFT processor

Figure 17. *Block Diagram of the FFT Process*

$$P' = P + Q$$
$$Q' = (P - Q) \times W$$
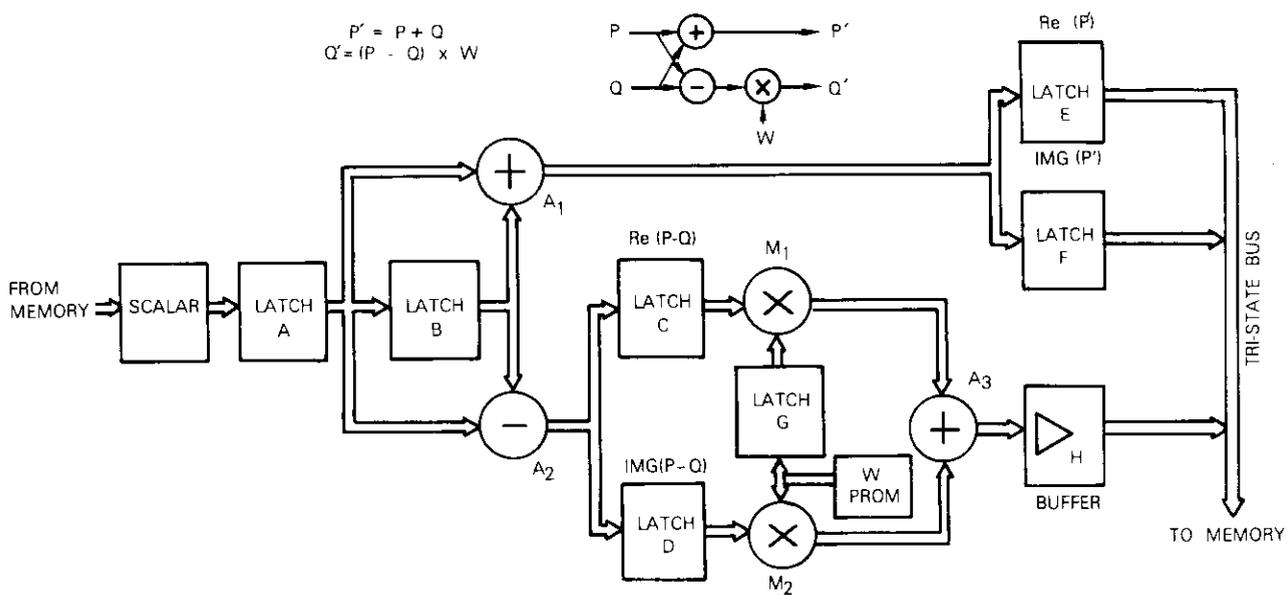
Figure 18. *Block Diagram of a High-Speed Butterfly*

of three 16-bit parallel adders labeled $A1$, $A2$, and $A3$; two parallel 16×16 multipliers (MPY16AJ), $M1$ and $M2$; and seven registers marked A through G for holding intermediate results or data. Registers E, F, and buffer H have tri-state outputs for selective storage in the memory. The basic butterfly operation requires eight clock periods and more than one operation is carried out per clock period. Four multiplications are achieved by loading the XM registers of $M1$ and $M2$ with LC and LD [equations (11c) and (11d), respectively]. The YM registers $M1$ and $M2$ are loaded with coefficients from latch G and from the output of the coefficient PROM, respectively. Latch G is also loaded from the coefficient PROM prior to the loading of the multipliers according to equations (11e) and (11f).

A pipeline operation is performed for which the sum and difference were calculated [equations (11a)–(11d)] during a previous butterfly cycle; the results are used for multiplication [equations (11e) and (11f)] in the current cycle. The scalar performs a divide-by-two as required by equation (10) to prevent the overflow.

During the first clock period, $Re(P')$ is stored in the memory from latch E. The contents of latch E are computed according to equation (11a) in the previous butterfly cycle. The contents of latches C and D [LC and LD are computed according to equations (11c) and (11d), respectively] are loaded into the XM register of multipliers $M1$ and $M2$, respectively. The contents of latch G [$Re(W)$] and the coefficient PROM output [$+IMG(W)$] are loaded into the YM registers of $M1$ and $M2$, respectively. The content of register XM of the multipliers (internal to the LSI) does not change for the rest of the butterfly cycle.

During the second clock period, latch F [$IMG(P')$] is stored in the memory. $IMG(W)$ from the coefficient PROM is loaded into latch G for the next multiplication, and $Re(W)$ is put on the output of the coefficient PROM. During the third clock period, $Re(P)$ is loaded into latch A from the memory, and during the fourth, the contents of latch A are pushed into latch B and $Re(Q)$ from memory is loaded into A. The results of the first multiplication are clocked out while the YM registers of $M1$ and $M2$ are loaded from G and the coefficient PROM, respectively, and a second multiplication is started. During the fifth clock period, the sum and difference [$Re(P')$ and LC] are loaded into latches E and C, respectively; latch A is loaded with $IMG(P)$ from memory. The sixth clock period allows the contents of A to be pushed into B, and A to be occupied by $IMG(Q)$. Also, $Re(W)$ is stored in G for the next cycle. During the seventh cycle, the sum and difference [$IMG(P')$ and LD] are loaded into F and D, respectively. At this time, the $Re(Q')$ is loaded into the memory by enabling

buffer H. During the eighth clock period, $IMG(Q')$ is loaded into the memory. The summarized algorithm is given in Table 8.

TABLE 8. SUMMARIZED ALGORITHM*

Clock No.	Operation
1	$[E] \rightarrow MEM$; $[C] \rightarrow M1$; $[D] \rightarrow M2$; $[G] \rightarrow M1$; $\pm IMG(W) \rightarrow M2$
2	$[F] \rightarrow MEM$; $\pm IMG(W) \rightarrow G$
3	$Re(P) \rightarrow A$
4	$Re(Q) \rightarrow B$; $[A] \rightarrow B$; $[G] \rightarrow M1$; $Re(W) \rightarrow M2$
5	$IMG(P) \rightarrow A$; $[A] + [B] \rightarrow E$; $[A] - [B] \rightarrow C$
6	$IMG(Q) \rightarrow A$; $[A] \rightarrow B$; $Re(W) \rightarrow G$
7	$[A] + [B] \rightarrow F$; $[A] - [B] \rightarrow D$; $[H] \rightarrow MEM$
8	$[H] \rightarrow MEM$

*[ ] indicates register contents.

The control circuit is implemented by a 32×8 PROM (HM 7603). Only 16 locations are used, the first eight for initialization, and the next eight for the routine program. Figure 19 is the timing diagram for the control program. The control PROM also provides an update clock for the coefficient memory address generation circuit.

The coefficient PROM is divided into four quadrants for simple address generation and quick transition from FFT to inverse fast Fourier transform (IFFT). Figure 20 is a block diagram of the coefficient address generation circuit. The counter is a divide-by-$4N$ binary counter which is updated four times every butterfly, where N is the number of FFT points. The two LSBS of the counter provide the two MSBS of the address for the coefficient PROM. For the FFT, the sequence is real, $-$imaginary, imaginary, and real; for the IFFT, the sequence becomes real, imaginary, $-$imaginary, and real. This change is accomplished by reversing the two address MSBS of the coefficient PROM. For address vector A_i ($i = 0$ through K) the sequence of the coefficient is generated by enabling A_0 to $A_K[K = \log_2 (N/4)]$ in pass 1, A_1 to A_K in pass 2, A_2 to A_K in pass 3, etc. until pass $\log_2 N$ is completed, in which only A_K is enabled. This method eliminates the requirement of a very large PROM. The contents of the coefficient PROM, which is organized as 256 words $\times$ 12 bits, are given in Table 9.

The basic butterfly operation is performed in 480 ns at a 16-MHz clock. A real-time, 128-complex-point FFT capable of performing a 256-point FFT on real input or a 128-point FFT on two real channels simultaneously has been designed using the ideas presented in this discussion. The al-
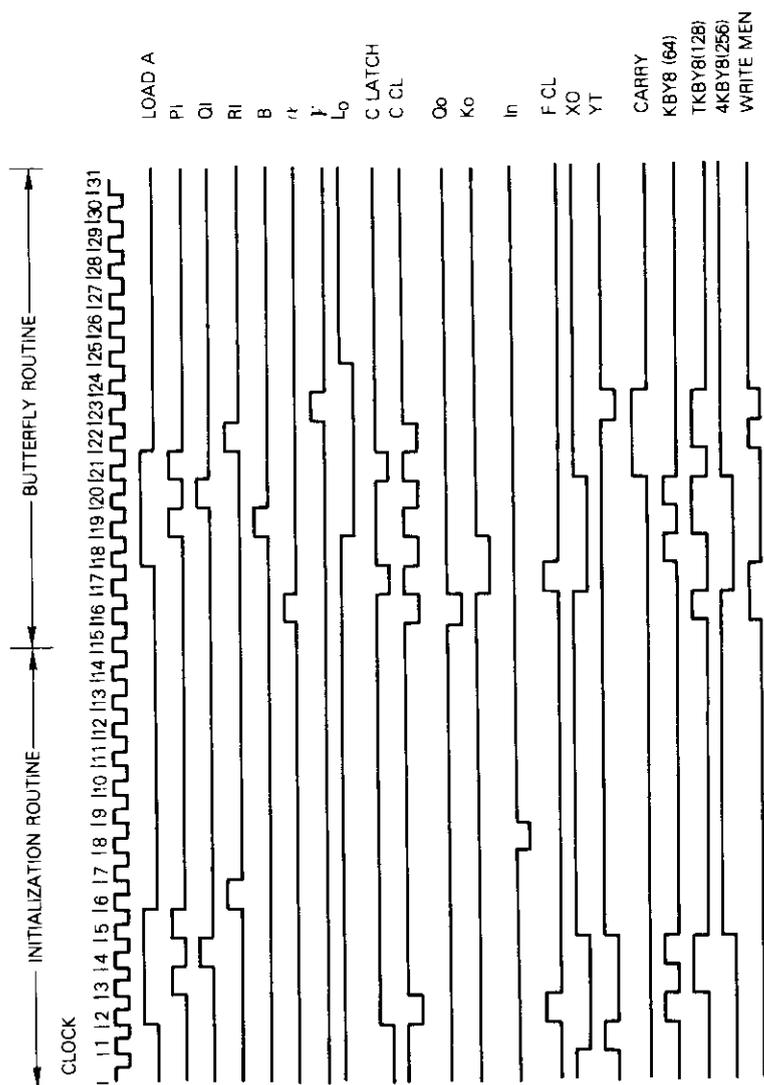
Figure 19. *Timing Diagram of FFT Butterfly Control*
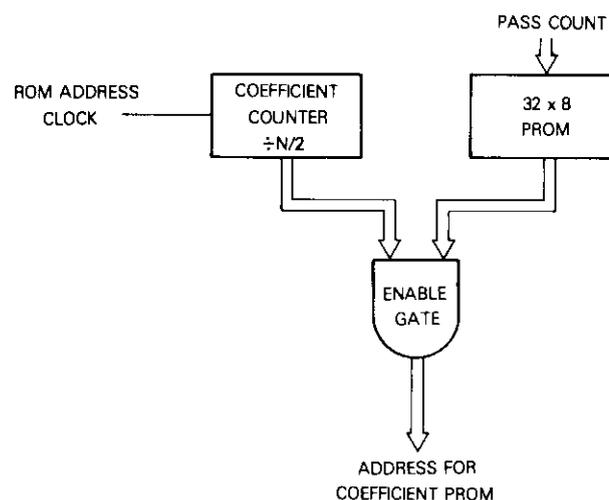
Figure 20. *Block Diagram of Address Generation Circuits for FFT Coefficient*

TABLE 9. CONTENTS OF THE 256×12 COEFFICIENT PROM

Location	Content
0–63	$\cos(2\pi n/N) = Re(W_n)$
64–127	$-\sin(2\pi n/N) = -IMG(W_n)$
128–191	$\sin(2\pi n/N) = IMG(W_n)$
192–255	$\cos(2\pi n/N) = Re(W_n)$

$^*n = 0, 1, \ldots, 63$, and $N = 128$.

gorithm chosen for the FFT is a radix-2, fixed-geometry, DIF algorithm, with ordered inputs and outputs. A 16-bit two's complement fixed-point arithmetic is used with a 12-bit coefficient word length. Automatic array scaling is utilized between passes with multiplication results rounded off to 16 bits. The complete processing requires 250 μs at a 16-MHz clock. The processor is housed on a 19- $\times$ 38-cm multilayered PC board (Figure 21) and is described in Reference 9.

Figures 22a and 22b represent the output due to a complex sinusoid and an impulse (at $t \neq 0$), respectively, in accordance with the predicted output. Table 10 lists the 116 chips used under functional headings.
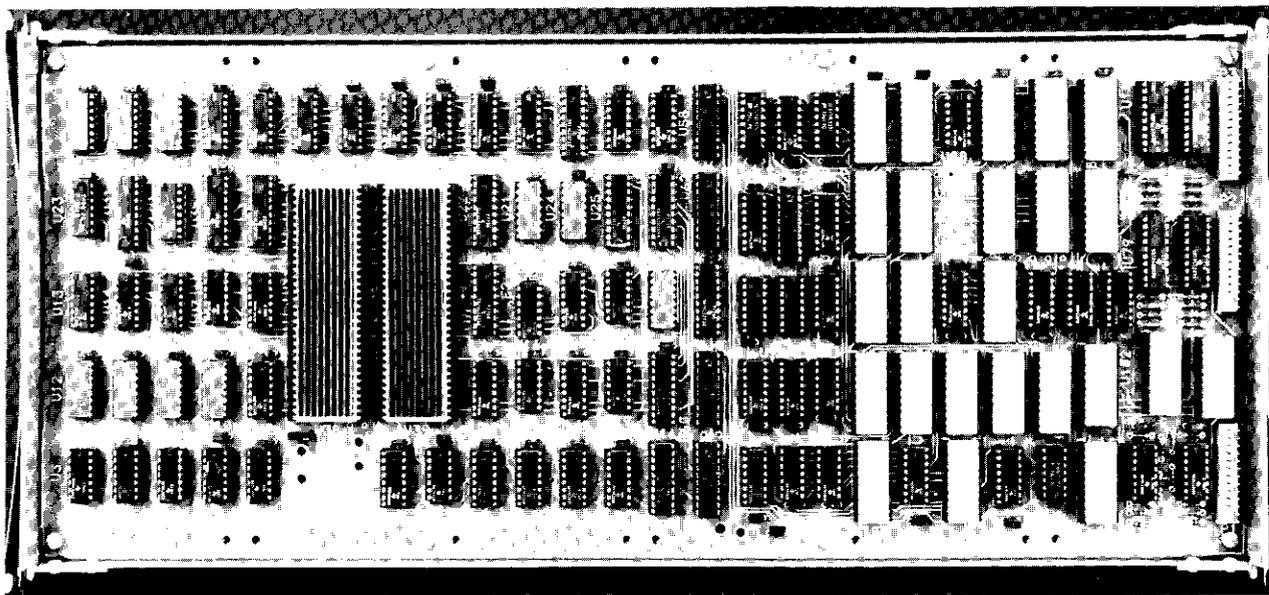
Figure 21. *High-Speed FFT Processor*
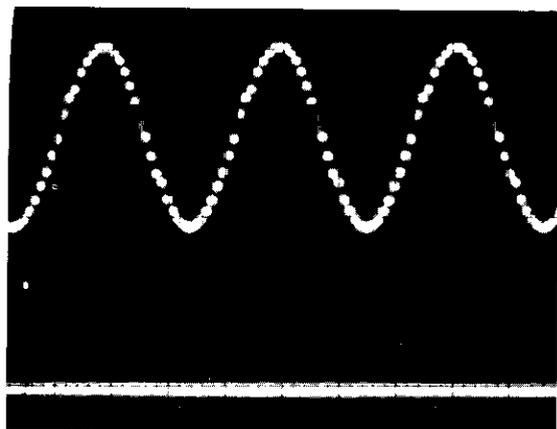
a. an impulse (t ≠ 0) resulting in a pure tone.
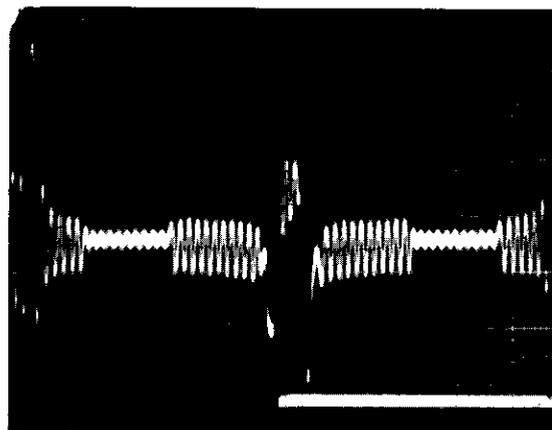
b. a sinusoid resulting in sin x/x

Figure 22. *Output of the FFT*

TABLE 10. CHIP-POWER COUNT FOR THE HIGH-SPEED FFT

	No. of Chips	Power (W)
High-Speed Butterfly LSIs		
Multipliers (MPY16AJ)	2	7.0
Address	12	6.0
Latches/Buffers	20	5.0
Coefficient Generation		
PROMs (256 × 4)	3	1.5
Latches/Buffers	12	2.4
Memory		
RAM (256 × 4)	24	7.2
Address Generation and Multiplying	26	5.0
Input/Output Buffers	4	0.4
Control		
PROM (32 × 8)	3	2.5
Counters and Flip-Flops	4	0.4
Latches	6	0.6
	116	38.0

Digital frequency synthesizer

Samples of a complex sinusoid may be generated by accumulating multiples of index K and using the accumulated value to calculate $\exp[j(2\pi/N)(nK)]$. This may be accomplished by storing 2^K values corresponding to the exponential in a PROM and reading the content of this PROM by the accumulated value as an address. The lowest frequency $f_0 = 1/NT$, n is the running index, and K is the frequency index, with 0 through $n-1$ as assumed values [8]. The phase can be changed by presetting a number C in the accumulator, thus forming the argument of the exponential as $[j(2\pi/N)nK + C)]$. Figure 23 is a block diagram of the synthesizer.

For large N values and $0 \leq Y \leq N - 1$, Y may be divided into several parts [8]. If $Y = q + r + s$, then

$$\exp\left[j\frac{2\pi Y}{N}\right] = \exp\left[j\frac{2\pi q}{N}\right]\exp\left[j\frac{2\pi r}{N}\right]\exp\left[j\frac{2\pi s}{N}\right] \qquad (12)$$

where each factor assumes less than N values and the overall storage is reduced at the expense of complex multiplications. A frequency syn-
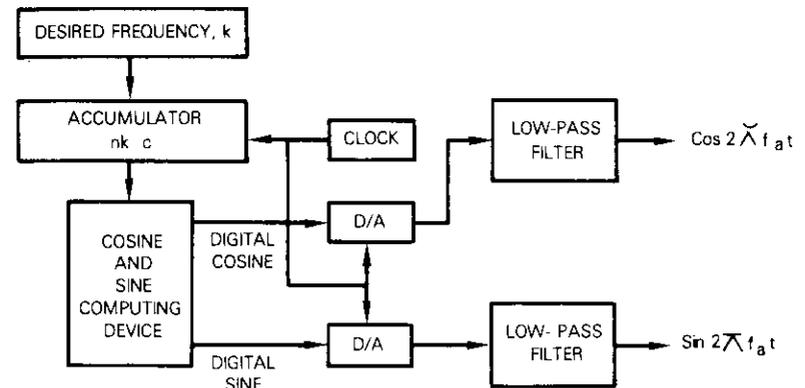
Figure 23. *Digital Synthesizer that Produces Quadrature Outputs*

thesizer has been designed with a 12×12 multiplier (MPY12AJ), yielding 65-dB signal purity. A bandwidth of $1/2T$ can be obtained for a quadrature output, and a 16-bit accumulator is used to produce $N = 2^{15}$ frequencies with a spacing of $1/NT$ Hz.

The exponential is factored as

$$\exp\left[j\frac{2K}{2^{15}}Y\right] = \exp(j\alpha)\exp(j\beta) \qquad (13)$$

where

$$\alpha = \frac{2K}{2^8}\left[\sum_{i=8}^{15} 2^{i-7}d_i + d_7\right]$$

and

$$\beta = \frac{2K}{2^{15}}\left[\sum_{i=1}^{6} 2^i d_i - 2^7 d_7\right]$$

and d_0 through d_{15} are the output of the accumulator. The index α represents eight higher order bits of the accumulator rounded by bit d_7; β represents six lower bits (d_6 through d_1) for $d_1 = 0$ and the two's complement of these bits for $d_7 = 1$. The value of α determines which of 2^8 equally coarsely spaced frequencies is nearest the desired frequency, and the value of β determines which of the 64 (256 in the total cycle) possible angular corrections should be added to or subtracted from the coarse point to achieve the desired result. Bit d_7 is used to divide the coarse interval in half. If this bit is one, the computation requires the coarse value to be

larger than the desired value. If d_7 is zero, the coarse value slightly lower than the desired value is adequate. Bit d_0 is retained for accumulation only.

The cosine component of $\exp(j\alpha)$ assumes values between 1.0 and 0.9999247, a difference in the 14th bit of its binary representation, and therefore it can be approximated to 1. The sine component is so small that the magnitude varies by no more than 5 bits. Thus, the PROM which is indexed by β may contain only 5 LSBs of the 11 bits plus sign representation of the sine corresponding to each of the 64 positive values of β. The modified equations for sinusoid generation can be written as

$$\sin\,(\alpha + \beta) = \sin\,\alpha + \cos\,\alpha \times \sin\,\beta \qquad (14a)$$

$$\cos\,(\alpha + \beta) = \cos\,\alpha - \sin\,\alpha \times \sin\,\beta \quad . \qquad (14b)$$

Figure 24 is a block diagram of the addressing circuit and the PROMS.
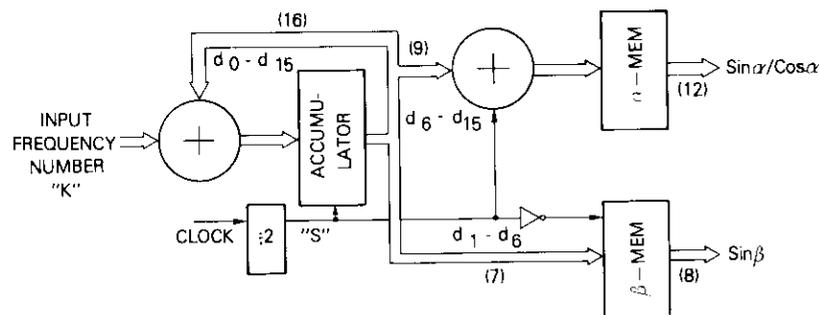
Figure 24. *Address Generation and Table Look-up Circuitry*

The input frequency number can be loaded either by switches or direct input into the accumulator. The coefficient PROM is loaded with sin α and sin β, respectively, where α and β have been defined earlier.

The computing circuit consists of a 12 $\times$ 12 parallel multiplier, a 12-bit adder, and two latches for holding the results. The processor is time shared between sine and cosine computations. Figure 25 shows the implementation of the circuit and utilizes 7 LSIs. For digital application, the output of the latches can be used directly, while for analog application, two LSI D/A converters are added, followed by low-pass filters with a cutoff at half the sampling frequency.

The multiplier (MPY12AJ) and adder are set for a pipeline operation.
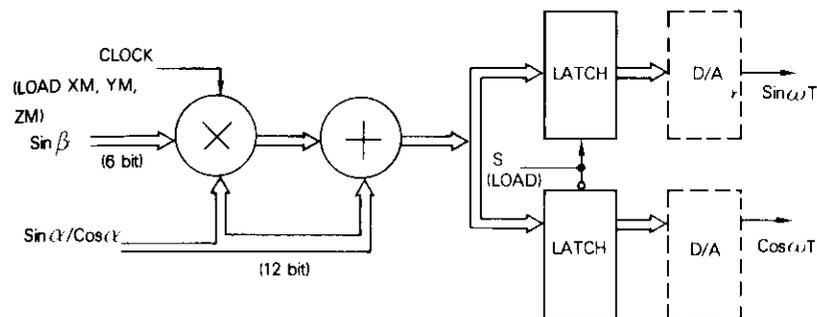
Figure 25. *Sine and Cosine Computing Circuit*

The sequence of operation is shown in Table 11.

TABLE 11. THE SEQUENCE OF OPERATION

Clock Period	Operation	Interpretation
1	a. $\cos\,\alpha \to XM$ b. $-\sin\,\beta \to YM$ c. $[ZM] + \cos\,\alpha \to$ latch 2	Calculate sine
2	a. $\sin\,\alpha \to XM$ b. $\sin\,\beta \to YM$ c. $[ZM] + \sin\,\alpha \to$ latch 1	Calculate cosine

Two clock periods are required per quadrature sample generation, and three simultaneous operations are performed in each clock period. During the first clock period, a multiplication producing $(-\cos\,\alpha\,\sin\beta)$ is initiated by loading XM with $\cos\,\alpha$ and YM with $-\sin\,\beta$. The result from the previous multiplication is added to $\cos\,\alpha$ to form the sine component. During the second clock period, multiplier registers XM and YM are loaded with $\sin\,\alpha$ and $\sin\,\beta$, respectively, and $\sin\,\alpha$ is added to the multiplier output from the previous cycle to form the cosine component.

Two PROMs, labeled α and β memories in Figure 24, are used. The α-memory contains 256 values corresponding to $\sin\,\alpha$. The cosine α is read out by offsetting the address by 64, which essentially performs the function $\cos\,\alpha = \sin\,(\alpha + \pi/2)$. The adder shown in Figure 24 accomplishes this process.

The chip-power count of the frequency synthesizer is given in Table 12.

TABLE 12. CHIP-POWER COUNT OF THE FREQUENCY SYNTHESIZER

Function	No. of Chips	Power (W)
Address generation	11–13	3.0
Processor	8–11	6.5
Control	2	0.5
	21–26	10.0

Figure 26 is a photograph of the synthesizer which is housed on a 19- × 13.5- × 4-cm wire-wrap board.
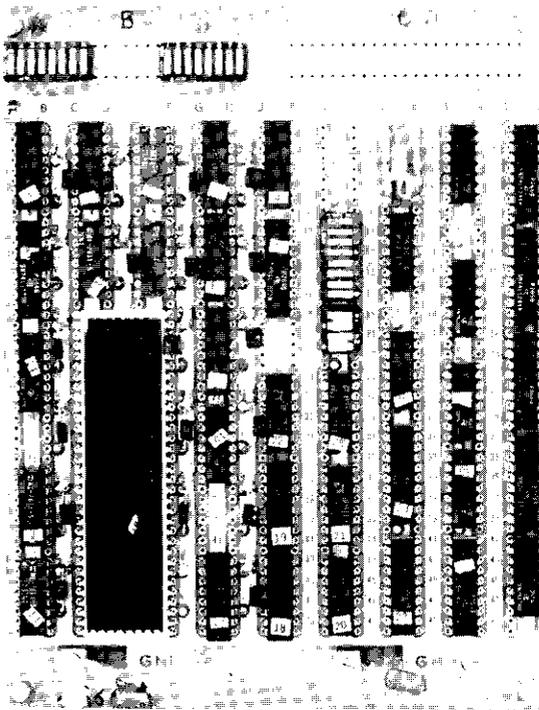
Figure 26. *All-Digital Frequency Synthesizer*

This synthesizer is capable of operating at a maximum of 4-MHz clock rate, thus producing a minimum frequency of 37.5 Hz and a maximum of 2.0 MHz in 37.5-Hz steps. The signal purity is over 35 dB for adjacent frequency and 65 dB for frequencies 75 Hz apart. This result is included in Figure 27. The signal purity may be increased by increasing the size of the accumulator.
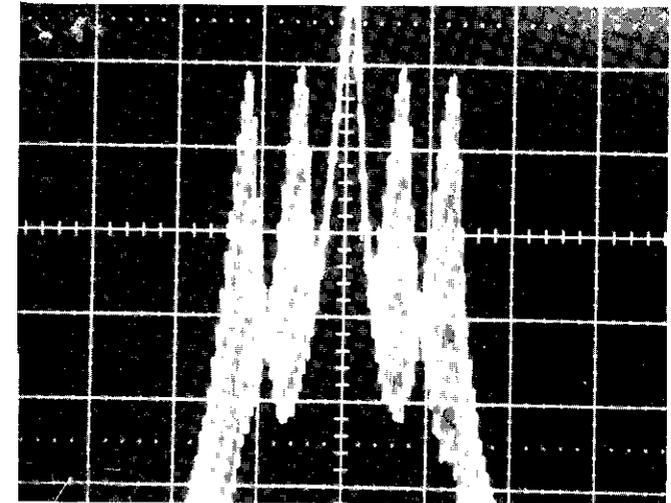
Figure 27. *Spectrum Analyzer Photograph of Two Frequencies Separated by* Δ

Application of the arithmetic processor

Background of the FDM/TDM transmultiplexer

Coexistence of time-division multiplex (TDM) and frequency-division multiplex (FDM) requires a means of direct translation from one to the other. It has been shown [1], [10]–[13] that such a transmultiplexer can be implemented by combining a bank of phase shifters, constituting a polyphase network and an FFT processor. This combination achieves a computation rate very close to optimum [1]; the highest efficiency is achieved when the number of channels is a power of 2. For an N-channel transmultiplexer, a $2N$-point FFT processor is required for each side.

The primary application of the transmultiplexer is the generation of FDM with 4-kHz spacing single-sideband suppressed carrier signals to accommodate "N" TDM channels on a multicarrier subcarrier at the transmit end and to convert the FDM signal to a TDM signal at the receive end. (Figure 28).
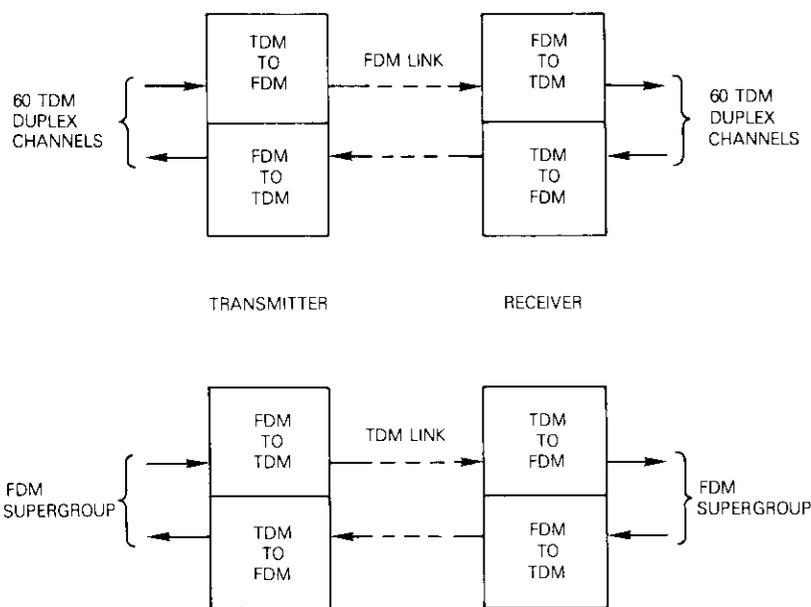
Figure 28. *Typical Application of TDM/FDM Transmultiplexers*

Traditionally, these subcarriers carry 12 voice channels (group), 60 channels (supergroup), and 300 voice channels (mastergroup). The FFT process is used efficiently for a large N [6]; however, the processing speed requires N to be small for economical realization of the transmultiplexer. Thus, a 60-channel system is most appropriate in terms of the state-of-the-art hardware. Also, since N is very close to a power of 2, four dummy channels are assumed for the implementation.

Since digital technology is expected to advance more rapidly than analog technology, an ever increasing number of transmission systems will be implemented digitally. However, since numerous analog transmission systems are already in existence, several decades may elapse before most transmission systems become digital. During this time, some practical

means of high-level multiplexed signal conversion is required to interconnect the two types of transmission systems.

Direct pulse code modulation (PCM) encoding of the supergroup requires a minimum of 9 bits/sample $\times$ 480 ksamples/s or 4.32 Mbit/s. Such direct encoding is inefficient. More efficient encoding of the channel content is achieved by converting the FDM format to a digital voice channel format, thereby reducing the bit rate required to carry a supergroup to 3.84 Mbit/s. Other source coding methods have become possible because of the availability of digital voice channel formats. Digital speech interpolation is capable of reducing the required transmitted bit rate to 8 bits/channel $\times$ 30 channels $\times$ 8 kHz = 1.92 Mbit/s, a reduction of better than 2:1 [14]. Techniques such as delta modulation adaptive differential pulse code modulation (ADPCM) offer further reduction. These bit-rate reduction techniques require demultiplexing of the supergroup into separate channels on one end and multiplexing the supergroup at the other end.

Theoretical considerations

FDM/TDM/PCM conversion

The incoming supergroup consists of 60 voice channels with lower sidebands occupying the frequency band (312 to 552 kHz) and one or more pilots at some known frequencies. The supergroup is translated to baseband (10 to 250 kHz) by mixing it with a 302-kHz tone and recovering the lower band by filtering with an analog low-pass filter with a cutoff at 250 kHz and an out-of-band loss of over 60 dB. The baseband translation results from the need to reduce the overall sampling rate, which in turn reduces the processing speed. A lower processing speed results in lower power consumption and simpler control circuits. The resulting signal, $S(t)$, is digitized at 512 kHz to form signal samples S_n. The sampled signal is composed of 60 voice channels (4-kHz band). The channel residing at $4L$ kHz will be referred to as the Lth channel; thus, the 60 channels are numbered 3 through 62. Dummy channels are assumed at frequencies of 0, 4, 8, and 252 kHz, and are numbered 0, 1, 2, and 63, respectively.

These channels are separated from adjacent channels and shifted to baseband by an 8-kHz sample rate by reducing the rate from 512 to 8 kHz with a transversal filter (cutoff at 2 kHz) to remove all except the adjacent channels. The transversal filter can be realized with 256 taps and can be shifted in frequency by $4L$ kHz by modifying the tap weights H_i to G^{Li}

according to the following operation:

$$G^{Li} = H_i \exp\left(j\frac{2\pi 4Li}{512}\right) = H_i \exp\left(j\frac{2\pi Li}{128}\right) = H_i W_{128}^{Li} \quad,$$

$$i = 0, 1, 2, \ldots, 255$$

$$L = 0, 1, \ldots, 63$$

where

$$W_{128}^{Li} = \exp\left(j\frac{2\pi Li}{128}\right) \quad.$$

The filtered signal $C_n(L)$ is expressed by

$$C_n(L) = \sum_{i=0}^{255} S_{64n-i} H_i W_{128}^{Li}$$

which can be rewritten as

$$C_n(L) = \sum_{i=0}^{127} X(n, i) \, W_{128}^{Li} \quad. \tag{15}$$

Equation (15) represents a 128-point DFT on a sequence $X(n, i)$ given by

$$X(n, i) = H_i S_{64n-i} + H_{128+i} S_{64n-128-i} \quad. \tag{16}$$

The transform is performed on an overlapped sequence, *i.e.*, a 128-point transform for every 64 input data points. This will require two real-time simultaneous transforms on $X(n, i)$.

The even channels are passed through a low-pass recursive filter with a cutoff at 2 kHz, thus removing the adjacent channel noise. The odd channels are recovered by shifting the recursive filter response to half the sampling rate. The output of the recursive filter is modulated up and down by 2 kHz for even and odd channels, respectively. The real part of the modulated output of the recursive filter (D_n^L) is the required time-multiplexed sequence [12]; that is,

$$PCM_n^L = Re\left\{D_n^L \exp\left[-j(-1)^L\frac{2\pi n}{4}\right]\right\} \quad. \tag{17}$$

Figure 29 is a block diagram of the conversion.
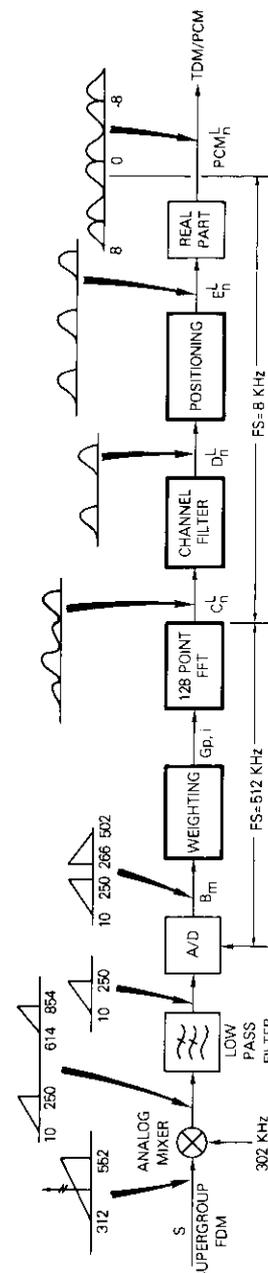
Figure 29. *Block Diagram of FDM/TDM Conversion*

TDM/FDM conversion

The input consists of 60 TDM channels at a sampling rate of 8 kHz. Four dummy channels numbered 0, 1, 2, and 63 are added, totaling 64. These channels are positioned so that the lower sideband of each Lth channel lies at the center frequency $4L$ kHz. This is accomplished by modulation described by

$$Z_n^L = PCM_n^L \exp\left[-j(-1)^L \frac{2\pi n}{4}\right] \quad , \tag{18}$$

$$L = 0, 1, \ldots, 63$$

$$n = 0, 1, \ldots .$$

The upper sidebands are removed with a low-pass recursive filter with its response shifted up for odd channels. The recursive filter output Y_n^L is filtered with the 256-tap transversal filter having a cutoff at 2 kHz, incorporating a sample rate increase of 8 to 512 kHz, to remove the remaining sidebands. These channel signals are summed over the 64 channels, resulting in the FDM signal.

The sample rate is increased by inserting 63 zeros [8] between two samples of Y_n^L. If this signal is denoted by X_m^L, the filtering process is described as

$$V_m = \sum_{L=0}^{63} \sum_{i=0}^{255} X_{m-i}^L H_i \exp\left(j\frac{2\pi Li}{128}\right) \quad . \tag{19}$$

It should be noted that the summation can be interchanged and X_{m-i}^L is zero except when $m - i$ is a multiple of 64. For $m = 64q + p, p = 0, 1, \ldots, 63$, and nonzero values denoted by Y_q^L, Y_{q-1}^L, Y_{q-2}^L, and Y_{q-3}^L for $i = p, p + 64, p + 128,$ and $p + 192$, respectively,

$$V_m = H_p W_q(p) + H_{p+64} W_{q-1}(p + 64) + H_{p+128} W_{q-2}(p)$$
$$+ H_{p+192} W_{q-3}(p + 46) \tag{20}$$

where

$$W_q(p) = \sum_{L=0}^{63} Y_{q-r}^L \exp\left(j\frac{2\pi pL}{128}\right) \tag{21}$$

and $r = 0, 1, 2, 3$, which is equivalent to a 128-point DFT for which the second half of the input sequence is zero. Two 128-point transforms are produced for each 128-data-point input, resulting in the supergroup FDM signal which is moved to the appropriate frequency band (312- to 552-kHz). This conversion is shown in Figure 30.

High-speed FFT

Each side of the transmultiplexer will require a 128-point FFT for every 64 data inputs. However, since the input $X(n, i)$ is real [equation (16)] for the FDM/TDM side, two transforms can be performed by utilizing a single hardware unit performing an FFT with a technique usually known as a "two-channel trick" [15]. The two-channel trick is applied by decomposing $X(n, i)$ into two sequences, $E(n, i)$ and $F(n, i)$, for n odd and even, respectively, and combining these sequences to form a complex sequence, $K(n, i)$, such that

$$K(n, i) = E(n, i) + jF(n, i)$$

and the DFT is expressed by

$$K_n(L) = E_n(L) + jF_n(L) \quad .$$

The DFTs of the original sequences can be retrieved by

$$E_n(L) = \frac{1}{2}[K_n(L) + K_n^*(128 - L)] \tag{22a}$$

$$F_n(L) = \frac{1}{2j}\left[K_n(L) - K_n^*(128 - L)\right] \tag{22b}$$

where * denotes the complex conjugate.

The output format is arranged as

$$\ldots E_n(0), E_n(1), \ldots E_n(63), F_n(0), F_n(1), \ldots F_n(63), \ldots$$

corresponding to equation (1) (for n even):

$$\ldots C_{n-1}(0), C_{n-1}(1), \ldots C_{n-1}(63), C_n(0), C_n(1), \ldots C_n(63), \ldots$$

which is a time-multiplexed sequence for 64 PCM channels.

The two-channel trick cannot be applied for the TDM/FDM side; since Y_n^L is complex, two FFT processors are required. A total of three FFT
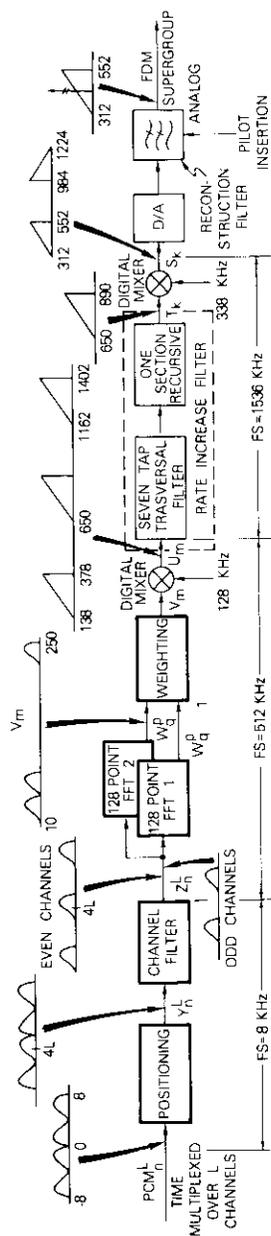
Figure 30. Block Diagram of TDM/FDM Conversion

processor modules is required in the system. At a 512-kHz sampling rate, the time allowed to perform a 128-point FFT is 250 μs. The stand-alone feature of this processor is an important requirement which enables it to be used as a black box in the system configuration.

Filter structure

Six filter modules are used to implement various functions. In Figures 29 and 30, the channel filters are the recursive filters described in the practical example. Weighting and transversal filtering are also accomplished by these modules. The frequency synthesizer is used to generate frequencies for the mixing operation, which is needed to translate the signal up or down from the supergroup slot.

Conclusions

This paper has presented the hardware development of digital signal processors, which can be used in various systems, such as speech analysis, seismic data analysis, radar, and others which perform spectral analysis. The processors are implemented in parallel, fixed-point, two's complement arithmetic, and their designs are very general and adaptable to specific needs.

Practical applications depicting the multiple use of these processors have been described. In particular, an FDM/TDM transmultiplexer was built and tested using these modular components. The arithmetic structure for digital filtering using these modules is readily reconfigured; therefore, it has been used as a multifunction component in the transmultiplexer.

References

[1] S. L. Freeny et al., "Design of Digital Filters for an All-Digital Frequency-Division-Multiplex, Time-Division-Multiplex Translator," *IEEE Transactions on Circuit Theory* (Special Issue on Active and Digital Networks), CT-18, November 1971, pp. 702–711.

[2] L. B. Jackson, J. F. Kaiser, and H. S. McDonald, "An Approach to the Implementation of Digital Filters," *IEEE Transactions on Audio Electroacoustics* (Special Issue on Digital Filters: The Promise of LSI Applied to Signal Processing), AU-16, September 1968, pp. 413–421.

[3] S. Zohar, "The Counting Recursive Digital Filter," *IEEE Transactions on Computers*, C-22, April 1973, pp. 338–347.

[4] S. L. Freeny, "Special Purpose Hardware Digital Filtering," *Proc. IEEE*, Vol. 63, No. 4, April 1975, pp. 633–648.

[5] Z. M. Ali, "A Configurable Parallel Arithmetic Structure for Recursive

Digital Filtering," IEEE International Symposium on Circuits and Systems, *Conference Record*, May 1978, pp. 289–296.

[6] A. V. Oppenheim and R. W. Schafer, *Digital Signal Processing*, New Jersey: Prentice Hall Inc., 1975.

[7] J. L. Buie and T. A. Zimmerman, "Very Large-Scale Integrated Circuits for Digital Signal Processing Circuits and Systems," February 1977.

[8] L. R. Rabiner et al., *Digital Signal Processing*, New York: IEEE Press, 1972.

[9] Z. M. Ali, "A High-Speed FFT Processor," *IEEE Transactions on Communications*, COM-26, No. 5, May 1978, pp. 690–696.

[10] M. G. Bellanger and J. L. Daguet, "TDM/FDM Transmultiplexer: Digital Polyphase and FFT," *IEEE Transactions on Communications*, COM-22, No. 9, September 1974, pp. 1199–1205.

[11] R. L. Greenspan et al., "Channel Demultiplexing by Fourier Transform Processing," *EASCON 1975 Record*, pp. 369–372.

[12] P. M. Terril et al., "A Digital Block Processor for SSB-FDM Modulation and Demodulation," *IEEE Transactions on Communications*, COM-25, February 1975, pp. 282–286.

[13] Z. M. Ali and G. D. Dill, "Application of FDM/TDM Transmultiplexer in INTELSAT Earth Stations," Fourth International Conference on Digital Satellite Communications, Montreal, Canada, October 1978.

[14] S. J. Campanella, "Digital Speech Interpolation," *COMSAT Technical Review*, Vol. 6, No. 1, Spring 1976, pp. 127–158.

[15] E. O. Brigham, *The Fast Fourier Transform*, New Jersey: Prentice-Hall Inc., 1974.

[16] T. A. Classen and W. F. McKlenbrouker, "A Generalized Scheme for an All-Digital Time-Division-Multiplex to Frequency-Division-Multiplex Translator," *International Conference on Communications*, 1977.

Zaheer M. Ali was born in Lahore, Pakistan, and received B.Sc. (Hons) and M.Sc. in Physics from Punjab University in 1966 and 1967, and an M.S.E.E. from City College of New York in 1974.

From 1967 to 1971 he worked for ELMAC Limited (a subsidiary of Phillips, Holland). From 1971 to 1972 he worked for Comstron-Seg. Corporation in New York. From 1974 to 1976 he was a member of the technical staff at the Advanced Communications Laboratory of RCA before joining COMSAT Labs as a member of the technical staff and project engineer for the FDM-TDM transmultiplexer development and advance digital processing techniques. He is currently employed by the Commercial Telecommunications Company.

Identification algorithms for adaptive filters

O. A. HORNA

(Manuscript received May 19, 1978)

Abstract

The theory of adaptive finite impulse response filters is based on the assumption that the input signal is a stationary ergodic process. As neither speech nor video signals fulfill these conditions theory and experimental results differ, especially when the filter has several hundred coefficients, as for example in telephone echo cancellers.

This paper derives the theory of adaptation by using Svoboda's rapidly converging least mean square (LMS) algorithm for pseudo-inversion of square matrices, revealing that all correction algorithms are special cases of Svoboda's algorithm. It is also proven, in terms of a multidimensional space, that all LMS algorithms guarantee only nondivergence, but not convergence, to the optimal solution. Various signal decorrelation methods are discussed, and an improved method using two statistically independent dither signals is analyzed using the known results of the sign correlation method.

Finally, a new fast adaptive algorithm based on multiplication of the coefficients by constants $1 \pm \Delta$, where $\Delta \ll 1$, is disclosed and the corresponding nondivergence criteria are derived. Some results of the experimental verification of the theories are shown on an actually implemented adaptive finite impulse filter with 256 coefficients.

Introduction

In recent years self-adaptive filters have become an important tool in

331

signal processing. For example, they have been used to reduce interference of radar signals, to monitor biological signals, to compensate transmission-line characteristics for digital and analog signaling, and to cancel "ghosts" in TV transmission. A survey of these applications, with references to the most important papers in this field, can be found in recent work by Widrow et al. [1].

Most adaptive networks use a finite impulse response (FIR) filter, which consists of a sampler, a delay line with equidistant taps, and a linear combiner with adjustable weights, h_i (see Figure 1). Analyses of the conditions for and the speed of convergence of the various adaptive algorithms have been the subject of many studies. A more recent paper by Widrow *et al* [2] shows that all methods are similar in that they result in Widrow and Hoff's LMS algorithm [3], which is based on the assumption that the input signal is a ". . . stationary ergodic process . . ." and that the sequence of the signal samples entering the adaptive network is ". . . uncorrelated over time . . ." [2].

Neither speech nor video signals fulfill the above conditions. Adjacent samples of speech or video taken at the Nyquist rate are characterized by autocorrelation coefficients $\rho_{xz} > 0.8$, and their short-term signal statistics
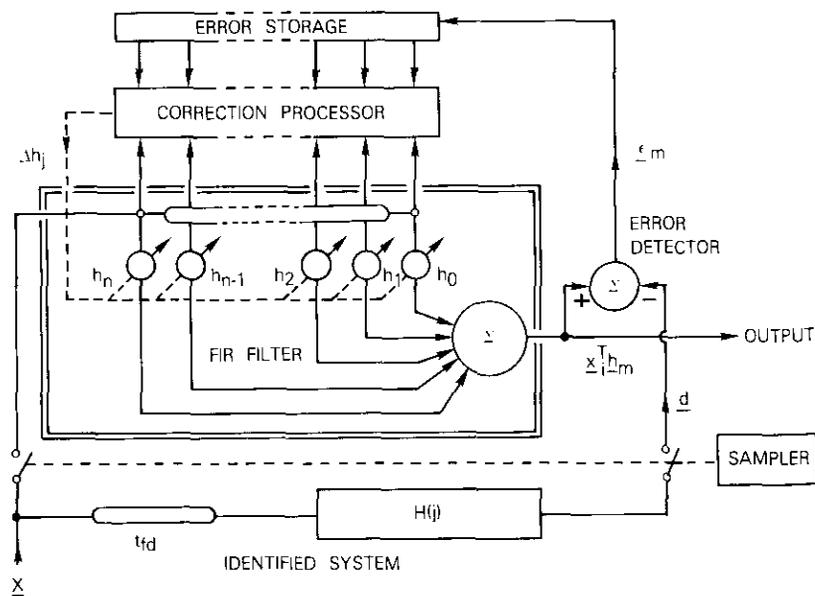
Figure 1. *Block Diagram for an Adaptive Finite Impulse Response (FIR) Filter Connected to Identify an Unknown*

vary substantially. Therefore, present theories agree with experimental results only for "short" filters with few taps and/or for adaptive networks driven by uncorrelated signals, such as the sum of two white noise inputs [2].

Since adaptive filters used for echo cancellation can dramatically improve the quality of long-distance telephone communications, substantial research has been performed in this field. Filters with several hundred coefficients capable of adapting to rapidly changing transmission conditions in fractions of a second are implemented in hardware for this purpose [4], [5]. For these "long" filters, a noticeable discrepancy exists between theoretical predictions and experimental results. This work will analyze the causes of these differences. An adaptive algorithm without restrictions on the statistical properties of the input signal will be derived, and conditions under which the filter converges to the optimum impulse response even with highly correlated input signals will be analyzed.

Adaptive algorithm

In 1951, Svoboda [6] designed a special analog computer for solving a system of linear simultaneous equations. The rapidly converging algorithm used in this device was later modified by Pokorná [7] and used for inversion of matrices on a digital computer.

A system of linear algebraic equations can be written in the matrix form

$$A \cdot h^T - d = 0 \quad . \tag{1}$$

It is assumed that matrix A is square and of order and rank $n + 1$ with elements $A = [a_{ij}]$, where $i = 0, 1, 2, \ldots, n$ denotes the rows and $j = 0, 1, 2, \ldots, n$ the columns; h is a row vector $h = [h_j]$ and h^T its transpose; d is a column vector $d = [d_i]$; $r_i = [a_{i0} \ldots a_{ij} \ldots a_{in}]$ are $n + 1$ linearly independent row vectors; and

$$a_j = \begin{bmatrix} a_{0j} \\ \cdot \\ \cdot \\ a_{ij} \\ \cdot \\ \cdot \\ a_{nj} \end{bmatrix} \tag{2}$$

are $n + 1$ linearly independent column vectors.

As the first approximation, equation (1) is solved for the unknown vector $\underline{h}$ according to Svoboda's [6] algorithm by choosing an arbitrary vector $\underline{h}_0$ and computing a "residue" or error column vector $\underline{\epsilon}_0$:

$$\underline{\epsilon}_0 = \underline{A} \cdot \underline{h}_0^T - \underline{d} \quad . \tag{3}$$

One component of vector $\underline{h}_0$ is selected (e.g., h_{0k}) and a correction, Δh_k, is subtracted, thus yielding

$$h_{1k} = h_{0k} - \Delta h_k \quad . \tag{4}$$

This new value is substituted for h_{0k}, thus forming a corrected vector $\underline{h}_1$ from which a new error vector is computed:

$$\underline{\epsilon}_1 = \underline{A} \cdot \underline{h}_1^T - \underline{d} \quad . \tag{5}$$

Substituting from equations (3) and (4) into equation (5) results in

$$\underline{\epsilon}_1 = \underline{\epsilon}_0 - \Delta h_k \underline{a}_k \quad , \qquad j = k \quad . \tag{6}$$

Convergence of the method is ensured if Δh_k is chosen to minimize the sum of squares of errors, i.e., the square of the length of the error vector $\|\underline{\epsilon}_1\|^2 = \underline{\epsilon}_1 \cdot \underline{\epsilon}_1^T$. This LMS condition is, according to equation (6):

$$\begin{aligned} \|\underline{\epsilon}_1\|^2 &= \|\underline{\epsilon}_0 - \Delta h_k \underline{a}_k\|^2 \\ &= \|\underline{\epsilon}_0\|^2 + \Delta h_k^2 \|\underline{a}_k\|^2 - 2\Delta h_k \underline{\epsilon}_0^T \cdot \underline{a}_k \quad . \end{aligned} \tag{7}$$

The optimum value of Δh_k, which follows from the LMS condition [7], is

$$\frac{d \|\underline{\epsilon}_1\|^2}{d\Delta h_k} = 0 \Longrightarrow \Delta h_{k0} = \frac{\underline{\epsilon}_0^T \cdot \underline{a}_k}{\|\underline{a}_k\|^2} \quad . \tag{8}$$

Substituting from equation (8) into equation (7) indicates the effect of correction Δh_k on error vector length:

$$\|\underline{\epsilon}_1\|^2 = \|\underline{\epsilon}_0\|^2 - \Delta h_{k0}^2 \|\underline{a}_k\|^2 \quad . \tag{9}$$

In the mth successive correction step, another component (e.g., h_{mj}) of

vector $\underline{h}_m$ is chosen and the optimum correction, Δh_{j0}, is computed from the same condition as equation (8):

$$\Delta h_{j0} = \frac{\underline{\epsilon}_m^T \cdot \underline{a}_j}{\|\underline{a}_j\|^2} \quad . \tag{10}$$

This correction minimizes the length of the error vector $\|\underline{\epsilon}_{m+1}\|$ whose components e_{m+1i} are

$$\underline{\epsilon}_{m+1} = [e_{m+1i}] = [e_{mi} - \Delta h_j a_{ij}] \quad . \tag{11}$$

This process is repeated until the square of the error vector length is reduced to the smallest permissible or attainable value $\|\underline{\delta}\|^2$:

$$\|\underline{\epsilon}_{m+1}\|^2 = \|\underline{\epsilon}_m\|^2 - \Delta h_{j0}^2 \|\underline{a}_j\|^2 \leq \|\underline{\delta}\|^2 \quad . \tag{12}$$

The condition of convergence, $\|\underline{\epsilon}_{m+1}\|^2 < \|\underline{\epsilon}_m\|^2$, is met, according to equation (12), for all $\Delta h_j^2 < \Delta h_{j0}^2$. Equations (10) and (12) define Svoboda's LMS iterative algorithm for solving equation (1) and its properties.

Convergence

This LMS algorithm converges for any nonsingular matrix $\underline{A}$, i.e., $|\underline{A}| \neq 0$, of rank $n + 1$ and for every vector $\underline{d}$ whose length $\|\underline{d}\| \neq 0$ [5]. However, the speed of convergence depends on many factors such as the initial choice of h_0, the structure of matrix $\underline{A}$, and the choice of the correction Δh_j, as evidenced by experimental tests on Svoboda's original analog computer and on a digital computer using Pokorná's program. It has been confirmed that the set of equations

$$\underline{A} \cdot \underline{h}_m^T - \underline{d} = \underline{\epsilon}_m \tag{13}$$

where

$$0 \leq \|\underline{\epsilon}_m\| \leq \|\underline{\delta}\| \tag{14}$$

has an infinite number of solutions for $\underline{h}_m$, which can be heuristically explained in terms of an $(n + 1)$-dimensional space.

Vector $\underline{h}$ represents the coordinates h_i of the point of interception of $n + 1$ hyperplanes in an $(n + 1)$-dimensional space. If the two or more planes intersect under a very sharp angle, even a small change in any component of $\underline{\epsilon}_m$ substantially changes the coordinates (vector $\underline{h}_m$). In this

case, convergence is slow and all solutions are unstable.

If two hyperplanes are parallel, *i.e.*, if two vectors $\underline{a}_j$ and $\underline{a}_{j+k}$ are linearly related,

$$\underline{a}_{j+k} = q\underline{a}_j \tag{15}$$

where q is a constant ($q \neq 0$), the rank of matrix $\underline{A}$ is reduced, and a true solution for $\underline{h}_m$ cannot be found although the LMS condition of equation (11) is met. Also, when all planes intersect under an angle close to 90° the convergence is fast and the solution is stable; *i.e.*, the changes in the length of the error vector $\|\underline{\varepsilon}_m\|$ have the least influence on solution $\underline{h}_m$. Therefore, without advanced analysis of matrix $\underline{A}$, it is impossible to determine the expected number of iterative steps necessary to solve equations (13) and (14). This has been confirmed by Černý and Marek [8], whose experiment and rigorous analysis have shown that the method must converge even if the sum of the absolute values of errors $\Sigma_i \, |e_{mi}|$ is minimized. A similar result was reported recently by Campanella et al. [4].

Invariably, as the product $\Delta h_j^2 \, \|\underline{a}_j\|^2$ in each step increases, the sum of squares $\|\underline{\varepsilon}_m\|^2$ of errors e_{mi} is reduced more rapidly [see equation (12)]. For fast convergence it is therefore necessary to choose for the next, *i.e.*, $(m + 1)$th, correction step the component h_{mj} for which $\Delta h_{j_0}^2 \, \|\underline{a}_j\|^2$ is maximal. Instead of computing these n products, the optimum can be found by rearranging equation (10):

$$|\Delta h_{j_0}| \, \|\underline{a}_j\|^2 = |\underline{\varepsilon}_m^T \cdot \underline{a}_j| \quad . \tag{16}$$

Obviously, the best choice of h_{mj} is the one for which the scalar (inner) product $\underline{\varepsilon}_m^T \cdot \underline{a}_j$ has the maximum absolute value.

Symmetric matrix

The algorithm defined by equations (10), (11), and (12) can be used directly to identify an unknown time-invariant system with impulse response $H(j)$. The input signal vector is $\underline{X}$; the "desired response," *i.e.*, the sampled response of system $H(j)$ [1]–[3], is defined by vector $\underline{d}$ (see Figure 1); and the coefficient vector $\underline{h}$ represents the gains assigned to different delay line taps. Matrix $\underline{A}$ is composed of a set of input signal row vectors

$$\underline{r}_i \equiv \underline{x}_i = [x_{i0}, x_{i1}, \ldots, x_{ij}, \ldots, x_{in}] \tag{17}$$

where components x_{ij} are input signal samples which are present at the delay line taps during the ith sampling interval. At successive intervals, the samples are shifted by one unit delay to the right in Figure 1 and thus components $x_{(i+1)j}$ of vector $\underline{x}_{(i+1)}$ is $x_{(i+1)j} = x_{i(j+1)}$. Therefore, for every $i, j \leq n$ the following relationship applies:

$$x_{ij} = x_{ji} = x_{i+j} \tag{18}$$

where $i + j = 0, 1, \ldots, 2n$. Input signal matrix $\underline{A}$ is therefore symmetric; for every $i = j$, column vector $\underline{a}_j$ and the ith row vector are identical:

$$\underline{a}_j = \underline{r}_i \equiv \underline{x}_i \equiv [x_i, \ldots, x_{i+j}, \ldots, x_{i+n}]$$
$$= [x_i, \ldots, x_{i+j}, \ldots, x_{n+j}] \quad . \tag{19}$$

Substituting from equation (18) into equation (10) makes it possible to express the optimum correction Δh_{j0} which minimizes $\|\underline{\varepsilon}_{m+1}\|^2$ as follows:

$$\Delta h_{jc} = \frac{\underline{\varepsilon}_m^T \cdot \underline{x}_i}{\|\underline{x}_i\|^2} = \frac{1}{\|\underline{x}_i\|^2} \sum_{i=0}^{n} e_{mi} x_{i+j} = \sum_{j=0}^{n} \partial h_j \tag{20}$$

where (at the ith sampling interval)

$$\partial h_j = \frac{e_{mi} x_{i+j}}{\|x_i\|^2} \tag{21}$$

and the components of error vector $\underline{\varepsilon}_m$ and $e_{mj} \equiv e_{mi}$ for every $i = j$.

This demonstrates that for a symmetric matrix $\underline{A}$ both correction strategies for coefficients h give identical results. Svoboda's method [6] applies the correction $\Delta h_j = \Sigma_j \, \partial h_j$ in one correction cycle to one selected component h_{mj} according to equation (6). For Suyderhoud's method, based on the application of the pseudo-inverse of the matrices [9], each component of vector $\underline{h}_m$ is corrected according to

$$\underline{h}_{m+1} = [h_{mj} - \partial h_j] \tag{22}$$

during every iteration. The latter method usually is easier to implement in hardware for long filters. Therefore, the different correction formulas derived and/or mentioned by Widrow [1], [2], Campanella et al. [4], and Wehrman [10] are special cases of equation (20) which differ in their

approximation of the true error vector $\underline{\epsilon}_m$.

To reduce the memory size and computation necessary to determine Δh_j or ∂h_j instead of the true vector $\underline{\epsilon}_m = [e_{mi}]$, a vector $\underline{\epsilon}_m'$ with equal components $e_{mi} = e_m$ is substituted [10] in equations (20) and/or (21):

$$\underline{\epsilon}_m \approx \underline{\epsilon}_m' = [e_m] \tag{23}$$

where e_m is estimated as an rms value or an average of absolute values. That is,

$$e_m = \text{Sgn}(e_{mi})(E[e_{mi}^2])^{1/2} \tag{24}$$

$$e_m = \text{Sgn}(e_{mi})E[|e_{mi}|] \tag{25}$$

where $\text{Sgn}(e_{mi})$ is the sign of the error vector component e_{mi}. In addition, e_m is approximated by the error of the last $(i = m)$ iteration, $e_m = e_{mm}$, or even by constant e_r and the sign of e_{mi}:

$$e_m = \text{Sgn}(e_{mi})e_r \quad . \tag{26}$$

This approximation often results in the simplest hardware implementation. When the constant e_r is properly chosen (see Reference 11), it can give approximately the same speed of adaptation and stability of response for long filters, as the other approximations listed above or those found in References 1, 2, 4, and 10.

Input signal vector

The adaptive algorithms used to identify the sampled impulse response $\underline{H}(j)$ of an unknown system are equivalent to or a close approximation of Svoboda's method [equations (10)–(13)] for solving a system of linear equations [equation (1)]. Therefore, these algorithms guarantee only non-divergence, not convergence, to the optimum solution $\underline{h}_m$, which, according to equation (12), emulates with LMS error $\|\delta\|_2$ the response $\underline{H}(j)$.

The fundamental condition for convergence must be met: the input signal matrix A must be of rank $n + 1$; that is, no single pair of vectors $\underline{x}_i = [x_{i+j}]$ [see equation (19)] composed of any sequence of $n + 1$ components x_{i+j} of input signal vector

$$\underline{X} = [x_0, \ldots, x_{i+j}, \ldots, x_{2n}] \tag{27}$$

can be linearly related. According to equation (15),

$$x_{i+k} \neq q x_i \tag{28}$$

for all $q \neq 0$, all $0 < k < 2n$, and $0 \leq i \leq n$. If both sides of inequality (28) are multiplied by $\underline{x}_i^T/(n + 1)$, then

$$\frac{1}{n+1} x_{i+k} \cdot \underline{x}_i^T \neq q \frac{1}{n+1} x_i \cdot \underline{x}_i^T \quad . \tag{29}$$

For a sufficiently large n, the left-hand term is the discrete approximation of the autocorrelation function $R_{xi}(k) = E[x_{i+j}x_{i+j+k}]$, and the right-hand term is the variance $\sigma_i^2 = E[x_{i+j}^2]$ of the signal $\underline{X}$. If equation (29) is rearranged, equation (28) can be rewritten as

$$q \equiv \rho_{xx}(k) = \frac{E[x_{i+j}x_{i+j+k}]}{E[x_{i+j}^2]} = \frac{R_{xi}(k)}{\sigma_i^2} = 0 \tag{30}$$

where $\rho_{xx}(k)$ is the discrete approximation of the autocorrelation coefficient. Therefore, only a random sequence of $2n + 1$ samples x_{i+j} can form asymmetric matrix $\underline{A}$ with rank $n + 1$, which can also be proven by using the Wiener-Hopf equation (WHE).

The discrete form of the WHE is [1]

$$R_{xd}(k) = \sum_{i=0}^{n} h_{mj}R_{xi}(k - j) \tag{31}$$

where $R_{xd}(k) = E[d_i x_{i+j+k}]$ is the discrete cross-correlation function between $\underline{X}$ and $\underline{d}$, and $\underline{h}_m = [h_{mi}]$ is the optimal impulse response.

Equation (31) can be unambiguously solved for $\underline{h}_m$ only if $R_{xi}(k) = 0$ for all $0 < |k| \leq 2n$ [also see equation (30)]. Only Poisson waves [12] or broadband noise signals have these properties. However, the long-term autocorrelation of successive samples (i.e., $k = 1$) for speech and video signals is $0.8 < \rho_{xx}(1) < 0.95$ when sampling at $1.2f_s$, where f_s is the Nyquist rate. Under these conditions, the probability that a symmetric matrix $\underline{A} = [x_{i+j}]$ will be of rank $n + 1$ decreases with increasing n; therefore, equation (13) is unsolvable for this kind of signal.

Heuristically, this result can also be interpreted [13] in the frequency domain as $H(j)$ represents the system response to a signal with the "flat" power density spectrum $F_{xx}(\omega) = \text{const}$. A coefficient $\rho_{xx}(k) \to 1$ for any $0 < |k| < 2n$ indicates that a part of the frequency spectrum is not present

in the input signal $\underline{X}$; thus, the system cannot find the desired response $\underline{d}$ for this part of the spectrum and is unable to properly adopt FIR filter coefficients h_m, as illustrated in Figure 2. Figure 2a shows part of the response $\underline{h}_m$ of an FIR filter [5] with $n = 256$ taps emulating a bandpass filter with 1-ms additional (flat) delay and white noise input. Figure 2b, which refers to the same configuration with a sine wave input signal, shows that with a
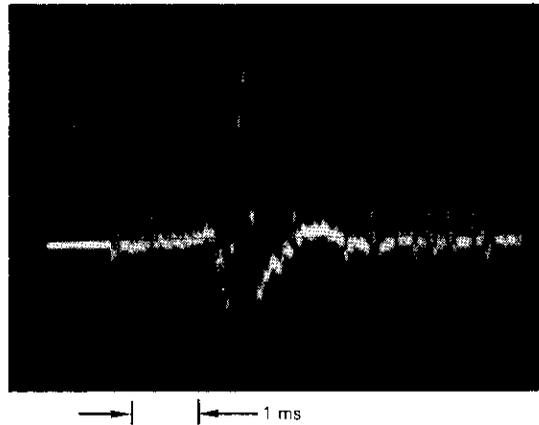
Figure 2a. *Significant Part of the FIR Filter Impulse Response Emulating a Bandpass Filter (500 Hz–2 kHz) with White Noise Input Signal X*
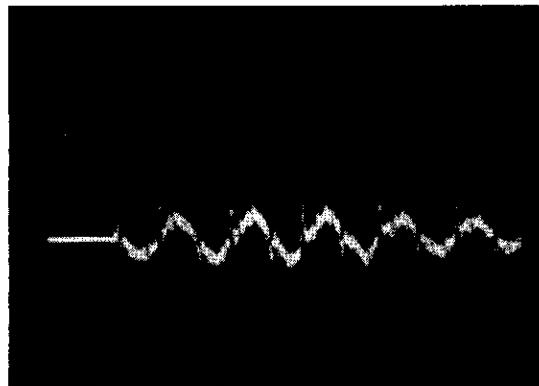
Figure 2b. *Response of the Same Configuration with Sine Wave Input of 750 Hz*

highly correlated signal the system is unable to adapt to the optimum response $\underline{h}_m$.

Decorrelation methods

To permit the solution of equation (13) or (31), the input signal must be uncorrelated; that is, it must have a constant power density spectrum $F_{xx}(\omega)$. Since the higher frequency part of the long-term power density spectrum of speech and video signals approaches

$$F_{xx}(\omega) \doteq \frac{\text{const}}{\omega^b} \tag{32}$$

where $1 < b < 2.5$, it has been suggested that pre-emphasis and de-emphasis filters with transfer characteristics $G_p = \omega^b$ and $G_d = 1/\omega^b$ be used to reduce the autocorrelation of these signals. As reported by Wehrman [9], this method (Figure 3) reduced the length of the vector $\|\underline{\delta}\|$ to
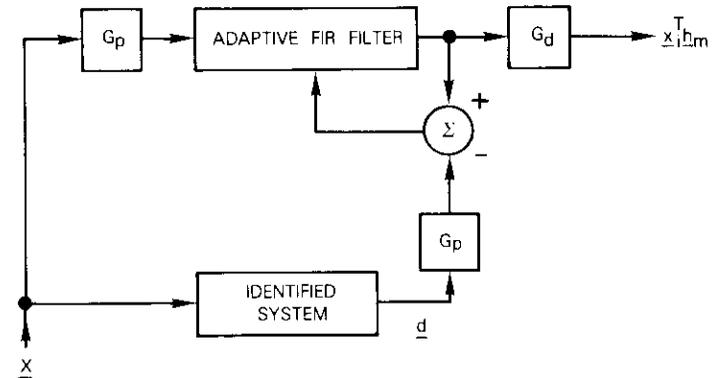
Figure 3. *Adaptive System with Pre-emphasis (G_k) and De-emphasis (G_d) Filters Used to Reduce Auotcorrelation of Speech and Video Signals*

one-third in a given system. COMSAT's experiments produced less favorable results [5]. This can be attributed to the inherent properties of speech which has a low average power but relatively large instantaneous amplitude near its upper frequency limit (4 kHz) and peak factor (the ratio of peak to rms values) up to 30 dB for integration intervals of several seconds [14]. Thus, the filter G_p substantially increases the probability of overloads, termed peak clipping.

Improved results can be obtained if the decorrelation process is applied only to the signal entering the correction processor (see Figure 4). In a sampled system, a Poisson wave can be approximated by a random or pseudorandom binary sequence $\underline{\Phi}_x = [\phi_{i+j}]$, where $\phi_{i+j} = 0, 1$, and $0 \leq i + j \leq 2n$.
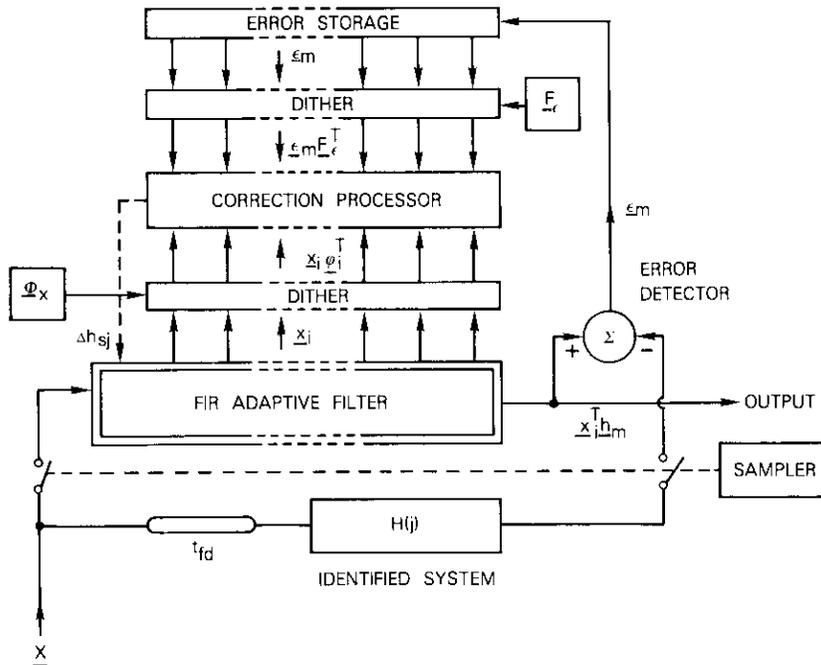
Figure 4. *Block Diagram of an Adaptive FIR Filter with Dither Signals* $\underline{\Phi}_x$ *and* F_ϵ

The scalar products of the components of $\underline{\Phi}_x$ and $\underline{X}$ form a new vector $\underline{X}_d = [x_{i+j}\phi_{i+j}]$, which retains the statistical properties of sequence $\underline{\Phi}_x$ and can be used simultaneously for computing corrections Δh_j according to equation (20):

$$\Delta h_{\phi j} = \frac{1}{||\underline{x}_i||^2} \sum_{i=1}^{n} e_{mi} x_{i+j} \phi_{i+j} \quad . \tag{33}$$

For any sequence $\underline{\Phi}_x$ of one and zeros, correction $|\Delta h_{\phi j}| \leq |\Delta h_{j0}|$; therefore, the condition of nondivergence [equation (12)] is fulfilled. Similarly,

the components e_{mi} of the error vector $\underline{\epsilon}_m$ can be multiplied by a random 2-valued sequence $\underline{F}_\epsilon$, which results in $\underline{\epsilon}_{md} = [e_{mi}f_i]$. The correction is then computed as

$$\Delta h_{fj} = \frac{1}{||\underline{x}_i||^2} \sum_{i=1}^{n} e_{mi} f_i x_{i+j} \tag{34}$$

where for every $\underline{F}_\epsilon$ it is $|\Delta h_{fj}| \leq |\Delta h_{j0}|$.

Sequences $\underline{\Phi}_x$ and $\underline{F}_\epsilon$ are also called dither functions. Both techniques of signal decorrelation by dither functions can be further refined if, instead of random sequences, pseudorandom functions are used with components [4]

$$\phi_{i+j} = 1 \quad , \quad \frac{|x_{i+j}|}{\alpha ||\underline{x}_i||} > 1 \tag{35a}$$

$$\phi_{i+j} = 0 \quad , \quad \text{otherwise} \tag{35b}$$

and, according to Reference 5,

$$f_i = 1 \quad , \quad \frac{|e_{mi}|}{\beta ||\underline{x}_i||} > 1 \tag{36a}$$

$$f_i = 0 \quad , \quad \text{otherwise} \tag{36b}$$

where α and β are constants.

Because $||\underline{x}_i||$ is proportional to the rms value of the input signal, the function ϕ_{i+j} selects samples with high absolute values $|x_{i+j}|$ according to the correction strategy outlined by equation (16). The components f_i initiate the correction process when the error $|e_{mi}|$ is greater than a fraction of the rms value of the input vector $\underline{x}_i$ and adjust the "gain" of the correction circuit to an optimum value. For large values of $2n$, $\underline{\Phi}_x$ and $\underline{F}_\epsilon$ are statistically independent. Proper selection of α and β can also fulfill some other conditions of adaptation [11]; e.g., the system can be prevented from adapting on continuous sine waves (see Figure 2b) or on FIR filter circuit noise when the input signal vector $\underline{X} \rightarrow 0$. Experiments with adaptive filters used in echo cancellers have confirmed that signal decorrelation with dither functions $\underline{\Phi}_x$ and F_ϵ is very effective and contributes to a stable solution for the vector h_m, which is independent of changes in the power

density spectrum $F_{zz}(\omega)$ of input signal vector $\underline{X}$.

The WHE and the discussion relative to equation (31) indirectly prove that $\underline{h}_m$ emulates the sampled impulse response $\underline{H}(j)$ of the unknown system.

Sign correlation

The random or decorrelated sequence of input signal samples $\underline{X}$ has the required autocorrelation function $R_{xi}(0) = \sigma_i^2$ and $R_{xi}(k) = 0$ for all $0 < |k| < 2n$, which permits unambiguous solution of the WHE [equation (31)]. Then the components of the unknown vector $\underline{H}(j) \doteq [h_{mj}]$ for $k = j$ are

$$h_{mj} = R_{xd}(j)R_{xi}^{-1}(0) = \frac{1}{\sigma_i^2} E[d_i x_{i+j}] \quad . \tag{37}$$

Berndt [15] has shown that the true discrete cross-correlation function $R_{xd}(j)$ can be approximately computed by using the sign correlation $B_{xd}(j)$:

$$R_{xd}(j) \doteq \gamma^2 B_{xd}(j) = \gamma^2 E[\text{Sgn}(x_{i+j}d_i) \, \text{Sgn}(d_i c_i)] \tag{38}$$

where γ^2 is a constant factor, and d_i and c_i are components of two statistically independent dither functions $\underline{D}_j = [d_j]$ and $\underline{C}_i = [c_i]$, i.e., two stochastic reference signals with specific properties.

If a vector $\underline{h}_0 = [h_{0j} = 0]$ is chosen for the first iteration, $\text{Sgn}(d_i) = \text{Sgn}(e_{mi})$ during the initial adaptation process. Because the sequences Φ_x and F_e fulfill the statistical condition for $\underline{D}_j$ and $\underline{C}_i$ [15], for a sufficiently large n, the cross-correlation function R_{xd} is approximately

$$R_{xd}(j) \doteq \frac{\gamma^2}{n} \sum_{i=0}^{n} \phi_{i+j} f_i \, \text{Sgn}(x_{i+j}) \, \text{Sgn}(e_{mi}) \tag{39}$$

and R_{xi} is approximately

$$R_{xi}(0) = \frac{1}{n} \|x_i\|^2 \quad . \tag{40}$$

Substituting these expressions into equation (37) yields

$$h_{mj} \doteq \frac{\gamma^2}{\|x_i\|^2} \sum_{i=0}^{n} \phi_{i+j} f_i \, \text{Sgn}(x_{i+j}) \, \text{Sgn}(e_{mi}) \quad . \tag{41}$$

Equation (20) for optimum correction Δh_j can be rearranged to yield

$$\Delta h_{j0} = \sum_{i=0}^{n} \frac{e_{mi}}{\|x_i\|} \frac{x_{i+j}}{\|x_i\|} \quad . \tag{42}$$

If ϕ_{i+j} and f_i from equations (35) and (36) are substituted into equation (42), corrections can be computed as follows for every $i = j$:

$$\Delta h_{sj} = \sum_{j=0}^{n} \partial h_{sj} = \alpha\beta \sum_{i=0}^{n} \phi_{i+j} f_i \, \text{Sgn}(x_{i+j}) \, \text{Sgn}(e_{mi}) \tag{43}$$

where the product $\alpha\beta$ can always be chosen so that the condition of non-divergence $|\Delta h_{sj}| \leq |\Delta h_{j0}|$ is met.

Substituting equations (41) and (43) into the basic correction equation (4) yields

$$h_{m+1j} = h_{mj} - \Delta h_{sj} = h_{mj} - \sum_{j=0}^{n} \partial h_{sj}$$

$$= \left(\frac{\gamma^2}{\|x_i\|^2} - \alpha\beta \right) \sum_{i=0}^{n} \phi_{i+j} f_i \, \text{Sgn}(x_{i+j}) \, \text{Sgn}(e_{mi}) \quad . \tag{44}$$

Thus, equation (44) shows that the sign correlation method can also identify the unknown system response $\underline{H}(j) \doteq [h_{mj}]$, regardless of the statistical properties of input vector $\underline{X} = [x_{i+j}]$, which also follows from Berndt's work [15].

Fast adaptive algorithm

The sign correlation algorithm [equation (44)] can be easily implemented with simple hardware [5], [11]; however, the main disadvantage is that the time of adaptation is directly proportional to the maximum amplitude of response $\underline{h}_m$ and therefore depends on the gain and transient response of the emulated system [4].

To fulfill the requirement of minimum resolution for all responses $\underline{H}(j)$, the constant correction increments Δh_{sj} or ∂h_{sj} must be equal to the smallest quantization step; thus, the number of iterations required to extend response $\underline{h}_m$ increases with the amplitude of coefficients h_{mj}. This can impose a definite limit on the adaptive process, especially when parameters $\underline{H}(j)$ of the identified systems vary rapidly over a wide dynamic range, as

in the case of echo cancellers in 4-wire telephone circuits [3], [5], [11].

Hence, another correction algorithm was developed [5]. Instead of adding ∂h_m to or subtracting it from h_{mj} according to equation (22), a new corrected coefficient vector is found by multiplication:

$$\underline{h}_{m+1} = [h_{mj}(1 - \Delta_s)] = [h_{mj} - h_{mj}\Delta_s] \tag{45}$$

where Δ_s is a positive or negative constant $|\Delta_s| \ll 1$. The correction step according to equation (45) is proportional to the amplitude h_{mj}; thus, the rate of change (speed of adaptation) and relative resolution of the sample h_{mj} is approximately constant over the whole dynamic range of $\underline{h}_m \doteq \underline{H}(j)$. In practical systems [11], this approach can increase the average rate of FIR filter adaptation by at least one order of magnitude under otherwise similar conditions.

According to equations (12) and (21), the condition of nondivergence for this correction strategy is

$$|\partial h_j| = \frac{|e_{mj}x_{i+j}|}{\|\underline{x}_i\|^2} > |h_{mj}\Delta_s| \quad . \tag{46}$$

Substituting from equations (35) and (36) when the condition of correction $\phi_{i+j} = f_i = 1$ is met [see equation (43)] yields the following relationship, which will ensure stable operation of the adaptive system:

$$\Delta_s \leq \frac{\alpha\beta}{|h_{mj}|} = \frac{|\partial h_j|}{|h_{mj}|} \quad . \tag{47}$$

For the fastest possible convergence, i.e., when $|\partial h_j| = |h_{mj}\Delta_s|$, the product $\alpha\beta$ must be adjusted according to the amplitude h_{mj}. Although this is relatively easy to implement, a compromise value $\alpha\beta$ can be chosen [5] to permit fast adaptation and stable operation of the FIR filter over a wide dynamic range of response $\underline{H}(j)$.

Experimental confirmation

An adaptive filter with 256 coefficients h_j was built using the sign correlation method defined by equations (43), (45), and (47), [5], [11], and used to emulate a Butterworth bandpass filter whose frequency characteristic is shown in Figure 5a.
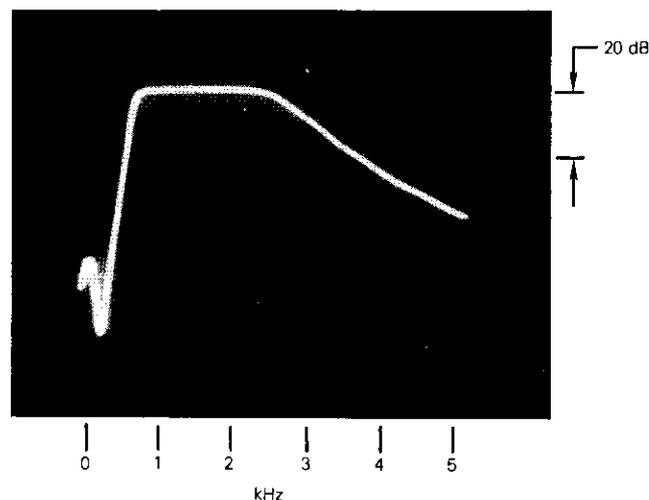
Figure 5a. *Frequency Characteristic of the Butterworth Bandpass Filter (600 Hz–2.4 kHz)*

White noise and a speech signal were used as input signal $\underline{X}$ (Figure 1) in the adaptive process. The response $\underline{h}_m$ was "frozen" after 10,000 iterations and the FIR filter transient and frequency characteristic were measured (see Figures 5b through 5e). The sampling frequency was 10 kHz
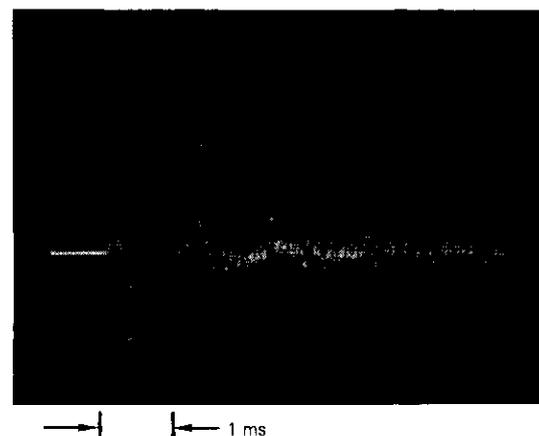
Figure 5b. *Significant Part of the FIR Filter Impulse Response with White Noise Input*
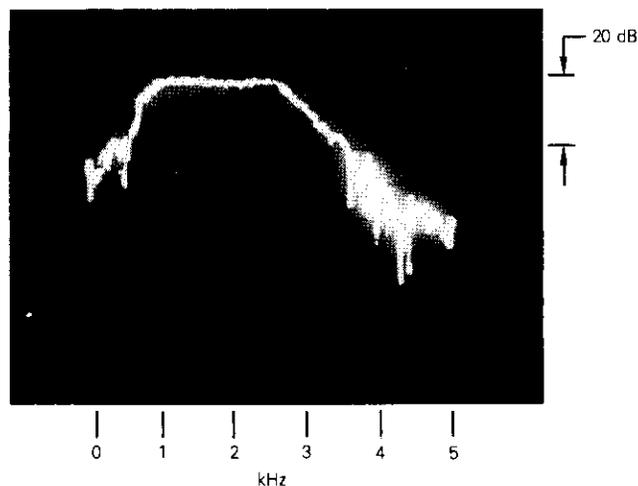
Figure 5c. *FIR Filter Impulse Response with Speech Input Signal*
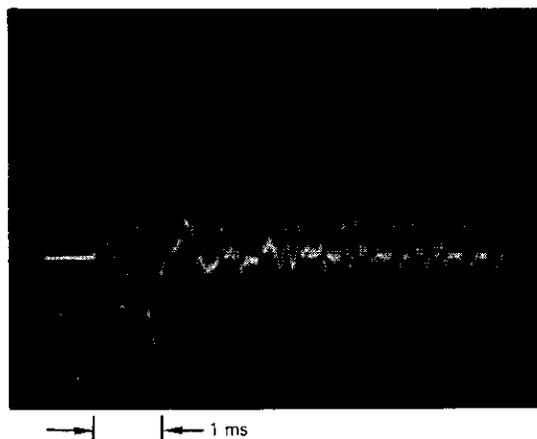
Figure 5d. *Frequency Characteristic of the FIR Filter with White Noise Input*

and the resolution was equivalent to 6 bits. The differences between the characteristics are not greater than the resolution of the FIR filter given by
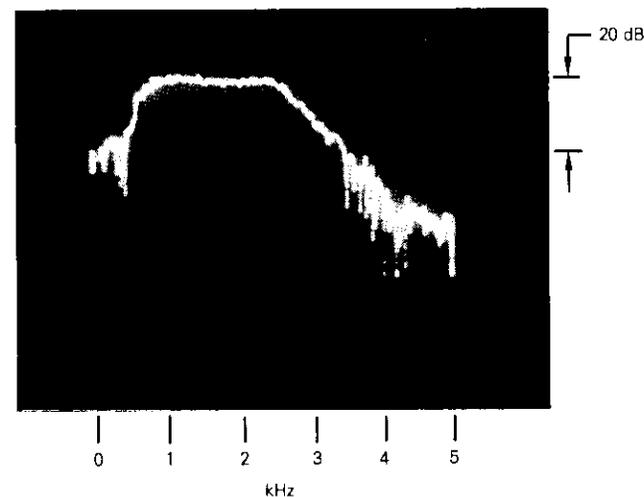
Figure 5e. *Frequency Characteristic of FIR Filter with Speech Input Signal*

sampling rate and quantization errors.* This result confirms the effectiveness of the sign correlation algorithm.

Conclusions

Svoboda's [6] fast converging LMS method for solving a system of linear simultaneous equations permits analysis of the identification algorithm without any *a priori* restrictions on statistical properties of the input signal. This analysis has shown that all known adaptive algorithms, [1], [2], [4] are only different approximations of Svoboda's basic correction formula and that they guarantee only a nondivergence of the adaptive process; the convergence to the optimum (LMS) solution can be ensured only if the signal entering the correlation processor is decorrelated by multiplying the sequence of signal samples by a random binary sequence. This method leads directly to the sign correlation identification algorithm which is easy to implement and permits the use of a faster correction method with correction steps proportional to the magnitude of the samples (coefficients) of the desired response. Experiments performed with

*For frequencies below 300 Hz and above 3.4 kHz the FIR filter characteristic is influenced by presampling and reconstruction filters which are part of the adaptive system.

adaptive filters with several hundred coefficients confirmed directly and indirectly the theoretical results.

Acknowledgment

The author would like to thank Professor A. Svoboda and H. Suyderhoud for many helpful discussions on the details of the manuscript, and G. Welti and Z. M. Ali for carefully reading the manuscript and contributing many helpful suggestions.

References

[1] B. Widrow et al., "Adaptive Noise Cancelling: Principles and Applications," *Proc. IEEE*, Vol. 63, December 1975, pp. 1692–1716.

[2] B. Widrow et al., "Stationary and Nonstationary Learning Characteristic of the LMS Adaptive Filter," *Proc. IEEE*, Vol. 64, No. 8, August 1976, pp. 1151–1162.

[3] B. Widrow and M. E. Hoff, "Adaptive Switching Circuit," *WESCON Convention Record*, 1960, Pt. 4, pp. 96–140.

[4] S. J. Campanella et al., "Analysis of an Adaptive Impulse Response Echo Canceller," *COMSAT Technical Review*, Vol. 2, No. 1, Spring 1972, pp. 1–36.

[5] O. A. Horna, "Echo Canceller Utilizing Pseudo-Logarithmic Coding," *NTC '77 Conference Record*, Vol. 1, pp. 04:7-1–04:7-8.

[6] A. Svoboda, "Linear Analyser in Czechoslovakia" (in Czech), *Czechoslovavak Journal for Physics*, Vol. 1, No. 10, October 1951.

[7] O. Pokorná, "Solution of a System of Algebraic Equation by Minimization of Squares of Residues," (in Czech), *Information Processing Machines*, Prague: Academia, Vol. II, 1954, pp. 111–116.

[8] V˙ Černý and A. Marek, "Application of the Method of Minimization of the Sum of Absolute Values . . ." (in Czech), *Information Processing Machines*, Prague: Academia, Vol. VI, 1958, pp. 209–225.

[9] E. H. Moore, *Memoirs of the American Philosophical Society*, Vol. 1, 1935.

[10] R. Wehrman, "State of Investigations and Possible Further Developments in the Field of Adaptive Cancellers," Third International Conference on Digital Satellite Communications, Kyoto, Japan, 1975.

[11] O. A. Horna, "Echo Canceller with Adaptive Transversal Filter Utilizing Pseudo-Logarithmic Coding," *COMSAT Technical Review*, Vol. 7, No. 2, Fall 1977, pp. 393–428.

[12] W. R. Bennett and J. R. Davey, *Data Transmission*, New York: McGraw-Hill, Inc., 1965.

[13] K. Kuepfmueller, *Die Systemtheorie der elektrischen Nachrichtenübertragung* Stuttgart, West Germany: Hirzel Verlag, 1968.

[14] J. L. Flanagan, *Speech Analysis, Synthesis and Perception*, New York: Academic Press, 1965.

[15] H. Berndt, "Correlation Function Estimation by a Polarity Method Using Stochastic Reference Signals," *IEEE Transactions on Information Theory*, IT-14, November 1968, pp. 796–801.

Otakar A. Horna studied at various European Universities and received an M.S. in electrical engineering from the Czech Institute of Technology, a Ph.D. in electronics from the Institute of Radio Technique and Electronics, and a State Diploma in Mathematical Logic from Charles University in Prague.

He was Senior Scientist and Secretary of the Scientific Council of the Research Institute for Mathematical Machines in Prague in charge of the Computer Technology Division. Later he became Senior Engineer with Multronics Corporation, Rockville, Md., where he worked in military electronics. He joined COMSAT Laboratories in 1969 and is presently a senior staff scientist in the Signal Processing Branch.

He is the author of five books, more than 30 U.S. and foreign patents, and numerous scientific and technical articles. His work was awarded a Gold Medal at the Brussels World Fair in 1958, and a Gold Medal at the Brno Fair in 1967. Recently he received the first COMSAT Research Award for his echo canceller design. He is a Senior Member of IEEE.

Efficient computation of Erlang loss functions

G. D. DILL AND G. D. GORDON

(Manuscript received November 8, 1977)

Abstract

A new form of the Erlang loss function is presented which significantly decreases the computation time required for large trunk groups. This form can be used to calculate directly the grade of service for a given traffic intensity and trunk group size. In conjunction with Newton's method, the maximum acceptable traffic intensity for any size trunk group can be determined for a prescribed grade of service.

A FORTRAN program illustrates the calculation method. The required computer time is less than a tenth of a second per traffic intensity calculated. An Erlang table is shown for five grades of service from 0.001 to 0.1 and for trunk sizes from 1 to 9,000.

Introduction

The Erlang B equation, which relates the number of circuits in a trunk, the traffic intensity, and the grade of service, has frequently been used to size small and moderate trunk groups [1], [2]. Tables based on this equation extend to only one or two hundred circuits, possibly because of the lack of interest in larger trunks or because the computations became more difficult. Although the use of approximation and continued fraction algorithms has been suggested to extend the Erlang B function [3], [4], these

techniques are either not completely accurate or require excessive processing time.

In this paper, the usual Erlang B equation has been modified to increase its suitability for computer calculations. An expression for the derivative of the function is also included. An initial value of maximum acceptable traffic intensity for a given grade of service is found by linear extrapolation; Newton's method is used to determine a more accurate value.

A FORTRAN subroutine is presented that calculates the maximum acceptable traffic intensity for a range of trunk sizes at a specific grade of service. A FORTRAN main program illustrates the use of this subroutine. A total of two minutes processing time was required to compute an extended Erlang table for trunk groups with up to 9,000 circuits.

Mathematical definitions and procedures

Representations of the Erlang B function

The probability of a call being blocked (grade of service) is the ratio of calls receiving a busy signal to the total number of calls initiated. The Erlang B equation assumes that the calls arrive at random and that all calls receiving a busy signal are lost; *i.e.*, they are not redialed.

The Erlang B equation [2] generally used to express the grade of service of a trunk group is

$$B(C, A) = \frac{A^C/C!}{\sum_{k=0}^{C} A^k/k!} \qquad (1)$$

where $B(C, A)$ = probability of a call being blocked
A = traffic intensity to be served, in Erlangs
C = total number of circuits in the trunk group.

As an example, assume that there are 20 circuits in a trunk ($C = 20$) and a traffic density of 12 calls ($A = 12$). This means that if the average number of calls per hour (both completed and blocked) is multiplied by the average call length, then the traffic intensity is approximately 12. Therefore, the probability of a call being blocked is determined from equation (1) to be 1 out of 100 ($B = 0.01$).

An integral representation of the Erlang B function ascribed to Fortet [4] is

$$B(C, A)^{-1} = A \int_0^\infty e^{-Ay} (1 + y)^C \, dy \quad . \qquad (2)$$

The function can also be written as

$$B(C, A)^{-1} = \frac{e^A}{A^C} \Gamma(C + 1, A) \qquad (3)$$

where Γ is the incomplete gamma function [5].

For a large number of circuits in a trunk group, *e.g.*, $C = 300$, the numerical calculation of the Erlang function becomes more difficult, and these formulas are not suitable. The challenge of calculating the Erlang function for many circuits with the series representation in equation (1) is due to four factors:

a. The series has many terms, and the higher order terms are more significant than the lower order terms.

b. The factorials and exponents in equation (1) exceed the normal limit of expressing numbers for most computers.

c. Equation (1) cannot be easily inverted to calculate A for a given value of B.

d. The largest term in the series is a high power of A; hence, small variations in A produce large variations in the series sum.

The next four subsections deal specifically with each of these factors. The first two difficulties are resolved by rewriting the series in a different form. The third problem, finding a value of A for a given B, is solved by performing an iteration with Newton's method. Finally, the large variation of the series sum with respect to A is minimized by techniques of estimating initial values close to the final solution.

Reversing the order of the series

From equation (1), the reciprocal of B can be expressed as

$$\frac{1}{B} = \frac{C!}{A^C} \sum_{k=0}^{C} \frac{A^k}{k!} = \frac{C!}{A^C} \left[1 + \frac{A}{1} + \frac{A^2}{2!} + \cdots + \frac{A^{C-1}}{(C-1)!} + \frac{A^C}{C!} \right] \quad . \qquad (4)$$

For small trunk groups, there are only a few terms; these are of the same order of magnitude. For large trunks (*e.g.*, $C = 300$ and $A = 277.1255$) there are many terms (301), and the terms near the end of the series are very large. (The final term is 10^{118}.) For efficient calculation, the order of the series must be reversed, so that the more significant terms are computed first. This is accomplished by setting $k = C - j$ in equation (4) as follows:

$$\frac{1}{B} = \frac{C!}{A^C} \sum_{j=0}^{C} \frac{A^{C-j}}{(C-j)!} = \frac{C!}{A^C} \left[\frac{A^C}{C!} + \frac{A^{C-1}}{(C-1)!} + \cdots + \frac{A}{1} + 1 \right] \quad . \quad (5)$$

If the terms are calculated in this order, the calculations can be terminated when the terms become negligible.

Successive calculation of terms

The numerically large terms in equation (5) are still difficult to handle in most computers. The next step is to multiply through by $C!/A^C$

$$\frac{1}{B} = \sum_{j=0}^{C} \frac{C!}{A^j(C-j)!}$$

$$= 1 + \frac{C}{A} + \frac{C}{A}\left[\frac{C-1}{A}\right] + \frac{C}{A}\left[\frac{C-1}{A}\right]\left[\frac{C-2}{A}\right] + \cdots + \frac{C!}{A^C} \quad . \quad (6)$$

The individual terms now start at unity, increase in magnitude slowly, and then decrease to a very small value. For $C = 300$, the largest term is the 24th, whose magnitude is only 2.6; the 150th term is only 10^{-15}; and the remaining terms are even smaller in magnitude.

The series can now be expressed so that each term is a product of the previous term and a simple factor:

$$\frac{1}{B} = \sum_{j=0}^{C} T_j \quad , \qquad T_j = \frac{C-j+1}{A} T_{j-1} \quad , \qquad T_0 = 1 \qquad (7)$$

thereby eliminating the need to calculate powers and factorials of large numbers. During the computations, the individual terms eventually become very small and have no significant effect on the series sum. A test determines when the calculations can be terminated. Given a trunk group of C circuits and a traffic intensity of A Erlangs, equation (7) may be employed to efficiently calculate the blocking probability or grade of service, B, for any size trunk group.

Iterative calculation by Newton's method

Frequently, the grade of service (B) is specified, and the maximum traffic intensity (A) that may be served by a given trunk group of circuits (C) must be calculated. Hence, a trial value of A is estimated, and the corresponding value of B is computed using the procedure previously outlined. If the resulting value of B is not sufficiently close to the specified

B, a more accurate value of A is determined. Newton's method may be conveniently used to calculate A to any desired accuracy by determining both the value of a function and its slope for a given value of A, and then extrapolating a straight line through the point having the prescribed slope to a new approximation of A.

The function F is defined as

$$F \equiv 1 - \frac{1}{B} + \sum_{j=1}^{C} T_j \quad , \qquad T_j = \frac{C!}{A^j(C-j)!} \qquad (8)$$

where the terms T_j are calculated for the given C and the trial value of A. For convenience in programming, the first term in the series, which is unity $(j = 0)$, has been written separately. A value of A for which the function F is zero must be determined. According to Newton's method, if A_n is an approximation of the desired A, then a better approximation, A_{n+1}, is given by

$$A_{n+1} = A_n - \left[\frac{F}{dF/dA}\right]_n = A_n \left[1 + \frac{F}{(-AdF/dA)}\right]_n \quad . \qquad (9)$$

The derivative of the function F is found by differentiating equation (8) to be

$$-A \frac{dF}{dA} = \sum_{j=1}^{C} jT_j \quad . \qquad (10)$$

Since the terms T_j must be calculated to find the function F, a computer program can easily multiply these terms by j and evaluate the derivative.

Determining an initial value of A

The first object of this study was to write a subroutine that would calculate the value of A for single values of B and C. However, attempts to discover a formula to determine an initial value of A were unsatisfactory. Therefore, the objective was modified to write a program that would generate an entire table. The first two values of $A(C = 1$ and $C = 2)$ are determined from exact equations. Subsequent initial values of A for equation (9) are determined by linear extrapolation.

For $C = 1$ and $C = 2$, the Erlang B equation [equation (6)] can be solved directly for A. For $C = 1$,

$$A = \frac{B}{1 - B} \tag{11}$$

and for $C = 2$,

$$A = \frac{B + \sqrt{B(2 - B)}}{1 - B} \ . \tag{12}$$

Succeeding initial values are determined by linear extrapolation from previous values in the table. Thus, $A_0(C)$ is equal to twice $A(C - 1)$ minus $A(C - 2)$. For example, if a table for $B = 0.01$ is being calculated, the initial value of A for $C = 3$ is determined by

$$A_0 = 2(0.1526) - 0.0101 = 0.2951 \tag{13}$$

which is not a particularly accurate approximation, compared to the actual value of 0.4555. However, linear extrapolation improves for higher values of C.

From these two principles, a table can start at $C = 1$ and increase by increments of 1 to any value of C. The increment of the table can also be greater than 1. For example, above $C = 150$ an increment of 2 may be desired; the starting value of A for $C = 152$ is obtained as twice the value of A for $C = 150$ minus the value for $C = 148$.

Summary of algorithm

An Erlang table for a single grade of service and a range of trunks from one up to a certain limit can be calculated as follows:

a. The first two values in the table are ascertained from the exact equations (11) and (12).

b. An initial estimate of A for the next entry in the table is determined by linear extrapolation [equation (13)].

c. The values of the function F and its derivative are found from equations (8) and (10) using this value of A.

d. A better estimate of A is obtained by using equation (9).

e. Steps *c* and *d* are repeated until the fractional change in A is less than some specified value.

With this process, convergence is usually achieved within 5 to 10 iterations. Although the number of iterations can be decreased by using quadratic extrapolation or a second-order term in Newton's method, the

improvement in convergence did not seem to justify the additional computations required in each iteration.

Computer programs and execution

A FORTRAN subroutine for the Erlang B calculations (Figure 1) was written using the numerical methods outlined in the previous subsections. This subroutine was implemented by calling it from a SPEAKEASY pro-

```
31          SUBROUTINE ERLF(A, B, MIN, MAX, INC)
       C GDGORDON - APRIL 77 - FINDS A AS A FUNCTION OF B AND C
       C    C IS NUMBER OF CIRCUITS IN A TRUNK
       C    B IS THE GRADE OF SERVICE (FRACTION OF BUSY SIGNALS)
       C    A IS THE TRAFFIC THE TRUNK CAN HANDLE
       C    MIN, MAX, INC ARE THE RANGE AND INCREMENT OF C
       C    IF MIN IS NOT ONE, VALUES OF A FOR C = MIN AND MIN + INC
       C       MUST BE FURNISHED BY THE CALLING PROGRAM
       C    PROCEDURE FINDS TRIAL A (AN) BY EXTRAPOLATION FROM LAST
       C       TWO VALUES, AND THEN FINDS A BY NEWTON'S METHOD.
       C    IF CONVERGENCE FAILS, A IS SET TO -666.
       C
32          DOUBLE PRECISION A(1), AN, TERM, F, FP, B
33          INTEGER C
34          IF (MIN .GT. 1) GO TO 5
35          A(1) = B/(1.D0 - B)
36          F = 1.D0 - 1.D0/B
37          A(2) = (1.D0+DSQRT(1.D0+2.D0*(-F)))/(-F)
38        5 MIN2 = MIN + 2*INC
       C          OUTER LOOP FINDS INCREMENTS C FROM MIN2 TO MAX
39          DO 10 C = MIN2, MAX, INC
40          NC = 1 + (C - MIN)/INC
41          AN = 2.D0*A(NC-1) - A(NC - 2)
       C          MIDDLE LOOP FINDS VALUE OF AN BY NEWTON'S METHOD
42          DO 25 J = 1,20
43          F = 1.D0 - 1.D0/B
44          FP = 0.
45          TERM = 1.D0
       C          INNER LOOP SUMS THE TERMS TO FIND F AND FP
46          DO 20 K = 1,C
47          TERM = TERM*(C-K+1)/AN
48          F = F + TERM
49          FP = FP + K * TERM
       C       WHEN TERM LESS THAN 1.E-12 SERIES SUMMATION ENDS
50          IF (TERM .LT. 1.D-12) GO TO 30
51       20 CONTINUE
52       30 AN = AN*(1 + F/FP)
       C       WHEN CHANGE LESS THAN 1.E-10 NEWTON'S ITERATION ENDS
53          IF ( DABS(F/FP) .LT. 1.D-10) GO TO 15
54       25 CONTINUE
55          AN = -666.
56       15 CONTINUE
57       10 A(NC) = AN
58          RETURN
59          END
```

Figure 1. *Subroutine for Erlang Calculations*

gram.* A FORTRAN main program (Figure 2) was also written to generate a table for five grades of service and for various numbers of circuits from 1 to 9,000. This program calculated 2,000 different points in two minutes of CPU (on an IBM 360/65) or about one minute per thousand points.

```
      C GDGORDON - APRIL 78 - CALCULATION OF ERLANG TABLE
      C   KMIN & KMAX ARE LIMITS OF C FOR EACH PAGE
      C     KFACT IS THE INCREMENT FOR EACH PAGE
      C   PROGRAM GENERATES 8 PAGES, 51 LINES, 5 COLUMNS
  1         DOUBLE PRECISION A(52,5), B(5)
  2         INTEGER KMIN(8), KMAX(8), KFACT(8), C
  3         DATA INC, C /1,1/, B /1.D-3, 3.D-3, 1.D-2, 3.D-2, 1.D-1/
  4         DATA KMIN /  2,  50, 100, 150, 250, 500, 1500, 4000 /
  5         DATA KMAX / 52, 100, 150, 250, 500,1500, 4000, 9000 /
  6         DATA KFACT/  1,   1,   1,   2,   5,  20,   50,  100 /
  7         DO 80 IPAGE = 1,8
  8         INC = KFACT(IPAGE)
  9         MIN = KMIN(IPAGE) - INC
 10         DO 20 KOL = 1, 5
 11      20 CALL ERLF (A(1,KOL), B(KOL), MIN, KMAX(IPAGE), INC)
      C               OUTPUT OF RESULTS
 12         WRITE(6,40) B
 13      40 FORMAT(1H1 //'    C ' , 5('    B =',F5.3)/)
 14         IF(IPAGE .EQ. 1) WRITE(6,50)C,(A(1,KOL),KOL=1, 5)
 15         DO 30 LINE = 1, 51
 16         C = LINE*INC + MIN
 17      30 WRITE(6,50) C,  (A(LINE + 1,KOL), KOL = 1, 5)
 18      50 FORMAT(1X, I5, 5F12.4)
      C       SET FIRST TWO VALUES OF NEXT PAGE
 19         IF(IPAGE .GE. 8) GO TO 90
 20         KI = -KFACT(IPAGE + 1) / KFACT(IPAGE)
 21         FC = KI + FLOAT(KFACT(IPAGE + 1)) / KFACT(IPAGE)
 22         DO 80 KOL = 1, 5
 23         A(1,KOL) = FC*A(KI + 51,KOL) + (1 - FC)*A(KI + 52,KOL)
 24         A(2, KOL) = A(52, KOL)
 25         IF (IPAGE .EQ. 1) A(1, KOL) = A(49, KOL)
 26         IF (IPAGE .EQ. 1) A(2, KOL) = A(50, KOL)
 27      80 CONTINUE
 28      90 WRITE(6,40)
 29         STOP
 30         END
```

Figure 2. *Program to Generate Erlang Table*

A similar program, written in PL/I, was 10 percent faster. Program execution is faster for small numbers of circuits (small C) and for poorer grades of service (large B).

Subroutine

There are five arguments for the subroutine call: A (output), B (grade of service), minimum C, maximum C, and increment of C. All variables are integer or double precision.

---

* SPEAKEASY is an interactive computer language developed at Argonne National Laboratories.

If the first value of C is not unity, the first two values of A are provided by the calling program. If the first value of C is unity (MIN = 1), then the first two values of A are calculated in lines 35 through 37 (see Figure 1). For succeeding values of C, an initial estimate of A is given in line 41 by linear extrapolation. The initial values of the series terms (TERM), the function F, and the derivative FP [equal to $-AdF/dA$ from equation (10)], are set in lines 43 through 45. Succeeding terms and their summation are calculated in lines 47 through 49. An improved value of A is determined in line 52; if the change is greater than one part of 10^{10}, the iteration is repeated.

The maximum number of iterations for Newton's method is set at 20; if convergence is not attained, the value of A is set to -666. In practice, this has never occurred. If convergence is not attained, the series tends to blow up; execution is then halted when the numbers become too large.

Use in SPEAKEASY

Originally, all the calculations were written in SPEAKEASY. After the numerical methods had been selected and tested, the SPEAKEASY program was converted to a FORTRAN subroutine to decrease execution time. The subroutine is usually called from SPEAKEASY for ease of output manipulation and other calculations.

Program to generate a table

A FORTRAN program was written to illustrate the use of the subroutine, to demonstrate the efficiency of the program, and to generate a table applicable to a larger number of circuits than any previous table. Five grades of service were chosen (B = 0.001, 0.003, 0.01, 0.03, and 0.1), ranging from excellent service (1 blocked call per 1,000) to poor service (1 blocked call in 10). The number of circuits per trunk group, C, ranges from 1 to 9,000 with increments varying up to 100 for the last part of the table.

Figure 2 is a listing of the main FORTRAN program, and the output is given in Table 1. All variables are either double precision or integer. The values of C, the number of circuits, for each of the 8 pages are given in lines 4 through 6. In general, KMIN is the lowest C for each page, KMAX is the highest value, and KFACT is the increment. For each page, the subroutine is called 5 times (line 11) for each value of B. The output is generated in lines 12 through 18. The last part of the program, lines 20 through 26, sets the first two values of A for use in the next iteration. Since the first page of the table presented some unique features, lines 14, 25, and 26 were inserted to accommodate them as a special case.

TABLE 1. ERLANG TABLE FOR $C = 1$ TO $C = 9{,}000$

C	B = 0.001	B = 0.003	B = 0.010	B = 0.030	B = 0.100
1	0.0010	0.0030	0.0101	0.0309	0.1111
2	0.0458	0.0806	0.1526	0.2816	0.5954
3	0.1358	0.2885	0.4555	0.7151	1.2708
4	0.4393	0.6021	0.8694	1.2589	2.0454
5	0.7621	0.9945	1.3608	1.8752	2.8811
6	1.1459	1.4468	1.9090	2.5431	3.7584
7	1.5786	1.9463	2.5009	3.2497	4.6662
8	2.0513	2.4837	3.1276	3.9865	5.5971
9	2.5575	3.0526	3.7825	4.7479	6.5464
10	3.0920	3.6480	4.4612	5.5294	7.5106
11	3.6511	4.2661	5.1599	6.3280	8.4871
12	4.2314	4.9038	5.8760	7.1410	9.4740
13	4.8305	5.5588	6.6072	7.9667	10.4699
14	5.4464	6.2290	7.3517	8.8035	11.4735
15	6.0772	6.9129	8.1080	9.6500	12.4838
16	6.7215	7.6091	8.8750	10.5052	13.5001
17	7.3781	8.3164	9.6516	11.3683	14.5217
18	8.0459	9.0339	10.4369	12.2384	15.5480
19	8.7239	9.7606	11.2301	13.1150	16.5787
20	9.4115	10.4958	12.0306	13.9974	17.6132
21	10.1077	11.2389	12.8378	14.8853	18.6512
22	10.8121	11.9893	13.6513	15.7781	19.6925
23	11.5241	12.7465	14.4705	16.6755	20.7367
24	12.2432	13.5100	15.2950	17.5772	21.7836
25	12.9689	14.2795	16.1246	18.4828	22.8331
26	13.7008	15.0545	16.9588	19.3922	23.8850
27	14.4385	15.8347	17.7974	20.3050	24.9390
28	15.1818	16.6199	18.6402	21.2211	25.9950
29	15.9304	17.4097	19.4869	22.1402	27.0529
30	16.6859	18.2039	20.3373	23.0623	28.1126
31	17.4420	19.0023	21.1912	23.9870	29.1740
32	18.2047	19.8047	22.0483	24.9144	30.2369
33	18.9716	20.6108	22.9087	25.8442	31.3013
34	19.7426	21.4205	23.7720	26.7763	32.3672
35	20.5174	22.2337	24.6381	27.7106	33.4343
36	21.2960	23.0501	25.5070	28.6470	34.5027
37	22.0781	23.8697	26.3785	29.5854	35.5722
38	22.8636	24.6922	27.2525	30.5258	36.6429
39	23.6523	25.5177	28.1288	31.4679	37.7147
40	24.4442	26.3459	29.0074	32.4118	38.7874
41	25.2391	27.1767	29.8882	33.3574	39.8612
42	26.0369	28.0101	30.7712	34.3046	40.9359
43	26.8374	28.8460	31.6561	35.2533	42.0114
44	27.6406	29.6842	32.5431	36.2035	43.0878
45	28.4466	30.5247	33.4317	37.1551	44.1650
46	29.2549	31.3674	34.3223	38.1081	45.2430
47	30.0657	32.2122	35.2146	39.0624	46.3218
48	30.8789	33.0591	36.1086	40.0180	47.4012
49	31.6943	33.9080	37.0042	40.9748	48.4813
50	32.5119	34.7588	37.9014	41.9327	49.5621
51	33.3316	35.6114	38.8001	42.8919	50.6435
52	34.1533	36.4659	39.7003	43.8521	51.7256

TABLE 1 (continued). ERLANG TABLE FOR $C = 1$ TO $C = 9{,}000$

C	B = 0.001	B = 0.003	B = 0.010	B = 0.030	B = 0.100
50	32.5119	34.7588	37.9014	41.9327	49.5621
51	33.3316	35.6114	38.8001	42.8919	50.6435
52	34.1533	36.4659	39.7003	43.8521	51.7256
53	34.9771	37.3221	40.6019	44.8134	52.8082
54	35.8028	38.1800	41.5049	45.7758	53.8914
55	36.6305	39.0396	42.4092	46.7391	54.9751
56	37.4599	39.9007	43.3149	47.7034	56.0594
57	38.2911	40.7634	44.2218	48.6687	57.1441
58	39.1241	41.6276	45.1299	49.6348	58.2294
59	39.9587	42.4933	46.0392	50.6019	59.3151
60	40.7950	43.3604	46.9497	51.5698	60.4013
61	41.6328	44.2290	47.8613	52.5385	61.4880
62	42.4723	45.0988	48.7740	53.5081	62.5750
63	43.3132	45.9700	49.6878	54.4784	63.6625
64	44.1557	46.8425	50.6026	55.4496	64.7504
65	44.9995	47.7163	51.5185	56.4214	65.8387
66	45.8448	48.5912	52.4353	57.3940	66.9274
67	46.6915	49.4674	53.3531	58.3673	68.0164
68	47.5395	50.3447	54.2718	59.3413	69.1058
69	48.3888	51.2232	55.1915	60.3160	70.1956
70	49.2394	52.1028	56.1120	61.2913	71.2857
71	50.0913	52.9835	57.0335	62.2673	72.3761
72	50.9444	53.8653	57.9558	63.2439	73.4668
73	51.7987	54.7480	58.8789	64.2211	74.5579
74	52.6542	55.6319	59.8028	65.1989	75.6492
75	53.5108	56.5167	60.7276	66.1773	76.7409
76	54.3685	57.4025	61.6531	67.1562	77.8328
77	55.2274	58.2892	62.5794	68.1358	78.9250
78	56.0873	59.1769	63.5065	69.1158	80.0175
79	56.9483	60.0655	64.4343	70.0964	81.1103
80	57.8104	60.9550	65.3628	71.0775	82.2033
81	58.6734	61.8454	66.2920	72.0591	83.2966
82	59.5375	62.7366	67.2219	73.0412	84.3901
83	60.4025	63.6287	68.1524	74.0238	85.4839
84	61.2685	64.5216	69.0837	75.0069	86.5778
85	62.1354	65.4154	70.0156	75.9904	87.6721
86	63.0033	66.3099	70.9481	76.9744	88.7665
87	63.8721	67.2052	71.8812	77.9589	89.8612
88	64.7417	68.1013	72.8150	78.9438	90.9561
89	65.6123	68.9982	73.7494	79.9291	92.0512
90	66.4837	69.8958	74.6843	80.9149	93.1465
91	67.3559	70.7941	75.6198	81.9010	94.2420
92	68.2290	71.6931	76.5560	82.8876	95.3376
93	69.1029	72.5929	77.4926	83.8746	96.4335
94	69.9776	73.4933	78.4298	84.8619	97.5296
95	70.8531	74.3944	79.3676	85.8497	98.6259
96	71.7294	75.2962	80.3059	86.8378	99.7223
97	72.6064	76.1987	81.2447	87.8263	100.8189
98	73.4842	77.1018	82.1840	88.8151	101.9157
99	74.3627	78.0055	83.1238	89.8043	103.0126
100	75.2420	78.9099	84.0642	90.7939	104.1098

TABLE 1 (continued). ERLANG TABLE FOR $C = 1$ TO $C = 9,000$

C	B = 0.001	B = 0.003	B = 0.010	B = 0.030	B = 0.100
100	75.2420	78.9099	84.0642	90.7039	104.1098
101	76.1220	79.8149	85.0050	91.7838	105.2070
102	77.0026	80.7205	85.9463	92.7741	106.3045
103	77.8840	81.6246	86.8880	93.7646	107.4021
104	78.7661	82.5334	87.8303	94.7555	108.4998
105	79.6488	83.4408	88.7729	95.7468	109.5577
106	80.5322	84.3487	89.7161	96.7383	110.6958
107	81.4163	85.2572	90.6597	97.7302	111.7940
108	82.3010	86.1662	91.6037	98.7224	112.8923
109	83.1863	87.0758	92.5481	99.7148	113.9908
110	84.0723	87.9859	93.4930	100.7006	115.0894
111	84.9588	88.8966	94.4383	101.7006	116.1181
112	85.8460	89.8078	95.3840	102.6940	117.2870
113	86.7338	90.7195	96.3301	103.6876	118.3860
114	87.6222	91.6317	97.2766	104.6815	119.4851
115	88.5112	92.5444	98.2235	105.6757	120.5843
116	89.4007	93.4576	99.1707	106.6702	121.6837
117	90.2908	94.3712	100.1184	107.6649	122.7832
118	91.1815	95.2854	101.0664	108.6599	123.8828
119	92.0727	96.2000	102.0148	109.6551	124.9825
120	92.9645	97.1151	102.9636	110.6506	126.0824
121	93.8568	98.0307	103.9128	111.6464	127.1823
122	94.7496	98.9467	104.8522	112.6423	128.2824
123	95.6430	99.8632	105.8121	113.6386	129.3826
124	96.5369	100.7801	106.7623	114.6351	130.4828
125	97.4312	101.6974	107.7128	115.6318	131.5832
126	98.3261	102.6152	108.6637	116.6287	132.6837
127	99.2215	103.5334	109.6149	117.6259	133.7843
128	100.1174	104.4521	110.5664	118.6233	134.8850
129	101.0138	105.3711	111.5183	119.6209	135.9858
130	101.9106	106.2906	112.4705	120.6188	137.0866
131	102.8080	107.2104	113.4230	121.6169	138.1876
132	103.7058	108.1307	114.3758	122.6151	139.2887
133	104.6040	109.0513	115.3289	123.6136	140.3898
134	105.5028	109.9724	116.2823	124.6123	141.4911
135	106.4019	110.8938	117.2360	125.6113	142.5924
136	107.3015	111.8156	118.1900	126.6104	143.6939
137	108.2016	112.7378	119.1443	127.6097	144.7954
138	109.1021	113.6604	120.0989	128.6092	145.8970
139	110.0030	114.5833	121.0538	129.6089	146.9987
140	110.9044	115.5066	122.0090	130.6088	148.1004
141	111.8062	116.4303	122.9645	131.6089	149.2023
142	112.7084	117.3543	123.9202	132.6092	150.3042
143	113.6110	118.2787	124.8762	133.6097	151.4062
144	114.5140	119.2034	125.8325	134.6103	152.5083
145	115.4174	120.1284	126.7890	135.6112	153.6105
146	116.3212	121.0538	127.7458	136.6122	154.7127
147	117.2255	121.9796	128.7029	137.6134	155.8150
148	118.1301	122.9056	129.6602	138.6148	156.9174
149	119.0351	123.8320	130.6178	139.6163	158.0199
150	119.9404	124.7588	131.5756	140.6180	159.1224

TABLE 1 (continued). ERLANG TABLE FOR $C = 1$ TO $C = 9,000$

C	B = 0.001	B = 0.003	B = 0.010	B = 0.030	B = 0.100
150	119.9404	124.7588	131.5756	140.6180	159.1224
152	121.7523	126.6132	133.4920	142.6220	161.3277
154	123.5657	128.4688	135.4094	144.6266	163.5332
156	125.3805	130.3258	137.3278	146.6318	165.7390
158	127.1968	132.1839	139.2470	148.6377	167.9451
160	129.0144	134.0432	141.1672	150.6442	170.1514
162	130.8335	135.9037	143.0883	152.6513	172.3580
164	132.6538	137.7653	145.0102	154.6590	174.5648
166	134.4755	139.6280	146.9330	156.6673	176.7719
168	136.2985	141.4918	148.8567	158.6761	178.9792
170	138.1227	143.3568	150.7812	160.6855	181.1867
172	139.9482	145.2227	152.7065	162.6954	183.3944
174	141.7749	147.0897	154.6326	164.7059	185.6023
176	143.6028	148.9577	156.5595	166.7169	187.8105
178	145.4319	150.8267	158.4872	168.7284	190.0188
180	147.2621	152.6967	160.4156	170.7404	192.2273
182	149.0935	154.5677	162.3447	172.7529	194.4361
184	150.9260	156.4396	164.2746	174.7659	196.6450
186	152.7595	158.3124	166.2051	176.7793	198.8541
188	154.5942	160.1862	168.1364	178.7932	201.0634
190	156.4299	162.0608	170.0684	180.8076	203.2728
192	158.2667	163.9363	172.0010	182.8224	205.4825
194	160.1045	165.8127	173.9343	184.8376	207.6923
196	161.9433	167.6900	175.8683	186.8533	209.9022
198	163.7831	169.5680	177.8028	188.8694	212.1124
200	165.6239	171.4470	179.7380	190.8859	214.3226
202	167.4657	173.3267	181.6739	192.9028	216.5331
204	169.3084	175.2072	183.6103	194.9201	218.7437
206	171.1520	177.0885	185.5473	196.9378	220.9544
208	172.9965	178.9706	187.4850	198.9559	223.1653
210	174.8420	180.8534	189.4232	200.9744	225.3763
212	176.6883	182.7370	191.3620	202.9932	227.5874
214	178.5355	184.6214	193.3013	205.0124	229.7987
216	180.3836	186.5065	195.2412	207.0320	232.0102
218	182.2326	188.3923	197.1816	209.0519	234.2217
220	184.0823	190.2787	199.1226	211.0722	236.4334
222	185.9329	192.1659	201.0641	213.0928	238.6452
224	187.7844	194.0538	203.0061	215.1137	240.8571
226	189.6366	195.9424	204.9487	217.1350	243.0692
228	191.4896	197.8316	206.8917	219.1566	245.2814
230	193.3434	199.7215	208.8353	221.1785	247.4937
232	195.1980	201.6120	210.7793	223.2008	249.7061
234	197.0533	203.5032	212.7238	225.2233	251.9186
236	198.9094	205.3950	214.6688	227.2462	254.1312
238	200.7662	207.2874	216.6143	229.2694	256.3439
240	202.6238	209.1805	218.5602	231.2928	258.5568
242	204.4821	211.0741	220.5066	233.3166	260.7697
244	206.3411	212.9684	222.4534	235.3406	262.9827
246	208.2008	214.8632	224.4007	237.3649	265.1959
248	210.0612	216.7587	226.3484	239.3895	267.4091
250	211.9222	218.6547	228.2965	241.4144	269.6225

TABLE 1 (continued). ERLANG TABLE FOR $C = 1$ TO $C = 9{,}000$

C	B =0.001	B =0.003	B =0.010	B =0.030	B =0.100
250	211.9222	218.6547	228.2965	241.4144	269.6225
255	216.5779	223.3971	233.1687	246.4778	275.1562
260	221.2376	228.1430	238.0435	251.5428	280.6905
265	225.9013	232.8922	242.9208	256.6095	286.2254
270	230.5689	237.6447	247.8005	261.6776	291.7608
275	235.2402	242.4003	252.6825	266.7472	297.2967
280	239.9152	247.1589	257.5668	271.8183	302.8331
285	244.5936	251.9205	262.4534	276.8907	308.3699
290	249.2756	256.6850	267.3420	281.9645	313.9072
295	253.9608	261.4523	272.2328	287.0396	319.4449
300	258.6494	266.2223	277.1255	292.1159	324.9830
305	263.3411	270.9949	282.0203	297.1935	330.5216
310	268.0359	275.7701	286.9169	302.2722	336.0605
315	272.7337	280.5478	291.8154	307.3521	341.5997
320	277.4344	285.3280	296.7157	312.4331	347.1394
325	282.1380	290.1105	301.6178	317.5153	352.6793
330	286.8444	294.8954	306.5215	322.5984	358.2196
335	291.5535	299.6825	311.4270	327.6826	363.7603
340	296.2653	304.4719	316.3341	332.7678	369.3012
345	300.9797	309.2634	321.2428	337.8539	374.8424
350	305.6966	314.0570	326.1530	342.9411	380.3839
355	310.4160	318.8527	331.0647	348.0291	385.9258
360	315.1378	323.6504	335.9780	353.1180	391.4678
365	319.8620	328.4501	340.8926	358.2078	397.0102
370	324.5886	333.2517	345.8087	363.2985	402.5528
375	329.3174	338.0552	350.7262	368.3900	408.0956
380	334.0484	342.8605	355.6450	373.4823	413.6387
385	338.7816	347.6677	360.5651	378.5753	419.1820
390	343.5170	352.4766	365.4865	383.6692	424.7256
395	348.2544	357.2872	370.4092	388.7638	430.2693
400	352.9939	362.0996	375.3331	393.8592	435.8133
405	357.7354	366.9136	380.2583	398.9553	441.3575
410	362.4789	371.7292	385.1846	404.0521	446.9019
415	367.2243	376.5464	390.1120	409.1495	452.4465
420	371.9717	381.3652	395.0407	414.2477	457.9912
425	376.7208	386.1856	399.9704	419.3465	463.5362
430	381.4718	391.0074	404.9012	424.4459	469.0813
435	386.2246	395.8307	409.8331	429.5460	474.6266
440	390.9792	400.6555	414.7660	434.6467	480.1721
445	395.7355	405.4817	419.7000	439.7480	485.7178
450	400.4934	410.3093	424.6350	444.8499	491.2636
455	405.2531	415.1382	429.5709	449.9524	496.8096
460	410.0144	419.9686	434.5079	455.0554	502.3557
465	414.7773	424.8002	439.4458	460.1590	507.9020
470	419.5418	429.6331	444.3846	465.2632	513.4484
475	424.3078	434.4674	449.3243	470.3679	518.9949
480	429.0754	439.3029	454.2650	475.4731	524.5416
485	433.8445	444.1396	459.2065	480.5788	530.0885
490	438.6150	448.9775	464.1490	485.6850	535.6355
495	443.3870	453.8167	469.0922	490.7917	541.1826
500	448.1605	458.6570	474.0364	495.8989	546.7298

TABLE 1 (continued). ERLANG TABLE FOR $C = 1$ TO $C = 9{,}000$

C	B =0.001	B =0.003	B =0.010	B =0.030	B =0.100
500	448.1605	458.6570	474.0364	495.8989	546.7298
520	467.2682	478.0297	493.8210	516.3324	568.5199
540	486.3971	497.4197	513.6180	536.7729	591.1118
560	505.5461	516.8262	533.4267	557.2201	613.3054
580	524.7139	536.2481	553.2463	577.6734	635.5005
600	543.8996	555.6845	573.0763	598.1325	657.6970
620	563.1022	575.1348	592.9159	618.5970	679.8947
640	582.3209	594.5981	612.7648	639.0665	702.0937
660	601.5548	614.0739	632.6224	659.5409	724.2937
680	620.8033	633.5615	652.4882	680.0197	746.4948
700	640.0656	653.0603	672.3619	700.5029	768.6968
720	659.3412	672.5699	692.2431	720.9900	790.8997
740	678.6295	692.0897	712.1313	741.4810	813.1034
760	697.9299	711.6194	732.0264	761.9756	835.3079
780	717.2419	731.1584	751.9280	782.4736	857.5132
800	736.5651	750.7064	771.8358	802.9750	879.7191
820	755.8989	770.2631	791.7495	823.4794	901.9256
840	775.2431	789.8281	811.6689	843.9868	924.1328
860	794.5972	809.4011	831.5938	864.4971	946.3405
880	813.9608	828.9817	851.5239	885.0100	968.5487
900	833.3336	848.5698	871.4590	905.5256	990.7575
920	852.7153	868.1649	891.3990	926.0435	1012.9667
940	872.1056	887.7670	911.3437	946.5640	1035.1764
960	891.5042	907.3757	931.2929	967.0867	1057.3865
980	910.9108	926.9908	951.2464	987.6116	1079.5970
1000	930.3251	946.6121	971.2041	1008.1386	1101.8079
1020	949.7470	966.2394	991.1658	1028.6676	1124.0191
1040	969.1761	985.8726	1011.1314	1049.1985	1146.2308
1060	988.6123	1005.5113	1031.1008	1069.7314	1168.4427
1080	1008.0553	1025.1556	1051.0739	1090.2660	1190.6549
1100	1027.5050	1044.8051	1071.0505	1110.8023	1212.8675
1120	1046.9611	1064.4597	1091.0305	1131.3404	1235.0804
1140	1066.4235	1084.1194	1111.0139	1151.8800	1257.2935
1160	1085.8920	1103.7839	1131.0004	1172.4212	1279.5069
1180	1105.3664	1123.4530	1150.9901	1192.9639	1301.7205
1200	1124.8466	1143.1268	1170.9828	1213.5081	1323.9344
1220	1144.3324	1162.8051	1190.9785	1234.0537	1346.1485
1240	1163.8236	1182.4876	1210.9770	1254.6006	1368.3628
1260	1183.3202	1202.1744	1230.9783	1275.1489	1390.5773
1280	1202.8213	1221.8653	1250.9823	1295.6984	1412.7921
1300	1222.3289	1241.5602	1270.9889	1316.2492	1435.0070
1320	1241.8407	1261.2590	1290.9981	1336.8012	1457.2221
1340	1261.3573	1280.9617	1311.0097	1357.3543	1479.4374
1360	1280.8786	1300.6680	1331.0238	1377.9086	1501.6529
1380	1300.4046	1320.3780	1351.0403	1398.4640	1523.8686
1400	1319.9350	1340.0915	1371.0591	1419.0204	1546.0844
1420	1339.4698	1359.8085	1391.0801	1439.5779	1568.3003
1440	1359.0089	1379.5288	1411.1033	1460.1364	1590.5164
1460	1378.5522	1399.2525	1431.1286	1480.6958	1612.7327
1480	1398.0996	1418.9794	1451.1561	1501.2562	1634.9491
1500	1417.6511	1438.7094	1471.1855	1521.8175	1657.1655

TABLE 1 (continued). ERLANG TABLE FOR $C = 1$ TO $C = 9,000$

C	B =0.001	B =0.003	B =0.010	B =0.030	B =0.100
1500	1417.6511	1438.7094	1471.1855	1521.8175	1657.1656
1550	1466.567	1488.0479	1521.2678	1572.2247	1712.7075
1600	1515.4656	1537.4047	1571.3619	1624.6372	1768.2501
1650	1564.4068	1586.7789	1621.4670	1676.0546	1823.7934
1700	1613.3690	1636.1696	1671.5827	1727.4934	1879.3373
1750	1662.3514	1685.5759	1721.7083	1778.9030	1934.8818
1800	1711.3530	1734.9973	1771.8434	1830.3335	1990.4268
1850	1760.3730	1784.4330	1821.9876	1881.7678	2045.9724
1900	1809.4105	1833.8823	1872.1403	1933.2058	2101.5184
1950	1858.4649	1883.3448	1922.3012	1984.6473	2157.0648
2000	1907.5355	1932.8197	1972.4700	2036.0921	2212.6116
2050	1956.6216	1982.3067	2022.6462	2087.5400	2268.1588
2100	2005.7226	2031.8052	2072.8296	2138.9908	2323.7064
2150	2054.8379	2081.3149	2123.0198	2190.4444	2379.2543
2200	2103.9671	2130.8351	2173.2166	2241.9008	2434.8025
2250	2153.1096	2180.3657	2223.4197	2293.3596	2490.3510
2300	2202.2650	2229.9061	2273.6289	2344.8209	2545.8998
2350	2251.4328	2279.4561	2323.8439	2396.2846	2601.4488
2400	2300.6125	2329.0153	2374.0645	2447.7504	2656.9981
2450	2349.8039	2378.5834	2424.2905	2499.2184	2712.5476
2500	2399.0064	2428.1600	2474.5217	2550.6884	2768.0974
2550	2448.2199	2477.7450	2524.7580	2602.1603	2823.6473
2600	2497.4438	2527.3380	2574.9990	2653.6341	2879.1974
2650	2546.5779	2576.9388	2625.2447	2705.1097	2934.7477
2700	2595.9219	2626.5472	2675.4950	2756.5870	2990.2982
2750	2645.1755	2676.1628	2725.7496	2808.0660	3045.8489
2800	2694.4584	2725.7856	2776.0084	2859.5466	3101.3997
2850	2743.7104	2775.4152	2826.2713	2911.0287	3156.9507
2900	2792.9911	2825.0515	2876.5382	2962.5122	3212.5018
2950	2842.2804	2874.6943	2926.8089	3013.9972	3268.0531
3000	2891.5781	2924.3434	2977.0834	3065.4835	3323.6044
3050	2940.8838	2973.9987	3027.3614	3116.9712	3379.1560
3100	2990.1974	3023.6599	3077.6429	3168.4601	3434.7076
3150	3039.5187	3073.3266	3127.9279	3219.9502	3490.2593
3200	3088.8475	3122.9996	3178.2161	3271.4415	3545.8112
3250	3138.1836	3172.6778	3228.5076	3322.9340	3601.3631
3300	3187.5268	3222.3614	3278.8021	3374.4276	3656.9152
3350	3236.8770	3272.0501	3329.0997	3425.9222	3712.4673
3400	3286.2339	3321.7441	3379.3614	3477.4179	3768.0196
3450	3335.5975	3371.4429	3429.7037	3528.9146	3823.5719
3500	3384.9675	3421.1467	3480.0099	3580.4122	3879.1243
3550	3434.3439	3470.8552	3530.3188	3631.9108	3934.6768
3600	3483.7264	3520.5683	3580.6304	3683.4103	3990.2294
3650	3533.1150	3570.2859	3630.9445	3734.9107	4045.7821
3700	3582.5095	3620.0080	3681.2612	3786.4120	4101.3348
3750	3631.9098	3669.7344	3731.5804	3837.9140	4156.8875
3800	3681.3157	3719.4650	3781.9019	3889.4169	4212.4405
3850	3730.7271	3769.1998	3832.2258	3940.9206	4267.9934
3900	3780.1440	3818.9386	3882.5520	3992.4250	4323.5464
3950	3829.5662	3868.6814	3932.8804	4043.9301	4379.0995
4000	3878.9936	3918.4280	3983.2109	4095.4360	4434.6526

TABLE 1 (continued). ERLANG TABLE FOR $C = 1$ TO $C = 9,000$

C	B =0.001	B =0.003	B =0.010	B =0.030	B =0.100
4000	3878.9936	3918.4280	3983.2109	4095.4360	4434.6526
4100	3977.8636	4017.9326	4083.8784	4198.4499	4545.7590
4200	4076.7531	4117.4518	4184.5541	4301.4665	4656.8656
4300	4175.6616	4216.9849	4285.2375	4404.4855	4767.9724
4400	4274.5881	4316.5315	4385.9284	4507.5067	4879.0793
4500	4373.5322	4416.0910	4486.6264	4610.5303	4990.1865
4600	4472.4931	4515.6630	4587.3313	4713.5561	5101.2938
4700	4571.4703	4615.2470	4688.0427	4816.5839	5212.4013
4800	4670.4632	4714.8426	4788.7605	4919.6136	5323.5089
4900	4769.4714	4814.4494	4889.4843	5022.6450	5434.6166
5000	4868.4942	4914.0669	4990.2140	5125.6780	5545.7245
5100	4967.5312	5013.6949	5090.9493	5228.7127	5656.8325
5200	5066.5820	5113.3330	5191.6900	5331.7503	5767.9406
5300	5165.6462	5212.9808	5292.4360	5434.7886	5879.0488
5400	5264.7233	5312.6381	5393.1870	5537.8283	5990.1571
5500	5363.8130	5412.3046	5493.9428	5640.8694	6101.2655
5600	5462.9149	5512.0799	5594.7034	5743.9118	6212.3740
5700	5562.0286	5611.8637	5695.4685	5846.9556	6323.4826
5800	5661.1538	5711.6558	5796.2380	5950.0006	6434.5913
5900	5760.2902	5811.4559	5897.0118	6053.0468	6545.7000
6000	5859.4375	5911.2640	5997.7897	6156.0942	6656.8089
6100	5958.5954	6011.0797	6098.5716	6259.1427	6767.9177
6200	6057.7636	6110.9031	6199.3574	6362.1922	6879.0267
6300	6156.9418	6210.7337	6300.1470	6465.2428	6990.1357
6400	6256.1299	6310.5716	6400.9400	6568.2943	7101.2448
6500	6355.3274	6410.4166	6501.7367	6671.3469	7212.3540
6600	6454.5343	6510.2685	6602.5368	6774.4003	7323.4632
6700	6553.7503	6610.1272	6703.3402	6877.4546	7434.5725
6800	6652.9751	6709.9925	6804.1469	6980.5098	7545.6818
6900	6752.2086	6809.8645	6904.9567	7083.5658	7656.7911
7000	6851.4504	6909.7429	7005.7696	7186.6226	7767.9005
7100	6950.7005	7009.6277	7106.5855	7289.6801	7879.0100
7200	7049.9587	7109.5187	7207.4042	7392.7384	7990.1195
7300	7149.2248	7209.4159	7308.2258	7495.7975	8101.2290
7400	7248.4986	7309.3191	7409.0501	7598.8572	8212.3386
7500	7347.7799	7409.2282	7509.8771	7701.9176	8323.4482
7600	7447.0686	7509.1431	7610.7067	7804.9787	8434.5579
7700	7546.3646	7609.0636	7711.5389	7908.0404	8545.6676
7800	7645.6675	7708.9897	7812.3735	8011.1027	8656.7773
7900	7744.9775	7808.9213	7913.2105	8114.1656	8767.8871
8000	7844.2941	7908.8583	8014.0499	8217.2291	8878.9969
8100	7943.6175	8008.8006	8114.8916	8320.2931	8990.1067
8200	8042.9473	8108.7481	8215.7356	8423.3577	9101.2166
8300	8142.2835	8208.7007	8316.5817	8526.4229	9212.3265
8400	8241.6259	8308.6583	8417.4300	8629.4885	9323.4364
8500	8340.9745	8408.6209	8518.2804	8732.5546	9434.5463
8600	8440.3292	8508.5884	8619.1328	8835.6212	9545.6563
8700	8539.6897	8608.5606	8719.9872	8938.6883	9656.7663
8800	8639.0560	8708.5375	8820.8436	9041.7559	9767.8763
8900	8738.4280	8808.5191	8921.7019	9144.8239	9878.9864
9000	8837.8056	8908.5052	9022.5621	9247.8923	9990.0964

References

[1] G. Dietrich et al., "Traffic Engineering Manual," Standard Electric Lorenz AG, Stuettgart, Germany, 1966.

[2] A. K. Erlang, "Solution of Some Problems in the Theory of Probabilities of Significance in Automatic Telephone Exchanges," *Post Office Electronics Engineers Journal*, No. 10, 1917, pp. 189.

[3] G. Levy-Soussan, "Numerical Evaluation of the Erlang Function Through a Continued-Fraction Algorithm," *Electrical Communications*, Vol. 42, No. 2, 1968, pp. 163–168.

[4] D. L. Jagerman, "Some Properties of the Erlang Function," *Bell System Technical Journal*, Vol. 53, No. 3, March 1974, pp. 525–551.

[5] H. Flieger, Private Communication.

George D. Dill received a B.S. in Applied Physics from the University of California in 1957. He joined COMSAT Laboratories in 1964 and later became Manager of the Digital Control Department of the Communications Processing Laboratory responsible for the development of multiple-access techniques, data transmission systems, signaling and switching systems, and monitor and control systems for communications satellite networks. He is co-inventor of the SPADE System and holds other patents on multiple access signaling and terrestrial interface systems. He is presently with Comtel in Santa Maria, California.

Gary D. Gordon received a B.A. from Wesleyan University in 1950 and a Ph.D. in physics from Harvard University in 1954. In 1958 he began working at the RCA Space Center, where he contributed to the thermal design of the TIROS weather satellite and was responsible for the thermal design of the RELAY communications satellite. He has taught courses on spacecraft thermal design, satellite orbits, satellite reliability, and computer programming. Dr. Gordon joined COMSAT Laboratories in 1969 and has worked on spacecraft spin stabilization, mechanical bearings, and system reliability analysis. He is presently Senior Staff Scientist in the Spacecraft Laboratory. He is listed in American Men of Science and in Who's Who in the East. He is a member of AIAA, AAPT, Sigma Xi, and Phi Beta Kappa.

Computer simulation of solid-state amplifiers

L. C. PALMER AND S. LEBOWITZ

(Manuscript received December 2, 1977)

Abstract

Modeling and computer simulation of an L-band class-C transistor amplifier has been performed to determine its AM/AM and AM/PM characteristics. A state-variable representation was developed leading to nonlinear first-order differential equations which were solved by using a standard software subroutine for a single sinusoidal input with various amplitudes. The AM/PM and AM/AM characteristics obtained from the computer model show good agreement with laboratory measurements on a similar amplifier.

These nonlinear characteristics were used in the CHAMP time-domain simulation program to determine the spectrum "re-growth" of single, filtered, conventional and offset QPSK and minimum shift keyed (MSK) signals after amplification. A comparison with available laboratory results again shows good agreement between the simulated (computer) and the laboratory (hardware) results.

Introduction

In an analysis of the impairments experienced in communications channels, some of the more important, and often more difficult, elements to model accurately are the nonlinearities encountered in real channels. An example is the helix-type traveling wave tube (TWT) which is used in most communications satellite transponders. This device is typically distin-

guished by two memoryless characteristics: a function that defines output amplitude (or power) as a function of input amplitude, and a function that defines output phase shift as a function of input envelope level. These two functions are commonly referred to as the nonlinear AM/AM and AM/PM characteristics of the traveling wave tube amplifier (TWTA), respectively. The zero-memory assumption is valid since the satellite transponder bandwidths are usually narrow compared to tube bandwidth.

The lack of memory in the helix-type TWT allows either analyses [1] or computer simulations [2], [3] to utilize static measurements of the AM/AM and AM/PM characteristics to map input signal envelope fluctuations into both output envelope levels and phase shift between input and output on an instantaneous basis. This mapping is independent of the rapidity of the input signal envelope or phase fluctuations:

To model communications channels accurately, memory in nonlinearities must be considered since this phenomenon can be an important source of impairment in certain devices or in configurations of devices. Typical configurations in which the zero-memory assumption is either known to be invalid, or is questionable, would include the following:

    a. Cascaded memoryless nonlinearities with intervening bandwidth-restricting elements such as filters. If the bandwidth of the filter is not much wider than the signaling bandwidth, and if the phase characteristics are not linear over the same wide bandwidth, then the two nonlinearities are not independent and the resulting memory can degrade certain transmission formats. Existing time/frequency-domain computer simulation models [2] are adequate to analyze specific configurations of cascaded nonlinearities, but these results need to be generalized.

    b. Nonlinear devices containing filtering or energy storage elements (*i.e.*, inductors and capacitors), where a nonlinear equivalent circuit can be developed. These devices cannot be modeled as memoryless nonlinearities separated by filters since the energy storage elements themselves may constitute the major nonlinearity in the circuit. Varactor diodes and UHF transistors are examples of such circuit elements.

    c. Devices containing inseparable nonlinearities and filtering elements for which equivalent circuits are not readily available. These would include microwave devices operated in the nonlinear region with signaling bandwidth comparable to the device bandwidth. Cavity-coupled TWTs are examples of devices in this category. Methods for analyzing or simulating such devices are not presently available.

These three cateogories constitute an arbitrary but convenient classification of highly nonlinear devices with memory according to the difficulty in analyzing them for communications applications. A distinction between "strong" and "weak" nonlinearities with memory must be made since analytical methods [4] can be applied to the latter.

The work reported in this paper deals with category *b* for which an equivalent circuit model may be obtained. A class-C transistor amplifier, which operates at L-band (1—2 GHz), is modeled and analyzed to reveal nonlinearities, specifically the AM/AM and AM/PM characteristics. To obtain these macroscopic characteristics, it has been necessary to model and simulate the device on a microscopic time scale with a time increment equal to a small fraction of an RF cycle. Figure 1 distinguishes between the time scale used in the microscopic (device) simulation and the macroscopic (complex envelope) communications channel simulations. For a transmission rate of 1 Msymbol/s in Figure 1b the communications channel simulation would typically utilize a sampling increment of $1/16 \mu s$ (16 sample/symbol), which is three orders of magnitude larger than the time increment used in the device simulation.

a. *microscopic or device model*

b. *macroscopic or complex-envelope model*
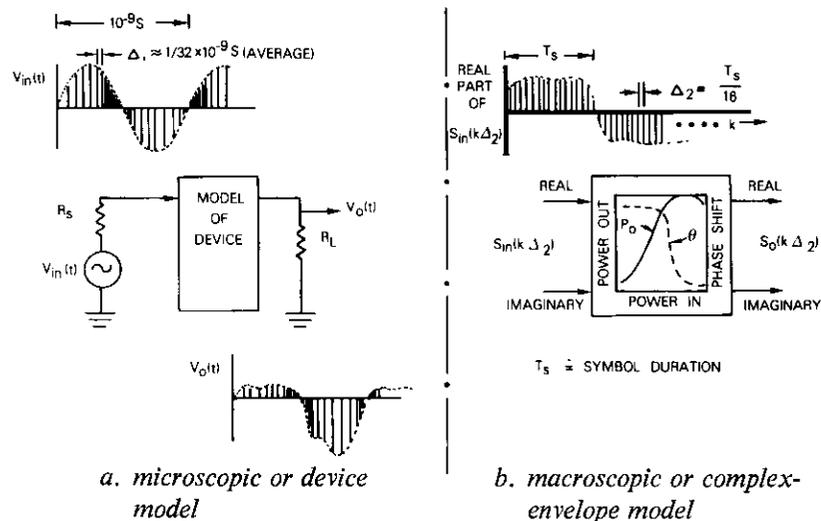
Figure 1. *The Two States of Simulation*

The model

The procedure used to model and characterize the class-C amplifier included the following steps:

  a. a model of the transistor was obtained;

  b. the transistor model was combined with a model of the overall amplifier;

  c. a state-variable representation [5] of the amplifier was derived;

  d. the state equations were solved for sinusoidal input signals;

  e. a series of these simulations, for various input signal levels, was obtained to measure the AM/AM and AM/PM characteristics of the amplifier.

Figure 2a shows the modified Ebers-Moll [6] model, which was used to represent the UHF power transistor. This model was included within a model of the overall class-C transistor amplifier (Figure 2b) that was adapted from Harrison [7] with some simplifications. The transistor model used in this work is within the dashed lines of Figure 2b. The elements included in the model are defined as follows:

C_E: total emitter capacitance; the parallel combination of emitter transition capacitance, C_{TE} (a function of base-to-emitter voltage, $v_{b''e''}$), and emitter diffusion capacitance, C_{DE} (a function of forward collector current, i_{cf})

i_{ef}: forward emitter current (a function of $v_{b''e''}$)

α_I: inverted current gain

α_N: normal transistor current gain

C_C: total collector capacitance; the parallel combination of collector transition capacitance, C_{TC} (a function of base-to-collector voltage, $v_{b''c''}$), and collector diffusion capacitance, C_{DC} (a function of i_{cf})

R_E, R_C: emitter and collector ohmic leakage resistances, respectively

R_{EE}, R_{BB}, R_{CC}: emitter bulk resistance, base spreading resistance, and collector bulk resistance, respectively.

Current sources i_{ef} and i_{cf} and capacitors C_{TE}, C_{DE}, C_{TC}, and C_{DC} constitute the nonlinearities in the circuit. The constants needed to characterize these individual nonlinear elements were obtained from Reference 7. Diffusion capacitances C_{DE} and C_{DC} are characterized by the normal active mode cutoff frequency, F_N, and the inverted mode cutoff frequency, F_I, respectively. These cutoff frequencies were assumed to be 2 GHz and 40 MHz, respectively. The nonlinear elements in the transistor model can be summarized by the following equations (units are volts, amperes, and farads, as applicable):

$$C_E = \frac{4.31 \times 10^{-12}}{(0.732 - v_{b''e''})^{0.27}} + 3.55 \times 10^{-9}(i_{ef} + 6.49 \times 10^{-9}) \quad (1)$$

$$C_C = \frac{1.04 \times 10^{-12}}{(0.371 - v_{b''c''})^{0.322}} + 2.18 \times 10^{-7}(i_{cf} + 6.54 \times 10^{-8}) \quad (2)$$

$$i_{ef} = 6.491 \times 10^{-9} \exp[(44.62 v_{b''e''}) - 1] \quad (3)$$

$$i_{cf} = 6.54 \times 10^{-8} \exp[(54.95 v_{b''c''}) - 1] \quad (4)$$

The elements in the transistor model are surrounded by the elements of the amplifier circuit which are defined below:

C_{40}: capacitance between emitter terminal and base terminal

C_{30}: capacitance between collector and base terminal

C_1: coupling capacitor

L_1, L_3: RF chokes

R_1, R_2: source and load resistors, respectively

C_2, L_2: output tuned circuit

V_{CC}: collector supply voltage

V_{in}: input voltage

V_{out}: output voltage.

To formulate the nodal equations for the circuit in Figure 2b, nine state variables were defined as the voltages across the six capacitors and the currents through the three inductors, as indicated in the figure. Table 1

TABLE 1. STATE VARIABLES FOR THE CIRCUIT IN FIGURE 2b (s DENOTES THE LAPLACE OPERATOR)

$X_1 = v_4 - v_5$	$X_6 = v_3$
$X_2 = -v_4/sL_1$	$X_7 = (v_3 - V_{CC})/sL_3$
$X_3 = v_4$	$X_8 = v_3 - v_6$
$X_4 = v_{b''} - v_{e''} \equiv v_{b''e''}$	$X_9 = (v_7 - v_6)/sL_3$
$X_5 = v_{b''} - v_{c''} \equiv v_{b''c''}$	

summarizes their relationship to the nodal voltages.

The substitution of the state definitions into the nodal equations, followed by considerable algebraic manipulation, yields the set of first-order differential equations

$$i_{cf} = \frac{I_{cs}}{1 - \alpha_N \alpha_I} \left[\exp\left(\frac{\Lambda v_{b''c''}}{M_c}\right) - 1 \right]$$

$$i_{ef} = \frac{I_{es}}{1 - \alpha_N \alpha_I} \left[\exp\left(\frac{\Lambda v_{b''e''}}{M_E}\right) - 1 \right]$$
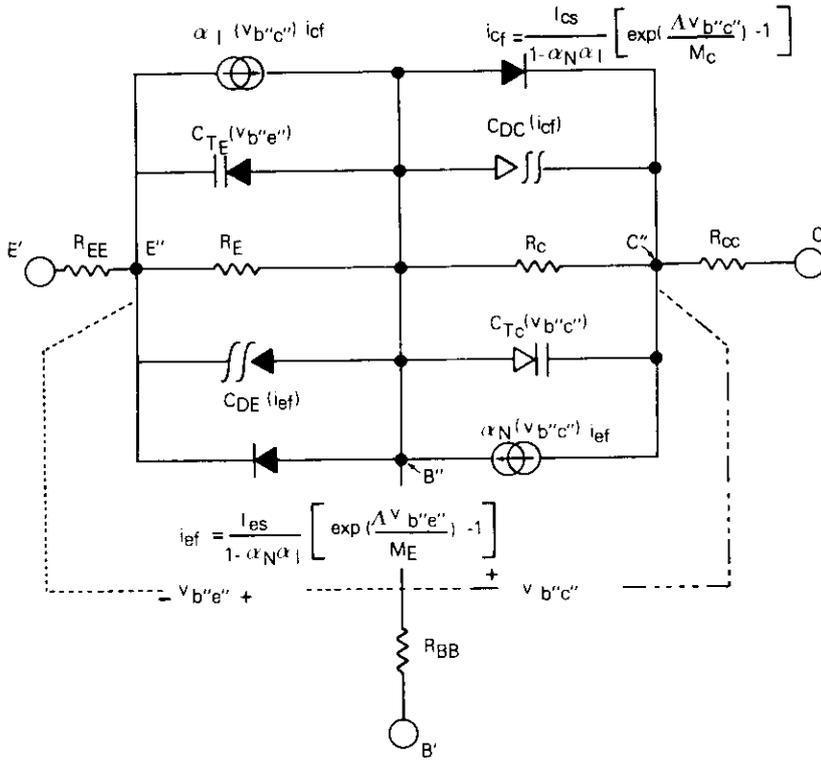
Figure 2a. *Ebers-Moll transistor model*
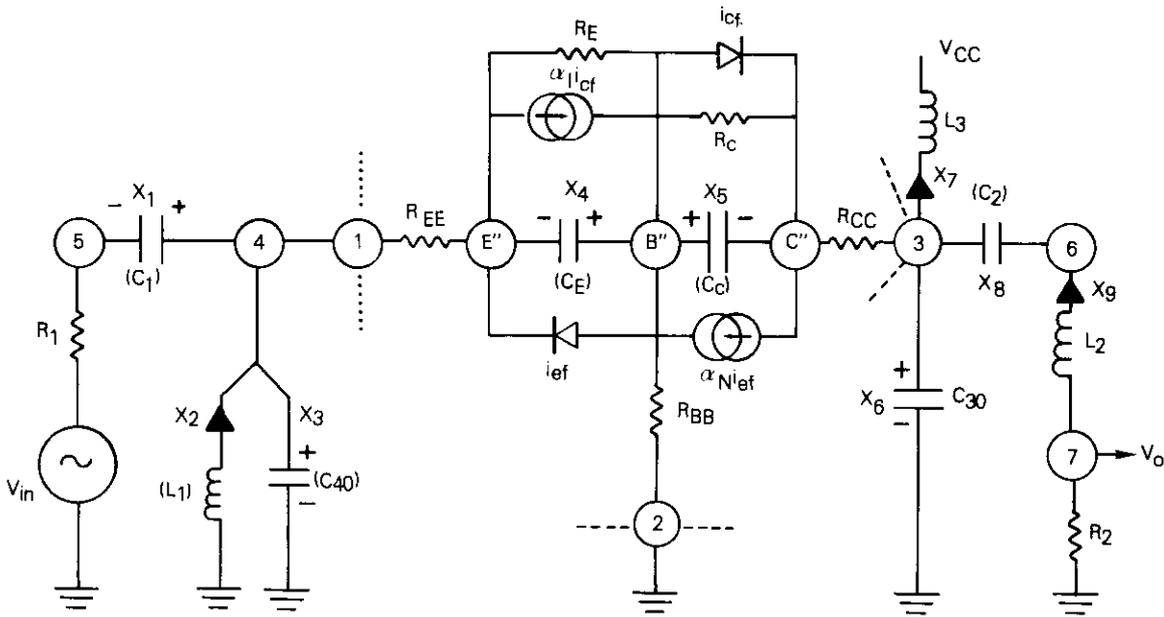
Figure 2b. *Circuit Diagram for Class-C Amplifier*

$$\dot{X} = \underline{A}X + \underline{B}V \qquad (5)$$

where $\dot{X}$ = 9-by-1 matrix containing the derivatives of the state variables.

$\underline{A}$ = 9-by-9 matrix containing the coefficients of the nine first-order state equations.

X = 9-by-1 matrix containing the state variables (voltages and currents).

B = 9-by-6 matrix containing the coefficients which couple the active sources in the model to the derivatives of the state variables. Figure 2b contains four current generators and two voltage generators; the latter include the V_{in} and the V_{CC}.

V = 6-by-1 matrix containing the active sources in the circuit diagram. In this case, the active current generators are functions of the state variables [for example, i_{ef} is a function of the $v_{b''c''}(X_4)$].

With the model reduced to the standard matrix form of equation (5), existing predictor-corrector computer routines can be used to solve for the state variables as a function of time for a given input waveform. A subroutine [8] based on Gear's algorithm [9], [10] was used for this purpose.

Simulation results

Figure 3 shows a typical simulation run for which the input was $V_{in}(t) = 5 \sin(2\pi\ 10^9 t)$. The circuit values were selected as $R_1 = 5\Omega$, $R_2 = 20\Omega$, $C_2 = 10\ pF$, $L_2 = 7\ nH$, (load reactance $\sim +j30\Omega$ at 1 GHz), $C_1 = 50\ pF$, and $L_1 = L_3 = 100\ nH$. The input consisted of 16 cycles of the input sine wave as indicated by curve 1 in Figure 3. Curve 2 is the output voltage which is obtained by multiplying the current through L_2 (the state variables X_9) by the load resistance. The third trace at the top of Figure 3 is the $v_{b''e''}(X_4)$.

The fourth trace in Figure 3 is the $v_{b''c''}(X_5)$, which begins at a value of -28 V (the V_{CC}) and then alternates about this value. For a commonly used definition of class-C operation,* this voltage should alternate $\pm V_{CC}$

_____

*Definitions vary for class-C operation in solid-state amplifiers. This paper is based on Harrison's [7] definition in which no bias is applied to the base-to-emitter junction; *i.e.*, RF choke L_1 in Figure 2 is returned to ground. With no bias, the amplifier draws no current from the collector supply unless the RF signal is applied. Alternative definitions of class-C refer to the configurations in which the base-to-emitter junction is reverse biased (L_1 returned to a small positive voltage level).

about the DC supply voltage. With sufficient input drive, the base-to-collector junction can become forward biased so that the "inverse transistor" in the model is activated.

Several additional observations can be made about $v_{b''c''}$ in Figure 3. First, the unequal sampling used by the solution algorithm is clearly evident. Sample points are very close together in certain parts of the waveform and have relatively wide spacing in others. The regions of close spacing coincide with the intervals where $v_{b''e''}$ changes polarity and the emitter-base diode is either beginning to conduct, or is being cut off. A second observation reveals an underlying low-frequency oscillation which is added to the main waveform. In a longer simulation run where only $v_{b''c''}$ is observed (Figure 4), the waveform stabilizes after about 30 ns.

These initial observations of the output waveforms led to the adoption of the following procedures to measure output power versus input power (AM/AM) and phase shift between input and output (AM/PM):

a. All of the state variables in the model were assigned values at the start of each run with values obtained from a single long run with a low input voltage level. This assignment minimized the transient "start-up" period in which accurate measurements could not be made.

b. Accurate measurements of output power and phase shift of the distorted output waveform required spectral analysis of the waveform using the discrete Fourier transform (DFT). The set of unequally spaced time samples produced by the solution algorithm were resampled (requiring interpolation) to produce a block of 512 uniformly spaced samples for the DFT.

c. Typical simulation runs were 40 to 60 ns long (40 to 60 input RF cycles) with approximately 75 percent of this interval allowed for output stabilization. Measurements were made over the final 10- to 15-ns segment of each run.

Figure 5 summarizes the measurements made during each simulation run, including input power, P_{in}; output power, P_o; power drawn from the collector supply, P_{DC}; and phase shift between the input and output voltage waveforms, θ. Lissajous' patterns were obtained by plotting the V_{out} versus V_{in} waveforms. Although these patterns are useful qualitative indicators of the dynamic input-output behavior of the amplifier, accurate measurements of power and phase shift at 1 GHz require spectral analysis of the output waveform. From the four basic quantities measured, power gain and DC-to-RF efficiency were also computed as a function of input power level.

The general operation of the class-C amplifier can be understood from
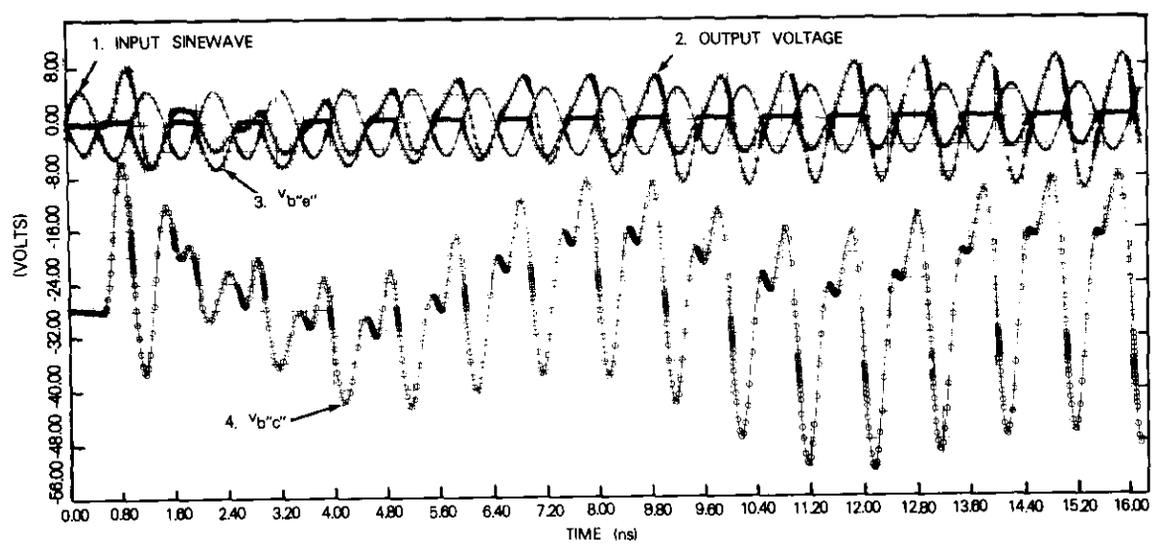
Figure 3. *Typical Solutions for $v_{b''e''}$, $v_{b''c''}$, and V_{out} for Sinusoidal Input*
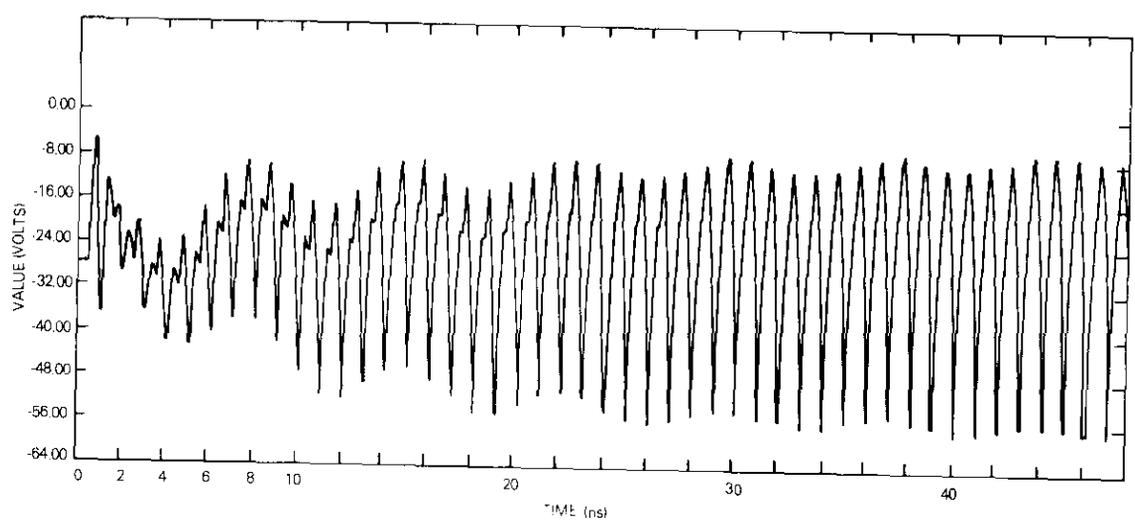
Figure 4. *Base-to-Collector Voltage ($v_{b''c''}$) for 48-ns Interval*
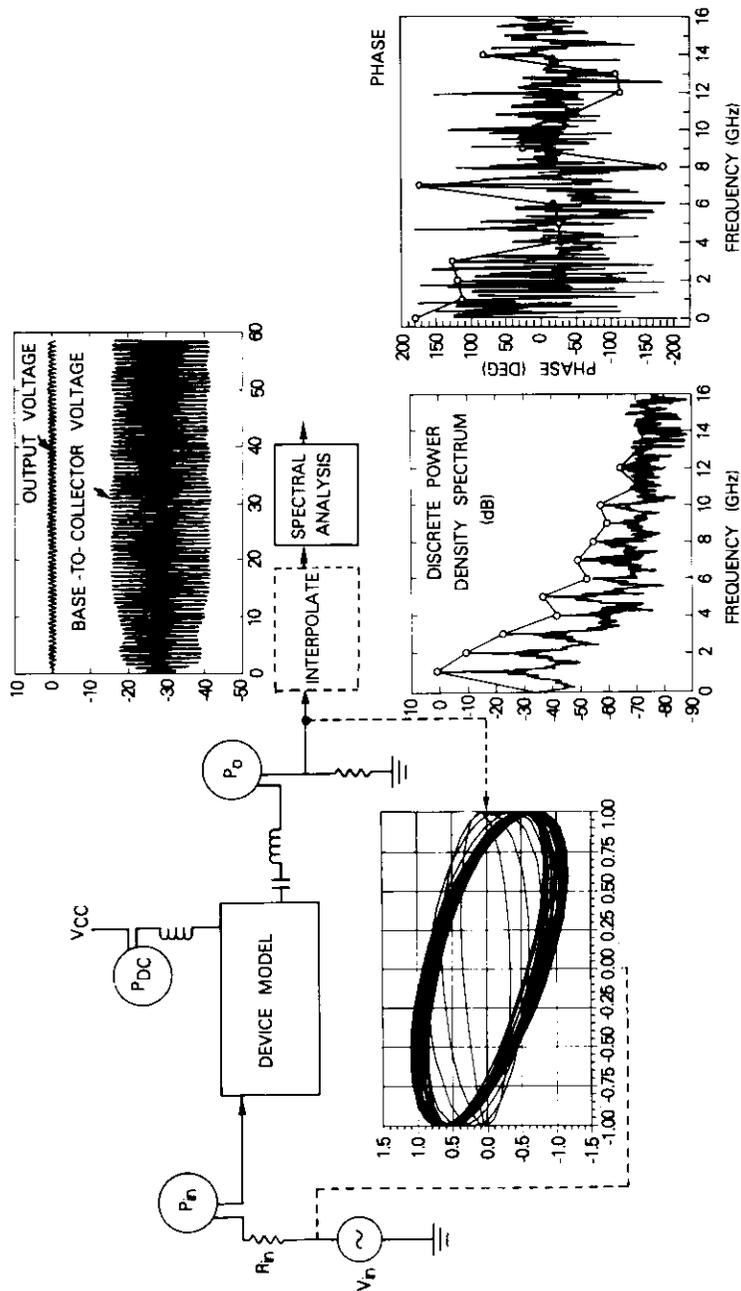
Figure 5. *Instrumentation of the Simulation Model*

Figure 6, which plots $v_{b''c''}$ versus $v_{b''e''}$ [11], [12]. This diagram is divided into three regions which are defined as follows:
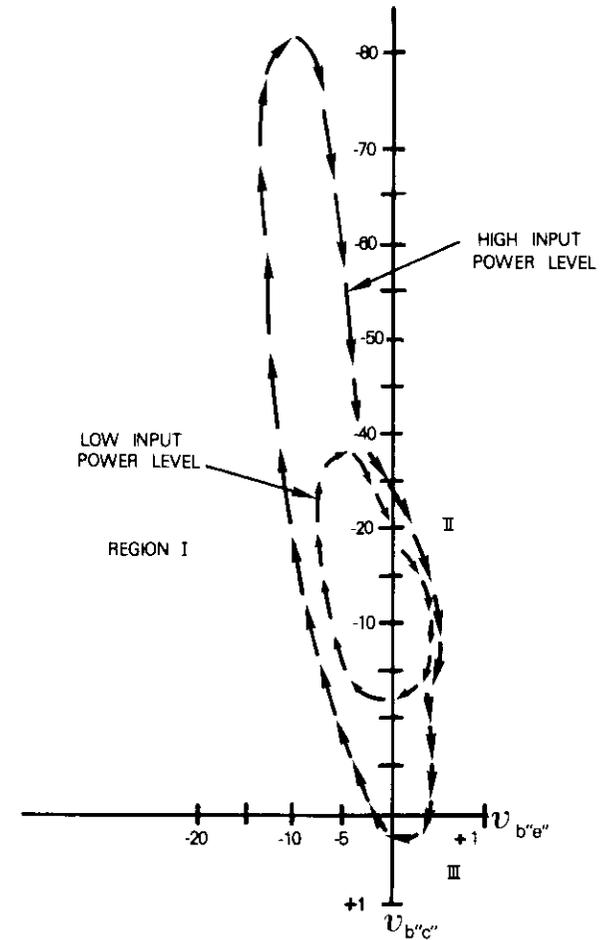
REGION I: "OFF" EMITTER JUNCTION REVERSE BIASED
             AND COLLECTOR JUNCTION REVERSE BIASED

REGION II   "ACTIVE" EMITTER JUNCTION FORWARD BIASED
             AND COLLECTOR JUNCTION REVERSE BIASED

REGION III: "ON" EMITTER JUNCTION FORWARD BIASED
             AND COLLECTOR JUNCTION FORWARD BIASED

Figure 6. *The Three Regions of Transistor Operation*

a. Region I. Both the emitter and collector diodes are reverse biased and the transistor is "off."

b. Region II. The emitter diode is forward biased ($v_{b''e''}$ is positive) and the collector diode is reverse biased. In this "active" region, current source i_{ef} is active and a large fraction, α_N, of this current is drawn from the collector supply.

c. Region III. Both the emitter and collector diodes are forward biased and the transistor is "on." In this region, all current sources in the model are active.

When the input sine wave is applied to the emitter of the grounded-base configuration, this excitation causes an excursion of $v_{b''e''}$ and $v_{b''c''}$. After steady state is reached, these voltages will move cyclically through two or three of the regions in Figure 6. For class-C operation, the transistor remains off for the positive excursions of the input sine wave. On the negative part of the input cycle, the emitter diode conducts causing the collector voltage to drop from its DC value of -28 V. With low levels of input power, the collector voltage drop is small and operation remains in region II. As the input power level is increased, the collector voltage can drop slightly below the base voltage and the transistor is fully on or saturated. The excursion into region III can last for a relatively large portion of the input RF cycle, resulting in an abrupt increase in phase shift through the device. The transition from the "saturated" to the off condition is accompanied by a large "backswing" in collector voltage and an abrupt increase in output power delivered to the load. Maximum DC-to-RF efficiency occurs approximately at the point of saturation.

This general description of transistor operation is illustrated by the output waveforms and Lissajous' patterns in Figure 7. Figures 7a and 7b apply when the input power level of -9.8 dBW is insufficient to saturate the transistor. A steady-state condition is reached after approximately 15 ns. Figure 7b shows the actual phase shift between input and output, which can be estimated as approximately $\theta = -32°$.

Figure 7c shows $v_{b''c''}$ and $-V_{out}$ when the input power is increased to -2.4 dBW. In this case, the amplifier requires about 15 ns (15 RF cycles) to reach saturation. Prior to this point, $v_{b''c''}$ swings (somewhat erratically) ± 28 V about the nominal value of -28 V. After reaching saturation, both $v_{b''c''}$ and V_{out} shift abruptly to larger values. It should also be noted that sustained saturation is accompanied by an additional phase shift of approximately 90° in V_{out}.

The phase diagram in Figure 7d indicates this abrupt shift in both phase and amplitude of V_{out}. This diagram, which is inclined in one

direction below saturation, changes to a totally different inclination when the amplifier saturates, and the peak-to-peak amplitude of V_{out} increases. Distortion in the output waveform is also evident during one-half of the output cycle. The change in phase can be estimated from Figure 7d by noting that the relative phasing between output and input is approximately $-30°$ below saturation; it changes to approximately $-150°$ when saturation is reached. The transition does not occur instantly, but lasts for approximately 5 RF cycles (5 ns).*

Results from a third example are shown in Figures 7e and 7f, in which the input level is sufficiently high (0 dBW) to produce a saturated condition almost immediately after application of the input signal. Even this case has a short (5-ns) transient period during which the output increases to its final value. A low-frequency amplitude modulation appears on the peak negative excursions of the $v_{b''c''}$, probably due to the long time constant of the biasing elements in the circuit. Table 2 summarizes the measurements from these three simulation runs.

TABLE 2. SUMMARY OF SIMULATION RUNS SHOWN IN FIGURE 7

Parameter	Figure		
	(a,b)	(c,d)	(e,f)
V_{in} (peak V)	2.82	4.5	5.6
P_{in} (dBW)	-9.8	2.43	0
P_{out} (at fundamental) (dBW)	-6.09	4.5	4.5
Power Gain (dB)	3.8	6.9	4.6
P_{DC} (W)	5.1	7.8	10.6
Average collector Current (mA)	180	280	380
Efficiency (%)	6.5	36	26
Phase Shift (deg)	-32	-153	-161

A series of runs similar to those shown in Figure 7 was made to obtain a complete characterization of the amplifier. The results in Figure 8 show power output (left scale) and efficiency (right scale) versus input power level. The power output rises abruptly at an input level of -3 dBW and maximum DC-to-RF conversion efficiency occurs at this input level.

Figure 9 contains the AM/AM and AM/PM characteristics obtained from

---

*This transient time has not been measured accurately but can be observed as the Lissajous pattern is plotted on the CRT.
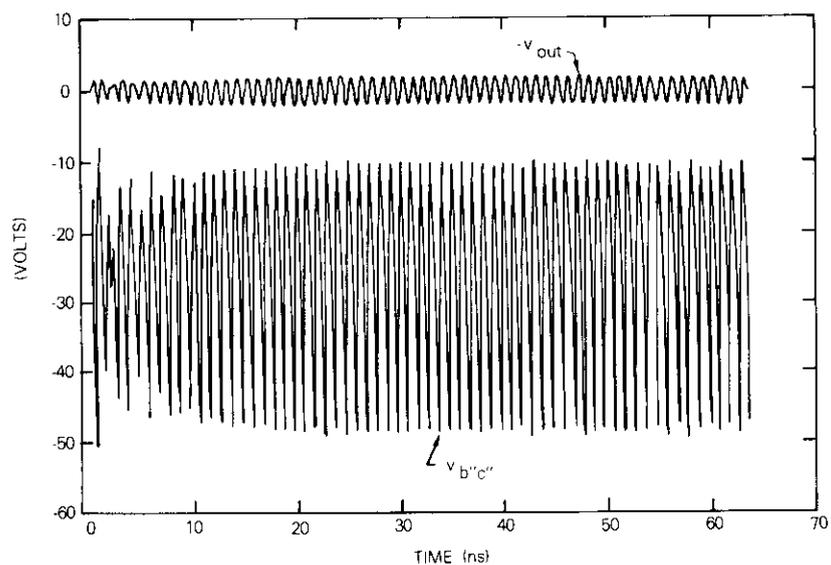
a. output and base-to-collector voltages
(input too low for saturation)

c. output and base-to-collector voltages
(saturation after 15 ns)

b. $-V_{out}$ vs V_{in} (operation never enters saturated region)

Figure 7. Simulation Results
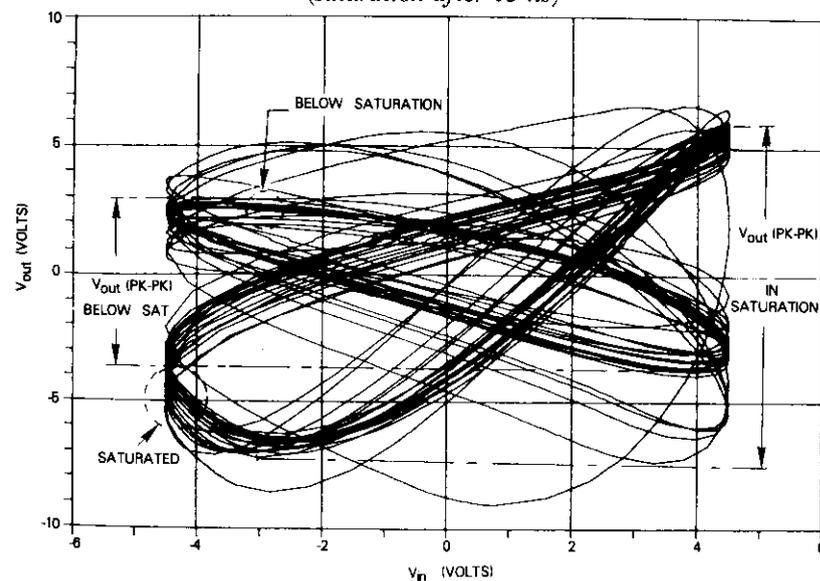
d. $-V_{out}$ vs V_{in} (transition from unsaturated to
saturated operation)

Figure 7. (continued) Simulation Results
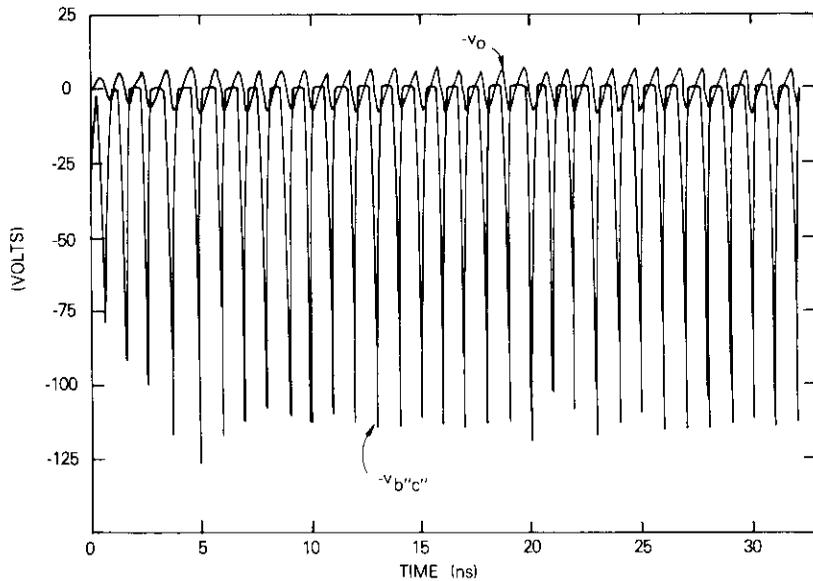
e. output and base-to-collector voltages
(input voltages 2 dB above saturation)
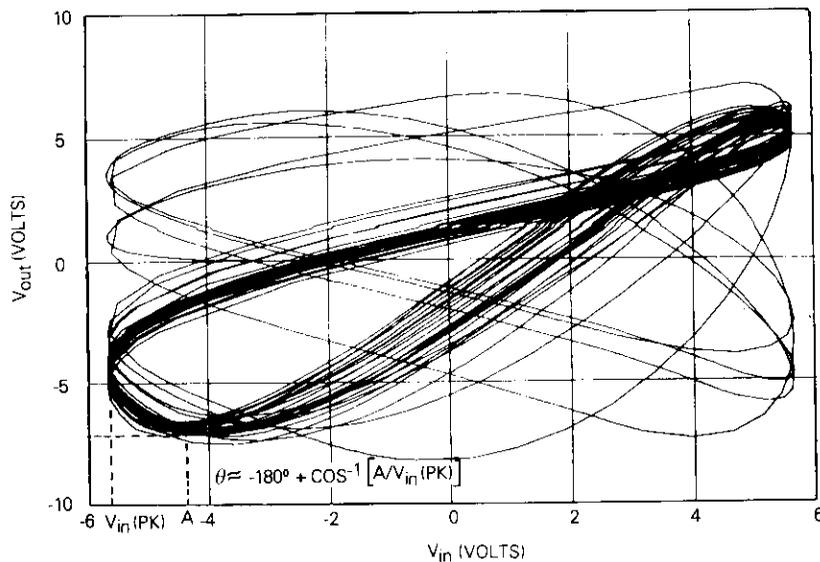
f. $-V_{out}$ vs V_{in} (amplifier is saturated for the entire run)

Figure 7. (continued) Simulation Results
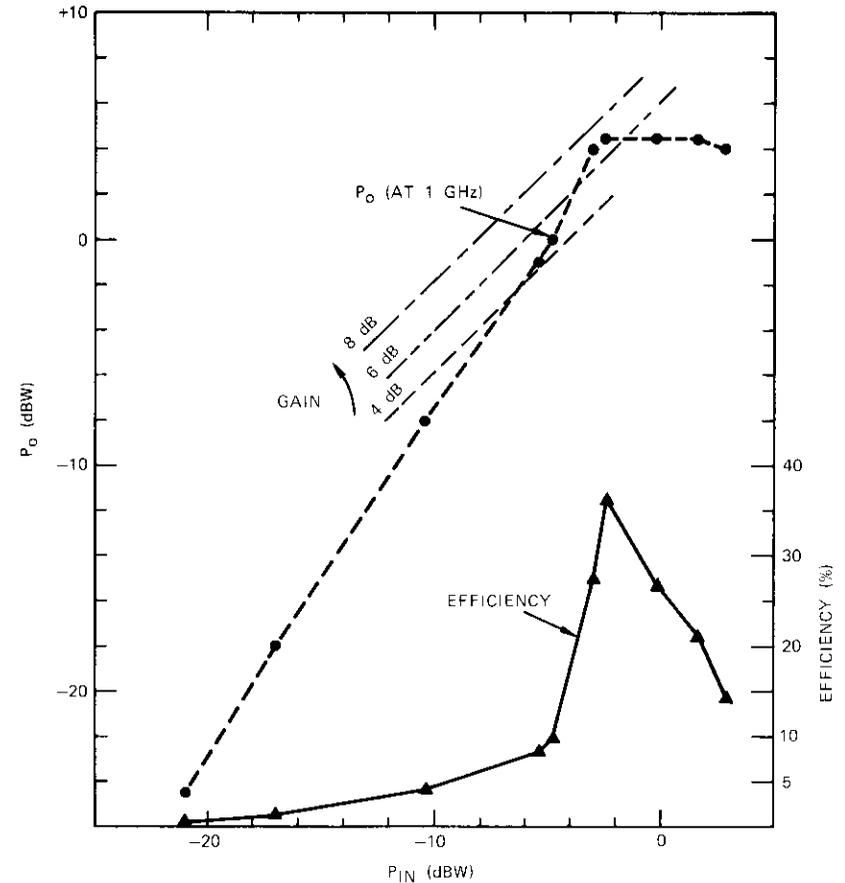
Figure 8. Output Power and Efficiency vs Input Power

the computer simulations. An amplifier of this type would be operated "overdriven," that is, at an input drive level 3 to 6 dB above the point that just produces maximum output. In this region, the AM/PM conversion coefficient is 5°/dB. A decrease in drive level to 0 dB relative to saturation (operation at the point of saturation) results in a doubled AM/PM coefficient, 10°/dB, which doubles again to 20°/dB for an additional 1-dB decrease in drive level.

The computer simulation model of the class-C amplifier gives consistent and repeatable results which are characteristic of devices of this type. For
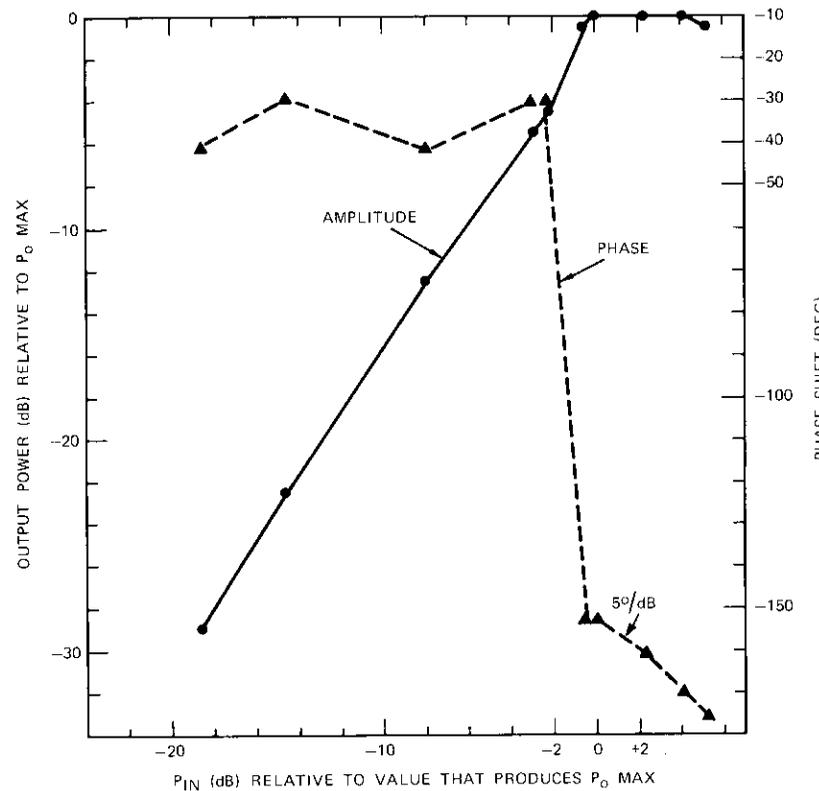
Figure 9. *Relative Output Power and Phase Shift vs Relative Input Power*

class-C operation, the amplifier is completely off (draws no current from the collector supply) until an RF signal is applied. For very small input signal levels, a small output is produced but with little or no gain. In this region, efficiency is also low. As the input is increased, gain, efficiency, and RF output increase abruptly and the amplifier produces several watts output with an approximate 7-dB power gain. In the present model, this abrupt change coincides with the point of transistor saturation, at which the RF output voltage experiences an additional phase shift greater than 90°.

The $v_{b''c''}$ waveforms in Figures 7a, 7c, and 7e reveal that the collector-to-emitter breakdown-voltage rating of a real transistor is probably being exceeded in the simulation model by the large backswing that occurs when

the transistor is turned off. This same observation can be drawn from Bailey's [11] results for a high-power transistor modeled at a 50-MHz frequency that exhibited a peak-collector-voltage excursion approximately five times the supply voltage (to 123 V when $V_{CC} = 24$ V). The results obtained tend to agree with Bailey's; however, microwave transistors may not be able to tolerate these high-voltage swings. Initial attempts to include the avalanche breakdown behavior in the simulation model have been unsuccessful. This area requires further investigation.

Comparison of simulation results to measured results

Laboratory measurements* on an L-band class-C transistor amplifier, as shown in Figures 10 and 11, can be compared with the characteristics derived from the computer simulation model. Figure 10 shows the measured AM/PM conversion coefficient in deg/dB versus input power level. Figure 11 gives both relative output power versus input power and phase shift versus input power for the simulation and laboratory-measured results, as well as additional reported data from Reference 13.
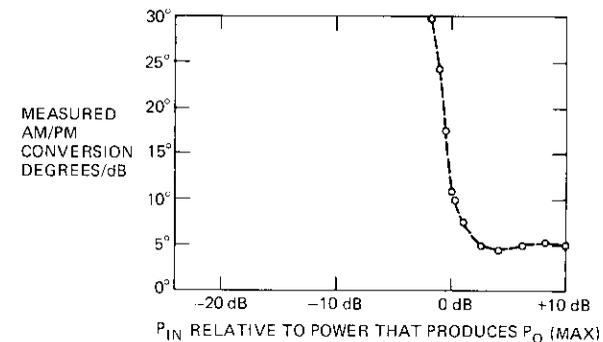
Figure 10. *Measured AM/PM Conversion vs Relative Input Power for the 50-W L-Band Class-C Transistor Amplifier*

The maximum measured power from the laboratory amplifier was +17.5 dBW (56 W), which was obtained for an input level of +14 dBm

*The Laboratory measurements on a 50-W L-band amplifier were taken by D. Weinreich of COMSAT Labs.
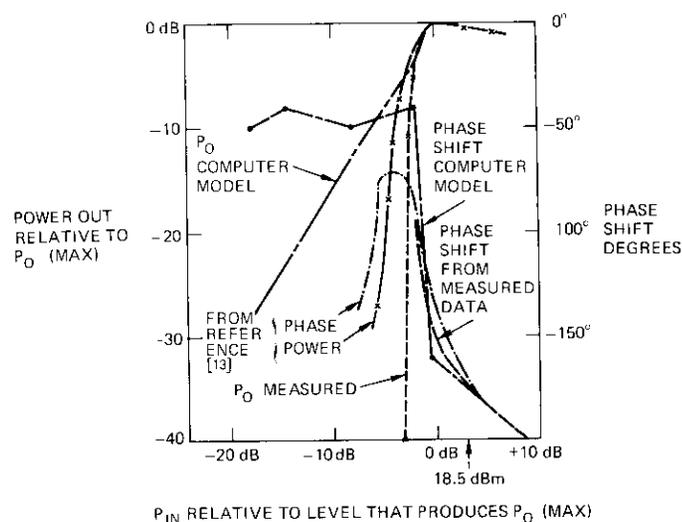
Figure 11. *Comparison of Measured AM/AM and AM/PM Characteristics with the Characterization Obtained from the Computer Simulation*

(25 mW) and remained constant as the input level increased. The nominal input level to the amplifier is +18.5 dBm (70 mW) so that the amplifier is normally operated at an input level 4.5 dB above the input that produces maximum power output. In this region, the AM/PM conversion is relatively small (approximately 5°/dB). As the input level to the amplifier is reduced, the AM/PM conversion increases to 10°/dB at 0-dB backoff and 30°/dB at −2-dB input backoff. For input power levels from −2-dB to +8-dB input backoff, the results obtained from the computer model and the laboratory-measured results agree closely. However, for −3-dB input backoff (input power reduced 7.5 dB below the nominal operating point), the measured output power decreases much more rapidly than the computer model predicts. The actual amplifier no longer produces an output, so that it is impossible to measure the AM/PM conversion coefficient in this region.

When the simulation results are compared with the measurements, it should be recognized that the computer model is only a single transistor stage, whereas the actual amplifier contains several driver stages and four paralleled class-C output stages. Thus, the real amplifier is far more com-

plex. Despite the significant differences between the two devices, the measured verification of the simulation model is encouraging.

Discussion of the simulation model

This technique for modeling nonlinearities has given results that agree reasonably well with laboratory measurements on similar devices. The general behavior of the class-C transistor amplifier, i.e., abrupt amplitude saturation accompanied by a large phase shift, is predicted by the simulation model. The AM/AM and AM/PM characteristics derived from the model are therefore useful in time-domain simulation models. Additional simulation efforts are needed with models of this type to characterize the memory effect in a form that is suitable for time-domain channel simulations. One approach may be to replace the static AM/AM and AM/PM tables with a more complex representation based on first, and possibly higher-order, derivatives of the envelope and phase of the input RF signals. The relations for these more complex models would be obtained from measurements made on the microscopic model.

Application of the model

The memoryless nonlinear characteristics measured with the model (summarized in Figure 11) were used in the CHAMP [2] time-domain simulation program to investigate the spectral regrowth experienced by filtered digitally modulated signals passed through the amplifier. Figure 12 shows the simulation model. A uniform random number generator is used to apply random ±1 modulation to either a conventional QPSK generator, an offset QPSK generator [14], or an MSK [15] generator. An arbitrary sampling rate, f_s, was selected as 1,024 Hz for the simulation, and each quaternary symbol was represented by 16 discrete samples. Thus, the symbol rate, R_s, for all three modulation formats was 64 symbol/s, or the binary rate was 128 bit/s.

The transmitted signals were passed through a transmitter filter consisting of a perfectly equalized 4-pole Butterworth filter with a total 3-dB bandwidth, B_3, and a symbol duration, T_s. The bandwidth of this filter was selected to give $B_3/R_s = B_3T_s = 1.5$ or 1.2. Spectra were obtained before and after the filter as references.

The simulated signal was scaled to have a transmitter power $P_T = 1$ W (dBW), and the filter was scaled to have unity gain at its center frequency. The power out of the filter, P_F, was measured and this signal was amplified, as necessary, to produce the correct drive level to the simulated
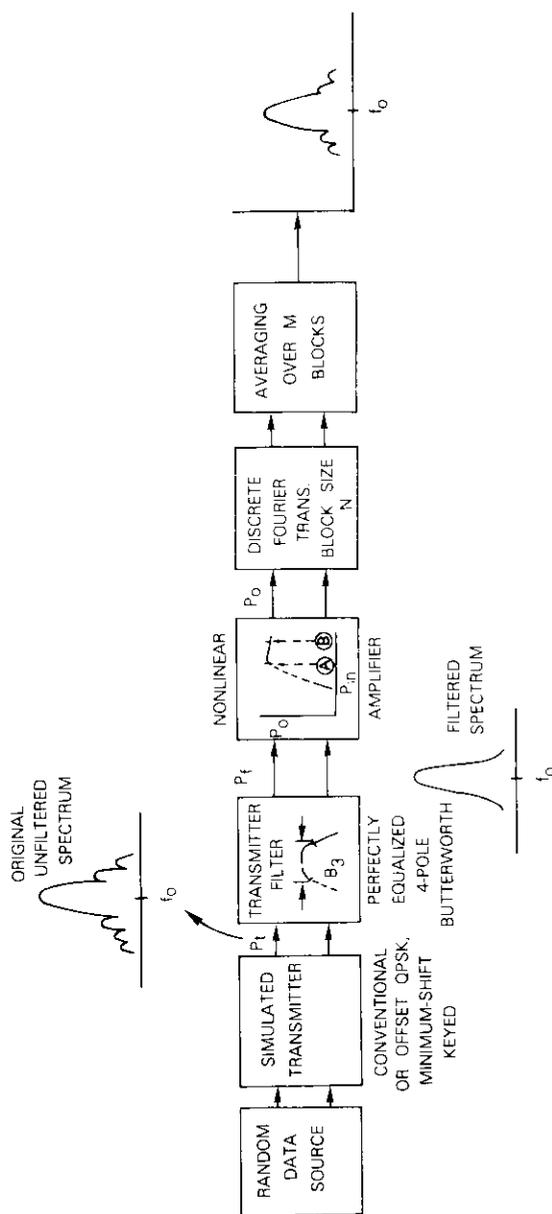
Figure 12. Channel Simulation Elements

nonlinearity. The nonlinearity* was similarly scaled to produce 1 W out for 1 W in at the point of saturation. Two operating points were used in the simulations: $P_{in} = 0$ dBW (amplifier just saturated), and $P_{in} = +3$ dBW (amplifier overdriven by 3 dB). The latter condition is more representative of the drive level that would be used with a class-C amplifier.

Each simulation consisted of the transmission of 1,024 random symbols (16,384 samples). Discrete spectral analysis used the DFT of blocks containing 512 complex samples giving a frequency resolution of 2 Hz. To allow for filter buildup, the first block in each run was not used in the spectral analysis so that the spectra represent an average over 31 blocks of simulated data.

Inaccuracies can occur in using this method of estimating the spectra of randomly modulated signals due to the following phenomena:

a. Aliasing which generally causes the simulated spectra to be 3 dB too large at frequencies $\pm 0.5 f_s$ (at ± 512 in this case).

b. Errors due to the random modulation, which is reduced in this case by averaging 31 separate spectra.

c. Errors in the DFT calculations when single-precision floating-point arithmetic is used. These errors tend to accumulate when multiple spectra are averaged and produce a "noise floor" approximately 50 or 60 dB down from the peak of the spectra, where the levels have no meaning.

Because of these sources of errors, the simulated spectra are accurate over only about half of the total range, ± 512 Hz. This range of ± 256 Hz corresponds to ± 4 times the symbol rate, which is the region of primary interest in most applications.

Figure 13 contains the simulation results. The original spectra for conventional QPSK are given in Figure 13a, followed by offset QPSK in Figure 13b, and MSK in Figure 13c. In each set of spectra, results for the relatively wide filter ($B_3 T_s = 1.5$) are shown in the center, and those for the narrower filter ($B_3 T_s = 1.2$) at the right. The overlaid results at the center and the right of each set show the spectra out of the nonlinear

---

*For these simulations, the AM/PM characteristics obtained by computer simulation (see Figure 11) were used. The AM/AM characteristic used decreased more rapidly below saturation than the characteristic obtained from the simulation model.
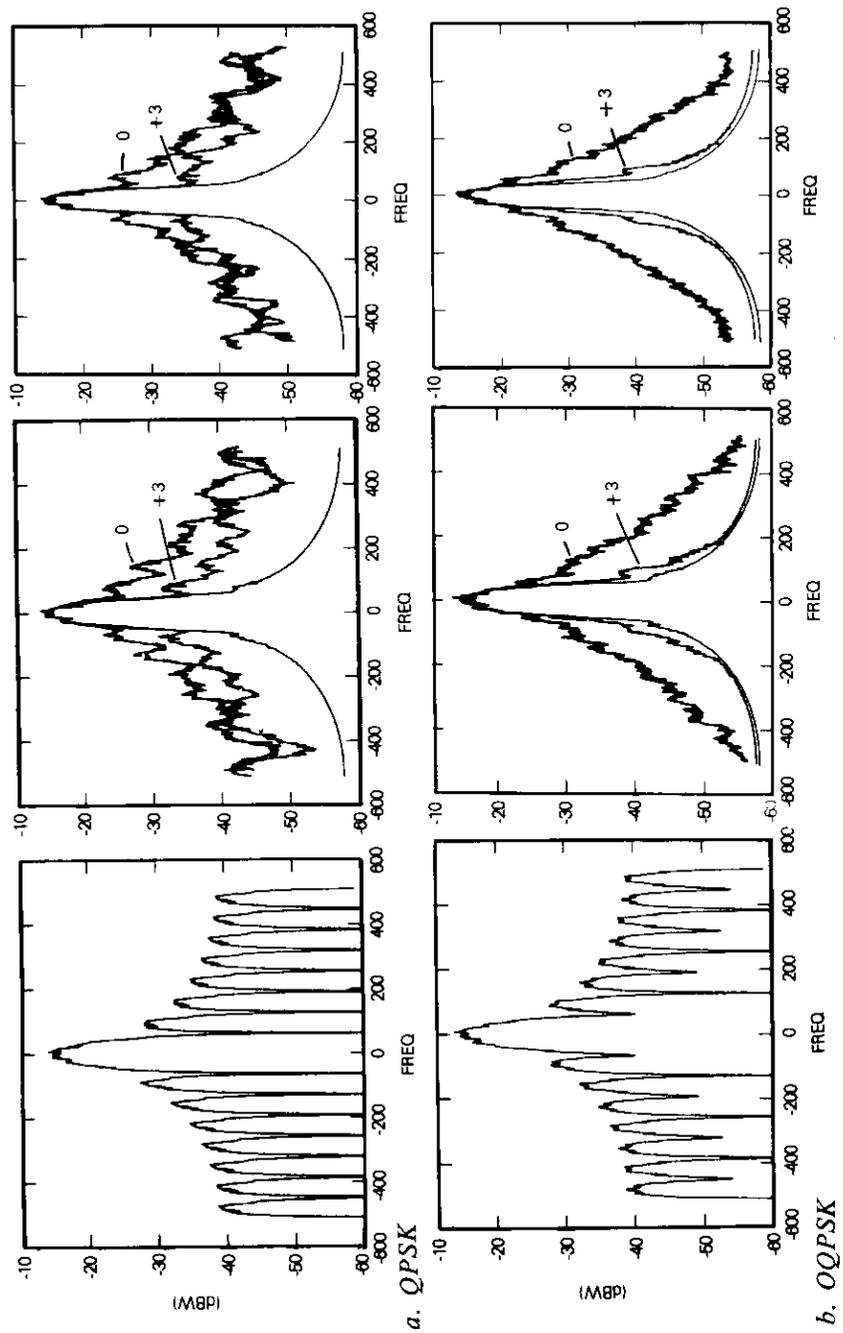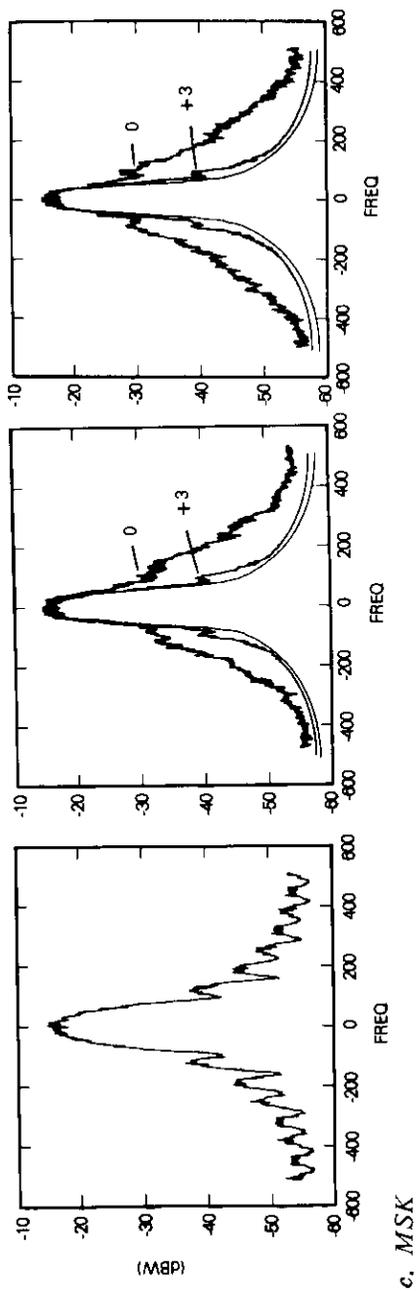
Figure 13. *Simulated Power Density Spectra*

amplifier for 0 and 3-dB input backoffs, as marked, along with the origi-
nally filtered spectra.

The spectra measured directly out of the transmitters exhibit the
characteristic $1/f^2$ and $1/f^4$ shapes of QPSK and MSK, respectively. If these
signals are then filtered, the resulting spectral densities assume the shape
of the filter characteristic. With tight filtering ($B_3T_s = 1.2$) the original
sidelobes can be attenuated considerably. After filtering, the envelope of
the signals will no longer be constant, and conventional QPSK will exhibit
relatively deep envelope nulls when 180° phase transitions occur in the
modulated signal. The filtered offset QPSK and MSK signals will also ex-
hibit envelope fluctuations after filtering; however, these fluctuations would
not be as severe as with conventional QPSK.

When these filtered signals are passed through an abrupt amplitude non-
linearity, the envelope fluctuations are compressed and the spectral
density is increased at frequencies removed from the carrier. Basically,
the spectra tend to revert to their original unfiltered form, a phenomenon
[16] referred to as "sideband regrowth" or "spectral spreading." Ampli-
tude to phase (AM/PM) nonlinearities can likewise convert the relatively
rapid envelope fluctuations of the filtered signals into rapid phase fluctua-
tions, which also increase the outlying spectra density levels. The net
result is that the nonlinearity tends to cancel the filtering that was per-
formed at the transmitter to limit out-of-band emission levels and prevent
adjacent channel interference.

The results in Figure 13 show the spectra regrowth for typical filtering
at the transmitter and for two conditions of input backoff to the class-C
amplifier. The spreading is somewhat larger for conventional QPSK than
for the other two modulation techniques. For all of the modulation
techniques, the spectra are highly sensitive to the drive level to the ampli-
fier. This would be expected, for unless the amplifier is overdriven, the
input envelope fluctuations tranverse the steepest part of both the AM/AM
and AM/PM nonlinearities.

A more quantitiative comparison of the results in Figure 13 is given in
the integrated spectral densities in Figure 14. The power spectral density
curves, shown in Figure 13, were numerically integrated over a frequency
span, B, centered at the nominal frequency, f_o, of the signal. This band-
width was varied over the limits of the discrete spectra, i.e., from $R_s/8$
to $16R_s$ in steps of $R_s/8$. The resulting cumulative power distribution
curves are useful for accurately determining the fraction of sidelobe or
mainlobe power that lies outside of, or within a specified frequency range.
For the cases of primary interest, spectral regrowth due to the transistor
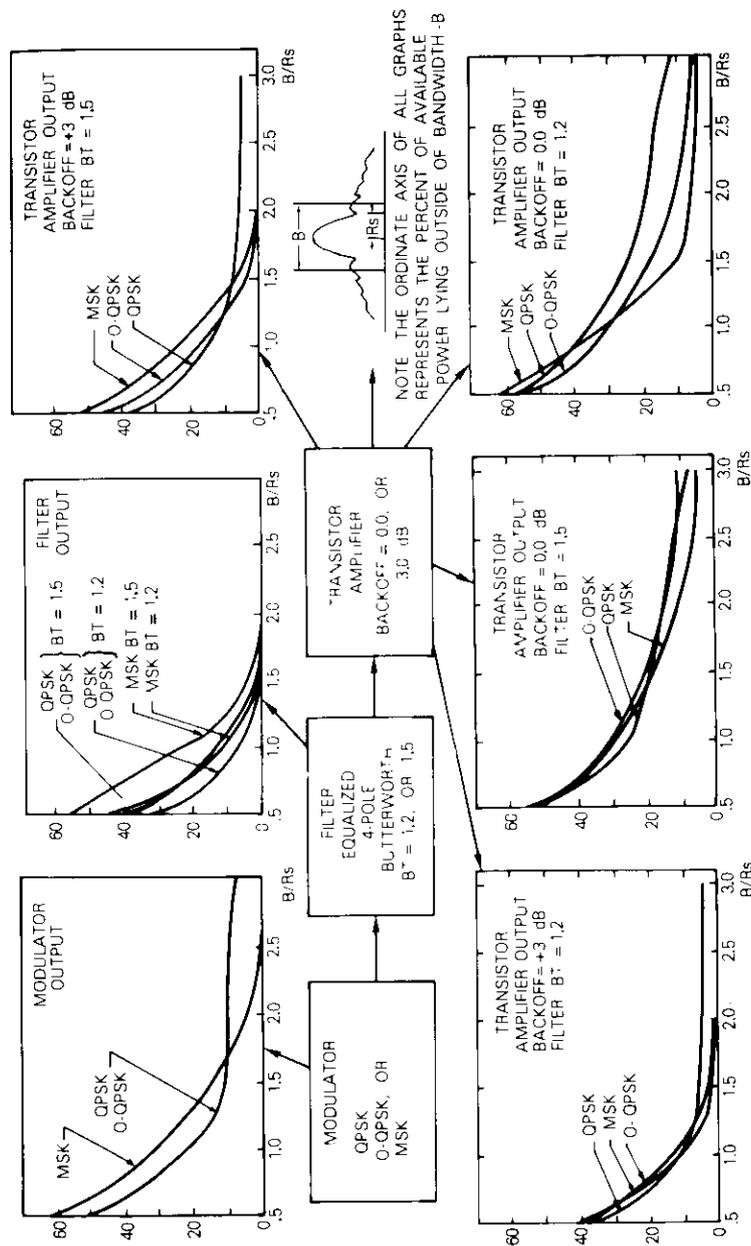
Figure 14. Distribution of Power in Simulated Spectra

amplifier and the percentage of power lying outside of bandwidth B have been plotted as a function of the normalized ratio B/R_s, as shown in Figure 14. These plots have been ordered so that each plot (or group) displays the comparison between the three modulation types at a particular point in the simulated channel (modulation-filter-amplifier).

Figure 14 shows that MSK has the least susceptibility to the spectral regrowth phenomena, followed by offset QPSK and then QPSK. Over the range of parametric variations that were run (two amplifier backoffs and two filter B_3T_s products), the sidelobe levels of MSK were roughly comparable to, and in some cases lower than offset QPSK, even though initially MSK has a 50-percent wider mainlobe. Conventional QPSK is severely affected by the nonlinear amplifier. For the case of 0-dB backoff and a filter B_3T_s product of 1.5, the sidelobe levels of QPSK are regenerated to higher levels than those that existed at the output of the modulator.

A final comparison of the simulation results to the laboratory measurements is given in Figure 15. The laboratory results were obtained with an

SPECTRA OUT OF CLASS-C TRANSISTOR AMPLIFIER
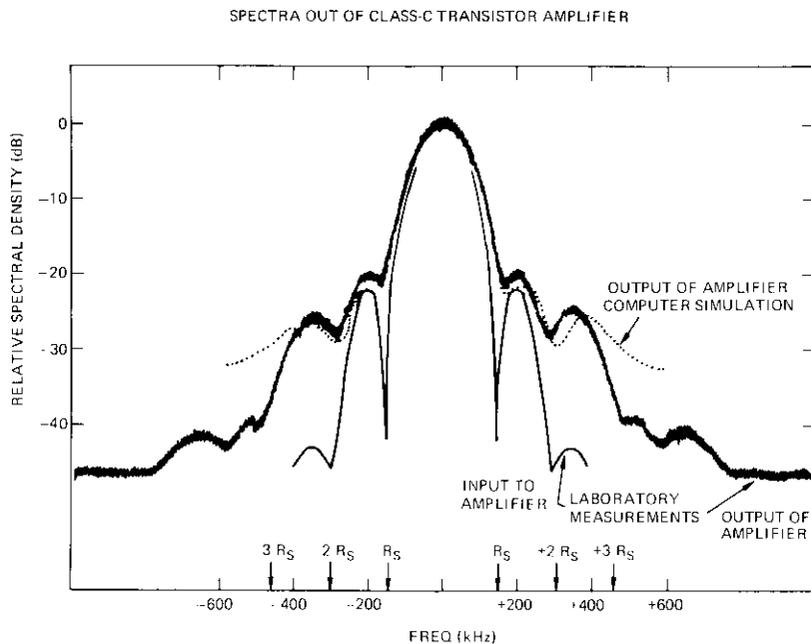
Figure 15. *Comparison of Measured and Simulated Spectra from the Class-C Amplifier*

offset QPSK modem with a symbol rate of 153.4 ksymbol/s. The transmit filter was a 4-pole Bessel filter with a relatively wide bandwidth ($B_3T_s = 2.0$). With this filter, the spectrum into the 50-W amplifier retains the characteristic lobes of the QPSK spectra except that the first sidelobes are approximately 20 dB below the spectral peak, and the second sidelobes are more than 40 dB below the peak. These same conditions were used in the computer simulation, and the simulated spectra agree closely with the laboratory measurements over the range $\pm 3R_s$.

Conclusions

The overall goal of this work was to characterize the major nonlinearities of a class-C transistor amplifier operating at microwave frequencies. Since this device is a candidate for use in future communications satellite earth stations and may also be applied to future satellite transponders, its nonlinear behavior could significantly impact the choice of digital modulation techniques in systems that utilize these amplifiers.

This work has included the steps of microscopic device and circuit modeling, simulation at the microscopic level to measure the device AM/AM and AM/PM characteristics, and the utilization of these characteristics in existing time/frequency-domain complex-envelope simulation programs. The latter simulations allow the investigation of the impairments to digital transmission caused by this particular nonlinear amplifier.

Although the motivation for this work was the need to characterize a particular type of nonlinearity, an equally important goal has been to gain experience and confidence with a problem-solving technique. Many circuit analysis programs [12], which are in widespread use, handle nonlinear circuit elements. Similarly, solution algorithms for nonlinear state-variable equations are available as standard software routines. Combining these two techniques yields a powerful tool for device analysis and simulation. Different approaches to this type of problem have been outlined and compared [17]; however, the simulation approach appears to be much more practical than the more analytically oriented approaches, and offers invaluable physical insight.

Subsequent comparisons of the computer simulation results with laboratory measurements on a similar, but more complex, L-band class-C transistor amplifier showed good agreement; these comparisons validate the simulation model.

In the future, these microscopic simulation models should prove useful in developing more realistic and accurate complex-envelope (macroscopic)

models of nonlinearities with memory. Such models can then be incorporated into communications channel simulation programs, such as CHAMP, to study impairments to digital transmission over these channels.

Acknowledgments

References

[1] O. Shimbo, "Effects of Intermodulation, AM/PM Conversion, and Additive Noise in Multicarrier TWT Systems," *Proc. IEEE*, Vol. 59, No. 2, February 1971, pp. 230–238.

[2] W. L. Cook, "Interactive Computer Simulation of Satellite Transmission Systems," *Proc. Fifth Annual Pittsburgh Conference on Modeling and Simulation*, April 1974, pp. 867–872.

[3] L. C. Palmer, "Computer Simulation of Communications Channels," *Proc. Fifth Annual Pittsburgh Conference on Modeling and Simulation*, April 1974.

[4] E. Bedrosian and S. O. Rice, "The Output Properties of Volterra Systems (Nonlinear Systems with Memory) Driven by Harmonic and Gaussian Inputs," *Proc. IEEE*, Vol. 59, No. 12, December 1971, pp. 1688–1707.

[5] E. S. Kuh and R. A. Rohrer, "The State-Variable Approach to Network Analysis," *Proc. IEEE*, Vol. 53, No. 7, July 1965, pp. 672–686.

[6] J. J. Ebers and J. L. Moll, "Large-Signal Behavior of Junction Transistors," *Proc. IRE*, Vol. 42, No. 12, December 1954, pp. 1761–1772.

[7] R. G. Harrison, "Computer Simulation of a Microwave Power Transistor," *IEEE Journal of Solid-State Circuits*, SC-6, No. 4, August 1971, pp. 226–235.

[8] "The IMSL Library," Vol. 1, DVOGER-1.

[9] C. W. Gear, "The Automatic Integration of Ordinary Differential Equations," *Communications of the ACM*, Vol. 14, No. 3, March 1971, pp. 176–179.

[10] C. W. Gear, "Algorithm 407, DIFSUB for Solution of Ordinary Differential Equations [D2]," *Communications of the ACM*, Vol. 14, No. 3, March 1971, pp. 185–190.

[11] R. L. Bailey, "Large-Signal Nonlinear Analysis of a High-Power High-Frequency Junction Transistor," *IEEE Transactions on Electron Devices*, ED-17, No. 2, February 1970, pp. 108–119.

[12] J. Lang, "A Survey of the Present State of Microwave Transistor Modeling and Simulation as Applied to Circuit Design," *IEEE Transactions on Electron Devices*, ED-18, No. 12, December 1971, pp. 1168–1174.

[13] G. Berretta, R. A. Gough, and J. Guijarro, "Predicting Amplifier Performance for Multicarriers Using Computer Simulation," *Microwave Journal*, July 1975, pp. 35–38.

[14] S. A. Rhodes, "Effect of a Noisy Phase Reference on Coherent Detection of Offset-QPSK Signals," *IEEE Transactions on Communications*, COM-22, No. 8, August 1974, p. 1046.

[15] S. A. Gronemeter and A. L. McBride, "MSK and Offset QPSK Modulation," *IEEE Transactions on Communications*, COM-24, No. 8, August 1976, pp. 809–820.

[16] S. A. Rhodes, "Effects of Hardlimiting on Bandlimited Transmissions with Conventional and Offset QPSK Modulation," NTC 1972, Houston, Texas, December 4–6, 1972, *Conference Record*, pp. 20F-1-20F-7.

[17] "Nonlinear System Modeling and Analysis with Applications to Communications Receivers," Signatron, Inc., June 1973. Prepared for Rome Air Development Center, AD-766-278.

Larry C. Palmer received a B.S. from Washington and Lee University and a B.E.E. from Rensselaer Polytechnic Institute, both in 1955, and an M.S. and Ph.D. from the University of Maryland in 1963 and 1970. Before joining COMSAT, *he was employed by Computer Sciences Corporation, participating in systems engineering studies related to digital communications systems, satellite communications and navigation systems, and digital signal processing systems, and supervised the development of time-domain simulation programs to investigate the impairments encountered in digital data transmission by satellite using FDMA and TDMA. Prior to this, he participated in a study of advanced trilateration tracking techniques for the U.S. Army ECOM and in studies and planning of the Advanced Defense Communications Satellite Program.*

Dr. Palmer is Senior Staff Scientist in the Transmission Systems Laboratory, responsible for computer simulation and system studies related to digital transmission via communications satellite with emphasis on modulation and multiple-access techniques for future global satellite systems. He is a member of Tau Beta Pi, Eta Kappa Nu, and IEEE.

Sheldon H. Lebowitz received a B.E.E. from the City College of New York in 1964. He has worked at the U.S. Navy Maritime Engineering Laboratory, the Electromagnetic Compatibility Analysis Center, Norden Division of United Aircraft, and Computer Sciences Corporation. In 1974 he joined COMSAT *Laboratories, where he has been involved with digital computer simulations of communications systems.*

Experimental study of cross polarization of feed horn clusters

P. NEYRET

(Manuscript received November 16, 1977)

Abstract

The polarization properties of open-ended waveguide feeds of square and circular cross section have been investigated experimentally. Effects of mutual coupling among closely spaced feeds on polarization isolation in the field of view of the reflector surface have been measured as a function of feed type, dimension, spacings, and frequency. Measurement results presented in this paper indicate that the best polarization performance is obtained with circular apertures having a diameter of one wavelength or more.

Introduction

A satellite antenna for frequency reuse by spatial and polarization isolation typically consists of an offset parabolic reflector fed by an array of feed horns. Tradeoffs among beam shaping, low sidelobes, size, weight, design complexity, and cost usually result in a planar array of identical feed horns as a preferred solution [1], [2]. Each feed typically has an aperture size of approximately one wavelength and radiates a beam intercepting the reflector approximately at its −3-dB co-polarization level.

If the polarization characteristics of the feed element determined in the array environment (with all elements match-terminated) approximate those of the Huygen's source, then the antenna will be virtually free of

cross polarization [3], [4]. Since no simple model accurately predicts the cross-polarized radiation characteristics of an array of small horn-type elements, an experimental investigation was undertaken to compare their polarization properties.

This paper describes the results of an experimental study of circularly polarized feed horns of square and circular cross section. Included are data for a single feed horn, a 2-element array of feeds, and an hexagonal array of seven feed horns. The feed horn aperture dimensions range from 0.7λ to 1.4λ.

Measurement procedure

Measurements were performed in an anechoic chamber over the frequency range of 5.925–6.425 GHz. The horn under test was mounted on a 3-axis positioner and connected to a crystal detector through a high-quality polarizer (axial ratio less than 0.1 dB across the band), orthomode transducer (OMT), and isolator. Figure 1 shows the coordinate system for the measurements as well as the waveguide hardware. The source assembly consisted of a horn and a polarizer assembly that could create an arbitrary polarization state by means of rotatable cascaded quarter- and half-wave polarizers as described in Reference 5. This arrangement was tuned to maintain less than 0.1-dB residual ellipticity of the circularly polarized field incident on the antenna under test. Radiation
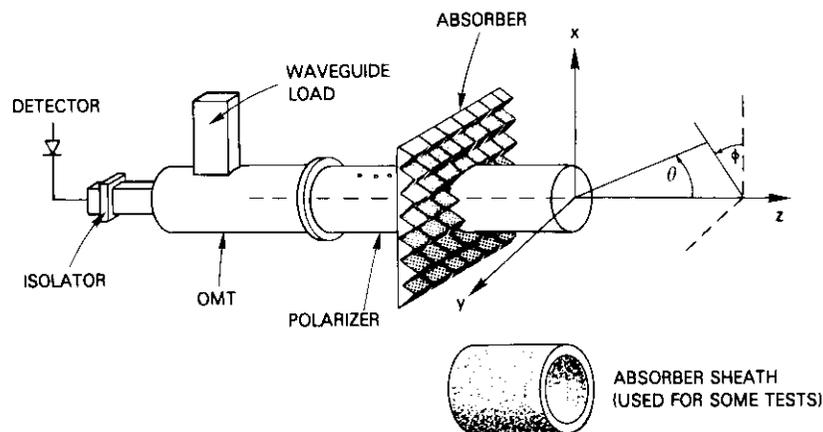
Figure 1. *Coordinate System and Horn Under Test*

pattern cuts and swept frequency measurements were performed. In all cases the co-polarized level on beam peak was taken as the 0-dB reference.

Single feed horn performance

Measurements were performed on four types of feed horns: a square waveguide 5.13 cm on a side, a circular 3.49-cm-diameter waveguide, a circular waveguide 4.83 cm on a side, and a 6.45-cm-diameter Potter horn [6]. The first three configurations are simple open-ended waveguide radiators with step transitions from the aperture opening down to the 3.49-cm waveguide size used for the OMT. The dual mode (Potter horn) dimensions [7] are shown in Figure 2.
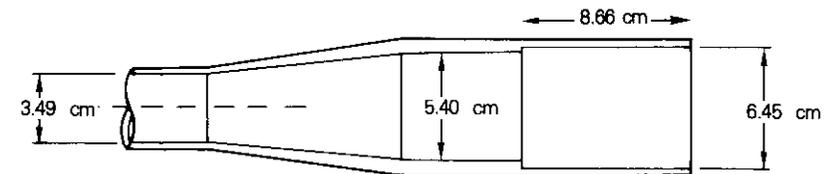
Figure 2. *Potter Horn Feed (sectional view)*

Pattern cuts as a function of polar angle θ for discrete values of ϕ measured with the 5.13-cm square waveguide showed a high level of cross polarization, reaching a value of -22 dB along the -3-dB co-polarization contour (Figure 3). A pattern measured with the 3.49-cm circular feed is shown in Figure 4. Although this antenna had better cross-polarization performance, the co-polarization patterns had very irregular frequency-dependent shapes which would not be predicted by Chu's equations [8] and which could be attributed to currents flowing on the external wall of the horn because of the broad radiation pattern. Measurements performed with the horn's external wall covered by an absorber sheath confirmed this hypothesis, resulting in patterns which coincided almost exactly with calculated patterns.

Patterns measured with the 4.83-cm circular waveguide showed only slight co-polarization pattern irregularities and low cross-polarization levels (Figure 5). Again, an absorber sheath restored good co-polarization patterns, and the cross-polarization levels became very low (Figure 6), actually better than predicted by Chu's equations.

A possible explanation of this phenomenon is a slight excitation in the
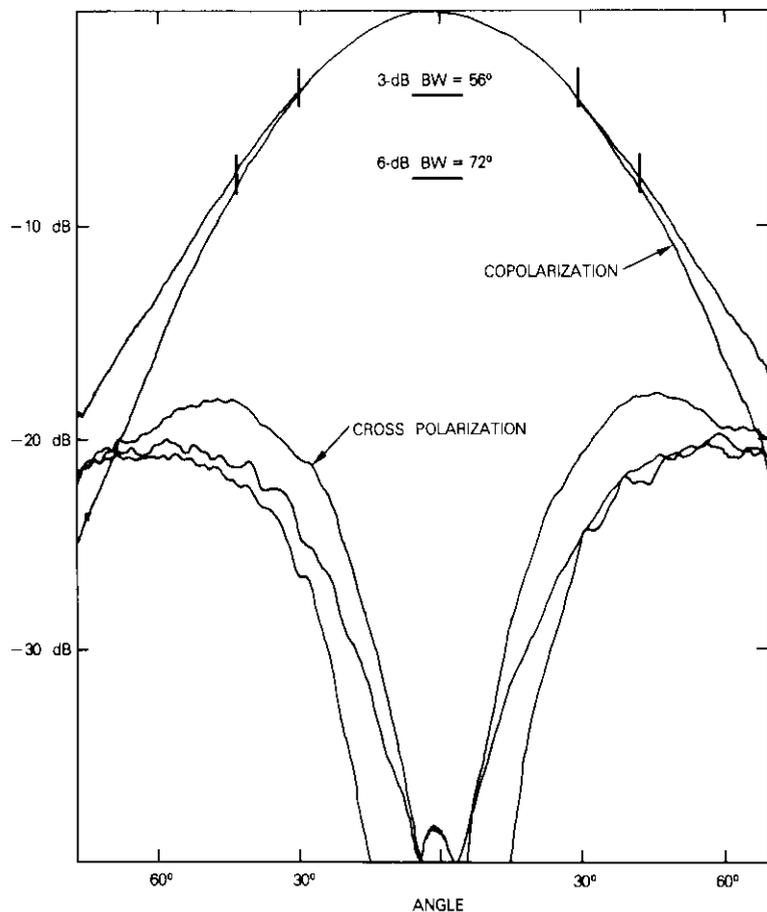
Figure 3. *Field Patterns of a Single 5.13-cm Square Waveguide Feed*

aperture plane of the TM_{11} mode, still below cutoff within the waveguide. It is well known that the presence of an approximately 14-percent TM_{11} mode phased properly with the TE_{11} mode can produce very low cross polarization. This radiator is known as a Potter horn. A measured pattern for a Potter horn, shown in Figure 7, illustrates the excellent polarization properties of this antenna. However, the bandwidth of this horn is limited by the phasing requirements for the TE_{11} and TM_{11} modes.
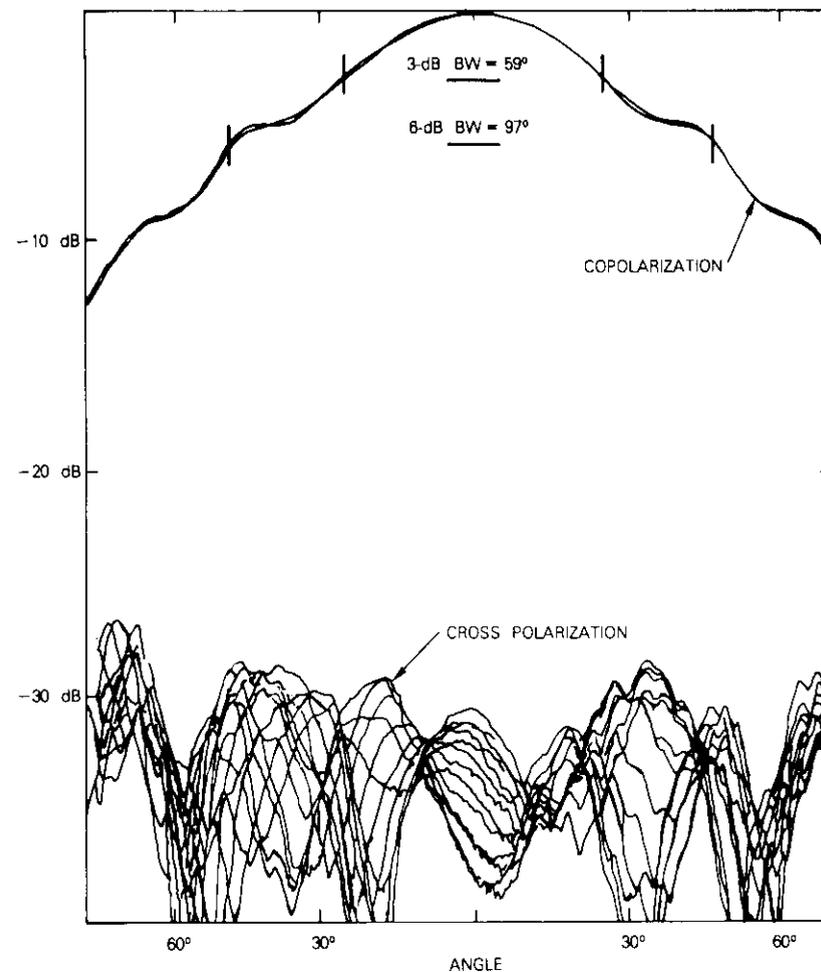
Figure 4. *Field Patterns of a 3.49-cm Circular Waveguide Feed*
($f = 6000$ MHz, without absorber)

Two-element array

A series of measurements as a function of element spacing was performed on an assembly of two identical feed horns. One feed horn was
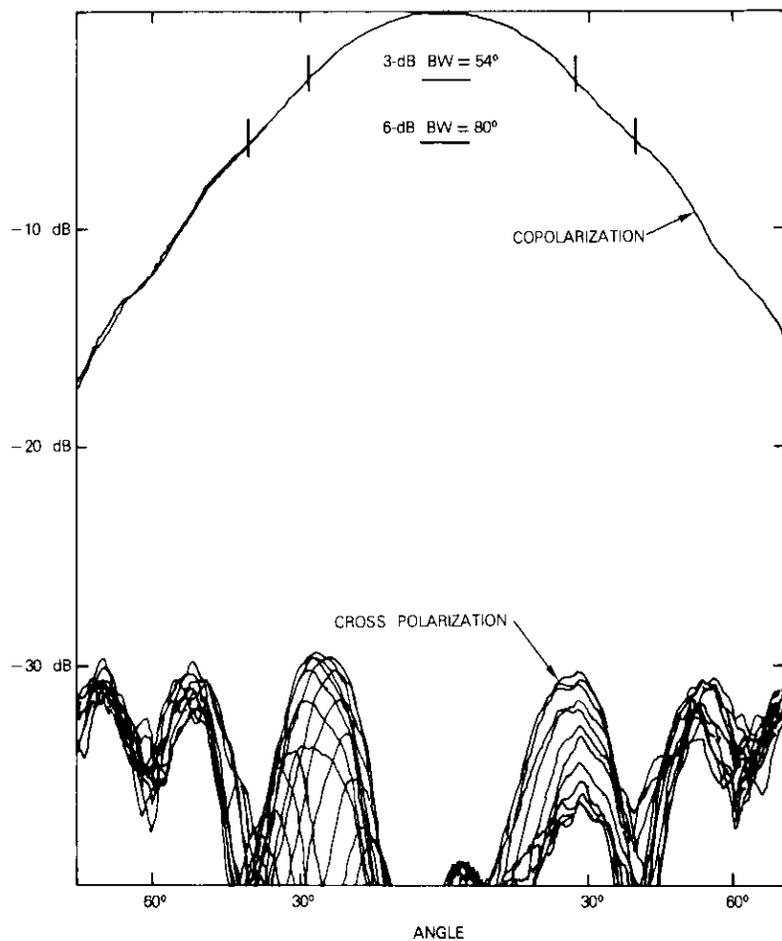
Figure 5. *Field Patterns of a 4.83-cm Circular Waveguide Feed*
(f = 6100 MHz, without absorber)

connected to the detector and the other was terminated in a matched load. A comparison of these data with those measured for the single element illustrates the mutual coupling effects. Figures 8–10 illustrate this comparison for three horn types and an element spacing of 5.72 cm. Data for an array of two Potter horns are not shown because of their low cross polarization and relative insensitivity to coupling.
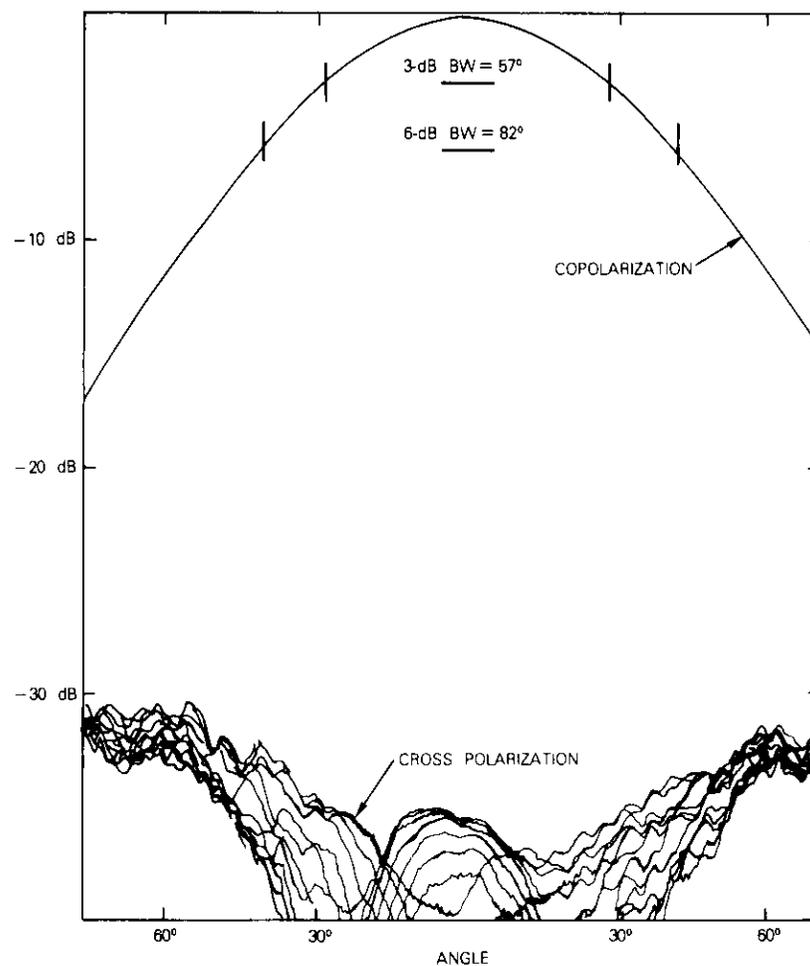
Figure 6. *Field Patterns of a 4.83-cm Circular Waveguide Feed*
(f = 6100 MHz, with absorber)

The hexagonal array

A hexagonal array of seven feed horns consisting of a center element and six symmetrically dispersed elements was constructed and evaluated. The center element was connected to the detector and the six outer elements
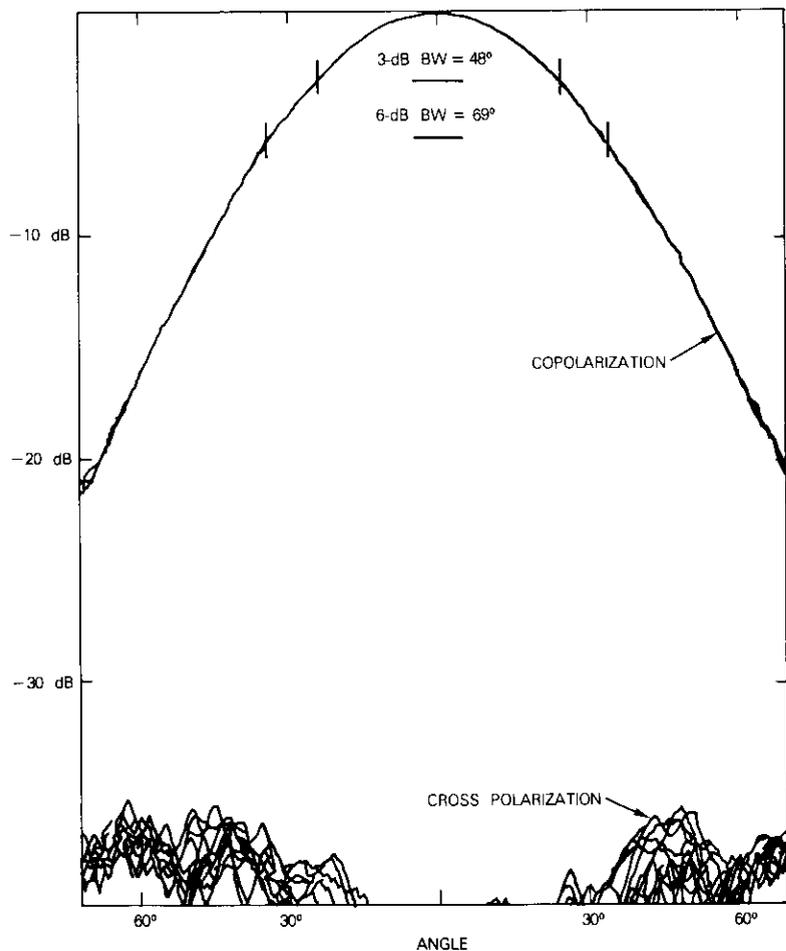
Figure 7. *Field Patterns of a Potter Horn* ($f = 6100$ MHz)

were connected to matched terminations. The assemblies are shown in Figure 11. Figure 12a shows the cross-polarization contours for the 3.49-cm circular horn, and Figure 12b shows those for the Potter horn measured in the hexagonal array. The element spacings are 5.72 cm and 7.16 cm, respectively. Some typical radiation pattern cuts for the 3.40-cm-

a. Single Feed   b. In the Presence of an Adjacent Feed
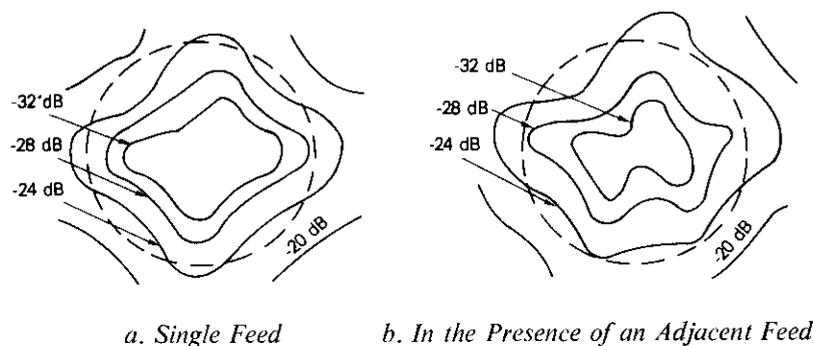
Figure 8. *Cross-Polarization Contours for a 5.13-cm Square Feed*

a. Single Feed   b. In the Presence of an Adjacent Feed
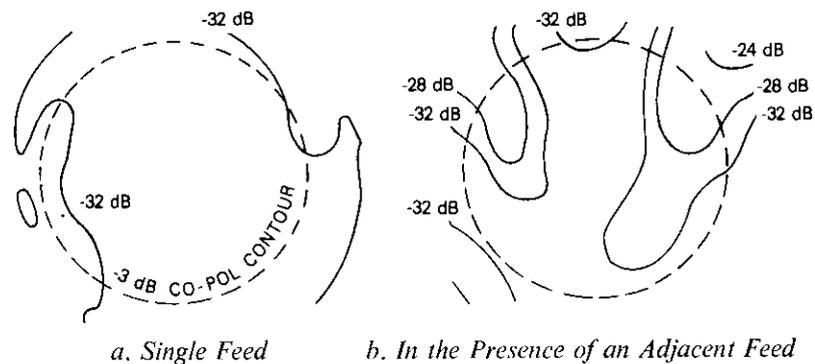
Figure 9. *Cross-Polarization Contours for a 3.49-cm Circular Feed*

a. Single Feed   b. In the Presence of an Adjacent Feed
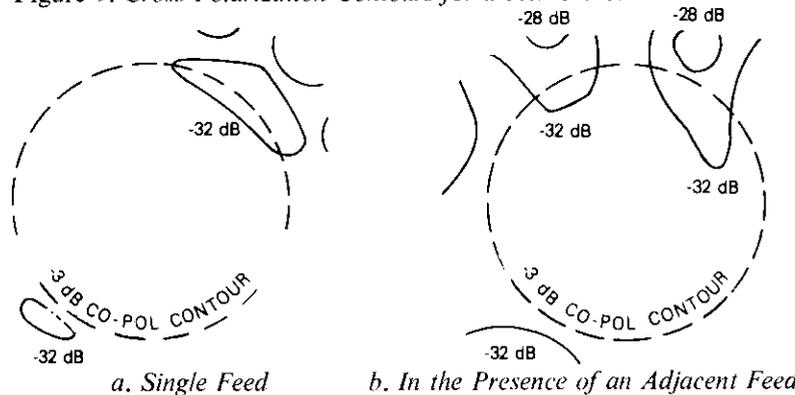
Figure 10. *Cross-Polarization Contours for a 4.83-cm Circular Diameter Feed*
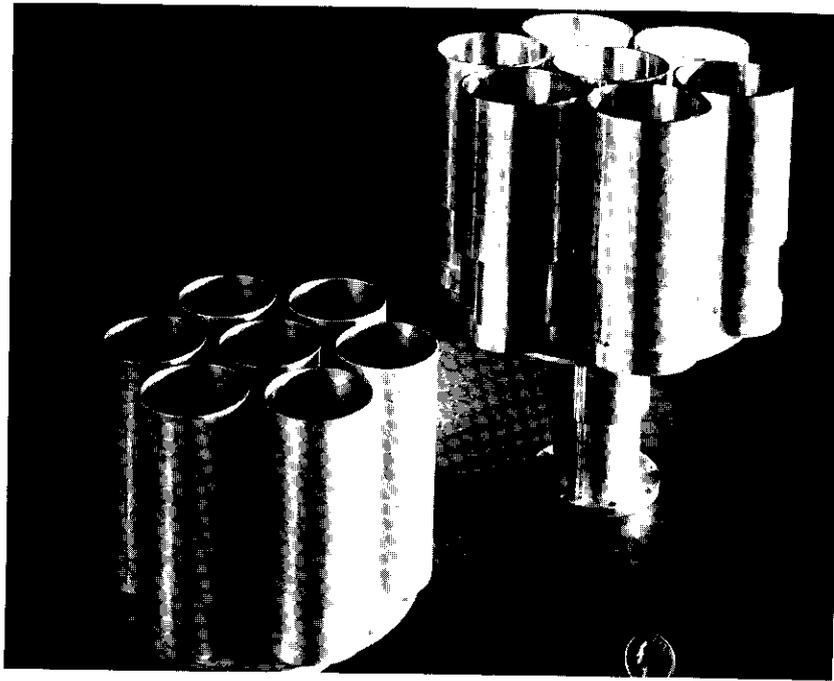
Figure 11. *Hexagonal Clusters of 4.83-cm-Diameter Circular Waveguide and Potter Feed Horns*
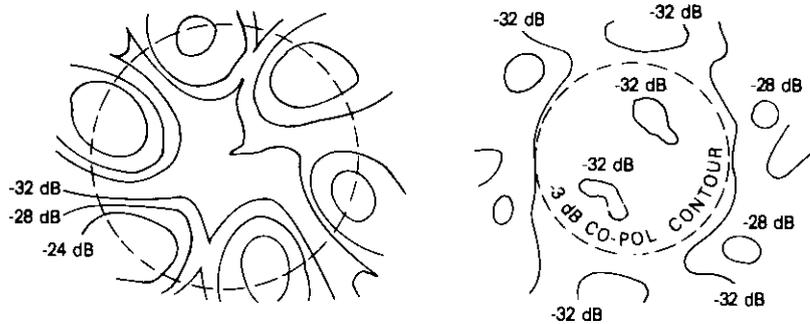
a. 3.49-cm Circular Waveguide Spacing = 5.72 cm

b. Potter Horn Spacing = 7.16 cm

Figure 12. *Cross-Polarization Contours of a Feed in a Hexagonal Cluster*

diameter horn, the 4.83-cm-diameter horn, and the Potter horn are shown in Figures 13–15, respectively.
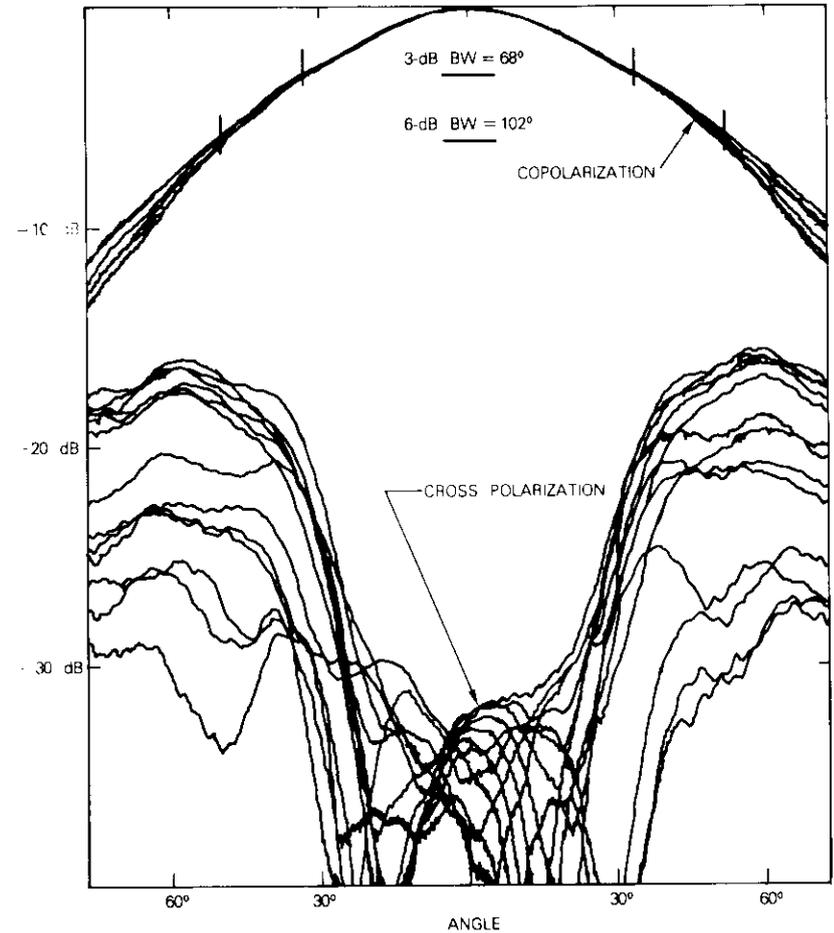
Figure 13. *Hexagonal Cluster of 3.49-cm Circular Waveguide (spacing = 3.81 cm, f = 6175 MHz)*

Figures 16 and 17, which show worst case cross-polarization data within the −3-dB co-polarization contour based on swept frequency measurements for hexagonal clusters of the three types of feeds and for various element spacings, S, also include the single element data for comparison.
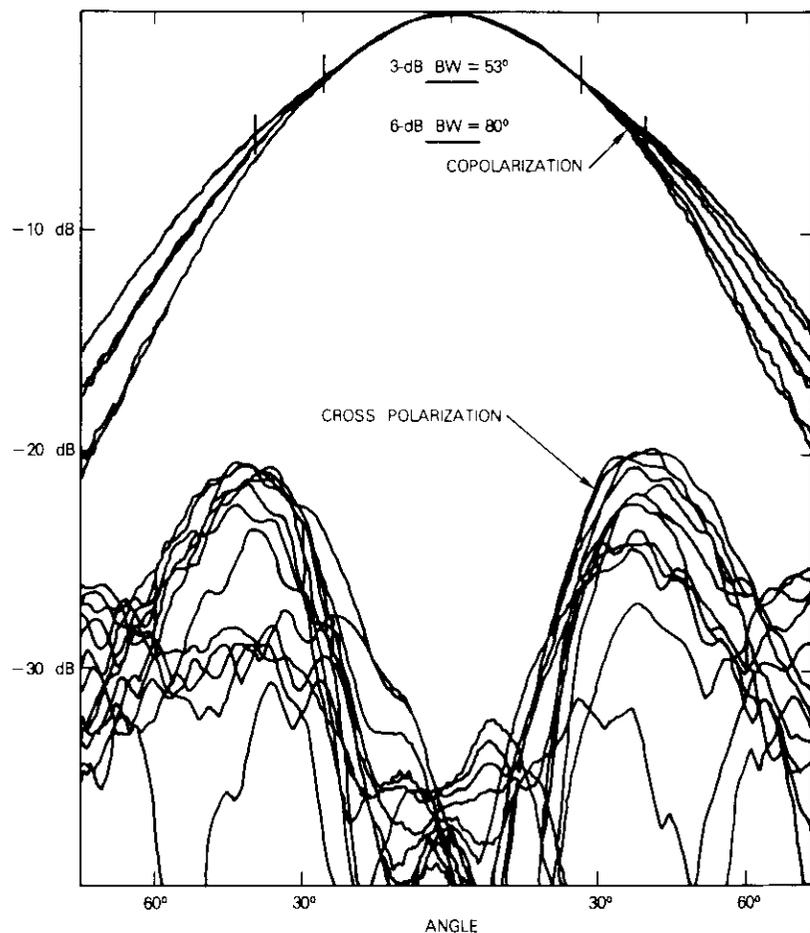
Figure 14. *Hexagonal Cluster of 4.83-cm Circular Waveguide*
(spacing = 5.08 cm, f = 6100 MHz)

For the Potter horn, an anomaly in the cross-polarization levels occurs at a frequency of 6.225 GHz. Figure 18, which plots the worst case cross-polarization level within the -1.25-dB contour, illustrates this anomaly. It has been noted that 6.225 GHz is the cut-off frequency of the TE_{31} mode in the Potter horn. The performance anomaly may be related to the excitation of this mode by a mutual coupling effect.
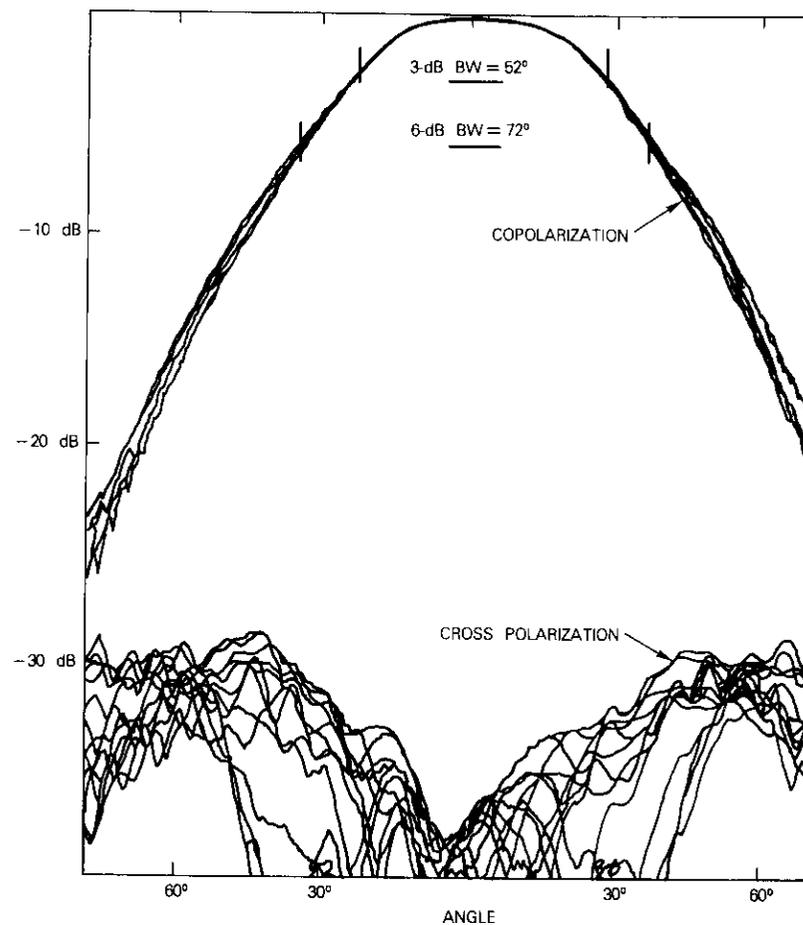
Figure 15. *Hexagonal Cluster of Potter Horns*
(spacing = 8.16 cm, f = 6100 MHz)

Conclusion

The results of this experimental study provide guidelines for the choice of a feed array for shaped beam antennas with dual circular polarization. The better polarization isolation performance of circular as opposed to
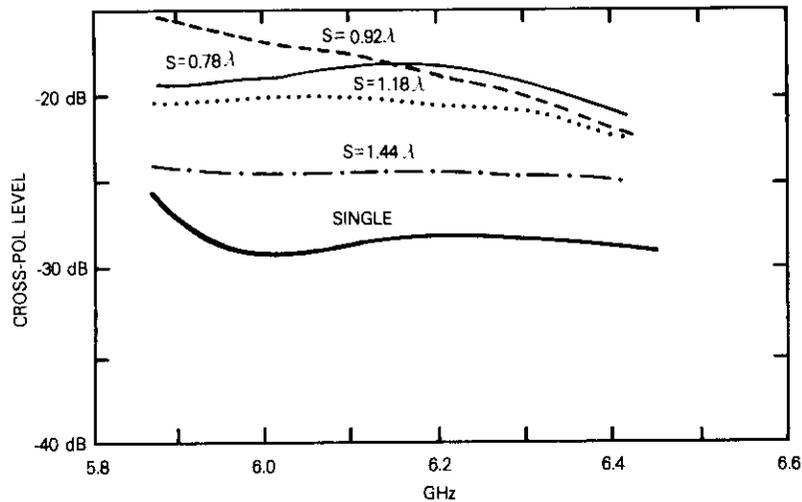
Figure 16. *Worst Cross-Polarization Level within the* -3-dB *Co-polarization Contour of a 3.49-cm Circular Waveguide Feed Hexagonal Cluster*
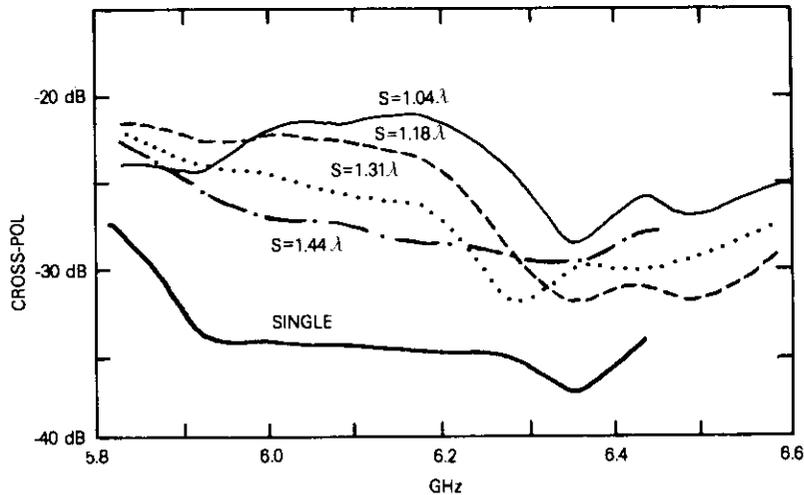
Figure 17. *Worst Cross-Polarization Level within the* -3-dB *Co-polarization Contour of a 4.83-cm Circular Waveguide Feed Hexagonal Cluster*

square apertures has been established for feed elements with an aperture size of approximately one wavelength, corresponding to the design generally preferred for beam shaping. Although smaller square apertures have
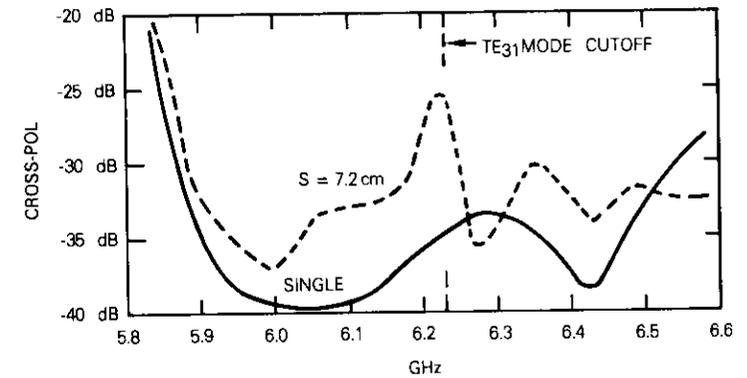
Figure 18. *Worst Cross-Polarization Level within the* -1.25-dB *Co-polarization Contour of a Potter Feed Hexagonal Cluster*

not been investigated, their broad radiation patterns, similar to that of a smaller circular aperture, could result in strong scattering degradation when used in an array. Potter horns are relatively insensitive to scattering and offer a useful solution over limited bandwidths. However, the occurrence of a pattern distortion at the cutoff frequency of the TE_{31} mode may result in a bandwidth limitation and requires further study. When large bandwidths are required, circular apertures with a diameter of approximately one wavelength yield acceptable polarization performance with a fairly simple feed horn geometry.

Acknowledgment

References

[1] F. Taormina et al., "INTELSAT IV-A Communications Antenna—Frequency Reuse Through Spatial Isolation," 1976 International Conference on Communications, ICC '76, June 1976, Philadelphia, PA, *Conference Record*, pp. 4-10-4-14.

[2] E. W. Matthews, W. G. Scott, and C. C. Han, "Advances in Multibeam Satellite Antenna Technology," *EASCON '76 Convention Record*, September 26-29, 1976, Washington, DC, pp. 132-A–132-O.

[3] D. F. DiFonzo, W. J. English, and J. A. Janken, "Polarization Character-istics of Offset Reflectors with Multiple Element Feeds," *G-AP International Symposium Digest*, 1973, pp. 302-305.

[4] T. S. Chu and R. N. Turrin, "Depolarization Properties of Offset Reflector Antennas," *IEEE Transactions on Antennas and Propagation*, AP-21, No. 3, May 1973, pp. 339-345.

[5] D. DiFonzo, W. Trachtman, and A. Williams, "Adaptive Polarization Control for Satellite Frequency Reuse Systems," *COMSAT Technical Review*, Vol. 6, No. 2, Fall 1976, pp. 253-283.

[6] P. Potter, "A New Horn Antenna with Suppressed Sidelobes and Equal Beamwidths," *Microwave Journal*, Vol. 6, June 1963, pp. 71-78.

[7] W. J. English, "The Circular Waveguide Step-Discontinuity Mode Trans-ducer," *IEEE Transactions on Microwave Theory and Techniques*, MTT-21, No. 10, October 1973, pp. 633-636.

[8] *Microwave Antenna Theory and Design*, S. Silver, editor, M.I.T. Radiation Laboratory Series, Vol. 12, New York: McGraw-Hill, 1949.

Pierre Neyret received the Diplome National Supe-rieur d'Ingenieur Radioelectricien from the Poly-technic Institute of Grenoble, France, in 1967. In 1967 and 1968, he was an assistant teacher at the Ecole Nationale d'Etude des Telecommunications of Algiers. In 1969 he joined Thompson-CSF, working first on military aerospace antennas, and then from 1970 to 1975, on satellite transmitters (Helio, Dialogue). From 1975 to 1978, he was an INTELSAT nominee assigned to the Antenna De-partment of the Microwave Laboratory at COMSAT Laboratories, where he was involved with studies of depolarization effects in feed arrays and the measurement of the depolarization properties of large earth station antennas. Presently at Thomson-CSF, he is working on both antennas and transponders for satellites.

A developmental program of satellite data collection

G. FORCINA, K. MANNING, AND K. SINGH

(Manuscript received June 23, 1978)

Abstract

The results of a developmental data collection system designed, implemented, and operated by COMSAT GENERAL are discussed. The objective of this experi-ment, which was initiated on October 28, 1977, and completed on June 19, 1978, was to demonstrate that this unique service using low bit rates and low-cost terminals can be incorporated into existing commercial communications satel-lites operating at C-band (4/6 GHz).

The system consists of 13 specially designed data collection platforms (DCPS) transmitting environmental data to Telesat's Anik I satellite, which relays the data to COMSAT GENERAL's Southbury earth station. Two platforms were located in Canada and 11 in the U.S. at data collection sites instrumented and operated by the United States Geological Survey (USGS). The U.S. DCP data received at Southbury are processed and transmitted via telephone line both upon request and automatically to designated USGS offices. Telesat also participated in the program with an earth station located close to Ottawa and capable of performing basically the same functions as the Southbury earth station. During the eight months of operation, the system performed well, and all the program objectives were met.

Introduction

In the past few years, considerable effort has been directed toward data collection via satellite. In the U.S., NASA and NOAA demonstrated the

feasibility of remote monitoring via both low-orbit and geosynchronous satellites carrying a dedicated data collection package. The up-link frequency was in the 400-MHz band, and the spacecraft telemetry carrier was used for the down-link. After extensive studies and market surveys, COMSAT GENERAL determined that a data collection system using existing 4/6-GHz geostationary communications satellites would offer both technical and nontechnical advantages.

Interest in this type of application was shared by Canada's Telesat and the USGS. COMSAT GENERAL and the USGS agreed to conduct an experimental program using part of a transponder of one of Telesat's Anik satellites and specially designed DCPs to collect environmental data from 13 points. The major objectives were to demonstrate that data could be collected from remote hydrological sensor sites, transmitted via an existing commercial communications satellite, and received at a central location by using relatively inexpensive remote terminals. The program was designed to avoid interference with the terrestrial microwave network and existing satellite systems using the same frequencies. Operation began on October 28, 1977, and performance has been evaluated through June 19, 1978. This paper describes the system, its major components, and the evaluation.

System description

Figure 1 is a block diagram of the developmental data collection system. Each DCP transmits data acquired from its associated hydrological sensor in short (∼250-ms) bursts. Since the bursts originating from the DCPs are not synchronized, the access method is random. The number of DCPs operating on the same frequency for a fully loaded system varies from two to three hundred depending upon the reliability of message reception required.

The DCPs are small transmit-only terminals powered by a rechargeable battery and equipped with a 1.2-m antenna, solid-state RF amplifier, modulator, and microprocessor. These terminals, which perform automatic data acquisition and unattended transmission, accept data from special hydrological sensors and are easily adaptable to other types of sensors. The sensor outputs are sampled at one of three constant selectable sampling rates. After the data are acquired from the sensors, they are formatted into a message and transmitted to the satellite in a burst mode. All the platforms transmit at the same frequency with no synchronization among the transmitted bursts; therefore, mutual interference may occur.
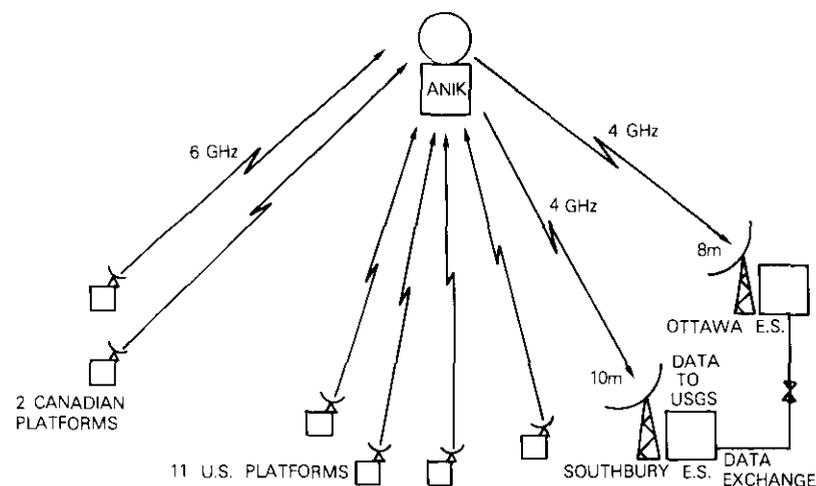
Figure 1. *Developmental Remote Monitoring System*

However, the transmitter duty ratio is sufficiently low to yield a small probability of mutual interference. This probability is further decreased because the platforms can transmit the same message twice. In addition, transmitted messages have an error detection code to prevent the acceptance of erroneous messages due to thermal noise or mutual interference.

Figure 2 shows a typical USGS monitoring station and DCP. Eleven USGS measuring stations, which are equipped with DCPs, are located in three different regions of the U.S.: southern Oregon (five sites), Pennsylvania (five sites), and Virginia (one site). Two DCPs have also been installed in Canada for use by Telesat. The satellite used in the program is Telesat Anik I located in geostationary orbit at 104°W longitude.

COMSAT GENERAL's Southbury earth station is the central receive station for the U.S. DCPs. A Canadian station located at Shirley's Bay, Ontario, receives data from the Telesat DCPs and serves as a backup to the COMSAT station. Special data collection receive equipment (DCRE) developed by COMSAT Laboratories permits each station to receive data from all the DCPs in use.

The data dissemination network, which is part of the data collection system, distributes the data received at the two earth stations to the users. Figure 3 shows the configuration of the data dissemination network. The minicomputer [or communication processor (CP)] and its peripherals
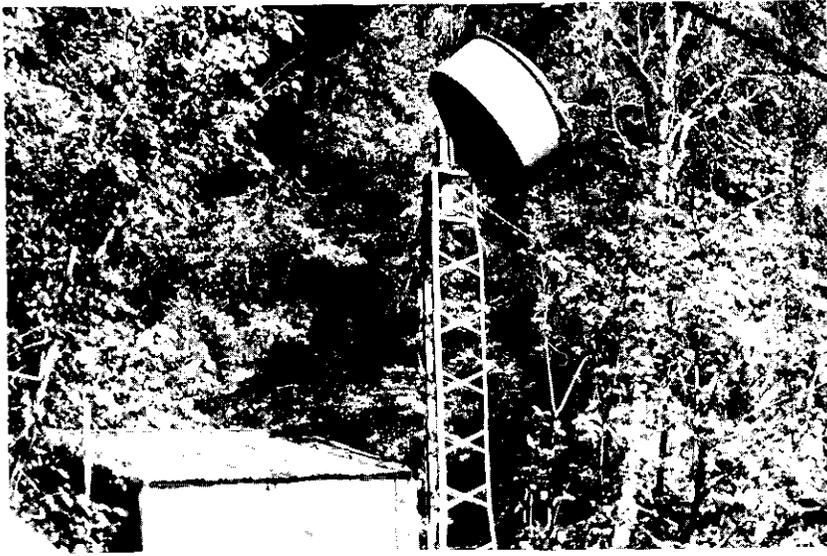
Figure 2. *Typical DCP Installation*

(which are a part of the DCRE) are shown for both receive earth stations. Basically, the data are delivered at two speeds:

a. 4,800-baud synchronous line either for automatic data transfer into the Reston IBM 370 computer or for data retrieval operations from two USGS district offices equipped with IBM 2780 terminals (or equivalent machines),

b. 110-baud synchronous line for "quick look" data retrieval from small portable terminals.

The USGS Pennsylvania and Oregon district offices are each equipped with a terminal equivalent to an IBM 2780 work station. These terminals can initiate the data request procedure after the telephone connection with the CP is established. (The user dials the telephone number of the earth station modem.) The third data access point is the USGS Headquarters in Reston, Virginia, which is equipped with an IBM 370/155 computer. In this case, the data request is forwarded to the CP by one of the two IBM 2780s or by a remote teletype. The processor then establishes a telephone connection with Reston and delivers the requested data. In addition to this type of data delivery, a periodic data dump operation
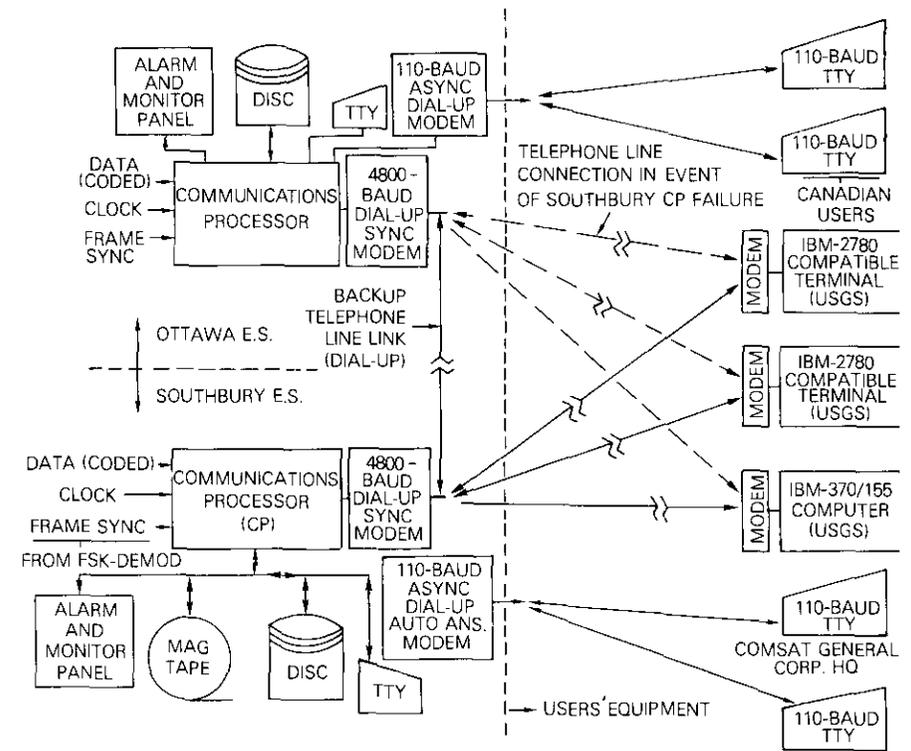
Figure 3. *Block Diagram of Data Dissemination Network*

into the Reston computer is automatically performed by the processor.

If the Southbury station fails, the user calls the Canadian processor. Upon restoration of operation in Southbury, the missed portions of the data are transferred to the local disc unit from the Canadian disc recorder via the 4,800-baud modem and a dial-up telephone connection. In a similar manner, the Canadian earth station can obtain data from Southbury. The mini-computer data files can also be accessed by a remote teletype via a dial-up telephone line and an asychronous 110-baud modem. This type of access, which is being used routinely by the Canadian users and occasionally by the USGS, is also used by COMSAT GENERAL Headquarters in Washington, D.C., to request the system status report from the CP.

Technical characteristics

Table 1 is the system technical summary, and Table 2 gives the DCP carrier link budget for the Southbury and Canadian receive earth stations. The accuracy of the measured carrier-to-noise density (C/N_o) ratios listed in Table 3 for all DCPS is expected to be within ± 1 dB. The C/N_o for DCPS 4, 7, 8, and 10 is within 1.6 dB of the theoretical value. The variations are due to different pointing errors and/or obstructions in the path. However, the carrier-to-noise (C/N) ratio of all DCP carriers is higher than the minimum required value of 46 dB-Hz.

For simplicity of implementation and low sensitivity to short-term

TABLE 1. DATA COLLECTION SYSTEM TECHNICAL SUMMARY

Number of DCPs	13
DCP Input Data	64 bits of digital input data or 8 analog inputs (8-bit encoding) or combinations thereof
Sensor Sampling Rate	15, 30, or 60 min
Message Transmission Rate	1, 2, or 4 messages/hr
Redundant Message Transmission	optional
DCP Transmitter Power	700 mW (minimum)
DCP Antenna Diameter	1.2 m
e.i.r.p.	33.5 dBW (minimum)
Modulation	binary, FSK ($\Delta f = \pm 750$ Hz)
Spectrum Bandwidth	3 kHz
Transmit Frequency	5950 MHz (5970.5 MHz alternative)
Type of Transmission	burst mode
Burst Duration	244 ms
Information Bits per Message	64
Overhead Bits per Message	180
Bit Rate	1 kbit/s
Bit Rate Accuracy	10^{-4}
Receive Antenna G/T	
U.S. Station	29.8 dB/K
Canadian Station	26.0 dB/K
Required DCP Carrier C/N_o	46 dB-Hz (minimum)
System Bit Error Rate	10^{-5} (maximum)
Link Margin	
U.S. Station	5.9 dB
Canadian Station	3.4 dB
Parity Check Code	CRC-16 (error detection)
Probability of Mutual Message Interference	1 percent (maximum)

TABLE 2. DCP CARRIER LINK BUDGET

Parameters	U.S.	Canada
Up-Link		
DCP Transmit e.i.r.p. (dBW)	33.5	33.5
Allowed Antenna Pointing Loss (dB)	1.5	1.5
Free Space Loss	199.5	199.5
Satellite G/T (dB/K)	−5.0	−5.0
Saturation Flux Density (dBW/m²)	−82.0*	−82.0
C/T (dBW/K)	−172.5	−172.5
Input Backoff (dB)	48.5	48.5
Output Backoff (dB)	43.3	43.3
Down-Link		
Saturated Satellite e.i.r.p. (dBW)	35.5	36.1
Carrier Down-Link e.i.r.p. (dBW)	−7.8	−7.2
Free Space Loss (dB)	195.8	195.9
Receive Antenna Pointing Loss (dB)	1.0	1.0
Receive Antenna G/T (dB/K)	29.8	26.0
C/T (dBW/K)	−174.8	−178.1
System Total C/T (dBW/K)	−176.7	−179.2
Total C/N_o (dB-Hz)	51.9	49.4
Required C/N_o (dB-Hz)	46.0	46.0
Margin (dB)	5.9	3.4

*The coverage contours of the Telesat Anik satellite are essentially the same for both the Oregon and Pennsylvania regions.

TABLE 3. MEASURED DCP C/N_o AT
SOUTHBURY RECEIVE STATION*

Location	DCP No.	C/N_o (dB-Hz)
Oregon	1	49.3
	2	49.3
	3	46.8
	4	50.2
	5	47.8
Reston	6	47.8
Pennsylvania	7	50.3
	8	50.3
	9	47.3
	10	50.3
	11	49.3
Canada	12	49.3
	13	49.3

*The system required minimum C/N_0 is 46 dB-Hz.

frequency jitter, binary FSK was chosen as the modulation scheme. A peak frequency deviation (Δf) of 750 Hz was selected because of computer simulations performed at COMSAT Laboratories, which essentially optimize for best error rate performance. The resulting modulation index is 1.5 for a 1-kbit/s transmission rate, resulting in a signal spectrum of about 3 kHz. The specified bit error rate performance is 10^{-5} at 46 dB-Hz. Figure 4 shows the results of a bit error rate test with the DCP and the receive station FSK demodulator connected in a satellite link configuration. The theoretical performance curve for noncoherent FSK is also plotted for reference.

The structure of the transmitted message is shown in Figure 5. The 100-ms carrier acquisition preamble is required for a low probability of missed carrier frequency acquisition (10^{-5} at C/N = 44 dB-Hz). The unique word bit is a 15-bit maximum length sequence that provides a "start of message" reference. The 2-bit sampling rate code contains information on the selected sampling rate (15, 30, or 60 min), and the 1-bit repetition code distinguishes the original transmission from the repetition. This information is used in the minicomputer to eliminate redundancy in the data stored on disc and later transmitted to the customer. The 64-bit sensor data block is a combination of water level data (digital sensor) and water quality data (analog sensor digitally encoded by the DCP). Water level information is composed of 16-bit blocks (one for each sensor) corresponding to a reading from 00.00 to 99.99 ft encoded in binary coded decimal (BCD) format. The analog inputs and DCP battery voltage are encoded in an 8-bit binary word. The type CRC-16 parity code, with $1 + x^2 + x^{15} + x^{16}$ as a generator polynomial, can detect error bursts up to 16 bits.

The probability of mutual message interference is about 1 percent in the worst case with all 13 DCPs transmitting every 15 minutes in a single transmission mode.

Data collection platform

The system provides a C-band communications link between remote data collection devices and the satellite ground receive station. The DCP accepts both analog and digital hydrological data, which are encoded, properly formatted, and transmitted at predetermined intervals. All internal functions and interfaces are microprocessor controlled. The DCP installation consists of five major components: antenna, mast electronics, DCP baseband/IF assembly, battery pack assembly, and interconnection assembly. Figure 6 is a block diagram of the DCP.
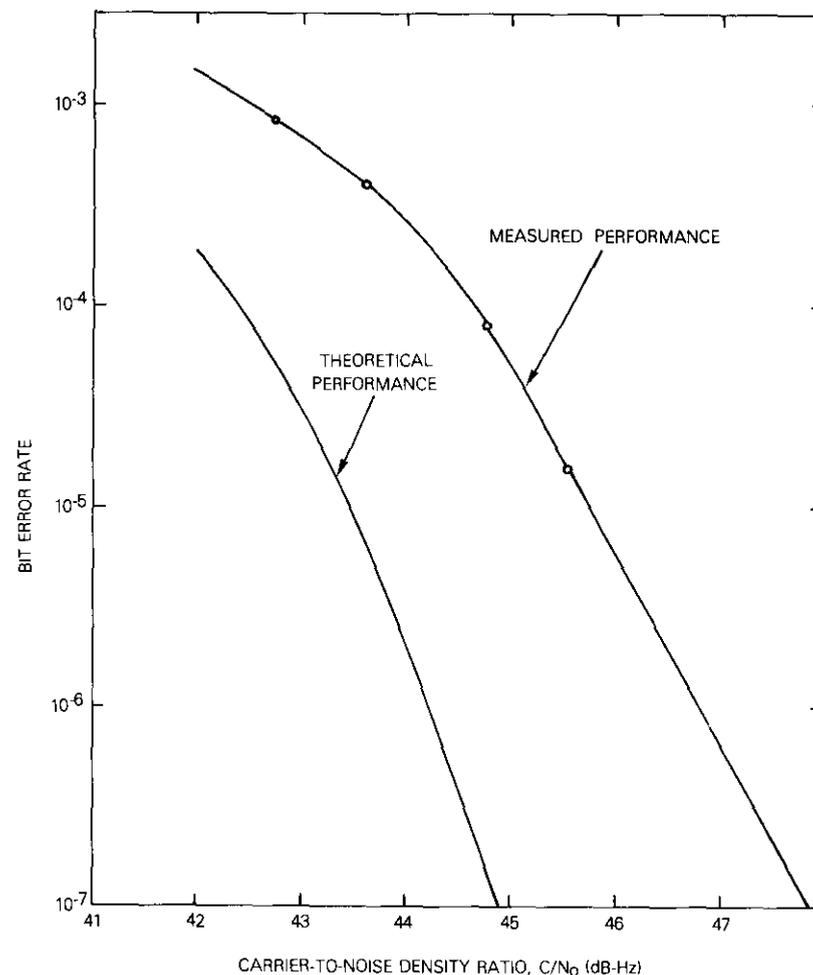
Figure 4. *Simulated System Performance, BER vs C/N_o (noncoherent FSK modulation)*

Figure 7 shows the DCP system configuration; the technical characteristics are listed in Table 4. The antenna is a 1.2-m parabolic dish mounted on a steel, self-supporting, triangular, gusseted tower. The antenna and feed are covered with a radome and the internal perimeter of the antenna
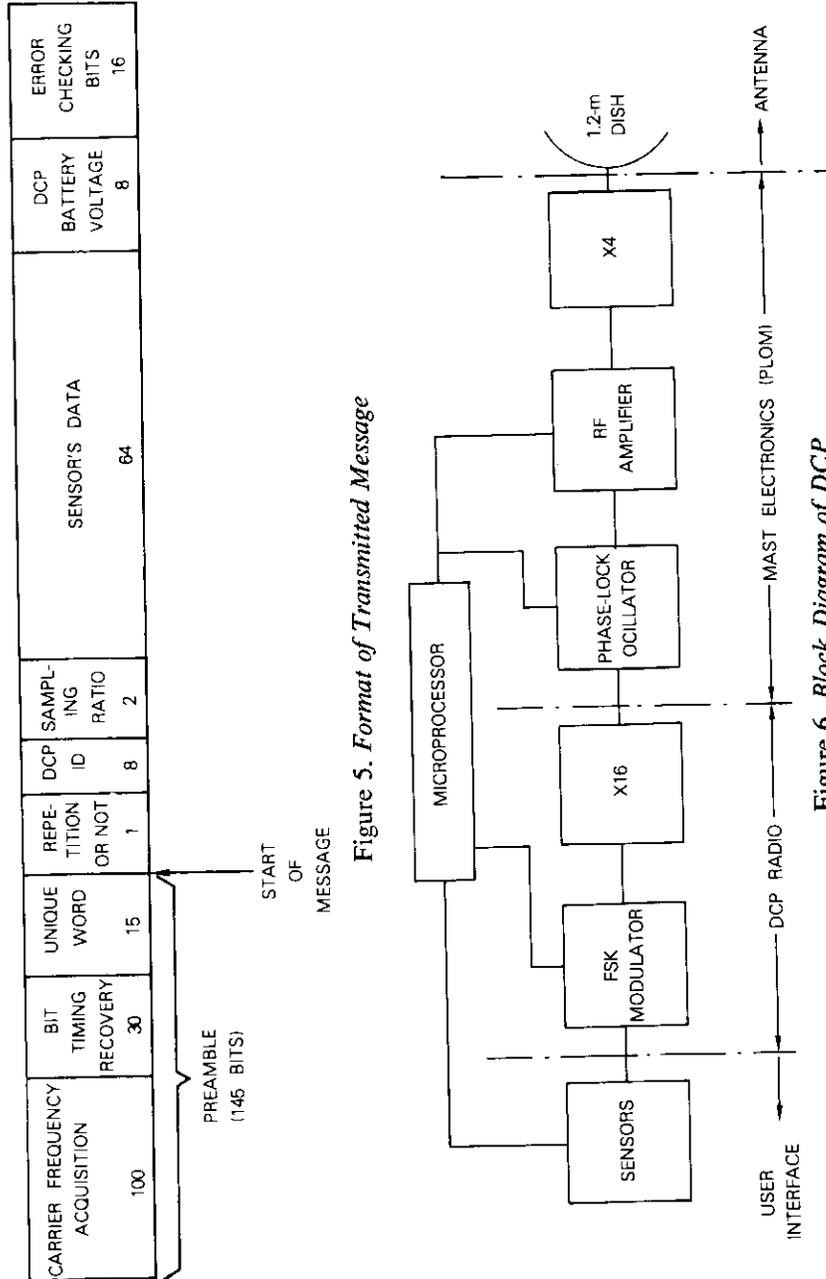
Figure 5. *Format of Transmitted Message*

Figure 6. *Block Diagram of DCP*
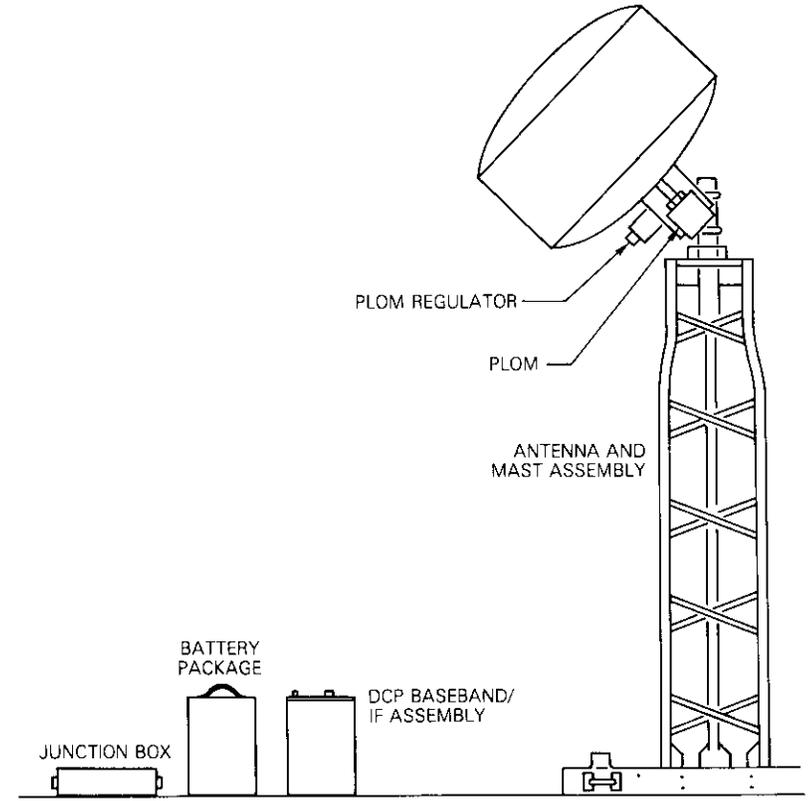
Figure 7. *DCP System*

is lined with RF absorbent material to reduce sidelobe radiation. The mast electronics consists of two packages: the phase-locked oscillator multiplier (PLOM) assembly, which is directly attached to the antenna waveguide feed, and the PLOM regulator assembly, which is attached to the antenna bracket and supplies DC power to the PLOM.

The baseband/IF assembly is packaged in an environmentally sealed canister and performs the interface, message formatting, and modulation functions. The battery pack assembly contains two 12-V, 20-Ah sealed rechargeable batteries configured to supply +24 VDC, and the interface assembly is used to connect the baseband/IF assembly to the sensors.

The DCPs are designed to interface with the specific sensor equipment used by the USGS for measuring water level and water quality. A Fisher &

TABLE 4. DCP TECHNICAL CHARACTERISTICS

Frequency	5950 MHz or 5970.5 MHz
Frequency Stability	$\pm 10^{-6}$/yr (all causes)
Frequency Jitter	100 Hz rms in 1 ms
RF Power Output	0.7 W
Antenna Diameter	1.2 m
e.i.r.p.	33.5 dBW
Bit Rate	1 kbit/s
Modulation	binary FSK
Frequency Deviation	± 750 Hz
Message Duration	244 ms
Information Bits per Message	64
Message Encoding	16-bit parity check
Overhead Bits	180
Sensor Sampling Rate	1, 2, or 4 per hour
Type of Sensors Interfaced	water level monitor and water quality monitor
Transmission Mode	unsynchronized RF bursts
Special Transmission Feature	optional repeated transmission
Temperature Range	$-25°C$ to $+50°C$

Porter Automatic Digital Recorder (ADR), which is used to measure water level, is a simple shaft-rotation input device capable of producing, on command, a punched hole, 4-place (16-bit) BCD word on paper tape. For telemetry applications, the machine is fitted with electrical output contacts which interface with the DCP. The water quality monitor (WQM) is a multichannel instrument for collecting various chemical and physical water data. Telemetry data are continuously available from the WQM analog voltage output port, which connects with an analog-to-digital converter within the DCP.

The interface function is controlled by a low-power C-MOS microprocessor, which also performs message formatting and encoding as well as various DCP housekeeping functions. A separate internal battery powers the microprocessor random access memory (RAM) so that the operating programs and parameters are preserved in case of temporary DCP battery failure. Because a microprocessor controls the data acquisition and transmission cycle, the DCP is adaptable to different sensors or operating modes.

A DCP internal timer regulates the sampling and transmission intervals. At the sampling instant, a reading is sequentially taken from all sensors connected to the DCP input and from the power supply line to measure the DCP battery voltage. The voltage is measured during transmission

under full load, digitally encoded, stored, and transmitted in the next message. While the WQM analog channels operate continuously, the ADRs are activated by the DCP shortly before the reading. These digital data are encoded, formatted, and transmitted immediately after the data acquisition cycle is completed. The time separation between consecutive sampling cycles is nominally 15, 30, or 60 min; however, a random delay of ± 1 min is added to prevent accidental time synchronization of two platforms. The repeated message is transmitted 5 min $\pm$ 10 s after the first transmission. The time randomizer is implemented by a pseudorandom number generator subroutine contained in the microprocessor software. The probability distribution of the random delay is uniform within the specified limits.

An RF output power of about 1 W and an antenna diameter of 1.2 m were selected for the DCP as the best compromise between transmitter power and antenna diameter, yielding the desired system transmission performance with minimum DCP cost and maximum battery life. Figure 8 shows the frequency bands and frequency multipliers of the DCP transmission system. The FSK modulator in the DCP radio consists of two 5-MHz temperature-compensated, voltage-controlled crystal oscillators. One oscillator is tuned to the DCP prime operating frequency, and the other, which can be remotely switched in using a special portable test set, is tuned to a preassigned backup frequency. The frequency is changed when a satellite transponder failure requires the traffic to be switched to a preassigned backup transponder.

The PLOM does not require mechanical tuning when it is switched from the prime operating frequency to the backup frequency. RF power amplification is performed at 1.5 GHz by a bipolar transistor amplifier, and the frequency is then multiplied up to 6 GHz. This method yields an overall DC/RF efficiency of about 10 percent as opposed to the 1- to 2-percent efficiency achievable with the 6-GHz amplifiers available when the DCPs were being designed.

The amplifier thermal design permits continuous transmission up to 50°C. The DC power is obtained from two 12-V, 20-Ah batteries. During the program, the batteries were replaced approximately every three months. At one U.S. site, a solar panel battery charging system was tested during the experimental program.

Each DCP monitors any RF power reduction, mechanical movement of the antenna (due to foreign objects striking the antenna), or fault which causes it to radiate a continuous carrier, instead of transmitting in the normal "burst type" mode. Continuous transmission would cause inter-
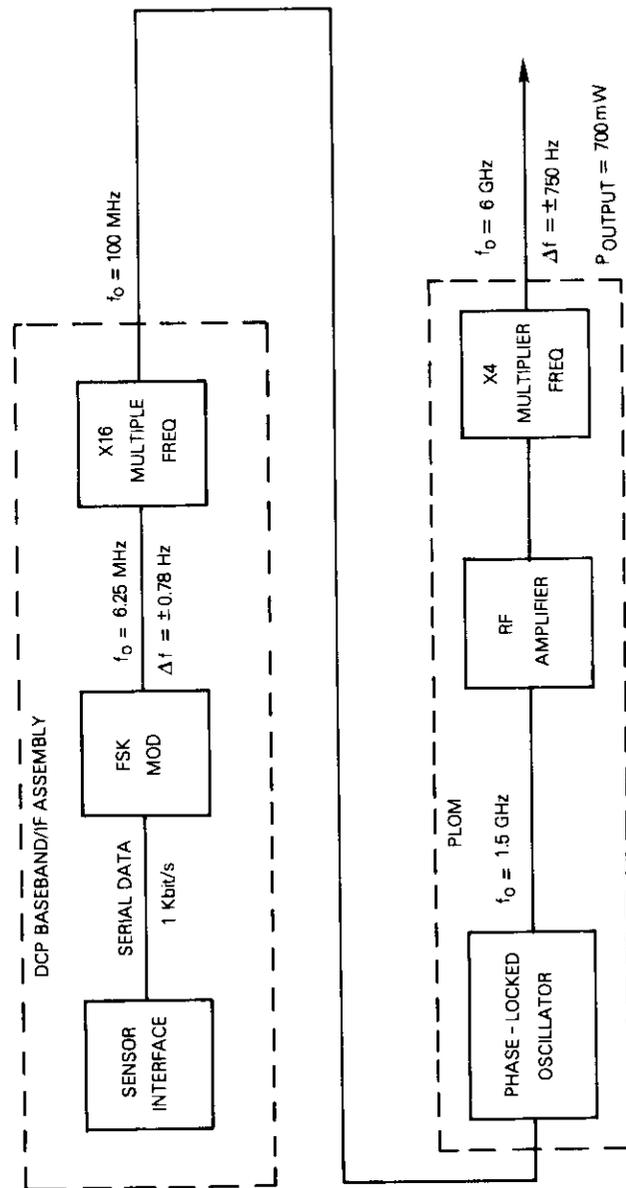
Figure 8. *Frequency Bands and Multiplication Stages in the DCP*

ference to the overall system. If any of these faults occur, however, the DCP will automatically shut off.

Three test sets and two portable pointing receivers were also procured. The test set is a portable unit used to load the operating program into the DCP RAM and to input selected values of the DCP operating parameters, *i.e.*, DCP identification, sampling time, number of sensors, single or repeated transmission mode, and standard or backup frequency selection. It is also used to display the contents of the DCP memory on a light-emitting diode (LED) read-out and to perform other monitoring functions. The pointing receiver consists of a low-noise receiver (LNR), which can be connected to the flange of the antenna feed, and an IF unit, which measures the level of a received 4-GHz beacon.

Receive earth stations

The Southbury receive station consists of an 11-m antenna, uncooled LNR, and associated down-converter equipment. The receive station configuration is shown in Figure 9, and the earth station terminal characteristics are listed in Table 5. The received 4-GHz DCP signal is down-converted to 70 MHz and fed to the data demodulator. Frequency un-

TABLE 5. SOUTHBURY DATA COLLECTION RECEIVE EARTH STATION RF TECHNICAL CHARACTERISTICS

Antenna Diameter	10 m
Pilot Carrier e.i.r.p.	50 dBW
Pilot Transmit Frequency	
Primary	5959.0 MHz
Backup	5979.5 MHz
Pilot Receive Frequency	
Primary	3734 MHz
Backup	3754.5 MHz
DCP Carrier Receive Frequency	
Primary	3725 MHz
Backup	3745.5 MHz
Up-Converter Frequency Stability	$\pm 1 \times 10^{-7}$/yr
Down-Converter Frequency Stability	$\pm 1 \times 10^{-7}$/yr
Receive Gain	50 dB
G/T	29.8 dB/K
Receive C/N_c	
DCP Carrier	46 dB-Hz (min.)
Pilot Carrier	62.5 dB-Hz (min.)

certainty due to the satellite oscillator long-term drift is removed by beating the frequency of the DCP signal with a reference pilot carrier, which is generated at 70 MHz, up-converted, transmitted to the satellite, and looped back to the same equipment. Figure 10 is a block diagram of the satellite frequency drift compensation system.

The DCRE, which includes all the hardware and software specifically designed for this operation by COMSAT Laboratories, consists of 70-MHz pilot generator, phase-lock loop pilot receiver, FSK data demodulator, monitor unit, minicomputer, and related software and peripheral equipment. Figure 11 is a block diagram of the DCRE, and Table 6 lists its major technical characteristics.

TABLE 6. DCRE TECHNICAL CHARACTERISTICS

Pilot Generator	
Frequency	70 MHz
Stability	
Long-Term	$\pm 1 \times 10^{-7}$/yr
Short-Term	> 1 Hz rms in 1 ms
Pilot Recovery Circuits	
Input C/N_o	62.5 dB-Hz (min.)
Allowed Frequency Offset from	
Nominal	23 kHz (max.)
Frequency Holding Capability	3 hr without input signal, $\leq \pm 200$-Hz variation
FSK Demodulator	
Bit Error Rate	
$C/N_o = 48$ dB-Hz	$> 1 \times 10^{-3}$
$C/N_o = 46$ dB-Hz	1×10^{-5}
$C/N_o = 43$ dB-Hz	1×10^{-2}
AFC Search Range	± 10 kHz
Probability of Missed Acquisition	10^{-5} at 44 dB-Hz
Minicomputer and Peripherals	
On-Line File Data Capacity	10 days of data
Data Retrieval Modes	4,800-baud synchronous line, 110-baud asychronous line

The demodulator down-converts the DCP carrier using the acquired pilot carrier as a reference signal, acquires the carrier frequencies, and demodulates the FSK DCP signals by a non-coherent FSK demodulator. The demodulated data and its bit timing and frame synchronization information are fed to the minicomputer input interface.

The monitor unit measures and displays the identification code of the message received and demodulated by the DCRE, carrier frequency, cumu-
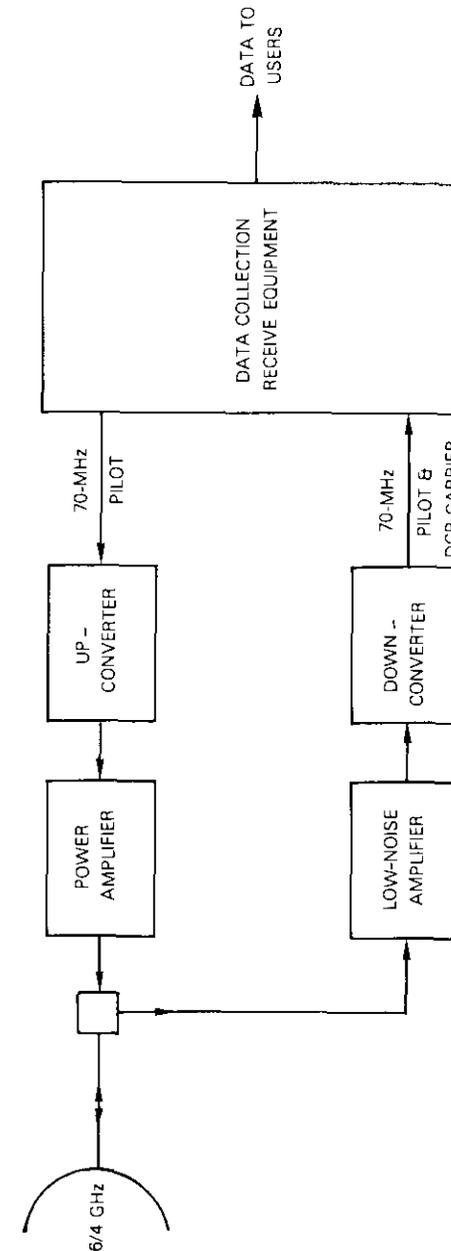
Figure 9. Southbury Data Collection Receive Earth Station Configuration

Δf = 23 kHz (MAXIMUM)

DCP FREQ = 5950 MHz

PILOT FREQ = 5959 MHz

DATA COLLECTION PLATFORM

DCP FREQ = 3940 + Δf
PILOT FREQ = 3949 + Δf

DCP FREQ = 61 MHz + Δf
PILOT FREQ = 70 MHz + Δf

PILOT FREQ = 70 MHz + Δf

PILOT RECOVERY CIRCUITS

DOWN-CONVERTER

DCP FREQ = 61 MHz + Δf

DCP FREQ = 9 MHz
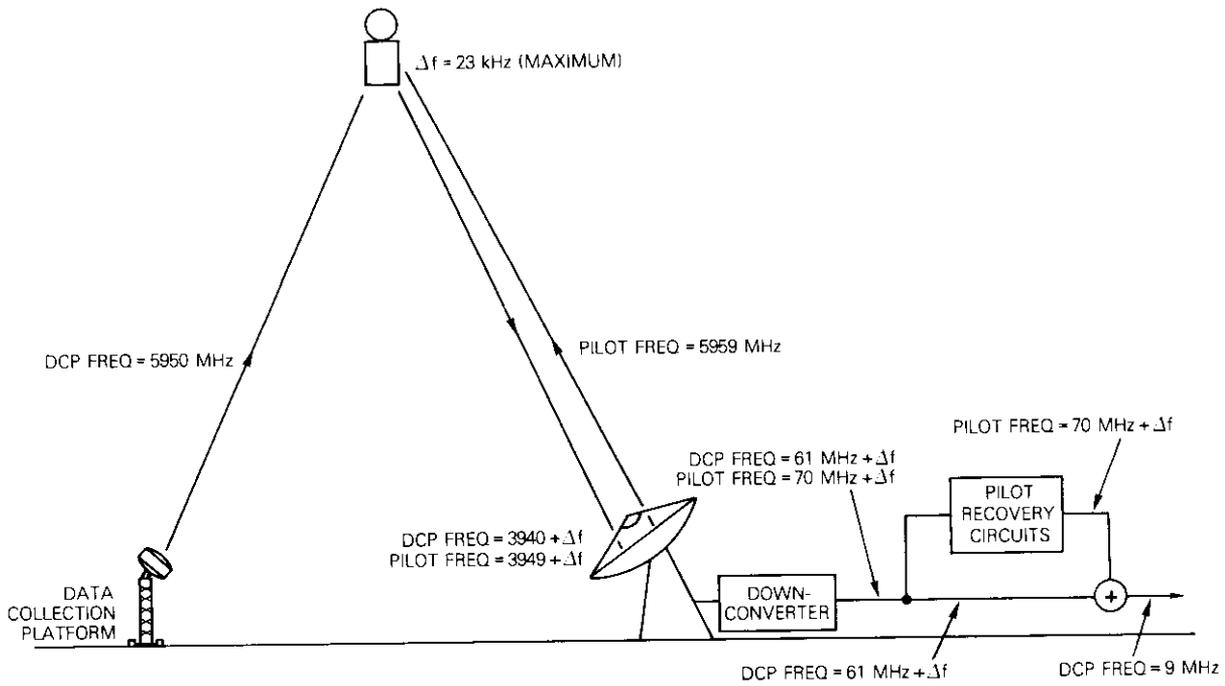
Figure 10. *Satellite Frequency Drift Compensation System*

TO UP-CONVERTER

PILOT GENERATOR (REDUNDANT)

FROM DOWN-CONVERTER

PILOT RECEIVER

DSK DEMOD

DATA
CLOCK
FRAME SYNC

E.S. INTERFACE

FRAME SYNC COUNT

DCP ID

DCP FREQ

PILOT FREQ

MONITOR UNIT

INTERFACE LOGICS

PHONE COMPANY INTERFACE

AUTO-CALL UNIT

HP 21 MX MINICOMPUTER

110-BAUD MODEM

DISC RECORDER

TTY

ALARM PANEL
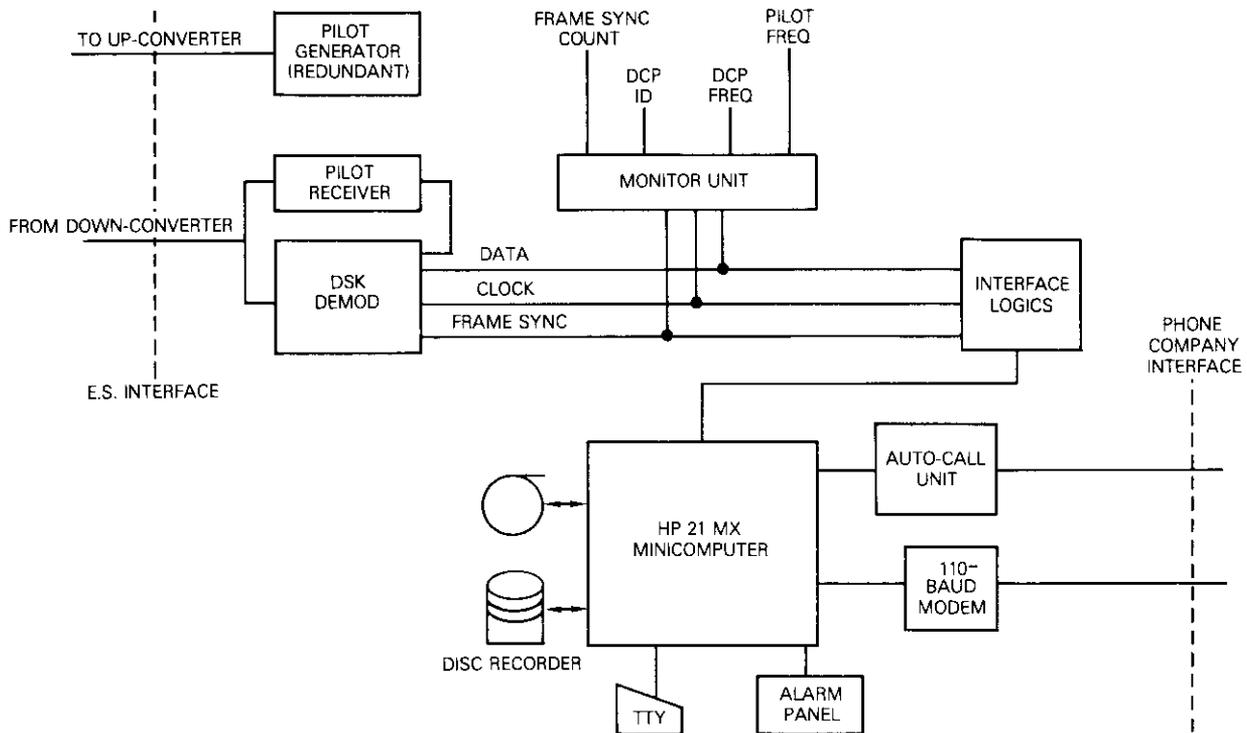
Figure 11. *DCRE Block Diagram*

lative received message count, and pilot carrier frequency in real time. When this unit is used in conjunction with a spectrum analyzer, the C/N_o ratio of each received DCP carrier burst can be evaluated.

The minicomputer performs the following functions:

   a. received data time tagging,

   b. data archival on magnetic tape file,

   c. error detection and data reduction,

   d. temporary data storage on discs for delivery on demand to the calling user terminal (via dial-up telephone line),

   e. system performance monitoring with alarm signals activated in case of detected failures,

   f. generation of system performance statistics,

   g. local processing of stored data,

   h. printing of the results on local or remote teletype.

Figure 12 is a typical system status report generated by the minicomputer and transmitted to a 110-baud portable terminal via a dial-up telephone line. For each DCP the following parameters are shown:

   a. identification,

   b. sampling interval (in minutes),

   c. transmission mode (single or double transmission),

   d. number of valid received messages (excluding redundant messages),

   e. number of expected messages,

```
PERIOD COVERED: FROM 126   0:  0 TO  23:57

1. DCP STATUS
```

DCP ID	SAMP TIME	DOUBLE TRANS.	# OF RCVD MESSAGES	# OF EXPCTD MESSAGES	ALARM ACTIVID	LAST BTRY VLTG	AVERAGE BTRY VTLG
1	60	YES	24	23	NO	24.5	24.6
2	15	YES	96	95	NO	24.9	25.0
3	15	YES	96	95	NO	24.3	24.4
4	15	YES	96	95	NO	23.4	23.4
5	15	YES	96	95	NO	24.5	24.6
6	15	YES	96	95	NO	22.7	32.7
7	30	YES	48	47	NO	23.9	24.0
8	15	YES	96	95	NO	24.0	25.8
9	15	YES	96	95	NO	27.0	25.8
10	30	YES	48	47	NO	23.8	23.8
11	60	YES	24	23	NO	24.0	24.0
12	60	YES	24	23	NO	23.9	23.9
13	15	YES	95	95	NO	25.5	25.5
14	15	YES	95	95	NO	24.4	24.4
15			NOT OPERATIONAL				

```
TOTAL # OF PARITY ERRORS:     13
```

Figure 12. *Computer Generated System Status Report*

   f. status of the DCP failure alarm flags (activated if more than three consecutive messages are missed),

   g. last reading of the battery voltage,

   h. average battery voltage from 0 hr (GMT) of the current day to time of status report request,

   i. number of received messages with detected parity errors.

The Canadian receive station, which is located at the Communications Research Centre (CRC), Department of Communications, at Shirley's Bay near Ottawa, consists of an 8-m-diameter antenna provided by the CRC, an LNR provided by Telesat, and the DCRE provided by COMSAT GENERAL. This equipment is housed in a small Telesat shelter and is normally unmanned. The signal processing is identical to that of the Southbury earth station except that this station is not equipped with a magnetic tape recorder. The link calculations are summarized in Table 2.

Frequency sharing considerations

The 5925- to 6425-MHz frequency band used by the data collection system is allocated to the fixed service (terrestrial radio links) and to the fixed satellite service (communications satellites). A major objective of the data collection developmental program was to demonstrate that a fully developed system can coexist with other services sharing the same frequency band without introducing excessive interference with these services or significantly constraining the planning and development of new ones.

Adjacent satellite interference

Interference has been calculated for the case in which the data collection system interferes with adjacent satellites, and for the reciprocal case in which an adjacent satellite interferes with the data collection system. The system parameters used for the calculations are listed in Table 7, and the results for the first case are summarized in Table 8.

The procedure for combining the interference contributions from the various DCPs is as follows. DCPs operate for a small percentage of time. Figure 13, which gives the probability of N simultaneous DCP transmissions vs the number of simultaneous transmissions N, evidences that the probability of exceeding 15 simultaneous transmissions from a population of 10,000 DCPs is about 1 percent (curve B). In the calculation of the number of picowatts of interference, 15 simultaneous transmissions have been assumed for all but two cases. The DCPs that transmit simultaneously

TABLE 7. DATA COLLECTION SYSTEM PARAMETERS

Data Collection Platform (up-link)
Frequency	5425–6425 MHz
Transient e.i.r.p.	33.5 dBW
Antenna Gain (peak)	35 dB
Off-Axis Antenna Gain	$32 - 25 \log \sigma$
Transmit Power	0.7 W
Burst Length	250 ms
Transmission Rate	2 bursts/15 min
No. of DCPs (fully developed system)	10,000
Multiple-Access Scheme	random-access TDMA/FDMA
Total No. of DCP Carriers	50

Satellite
Existing Domestic Satellite Down-Link e.i.r.p. (reference value)	−7.5 dBW

Receive Station (down-link)
Frequency	3700–4200 MH
G/T	30 dB/K

System
C/N_0 for Received DCP Carrier (1-kHz BW)	16 dB (min.)
Allowed Carrier-to-Interference Ratio, C/I (1-kHz BW)	25 dB

will generally use several of the 50 frequency channels assigned to the system. For the calculations, it has been assumed that only one frequency channel will be used and that its frequency will cause the desired carrier to experience the maximum amount of interference. However, for the two (108- and 12-channel) narrowband carriers, it has been assumed, more realistically, that only one-third of the 15 interfering bursts will be located at a frequency which will contribute significantly to the total interference. The K factor (which relates baseband noise to C/I and depends upon the desired and interfering spectrum shapes) for these carriers has been assumed to equal the worst possible value. Other conservative assumptions for the calculation are 3.8° satellite spacing (4° − 0.2° due to orbital position instability), and 0-dB cross-polarization isolation between the interfering and desired signals.

The results of the interference calculations in Table 8 demonstrate that a fully developed data collection system does not cause a significant amount of interference with adjacent satellites. Interference from other satellite systems into the data collection system was also calculated. The results show that about 90 percent of the 500-MHz satellite frequency band can be shared by the data collection system without any significant transmis-

TABLE 8. INTERFERENCE FROM THE DATA COLLECTION SYSTEM INTO OTHER DOMESTIC SATELLITE SYSTEMS [a]

Desired System	Modulation Index	Receive Antenna Diameter (m)	C/I (dB)			K-Factor [b] (dB)	Noise Power (pWOp)
			Up-Link	Down-Link	System Total		
1,200 Channels	0.457	30	70.6	83.9	70.4	−6.9	90
900 Channels	0.736	30	63.4	77.9	63.2	5.1	30
360 Channels	1.174	10	62.3	71.7	61.8	12.2	15
108 Channels	0.9	8	54.0	63.0	53.5	8.6	65
12 Channels	3.1	30	44.0	64.0	44.0	24.1	60

[a] Noise reduction due to cross polarization isolation is not considered. A 3.80° spacing between adjacent satellites is assumed.

[b] K-factor corresponds to location of all data collection system carriers at a separation equal to the top baseband frequency of the desired carrier (worst case). Fifteen data collection system carriers were assumed except for the case of the 109- and 12-channel carriers, in which five data collection system carriers were assumed (see text). Note that the C/I values are given for one data collection system carrier; 15 or 5 data collection system carriers are assumed to calculate the noise power.
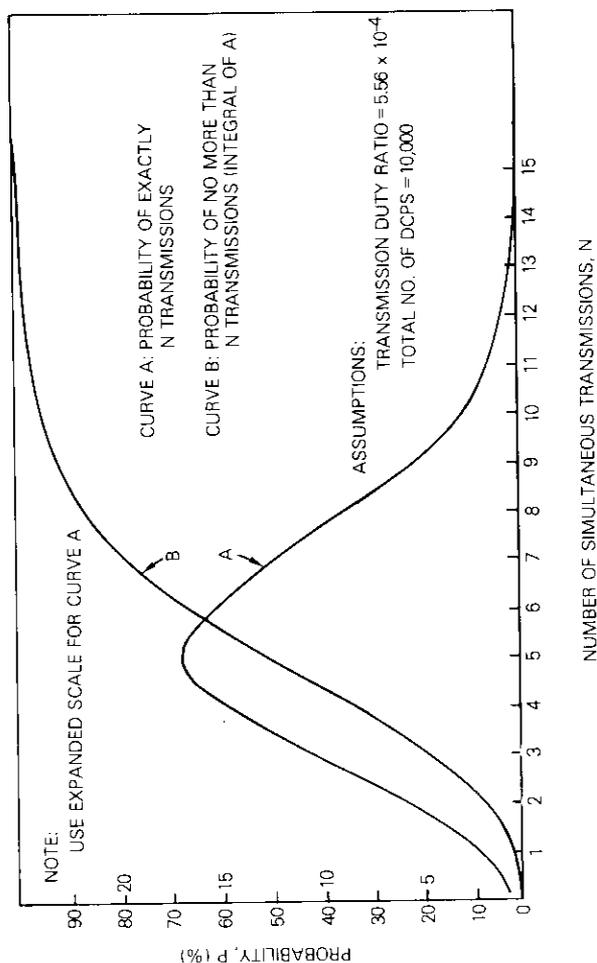
Figure 13. *Probability of Simultaneous DCP Transmissions*

sion performance degradation. Typical transmissions include carriers with very high levels of concentrated power, *e.g.*, the transmission of an all white TV picture. The DCP carriers must avoid these portions of the spectrum, which constitute about 10 percent of the 5925- to 6425-MHz frequency band.

Frequency sharing with terrestrial radio links

The formula given in part 25 of *FCC Rules and Regulations*, which imposes constraints on the interference caused by an earth station to an existing radio link, is based upon the following interference criterion:

 a. long-term interference noise: 250 pW0p (not to be exceeded for more than 20 percent of the time),

 b. short-term interference: 50,000 pW0p (not to be exceeded for more than 0.0025 percent of the time).

These interference objectives are derived from C.C.I.R. recommendations (1,000 pW0p of long-term interference, and 50,000 pW0p for no more than 0.01 percent of the time) and from a model that assumes four earth stations interfering with a long-haul terrestrial radio link.

A DCP can be regarded as an earth station with special characteristics, including extremely low transmission duty ratio, narrowband signal, and a potentially large number of deployed DCPs. The same interference criterion adopted in part 25 for a domestic satellite earth station (*i.e.*, 250 pW0p and 50,000 pw0p of long- and short-term interference, respectively) can be adopted for a DCP, since the very low transmission duty ratio compensates for the large number of DCPs that could be deployed.

A conservative model with a large number (10,000) of DCPs deployed over the U.S. is assumed. One-tenth or 1,000 of the DCPs are within coordination distance of a given long-haul radio link. Each DCP will be coordinated to meet the 250- and 50,000-pW0p interference constraints. In addition, the following worst-case situation is assumed:

$$\text{transmission rate} = 2 \text{ bursts/15 min}$$
$$\text{burst duration} = 250 \text{ ms}$$

or

$$\text{duty ratio} = \frac{0.250}{7.5 \times 60} = 5.56 \times 10^{-4} \quad .$$

The probability that more than one DCP will be simultaneously transmitting, which is obtained by assuming a binomial distribution model, is

$$P = 1 - (1 - d)^N - Nd (1 - d)^{N-1} = 10.8\% \qquad (1)$$

where d is the *DCP* duty ratio and N is the total number of interfering DCPS (assumed to be 1,000). Since P is less than 20 percent, simultaneous DCP transmissions should be ignored when long-term interference noise is being considered. In terms of long-term interference, only one DCP from the entire network will be active at any one time; therefore, the same long-term interference criterion used for domestic earth stations (*i.e.*, 250 pW0p) is justified.

For a short-term interference model, it has been assumed that each of the 1,000 DCPs which are capable of interfering with a given radio link has been frequency coordinated to yield no more than 50,000 pW0p for no more than 0.0025 percent of the time. Each DCP is assumed to contribute exactly 50,000 pW0p for exactly 0.0025 percent of the time. The percentage of the time for which the total interference noise equals 50,000 pW0p is given by the sum of the percentages of time for each DCP:

$$P_s = Nd(0.0025) = 1,000 \times 5.6 \times 10^{-4} \times 0.0025 = 0.0012\% \quad . \quad (2)$$

The term $d \times 0.0025$ in equation (2) can be regarded as the actual percentage of time that the single DCP contributes 50,000 pW0p of interference. (The value for continuous transmission will be 0.0025 percent while the transmission duty cycle is actually d.) It can be concluded from equation (2) that, since the total percentage of time P_s is less than 0.0025 percent, the short-term criterion of part 25 is satisfied.* Therefore, the interference criterion of 250- and 50,000-pW0p long- and short-term interference established for domestic earth stations also applies to the DCP.

The computation procedure for coordinating the DCPs with terrestrial radio links is as follows. Part 25 assigns the maximum interference power density injected in a radio link repeater, *i.e.*, −154 dBW/4 kHz (long term) and −131 dBW/4 kHz (short term). These values of interference power density are derived by assuming the 250/50,000-pW0p long-term/short-term criterion and the worst type of interfering signal. The formulas are correct for a wideband flat spectrum type of signal, but impose an excessive restriction on narrowband carriers such as those transmitted by the DCPs. A total of fifty 3-kHz-bandwidth carriers will be required for

---

* More than 50,000 pW0p of interference could be also obtained when 200 DCPS contributing 250 pW0p transmit simultaneously. However the probability of this event occurring is about 10^{-18}.

a fully developed data collection system, resulting in a total bandwidth occupancy of 150 kHz or 0.03 percent of the 500-MHz band assigned to the terrestrial links operating at 6 GHz. Therefore, carrier frequencies that do not cause maximum interference with the terrestrial links can easily be selected. In FM transmission, baseband interference noise is proportional to the K-factor, which is obtained by convolving the spectrum of the interfering carrier with the spectrum of the desired carrier. A special computer program computes K-factor vs frequency separation using the DCP signal interfering carrier and three typical radio link carriers as desired carriers.

The K-factor plots and the modulation parameters of the three radio link carriers are given in Figures 14–16. These figures show that K is always greater than zero if the interfering carrier frequency is outside a band not wider than 3 MHz, whose center is displaced from the carrier center frequency by an amount equal to the top baseband frequency. Therefore, K is assumed to equal 0 in the DCP interference calculations.

A simple interference model based upon a typical radio link hop in which a DCP is interfering with a repeater will be used to determine the "restricted" area around the repeater where the DCP cannot be located if the 250-pW0p long-term interference criterion is to be satisfied. It is assumed (and proven by the results of the calculations) that this locus of points of equal interference is contained within a 20- to 25-km circle around the repeater, and that the long-term interference is the controlling factor. The geometry of this interference model is shown in Figure 17. The radio link has conservatively been assumed to run parallel to the DCP-to-satellite signal path (in azimuth). Other assumptions are as follows:

    a. 33.5-dBW DCP e.i.r.p.,

    b. 35-dB DCP antenna main beam gain,

    c. 53-dBW radio link e.i.r.p.,

    d. 43.1-dB radio link receive antenna (horn type) gain,

    e. $32 - 25 \log \sigma$ off-axis radiation pattern for both the radio link and DCP antenna,

    f. no cross-polarization advantage.

With these assumptions, the locus of points for which the noise injected by the DCP into the radio link repeater receiver is equal to 250 pW0p can be computed. Figure 18, which plots the results, shows that the restricted area (the area for which all internal points, if regarded as DCP sites, correspond to an interference level higher than the maximum limit assumed) is an elongated strip less than 1.2 km long with an average width of less than 45 m. If a more stringent interference constraint were adopted
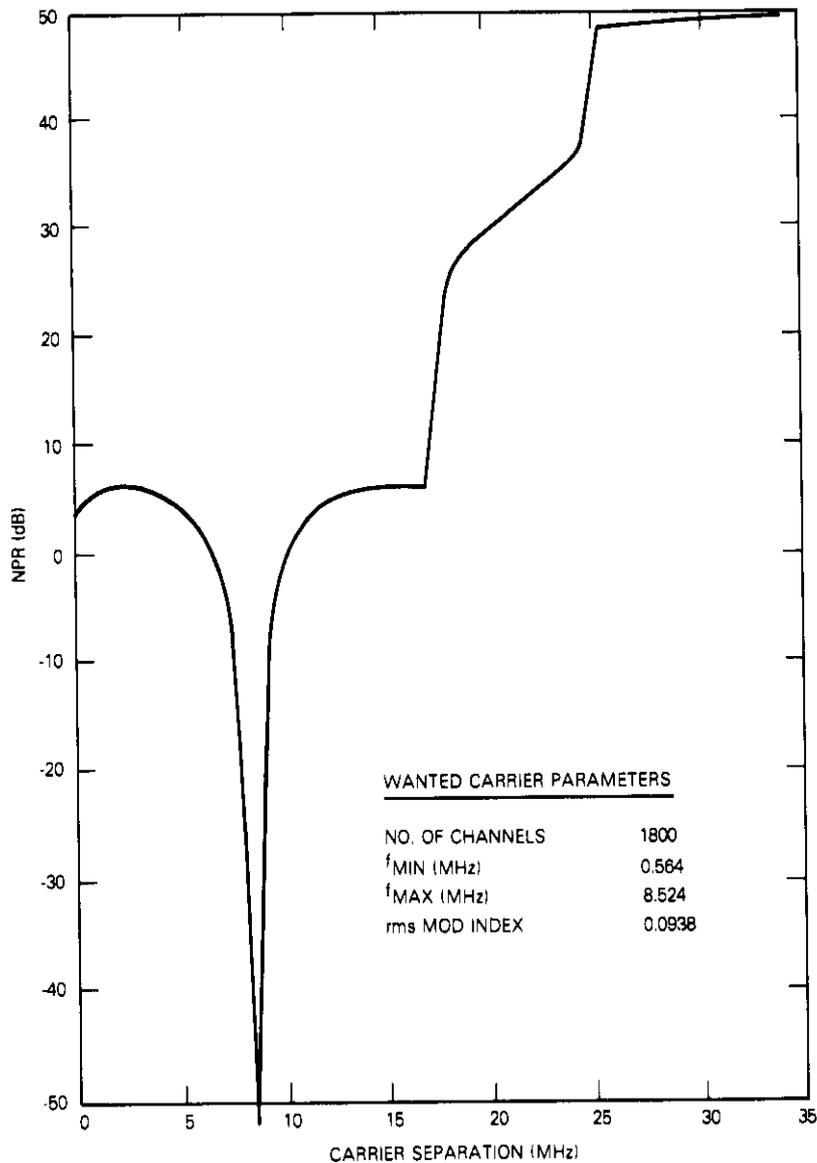
Figure 14. *NPR of Top Baseband Channel (K-factor) vs Carrier Separation*
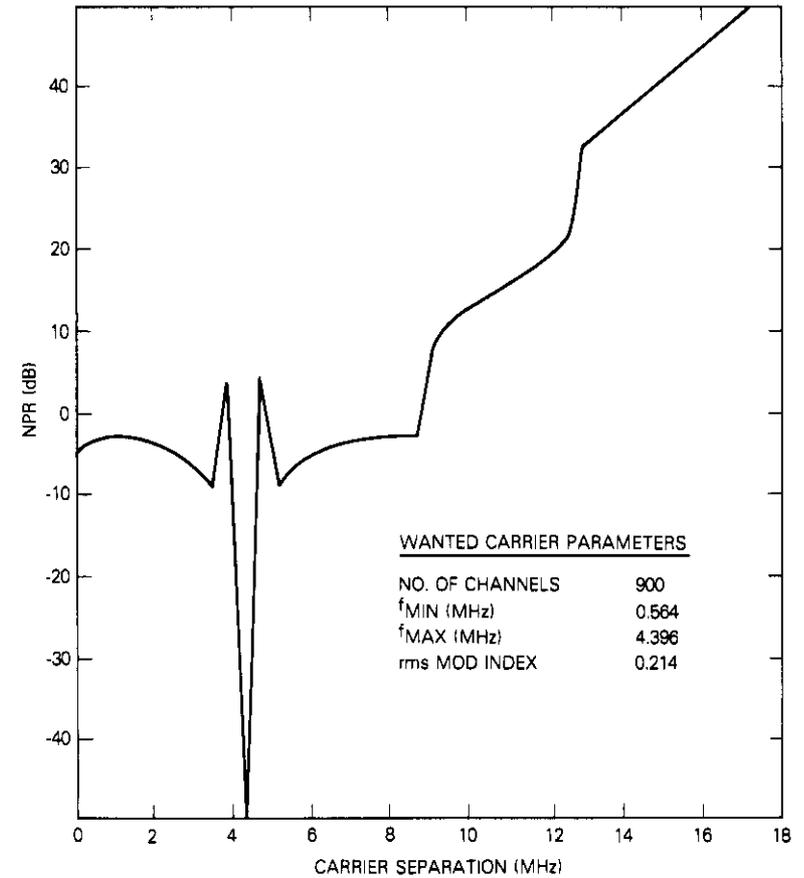
Figure 15. *NPR of Top Baseband Channel (K-factor) vs Carrier Separation*

(*e.g.*, a maximum limit of 5 pW0p), the size of the restricted area would be approximately 8 km by 320 m, which does not seriously limit DCP deployment.

Although the results of this analysis are only representative, they indicate that coordination of the DCP with existing radio links is not a problem for the data collection system and that satisfactory frequency coordination should be possible for a majority of DCP sites. For further confirmation, great circle frequency coordination was accomplished for 10 DCP locations in an area of the U.S. (New England), which has a very high density of radio link routes. On the basis of the −154/−131-dBW/4-kHz criterion,

Figure 16. *NRP of Top Baseband Channel (K-factor) vs Carrier Separation*

a. *Horizontal View*

b. *Vertical View*
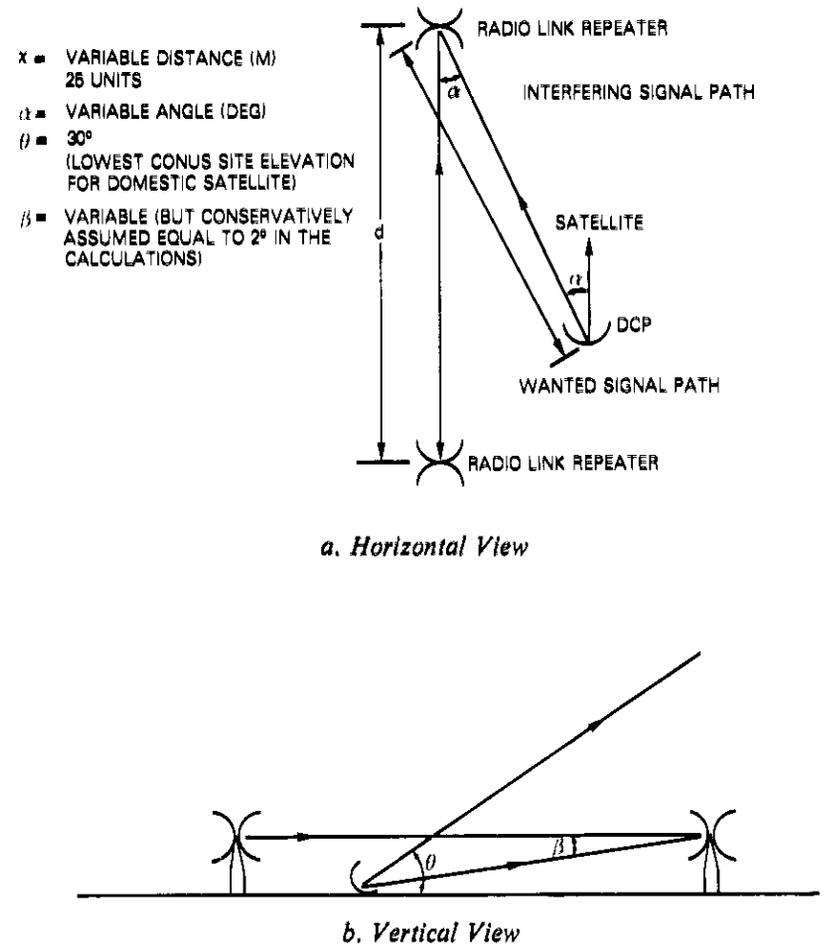
Figure 17. *Interference Model Geometry*

it was determined that 70 percent of the sites could be coordinated when the actual path profile loss was included in the computation of propagation loss.

Frequency sharing with existing radio links is not a difficult problem; however, it is possible that a DCP in a critical location may affect the planning of a new or modified radio link, thereby increasing construction costs. Therefore, the data collection system should be given the status of a secondary service so that the DCP would be either relocated or its transmission frequency would be changed.

Conclusions

The developmental data collection program has successfully demonstrated that this unique service utilizing low bit rates and low-cost terminals can operate with existing commercial communications satellites. The program proved the viability of a 6-GHz DCP, a multi-user data distribution system based on both scheduled and on-demand real-time and batch-mode data retrieval, automatic central monitoring of the system status, and coexistence with other services (commercial satellite and terrestrial systems) using the same frequency bands.

Acknowledgment

Figure 18. *Locus of Equal Interference Points*

GianPiero Forcina graduated from the University of Rome in electrical engineering in 1965 and performed post-graduate work at the George Washington University in Washington, D.C. He was engaged in circuit development at Marconi, England, and satellite systems design at Telespazio, Rome, Italy. From 1970 to 1972 he was an INTELSAT *nominee at* COMSAT *Laboratories, assigned to the Systems Laboratory. He subsequently became involved in satellite simulation analysis at Fairchild Space and Electronics Company. In 1974 he joined* COMSAT GENERAL, *where he has been concerned with the development of new satellite applications. He is presently Manager of Remote Monitoring Systems Development.*

Kenneth F. Manning received a B.S. degree from the University of Southampton, England, and an M.S. degree from McGill University, Canada. Since joining COMSAT *in 1967, he has been involved with the system design of* INTELSAT III and IV, *the U.S. domestic satellite systems, and the data collection developmental programs. Presently, he directs* COMSAT GENERAL *programs for the communications satellite system to serve the Arab states. Prior to joining* COMSAT, *he was involved with the development of attitude control systems for low-altitude orbit satellites.*

Kiran J. Singh is a Senior Staff Engineer in the ARABSAT *Program Office in* COMSAT GENERAL. *He is presently responsible for the satellite system definition, traffic forecasting, and economic feasibility studies in the* ARABSAT *system. He has also been involved in system design and analysis of Remote Monitoring Systems using satellites, and land-mobile satellite systems. Prior to joining* COMSAT *in 1975, he was a System Engineer at RCA GlobCom, responsible for the design of satellite digital communications. He received an M.S. in 1972 from State University of New York at Stony Brook.*

Tabulations of raindrop induced forward and backward scattering amplitudes

D. J. FANG AND F. J. LEE

Abstract

Rain induced attenuation and depolarization are important factors in the design of satellite-earth and terrestrial microwave communications systems. Computations of these two quantities from purely theoretical considerations require the forward scattering amplitudes (FSAS) of raindrops. FSAS are tabulated for a wide range of frequencies (4, 6, 8, 11, 14, 19, 24, 28, 30, and 33 GHz) and propagation zenith angles ($\psi = 90°, 75°, 60°, 45°, 30°,$ and $15°$). An example which demonstrates the use of FSAS in evaluating attenuation and phase shift is also presented. In addition, the backward scattering amplitudes (BSAS) are tabulated for the same frequencies and propagation angles. These data, unavailable in the literature, may be used to perform multiple scattering analyses, radar backscattering calculations, and common volume interference evaluations, all of which have become increasingly important in propagation studies.

Background

For the design of satellite-earth and terrestrial microwave communications systems, rain induced attenuation and depolarization must be calcu-

lated. These two quantities can be computed from purely theoretical considerations, as shown in Figure 1 where $f_H(\psi)$ and $f_V(\psi)$ are defined in References 1 through 4, using the FSA of raindrops. Since presently avail-
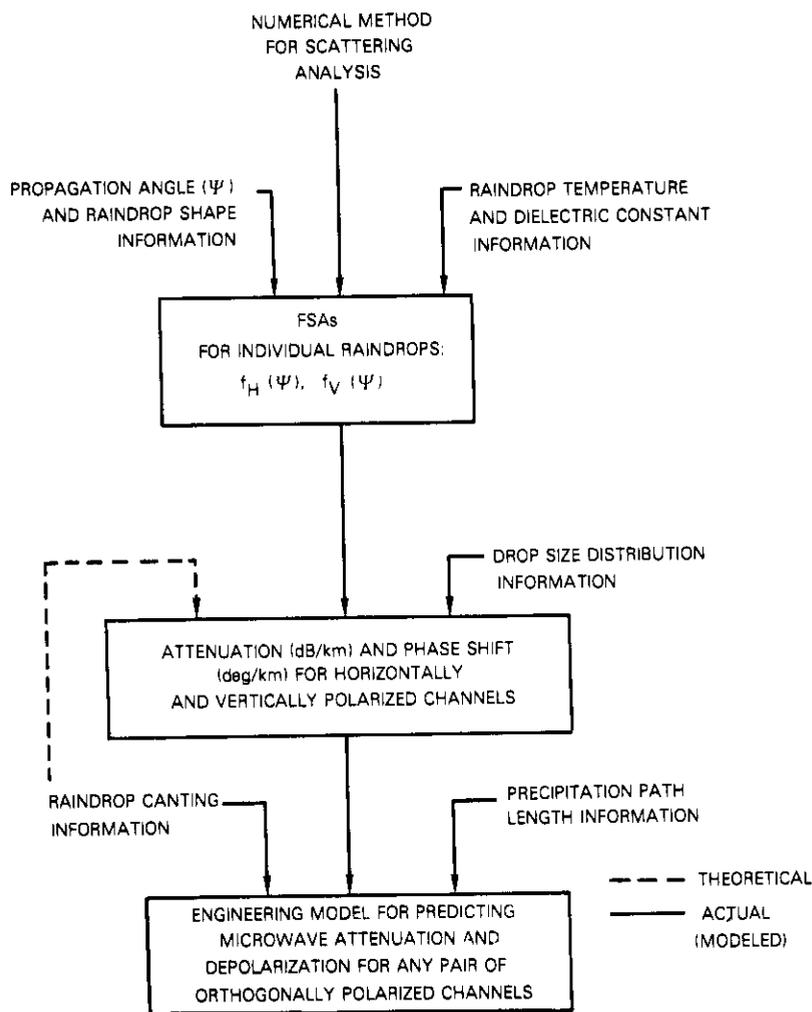
Figure 1. *Flow Diagram for Establishing Engineering Models for Microwave Attenuation and Depolarization Studies*

able calculated FSA values are limited [1]-[3], [5], the engineering models generated from these values are also limited.

Because of the importance of FSA availability, the following factors were investigated:

    a. accuracy and computation economy of various numerical methods for scattering analysis;

    b. geometrical representations describing the raindrop shape for different drop sizes;

    c. formulas for the evaluation of dielectric constants and the appropriate drop temperature.

The results indicated that the unimoment method [6], [7] for scattering analysis, the Pruppacher and Pitter [8] representation of raindrops, a temperature of 10°C, and Ray's equation [9] for dielectric constants were suitable bases for the computations.

The theoretical analysis and the computer program were developed by an outside contractor. The basic approach and essential equations are summarized in Appendix A. (A more detailed documentation of the methodology will be published subsequently.) Appendix B compares and checks the FSA results generated by the unimoment method and by Oguchi [2] at 11 and 19.3 GHz. After the program was improved, batch runs of FSA were performed using the IBM 360/65 computer at COMSAT Laboratories. Tabulations of FSA (*i.e.*, the quantities f_H and f_V given in References 1 through 4) are presented in Tables 1 through 60 for a wide range of frequencies and propagation angles, where ψ is the angle between the symmetry axis of the raindrop and the normal to the incident wavefront. Appendix C presents an example which uses the FSAS to evaluate attenuation and phase shift. The BSAS, which are also tabulated for the same frequencies and propagation angles, may be used to perform multiple scattering analyses, radar backscattering calculations, and common volume interference evaluations.

In summary, these tabulations of raindrop scattering amplitudes should be valuable for modeling microwave-precipitation phenomena for applications in satellite-earth and terrestrial communications, interference calculations, and radar scattering problems. Although these tabulations are presently being modeled by analytic functions, the task is complicated and the results are not yet available. Figure 2 is a plot of the scattering amplitudes for a 2-mm raindrop at 10°C propagating at an angle of 45°.

TABLE 1. FORWARD AND BACKWARD SCATTERING AMPLITUDES
AT $T = 10°C$, $f = 4$ GHz, AND $\alpha = 90°$

| Raindrop Radius (mm) | Forward Scattering | | | | Backward Scattering | | | |
| | Vertical Polarization | | Horizontal Polarization | | Vertical Polarization | | Horizontal Polarization | |
	Real	Imaginary	Real	Imaginary	Real	Imaginary	Real	Imaginary
0.25	1.0548e-7	-1.2391e-9	1.0578e-7	-1.2462e-9	1.0524e-7	-1.1693e-9	1.0555e-7	-1.1762e-9
0.50	8.3908e-7	-1.0630e-8	8.5390e-7	-1.0988e-8	8.3153e-7	-8.3659e-9	8.4650e-7	-8.6911e-9
0.75	2.8056e-6	-4.0208e-8	2.9286e-6	-4.3374e-8	2.7480e-6	-2.2629e-8	2.8688e-6	-2.5099e-8
1.00	6.5683e-6	-1.1101e-7	7.1107e-6	-1.2650e-7	6.3229e-6	-3.4582e-8	6.8478e-6	-4.4161e-8
1.25	1.1812e-5	-2.3923e-7	1.4130e-5	-3.2021e-7	1.1354e-5	-2.0674e-8	1.3299e-6	-5.0578e-8
1.50	2.0481e-5	-5.1445e-7	2.5478e-5	-7.2400e-7	1.9088e-5	5.7946e-8	2.3256e-5	2.9021e-8
1.75	3.2794e-5	-1.0436e-6	4.2495e-5	-1.5488e-6	2.9397e-5	2.9227e-7	3.7279e-5	3.2109e-7
2.00	4.9660e-5	-2.0290e-6	6.7053e-5	-3.1914e-6	4.2406e-5	8.4041e-7	5.5901e-5	1.1056e-6
2.25	7.2253e-5	-3.8242e-6	1.0143e-4	-6.4081e-6	5.8107e-5	1.9862e-6	7.9248e-5	2.9654e-6
2.50	1.0178e-4	-6.9815e-6	1.4887e-4	-1.2706e-5	7.5743e-5	4.2843e-6	1.0708e-4	7.1440e-6
2.75	1.4050e-4	-1.2690e-5	2.1381e-4	-2.5364e-5	9.5428e-5	8.6613e-6	1.3828e-4	1.6472e-5
3.00	1.9073e-4	-2.2974e-5	3.0178e-4	-5.1584e-5	1.1571e-4	1.6990e-5	1.7102e-4	3.7490e-5
3.25	2.5551e-4	-4.1775e-5	4.1724e-4	-1.0801e-4	1.3504e-4	3.2911e-5	2.0529e-4	8.5780e-5
3.50	3.1576e-4	-8.3113e-5	5.4831e-4	-2.1876e-4	1.4889e-4	5.0302e-5	2.5819e-4	1.8300e-4

TABLE 2. FORWARD AND BACKWARD SCATTERING AMPLITUDES
AT $T = 10°C$, $f = 4$ GHz, AND $\alpha = 75°$

| Raindrop Radius (mm) | Forward Scattering | | | | Backward Scattering | | | |
| | Vertical Polarization | | Horizontal Polarization | | Vertical Polarization | | Horizontal Polarization | |
	Real	Imaginary	Real	Imaginary	Real	Imaginary	Real	Imaginary
0.25	1.0550e-7	-1.2396e-9	1.0578e-7	-1.2462e-9	1.0526e-7	-1.1697e-9	1.0555e-7	-1.1763e-9
0.50	8.4008e-7	-1.0653e-8	8.5402e-7	-1.0988e-8	8.3253e-7	-8.3705e-9	8.4637e-7	-8.7176e-9
0.75	2.8138e-6	-4.0397e-8	2.9286e-6	-4.3351e-8	2.7962e-6	-2.2549e-8	2.8689e-6	-2.5519e-8
1.00	6.6040e-6	-1.1185e-7	7.1101e-6	-1.2630e-7	6.3589e-6	-3.3837e-8	6.8485e-6	-4.6821e-8
1.25	1.1962e-5	-5.3789e-7	1.4124e-5	-6.1483e-7	1.1481e-5	-2.5930e-7	1.3295e-5	-3.1482e-7
1.50	2.0801e-5	-9.0217e-7	2.5463e-5	-1.1000e-6	1.9376e-5	-2.3161e-7	2.3263e-5	-3.4027e-7
1.75	3.3405e-5	-1.5093e-6	4.2458e-5	-1.9871e-6	2.9986e-5	-2.7953e-8	3.7320e-5	-1.2429e-7
2.00	5.0733e-5	-2.5528e-6	6.6961e-5	-3.6495e-6	4.3413e-5	5.1676e-7	5.6027e-5	5.3780e-7
2.25	7.4000e-5	-4.3815e-6	1.0123e-4	-6.8135e-6	5.9820e-5	1.6922e-6	7.9558e-5	2.2184e-6
2.50	1.0445e-4	-7.4964e-6	1.4840e-4	-1.2851e-5	7.8436e-5	4.1520e-6	1.0772e-4	6.1803e-6
2.75	1.4445e-4	-1.3240e-5	2.1287e-4	-2.5088e-5	9.9479e-5	8.6117e-6	1.3958e-4	1.4897e-5
3.00	1.9638e-4	-2.3563e-5	3.0002e-4	-5.0294e-5	1.2162e-4	1.7065e-5	1.7355e-4	3.4742e-5
3.25	2.6330e-4	-4.2426e-5	4.1432e-4	-1.0429e-4	1.4347e-4	3.3171e-5	2.0991e-4	8.0490e-5
3.50	3.2696e-4	-6.3689e-5	5.4403e-4	-2.0886e-4	1.6124e-4	5.5324e-5	2.6343e-4	1.7320e-4

TABLE 3. FORWARD AND BACKWARD SCATTERING AMPLITUDES
AT $T = 10°C$, $f = 4$ GHz, AND $\alpha = 60°$

| Raindrop Radius (mm) | Forward Scattering | | | | Backward Scattering | | | |
| | Vertical Polarization | | Horizontal Polarization | | Vertical Polarization | | Horizontal Polarization | |
	Real	Imaginary	Real	Imaginary	Real	Imaginary	Real	Imaginary
0.25	1.0555e-7	-1.2409e-9	1.0578e-7	-1.2462e-9	1.0532e-7	-1.1710e-9	1.0555e-7	-1.1764e-9
0.50	8.4280e-7	-1.0715e-8	8.5401e-7	-1.0985e-8	8.3526e-7	-8.4330e-9	8.4639e-7	-8.7458e-9
0.75	2.8361e-6	-4.0914e-8	2.9284e-6	-4.3288e-8	2.7785e-6	-2.3069e-8	2.8692e-6	-2.5984e-8
1.00	6.7017e-6	-1.1415e-7	7.1085e-6	-1.2577e-7	6.4570e-6	-3.6213e-8	6.8505e-6	-4.9681e-8
1.25	1.2366e-5	-8.2372e-7	1.4104e-5	-8.8680e-7	1.1832e-5	-4.9873e-7	1.3290e-5	-5.6402e-7
1.50	2.1663e-5	-1.3794e-6	2.5411e-5	-1.4415e-6	2.0159e-5	-5.3879e-7	2.3283e-5	-6.5723e-7
1.75	3.5052e-5	-1.9748e-6	4.2330e-5	-2.3638e-6	3.1514e-5	-4.0489e-7	3.7423e-5	-5.7603e-7
2.00	5.3818e-5	-3.0993e-6	6.6866e-5	-3.9901e-6	4.6211e-5	6.5523e-8	5.6335e-5	-8.7175e-8
2.25	7.8695e-5	-5.0029e-6	1.0059e-4	-8.9741e-6	6.4423e-5	1.1498e-6	8.0300e-5	1.2824e-6
2.50	1.1170e-4	-9.1478e-6	1.4704e-4	-1.2464e-5	8.5707e-5	3.5544e-6	1.0927e-4	4.6741e-6
2.75	1.5517e-4	-1.4037e-5	2.1030e-4	-2.3581e-5	1.1036e-4	7.7836e-6	1.4270e-4	1.2088e-5
3.00	2.1170e-4	-2.4572e-5	2.9507e-4	-4.6097e-5	1.3737e-4	1.5880e-5	1.7938e-4	2.9013e-5
3.25	2.8480e-4	-4.3763e-5	4.0613e-4	-9.3976e-5	1.6568e-4	3.1440e-5	2.1979e-4	6.7987e-5
3.50	3.5800e-4	-6.5427e-5	5.3270e-4	-1.8220e-4	1.9409e-4	5.2392e-5	2.7951e-4	1.4619e-4

TABLE 4. FORWARD AND BACKWARD SCATTERING AMPLITUDES
AT $T = 10°C$, $f = 4$ GHz, AND $\alpha = 45°$

| Raindrop Radius (mm) | Forward Scattering | | | | Backward Scattering | | | |
| | Vertical Polarization | | Horizontal Polarization | | Vertical Polarization | | Horizontal Polarization | |
	Real	Imaginary	Real	Imaginary	Real	Imaginary	Real	Imaginary
0.25	1.0563e-7	-1.2426e-9	1.0578e-7	-1.2461e-9	1.0540e-7	-1.1728e-9	1.0555e-7	-1.1764e-9
0.50	8.4652e-7	-1.0801e-8	8.5400e-7	-1.0980e-8	8.3899e-7	-8.5438e-9	8.4640e-7	-8.7715e-9
0.75	2.8666e-6	-4.1619e-8	2.9281e-6	-4.3202e-8	2.8091e-6	-2.4155e-8	2.8695e-6	-2.6363e-8
1.00	6.8352e-6	-1.1728e-7	7.1064e-6	-1.2503e-7	6.5910e-6	-4.1733e-8	6.8531e-6	-5.2447e-8
1.25	1.2916e-5	-1.0755e-6	1.4074e-5	-1.1181e-6	1.2312e-5	-7.2503e-7	1.3283e-5	-7.8037e-7
1.50	2.2839e-5	-1.6171e-6	2.5337e-5	-1.7265e-6	2.1230e-5	-8.5125e-7	2.3311e-5	-9.5595e-7
1.75	3.7298e-5	-2.4015e-6	4.2150e-5	-2.6636e-6	3.3623e-5	-8.2460e-7	3.7561e-5	-9.9058e-7
2.00	5.7552e-5	-3.6181e-6	6.6253e-5	-4.2174e-6	4.9993e-5	-5.0493e-7	5.6742e-5	-7.0396e-7
2.25	8.5092e-5	-5.6228e-6	9.9697e-5	-6.9465e-6	7.0688e-5	3.5604e-7	8.1278e-5	2.7803e-7
2.50	1.2160e-4	-8.8454e-6	1.4517e-4	-1.1730e-5	9.5612e-5	2.4590e-6	1.1134e-4	2.9219e-6
2.75	1.6981e-4	-1.4949e-5	2.0652e-4	-2.1325e-5	1.2518e-4	6.1165e-6	1.4679e-4	8.8546e-6
3.00	2.3263e-4	-2.5807e-5	2.8826e-4	-4.0184e-5	1.5879e-4	1.3336e-5	1.8695e-4	2.1472e-5
3.25	3.1380e-4	-4.5497e-5	3.9487e-4	-7.8766e-5	1.9582e-4	2.7570e-5	2.3231e-4	5.1086e-5
3.50	4.0064e-4	-6.7869e-5	5.1729e-4	-1.4581e-4	2.3371e-4	4.7788e-5	2.9462e-4	1.0859e-4

TABLE 5. FORWARD AND BACKWARD SCATTERING AMPLITUDES
AT $T = 10°C$, $f = 4$ GHz, AND $\alpha = 30°$

| Raindrop Radius (mm) | Forward Scattering | | | | Backward Scattering | | | |
| | Vertical Polarization | | Horizontal Polarization | | Vertical Polarization | | Horizontal Polarization | |
	Real	Imaginary	Real	Imaginary	Real	Imaginary	Real	Imaginary
0.25	1.0571e-7	-1.2443e-9	1.0578e-7	-1.2461e-9	1.0547e-7	-1.1747e-9	1.0555e-7	-1.1765e-9
0.50	8.5025e-7	-1.0886e-8	8.5398e-7	-1.0976e-8	8.4272e-7	-8.6712e-9	8.4642e-7	-8.7924e-9
0.75	2.8971e-6	-4.2324e-8	2.9279e-6	-4.3116e-8	2.8398e-6	-2.5487e-8	2.8698e-6	-2.6700e-8
1.00	6.9686e-6	-1.2042e-7	7.1042e-6	-1.2429e-7	6.7249e-6	-4.8750e-8	6.9560e-6	-5.4773e-8
1.25	1.3465e-5	-1.2731e-6	1.4045e-5	-1.2946e-6	1.2792e-5	-9.1571e-7	1.3277e-5	-9.4791e-7
1.50	2.4013e-5	-1.8855e-6	2.5263e-5	-1.9407e-6	2.2299e-5	-1.1288e-6	2.3339e-5	-1.1913e-6
1.75	3.9542e-5	-2.7471e-6	4.1969e-5	-2.8792e-6	3.5730e-5	-1.2259e-6	3.7698e-5	-1.3291e-6
2.00	6.1483e-5	-4.0499e-6	6.5836e-5	-4.3516e-6	5.3769e-5	-1.0937e-6	5.7143e-5	-1.2305e-6
2.25	9.1486e-5	-6.1569e-6	9.8791e-5	-6.8225e-6	7.6942e-5	-5.2405e-7	8.2238e-5	-4.2697e-7
2.50	1.3151e-4	-9.4706e-6	1.4330e-4	-1.0915e-5	1.0550e-4	1.1381e-6	1.1337e-4	1.2585e-6
2.75	1.8447e-4	-1.5797e-5	2.0284e-4	-1.8991e-5	1.3997e-4	4.0459e-6	1.5080e-4	5.0994e-6
3.00	2.5359e-4	-2.6994e-5	2.8144e-4	-3.4194e-5	1.8017e-4	1.0121e-5	1.9432e-4	1.3951e-5
3.25	3.4289e-4	-4.7204e-5	3.8357e-4	-6.3871e-5	2.2590e-4	2.2633e-5	2.4431e-4	3.4065e-5
3.50	4.4347e-4	-7.0318e-5	5.0189e-4	-1.0933e-4	2.8323e-4	4.0542e-5	3.1255e-4	7.0344e-5

TABLE 6. FORWARD AND BACKWARD SCATTERING AMPLITUDES
AT $T = 10°C$, $f = 4$ GHz, AND $\alpha = 15°$

| Raindrop Radius (mm) | Forward Scattering | | | | Backward Scattering | | | |
| | Vertical Polarization | | Horizontal Polarization | | Vertical Polarization | | Horizontal Polarization | |
	Real	Imaginary	Real	Imaginary	Real	Imaginary	Real	Imaginary
0.25	1.0576e-7	-1.2456e-9	1.0578e-7	-1.2461e-9	1.0553e-7	-1.1761e-9	1.0555e-7	-1.1765e-9
0.50	8.5297e-7	-1.0949e-8	8.5397e-7	-1.0973e-8	8.4544e-7	-8.7734e-9	8.4643e-7	-8.8061e-9
0.75	2.9194e-6	-4.2840e-8	2.9277e-6	-4.3053e-8	2.8620e-6	-2.6579e-8	2.8701e-6	-2.6923e-8
1.00	7.0663e-6	-1.2271e-7	7.1027e-6	-1.2379e-7	6.8229e-6	-5.4603e-8	6.8580e-6	-5.6328e-8
1.25	1.3867e-5	-1.3994e-6	1.4023e-5	-1.4052e-6	1.3143e-5	-1.0445e-6	1.3273e-5	-1.0539e-6
1.50	2.4873e-5	-2.0585e-6	2.5207e-5	-2.0734e-6	2.3081e-5	-1.3238e-6	2.3360e-5	-1.3421e-6
1.75	4.1185e-5	-2.9729e-6	4.1836e-5	-3.0085e-6	3.7270e-5	-1.3199e-6	3.7797e-5	-1.3510e-6
2.00	6.4362e-5	-4.3371e-6	6.5528e-5	-4.4183e-6	5.6530e-5	-1.3435e-6	5.7434e-5	-1.5865e-6
2.25	9.6187e-5	-6.5201e-6	9.8514e-5	-6.6991e-6	8.1514e-5	-1.2201e-6	8.2933e-5	-1.2250e-6
2.50	1.3876e-4	-9.9047e-6	1.4193e-4	-1.0292e-5	1.1274e-4	4.9669e-8	1.1483e-4	8.4076e-8
2.75	1.9521e-4	-1.6198e-5	2.0013e-4	-1.7255e-5	1.5080e-4	3.3260e-6	1.5371e-4	3.5803e-6
3.00	2.6896e-4	-2.7849e-5	2.7643e-4	-2.9781e-5	1.9582e-4	7.4325e-6	1.9982e-4	8.4186e-6
3.25	3.6440e-4	-4.8458e-3	3.7528e-4	-5.2928e-5	2.4791e-4	1.8488e-5	2.5287e-4	2.1496e-5
3.50	4.7494e-4	-7.2111e-5	4.9081e-4	-8.2575e-5	3.1579e-4	3.4089e-5	3.2371e-4	4.1973e-5

TABLE 7. FORWARD AND BACKWARD SCATTERING AMPLITUDES
AT $T = 10°C$, $f = 6$ GHz, AND $\alpha = 90°$

Raindrop Radius (mm)	Forward Scattering				Backward Scattering			
	Vertical Polarization		Horizontal Polarization		Vertical Polarization		Horizontal Polarization	
	Real	Imaginary	Real	Imaginary	Real	Imaginary	Real	Imaginary
0.25	2.3758e-7	-4.2957e-9	2.3825e-7	-4.3196e-9	2.3650e-7	-3.8203e-9	2.3721e-7	-3.8436e-9
0.50	1.8983e-6	-4.0074e-8	1.9315e-6	-4.1351e-8	1.8658e-6	-2.4375e-8	1.8975e-6	-2.5423e-8
0.75	6.3961e-6	-1.7123e-7	6.6771e-6	-1.8353e-7	6.1279e-6	-4.5467e-8	6.3990e-6	-5.2681e-8
1.00	1.5141e-5	-5.4478e-7	1.6398e-5	-6.1272e-7	1.3985e-5	3.6191e-7	1.5158e-5	6.0582e-9
1.25	2.7606e-5	-1.3283e-6	3.3108e-5	-1.7610e-6	2.4834e-5	1.5178e-6	2.9121e-5	4.0346e-7
1.50	4.8751e-5	-3.3270e-6	6.0925e-5	-4.6754e-6	4.1056e-5	4.6865e-6	5.0074e-5	1.9535e-6
1.75	7.9646e-5	-7.8373e-6	1.0433e-4	-1.1919e-5	6.1283e-5	1.2490e-5	7.8572e-5	6.6855e-6
2.00	1.2367e-4	-1.7923e-5	1.6887e-4	-2.9859e-5	8.5691e-5	3.0880e-5	1.1485e-4	2.0065e-5
2.25	1.8378e-4	-4.0150e-5	2.5727e-4	-7.3567e-5	1.1387e-4	7.1825e-5	1.6303e-4	5.5509e-5
2.50	2.5843e-4	-8.7552e-5	3.5101e-4	-1.6743e-4	1.4939e-4	1.4940e-4	2.5051e-4	1.3421e-4
2.75	3.2910e-4	-1.7639e-4	3.9215e-4	-2.9391e-4	2.1596e-4	2.4575e-4	4.4510e-4	2.3258e-4
3.00	3.5365e-4	-2.9263e-4	4.0191e-4	-3.6111e-4	3.5857e-4	2.9004e-4	7.3610e-4	2.4681e-4
3.25	3.3339e-4	-3.7252e-4	4.7881e-4	-3.8879e-4	5.7814e-4	2.8495e-4	1.0309e-3	1.7465e-4
3.50	3.3674e-4	-4.1557e-4	6.3985e-4	-4.7057e-4	7.1315e-4	2.8495e-4	1.3268e-3	5.5081e-5

TABLE 8. FORWARD AND BACKWARD SCATTERING AMPLITUDES
AT $T = 10°C$, $f = 6$ GHz, AND $\alpha = 75°$

Raindrop Radius (mm)	Forward Scattering				Backward Scattering			
	Vertical Polarization		Horizontal Polarization		Vertical Polarization		Horizontal Polarization	
	Real	Imaginary	Real	Imaginary	Real	Imaginary	Real	Imaginary
0.25	2.3762e-7	-4.2973e-9	2.3827e-7	-4.3198e-9	2.3655e-7	-3.8218e-9	2.3719e-7	-3.8436e-9
0.50	1.9005e-6	-4.0153e-8	1.9321e-6	-4.1352e-8	1.8658e-6	-2.4392e-8	1.8969e-6	-2.5511e-8
0.75	6.4146e-6	-1.7189e-7	6.6768e-6	-1.8336e-7	6.1465e-6	-4.5203e-8	6.3994e-6	-5.4167e-8
1.00	1.5223e-5	-5.4777e-7	1.6395e-5	-6.1117e-7	1.4068e-5	3.0238e-8	1.5162e-5	-3.5492e-9
1.25	2.7953e-5	-1.7798e-6	3.3087e-5	-2.1880e-6	2.5136e-5	7.3699e-8	2.9135e-5	2.0826e-6
1.50	4.9501e-5	-3.9122e-6	6.0860e-5	-5.1808e-6	4.1745e-5	1.2102e-6	5.0164e-5	1.4173e-6
1.75	8.1096e-5	-8.4173e-6	1.0413e-4	-1.2237e-5	6.2703e-5	4.5626e-6	7.8863e-5	6.0033e-6
2.00	1.2624e-4	-1.8616e-5	1.6841e-4	-2.9774e-5	8.8284e-5	1.2467e-5	1.1562e-4	1.8784e-5
2.25	1.8802e-4	-4.0976e-5	2.5659e-4	-7.2196e-5	1.1310e-4	3.1003e-5	1.6460e-4	5.2715e-5
2.50	2.6501e-4	-8.8399e-5	3.5141e-4	-1.6300e-4	1.5669e-4	7.2366e-5	2.5232e-4	1.2816e-4
2.75	3.3905e-4	-1.7756e-4	3.9789e-4	-2.8730e-4	2.2765e-4	1.4988e-4	4.4475e-4	2.2243e-4
3.00	3.6823e-4	-2.9443e-4	4.1331e-4	-3.5893e-4	3.7661e-4	2.4515e-4	7.3252e-4	2.3595e-4
3.25	3.5417e-4	-3.7555e-4	4.9005e-4	-3.9074e-4	6.0397e-4	2.8658e-4	1.0292e-3	1.6183e-4
3.50	3.6631e-4	-4.1051e-4	6.5023e-4	-4.6013e-4	7.5279e-4	2.9754e-4	1.3277e-3	4.8403e-5

TABLE 9. FORWARD AND BACKWARD SCATTERING AMPLITUDES
AT $T = 10°C$, $f = 6$ GHz, AND $\alpha = 60°$

Raindrop Radius (mm)	Forward Scattering				Backward Scattering			
	Vertical Polarization		Horizontal Polarization		Vertical Polarization		Horizontal Polarization	
	Real	Imaginary	Real	Imaginary	Real	Imaginary	Real	Imaginary
0.25	2.3775e-7	-4.3016e-9	2.3826e-7	-4.3197e-9	2.3667e-7	-3.8262e-9	2.3719e-7	-3.8439e-9
0.50	1.9067e-6	-4.0366e-8	1.9320e-6	-4.1329e-8	1.8719e-6	-2.4604e-8	1.8969e-6	-2.5617e-8
0.75	6.4652e-6	-1.7367e-7	6.6759e-6	-1.8290e-7	6.1974e-6	-4.6996e-8	6.4006e-6	-5.5874e-8
1.00	1.5445e-5	-5.5595e-7	1.6387e-5	-6.0691e-7	1.4292e-5	1.2845e-8	1.5129e-5	-1.5462e-8
1.25	2.8882e-5	-2.2263e-6	3.3009e-5	-2.5578e-6	2.5959e-5	-2.5465e-7	2.9171e-5	8.0173e-7
1.50	5.1501e-5	-4.5159e-6	6.0634e-5	-5.5437e-6	4.3605e-5	7.8448e-7	5.0372e-5	4.9741e-6
1.75	8.5003e-5	-9.0823e-6	1.0352e-4	-1.2162e-5	6.6534e-5	4.1339e-6	7.9541e-5	1.6343e-5
2.00	1.3314e-4	-1.9510e-5	1.6705e-4	-2.8499e-5	9.5216e-5	1.1827e-5	1.1727e-4	4.6466e-5
2.25	1.9937e-4	-4.2212e-5	2.5453e-4	-6.7348e-5	1.2997e-4	2.9958e-5	1.6752e-4	1.1379e-4
2.50	2.8275e-4	-9.0030e-5	3.5227e-4	-1.5008e-4	1.7556e-4	7.0724e-5	2.5343e-4	2.4108e-4
2.75	3.6578e-4	-1.8010e-4	4.1313e-4	-2.6844e-4	2.5680e-4	1.4655e-4	4.3313e-4	2.3301e-4
3.00	4.0737e-4	-2.9863e-4	4.4370e-4	-3.5004e-4	3.9313e-4	2.3913e-4	7.0905e-4	2.3301e-4
3.25	4.1000e-4	-3.8292e-4	5.1970e-4	-3.9491e-4	6.6531e-4	2.7281e-4	1.0098e-3	1.5951e-4
3.50	4.5075e-4	-4.1601e-4	6.8090e-4	-4.5423e-4	8.5162e-4	2.8864e-4	1.3163e-3	6.1840e-5

TABLE 10. FORWARD AND BACKWARD SCATTERING AMPLITUDES
AT $T = 10°C$, $f = 6$ GHz, AND $\alpha = 45°$

Raindrop Radius (mm)	Forward Scattering				Backward Scattering			
	Vertical Polarization		Horizontal Polarization		Vertical Polarization		Horizontal Polarization	
	Real	Imaginary	Real	Imaginary	Real	Imaginary	Real	Imaginary
0.25	2.3792e-7	-4.3075e-9	2.3826e-7	-4.3196e-9	2.3685e-7	-3.8323e-9	2.3719e-7	-3.8443e-9
0.50	1.9151e-6	-4.0656e-8	1.9320e-6	-4.1298e-8	1.8804e-6	-2.4980e-8	1.8970e-6	-2.5720e-8
0.75	6.5342e-6	-1.7611e-7	6.6747e-6	-1.8226e-7	6.2667e-6	-5.0723e-8	6.4022e-6	-5.7599e-8
1.00	1.5749e-5	-5.6711e-7	1.6377e-5	-6.0109e-7	1.4599e-5	2.5932e-9	1.5185e-5	-2.8089e-8
1.25	3.0147e-5	-2.6316e-6	3.2898e-5	-2.8543e-6	2.7079e-5	-6.0873e-7	2.9218e-5	-7.2196e-7
1.50	5.4223e-5	-5.0839e-6	6.0313e-5	-5.7737e-6	4.6132e-5	2.5204e-7	5.0642e-5	1.7820e-7
1.75	9.0329e-5	-9.7547e-6	1.0268e-4	-1.1813e-5	7.1743e-5	3.3903e-6	8.0419e-5	3.7685e-6
2.00	1.4255e-4	-2.0479e-5	1.6517e-4	-2.6483e-5	1.0462e-4	1.0547e-5	1.1938e-4	1.3236e-5
2.25	2.1485e-4	-4.3650e-5	2.5166e-4	-6.0435e-5	1.4577e-4	2.7711e-5	1.7099e-4	3.8175e-5
2.50	3.0698e-4	-9.2104e-5	3.5338e-4	-1.3219e-4	2.0102e-4	6.6938e-5	2.5734e-4	9.4530e-5
2.75	4.0229e-4	-1.8345e-4	4.3390e-4	-2.4243e-4	2.9581e-4	1.3941e-4	4.1472e-4	1.7359e-4
3.00	4.6085e-4	-3.0425e-4	4.8515e-4	-3.3849e-4	4.7743e-4	2.4949e-4	6.7207e-4	2.1037e-4
3.25	4.8639e-4	-3.9287e-4	5.5998e-4	-4.0062e-4	7.4656e-4	2.4945e-4	9.7794e-4	1.6629e-4
3.50	5.6792e-4	-4.2841e-4	7.2295e-4	-4.5274e-4	9.8361e-4	2.5765e-4	1.2952e-3	9.0845e-5

TABLE 11. FORWARD AND BACKWARD SCATTERING AMPLITUDES
AT $T = 10°C$, $f = 6$ GHz, AND $\alpha = 30°$

Raindrop Radius (mm)	Forward Scattering				Backward Scattering			
	Vertical Polarization		Horizontal Polarization		Vertical Polarization		Horizontal Polarization	
	Real	Imaginary	Real	Imaginary	Real	Imaginary	Real	Imaginary
0.25	2.3809e-7	-4.3134e-9	2.3826e-7	-4.3194e-9	2.3702e-7	-3.8385e-9	2.3719e-7	-3.8464e-9
0.50	1.9235e-6	-4.0946e-8	1.9319e-6	-4.1267e-8	1.8888e-6	-2.5413e-8	1.8971e-6	-2.5807e-8
0.75	6.6032e-6	-1.7855e-7	6.6735e-6	-1.8162e-7	6.3361e-6	-5.5284e-8	6.4038e-6	-5.9089e-8
1.00	1.6053e-5	-5.7828e-7	1.6367e-5	-5.9527e-7	1.4905e-5	-2.1771e-8	1.5198e-5	-3.9342e-8
1.25	3.1409e-5	-2.9574e-6	3.2785e-5	-3.0696e-6	2.8197e-5	-9.3956e-7	2.9265e-5	-1.0111e-6
1.50	5.6941e-5	-5.5531e-6	5.9987e-5	-5.8998e-6	4.8650e-5	-2.9296e-7	5.0904e-5	-3.6258e-7
1.75	9.5655e-5	-1.0336e-5	1.0183e-4	-1.1368e-5	7.6932e-5	5.5122e-6	8.1271e-5	2.6315e-6
2.00	1.5196e-4	-2.1353e-5	1.6328e-4	-2.4360e-5	1.1400e-4	8.9697e-6	1.2139e-4	1.0190e-5
2.25	2.3033e-4	-4.4998e-5	2.4875e-4	-5.3403e-5	1.6150e-4	2.4890e-5	1.7418e-4	2.9915e-5
2.50	3.3125e-4	-9.4132e-5	3.5448e-4	-1.1420e-4	2.2633e-4	6.1855e-5	2.5281e-4	7.5310e-5
2.75	4.3888e-4	-1.8678e-4	4.5471e-4	-2.1630e-4	3.3450e-4	1.3049e-4	3.9449e-4	1.4675e-4
3.00	5.1451e-4	-3.0986e-4	5.2671e-4	-3.2696e-4	5.3429e-4	2.0911e-4	6.3238e-4	2.0007e-4
3.25	5.6317e-4	-4.0287e-4	6.0016e-4	-4.0661e-4	8.2681e-4	2.2234e-4	9.4322e-4	1.7772e-4
3.50	6.8656e-4	-4.4271e-4	7.6486e-4	-4.5437e-4	1.1141e-3	2.1494e-4	1.2707e-3	1.2537e-4

TABLE 12. FORWARD AND BACKWARD SCATTERING AMPLITUDES
AT $T = 10°C$, $f = 6$ GHz, AND $\alpha = 15°$

Raindrop Radius (mm)	Forward Scattering				Backward Scattering			
	Vertical Polarization		Horizontal Polarization		Vertical Polarization		Horizontal Polarization	
	Real	Imaginary	Real	Imaginary	Real	Imaginary	Real	Imaginary
0.25	2.3822e-7	-4.3177e-9	2.3826e-7	-4.3193e-9	2.3714e-7	-3.8431e-9	2.3719e-7	-3.8448e-9
0.50	1.9296e-6	-4.1159e-8	1.9319e-6	-4.1245e-8	1.8949e-6	-2.5756e-8	1.8971e-6	-2.5866e-8
0.75	6.6538e-6	-1.8033e-7	6.6726e-6	-1.8116e-7	6.3868e-6	-5.9021e-8	6.4049e-6	-6.0103e-8
1.00	1.6275e-5	-5.8646e-7	1.6360e-5	-5.9101e-7	1.5129e-5	-4.2049e-8	1.5208e-5	-4.7133e-8
1.25	3.2333e-5	-3.1691e-6	3.2702e-5	-3.1993e-6	2.9012e-5	-1.1785e-6	2.9298e-5	-1.2002e-6
1.50	5.8930e-5	-5.8638e-6	5.9746e-5	-5.9570e-6	5.0489e-5	-7.0707e-7	5.1092e-5	-7.3123e-7
1.75	9.9555e-5	-1.0733e-5	1.0121e-4	-1.1010e-5	8.0720e-5	1.7990e-6	8.1883e-5	1.8192e-6
2.00	1.5885e-4	-2.1963e-5	1.6188e-4	-2.2770e-5	1.2084e-4	7.6656e-6	1.2283e-4	9.7720e-6
2.25	2.4168e-4	-4.5959e-5	2.4662e-4	-4.8213e-5	1.7299e-4	2.2545e-5	1.7639e-4	2.3856e-5
2.50	3.4905e-4	-9.5607e-5	3.5528e-4	-1.0099e-4	2.4481e-4	5.7675e-5	2.5194e-4	6.1214e-5
2.75	4.6574e-4	-1.8921e-4	4.6999e-4	-1.9713e-4	3.6271e-4	1.2310e-4	3.7888e-4	1.2731e-4
3.00	5.5394e-4	-3.1399e-4	5.5721e-4	-3.1857e-4	5.7569e-4	1.9618e-4	6.0211e-4	1.9346e-4
3.25	6.1964e-4	-4.1024e-4	6.2959e-4	-4.1122e-4	8.8523e-4	2.0051e-4	9.1655e-4	1.8805e-4
3.50	7.7427e-4	-4.5383e-4	7.9541e-4	-4.5686e-4	1.2091e-3	1.7808e-4	1.2513e-3	1.5302e-4

TABLE 13. FORWARD AND BACKWARD SCATTERING AMPLITUDES
AT $T = 10°C$, $f = 8$ GHz, AND $\alpha = 90°$

| Raindrop Radius (mm) | Forward Scattering | | | | Backward Scattering | | | |
| | Vertical Polarization | | Horizontal Polarization | | Vertical Polarization | | Horizontal Polarization | |
	Real	Imaginary	Real	Imaginary	Real	Imaginary	Real	Imaginary
0.25	4.2284e-7	-1.0490e-8	4.2400e-7	-1.0547e-8	4.1983e-7	-8.7380e-9	4.2111e-7	-8.7929e-9
0.50	3.3963e-6	-1.0663e-7	3.4569e-6	-1.0988e-7	3.2989e-6	-4.7564e-8	3.3581e-6	-4.9875e-8
0.75	1.1545e-5	-5.1041e-7	1.2054e-5	-5.4458e-7	1.0790e-5	-2.0162e-8	1.1272e-5	-3.4006e-8
1.00	2.7669e-5	-1.8348e-6	2.9980e-5	-2.0496e-6	2.4419e-5	5.1598e-7	2.6499e-5	5.0014e-7
1.25	5.0992e-5	-4.9636e-6	6.1557e-5	-6.6323e-6	4.2567e-5	2.3788e-6	5.0527e-5	2.9623e-6
1.50	9.1220e-5	-1.4012e-5	1.1452e-4	-2.0066e-5	6.9622e-5	8.7990e-6	8.6561e-5	1.2073e-5
1.75	1.4901e-4	-3.6914e-5	1.9214e-4	-5.6664e-5	1.0567e-4	2.6741e-5	1.4119e-4	3.9709e-5
2.00	2.1836e-4	-8.8009e-5	2.7664e-4	-1.3557e-4	1.6070e-4	6.8576e-5	2.4596e-4	9.9746e-5
2.25	2.7274e-4	-1.7144e-4	3.3216e-4	-2.2883e-4	2.6865e-4	1.3374e-4	4.4920e-4	1.5362e-4
2.50	2.9669e-4	-2.4986e-4	4.0190e-4	-2.9162e-4	4.4823e-4	1.7669e-4	7.1947e-4	1.3513e-4
2.75	3.2868e-4	-3.0198e-4	5.3246e-4	-3.6668e-4	6.5720e-4	1.6379e-4	1.0072e-3	4.5560e-5
3.00	3.8965e-4	-3.5158e-4	7.0534e-4	-4.9307e-4	8.5719e-4	1.1476e-4	1.3004e-3	-6.3288e-5
3.25	4.7085e-4	-4.2054e-4	9.0340e-4	-6.7315e-4	1.0470e-3	5.9881e-5	1.6067e-3	-1.9744e-4
3.50	5.4559e-4	-5.0267e-4	1.1215e-3	-9.1631e-4	1.2020e-3	3.1043e-5	1.9420e-3	-3.4668e-4

TABLE 14. FORWARD AND BACKWARD SCATTERING AMPLITUDES
AT $T = 10°C$, $f = 8$ GHz, AND $\alpha = 75°$

| Raindrop Radius (mm) | Forward Scattering | | | | Backward Scattering | | | |
| | Vertical Polarization | | Horizontal Polarization | | Vertical Polarization | | Horizontal Polarization | |
	Real	Imaginary	Real	Imaginary	Real	Imaginary	Real	Imaginary
0.25	4.2292e-7	-1.0494e-8	4.2406e-7	-1.0548e-8	4.1992e-7	-8.7417e-9	4.2108e-7	-8.7925e-9
0.50	3.4003e-6	-1.0681e-7	3.4568e-6	-1.0985e-7	3.3029e-6	-4.7602e-8	3.3581e-6	-5.0116e-8
0.75	1.1578e-5	-5.1201e-7	1.2053e-5	-5.4390e-7	1.0824e-5	-1.9562e-8	1.1273e-5	-3.7752e-8
1.00	2.7816e-5	-1.8424e-6	2.9973e-5	-2.0429e-6	2.4570e-5	5.2167e-7	2.6510e-5	4.7500e-7
1.25	5.1641e-5	-5.4527e-6	6.1499e-5	-7.0160e-6	4.3169e-5	2.2573e-6	5.0601e-5	2.5640e-6
1.50	9.2627e-5	-1.4677e-5	1.1436e-4	-2.0341e-5	7.0984e-5	8.7890e-6	8.6848e-5	1.1334e-5
1.75	1.5177e-4	-3.7792e-5	1.9201e-4	-5.6252e-5	1.0844e-4	2.6914e-5	1.4187e-4	3.7997e-5
2.00	2.2328e-4	-8.8977e-5	2.7768e-4	-1.3341e-4	1.6602e-4	6.9249e-5	2.4848e-4	9.6095e-5
2.25	2.8101e-4	-1.7294e-4	3.3649e-4	-2.2657e-4	2.7803e-4	1.3441e-4	4.4836e-4	1.4796e-4
2.50	3.0981e-4	-2.5242e-4	4.0809e-4	-2.9150e-4	4.6359e-4	1.7651e-4	7.1875e-4	1.2780e-4
2.75	3.4869e-4	-3.0653e-4	5.3916e-4	-3.6707e-4	6.8081e-4	1.6147e-4	1.0082e-3	4.2812e-5
3.00	4.1868e-4	-3.6177e-4	7.1420e-4	-4.9233e-4	8.9195e-4	1.0947e-4	1.3036e-3	-8.2628e-5
3.25	5.1179e-4	-4.3569e-4	9.1683e-4	-6.7354e-4	1.0970e-3	4.7822e-5	1.6135e-3	-2.2996e-4
3.50	6.0291e-4	-5.3354e-4	1.1415e-3	-9.2205e-4	1.2744e-3	1.7027e-5	1.9545e-3	-3.9512e-4

TABLE 15. FORWARD AND BACKWARD SCATTERING AMPLITUDES
AT $T = 10°C$, $f = 8$ GHz, AND $\alpha = 60°$

| Raindrop Radius (mm) | Forward Scattering | | | | Backward Scattering | | | |
| | Vertical Polarization | | Horizontal Polarization | | Vertical Polarization | | Horizontal Polarization | |
	Real	Imaginary	Real	Imaginary	Real	Imaginary	Real	Imaginary
0.25	4.2314e-7	-1.0504e-8	4.2406e-7	-1.0548e-8	4.2014e-7	-8.7520e-9	4.2105e-7	-8.7934e-9
0.50	3.4113e-6	-1.0712e-7	3.4567e-6	-1.0976e-7	3.3139e-6	-4.8110e-8	3.3583e-6	-5.0398e-8
0.75	1.1668e-5	-5.1639e-7	1.2050e-5	-5.4203e-7	1.0916e-5	-2.3955e-8	1.1276e-5	-4.2528e-8
1.00	2.8219e-5	-1.8633e-6	2.9952e-5	-2.0244e-6	2.4979e-5	5.0037e-7	2.6538e-5	4.1896e-7
1.25	5.3382e-5	-5.9751e-6	6.1307e-5	-7.2379e-6	4.4799e-5	1.9800e-6	5.0772e-5	2.0487e-6
1.50	9.6392e-5	-1.5459e-5	1.1387e-4	-2.0023e-5	7.4650e-5	8.3877e-6	8.7435e-5	1.0052e-5
1.75	1.5911e-4	-3.8973e-5	1.9148e-4	-5.3839e-5	1.1582e-4	2.6207e-5	1.4288e-4	3.4358e-5
2.00	2.3653e-4	-9.0668e-5	2.8030e-4	-1.2643e-4	1.7992e-4	6.8007e-5	2.4528e-4	8.7909e-5
2.25	3.0324e-4	-1.7596e-4	3.4792e-4	-2.1914e-4	3.0182e-4	1.1134e-4	4.4021e-4	1.3845e-4
2.50	3.4523e-4	-2.5815e-4	4.2491e-4	-2.8960e-4	5.0176e-4	1.6947e-4	7.0859e-4	1.2274e-4
2.75	4.0030e-4	-3.1767e-4	5.5699e-4	-3.6650e-4	7.3917e-4	1.4699e-4	1.0035e-3	3.8705e-5
3.00	4.9842e-4	-3.8317e-4	7.3771e-4	-4.8895e-4	9.7608e-4	8.2785e-5	1.3085e-3	-9.1922e-5
3.25	6.2447e-4	-4.7613e-4	9.5242e-4	-7.2379e-4	1.2191e-3	-1.3359e-5	1.6307e-3	-2.5477e-4
3.50	7.6035e-4	-6.0981e-4	1.1954e-3	-9.2782e-4	1.4466e-3	-6.0604e-5	1.9854e-3	-4.4059e-4

TABLE 16. FORWARD AND BACKWARD SCATTERING AMPLITUDES
AT $T = 10°C$, $f = 8$ GHz, AND $\alpha = 45°$

| Raindrop Radius (mm) | Forward Scattering | | | | Backward Scattering | | | |
| | Vertical Polarization | | Horizontal Polarization | | Vertical Polarization | | Horizontal Polarization | |
	Real	Imaginary	Real	Imaginary	Real	Imaginary	Real	Imaginary
0.25	4.2345e-7	-1.0518e-8	4.2406e-7	-1.0547e-8	4.2045e-7	-8.7665e-9	4.2105e-7	-8.7944e-9
0.50	3.4262e-6	-1.0802e-7	3.4565e-6	-1.0965e-7	3.3290e-6	-4.9010e-8	3.3585e-6	-5.0689e-8
0.75	1.1792e-5	-5.2238e-7	1.2047e-5	-5.3947e-7	1.1041e-5	-3.3011e-8	1.1281e-5	-4.7655e-8
1.00	2.8763e-5	-1.8918e-6	2.9923e-5	-1.9992e-6	2.5537e-5	4.5249e-7	2.6576e-5	3.9786e-7
1.25	5.5752e-5	-6.4783e-6	6.1036e-5	-7.3236e-6	4.7012e-5	1.5452e-6	5.0990e-5	1.4894e-6
1.50	1.0151e-4	-1.6260e-5	1.1317e-4	-1.9311e-5	7.9620e-5	7.5810e-6	8.8156e-5	8.4724e-6
1.75	1.6909e-4	-4.0280e-5	1.9069e-4	-5.0208e-5	1.2580e-4	2.4601e-5	1.4395e-4	2.9596e-5
2.00	2.5461e-4	-9.2751e-5	2.8382e-4	-1.1662e-4	1.9866e-4	6.4828e-5	2.4263e-4	7.7132e-5
2.25	3.3360e-4	-1.7984e-4	3.6346e-4	-2.0866e-4	3.3371e-4	1.2465e-4	4.2684e-4	1.2720e-4
2.50	3.9369e-4	-2.6569e-4	4.4679e-4	-2.8667e-4	5.5269e-4	1.5602e-4	6.9164e-4	1.2043e-4
2.75	4.7749e-4	-3.3266e-4	5.8087e-4	-3.6532e-4	8.1693e-4	1.2145e-4	9.9394e-4	1.1663e-5
3.00	6.0828e-4	-4.1253e-4	7.6940e-4	-4.8380e-4	1.0927e-3	3.7232e-5	1.3130e-3	-9.1431e-5
3.25	7.8003e-4	-5.3256e-4	1.0008e-3	-6.6366e-4	1.3813e-3	-8.2004e-5	1.6537e-3	-2.6951e-4
3.50	9.7790e-4	-7.1408e-4	1.2700e-3	-9.3120e-4	1.6725e-3	-1.9208e-4	2.0272e-3	-4.7599e-4

TABLE 17. FORWARD AND BACKWARD SCATTERING AMPLITUDES
AT $T = 10°C$, $f = 8$ GHz, AND $\alpha = 30°$

| Raindrop Radius (mm) | Forward Scattering | | | | Backward Scattering | | | |
| | Vertical Polarization | | Horizontal Polarization | | Vertical Polarization | | Horizontal Polarization | |
	Real	Imaginary	Real	Imaginary	Real	Imaginary	Real	Imaginary
0.25	4.2375e-7	-1.0532e-8	4.2406e-7	-1.0547e-8	4.2075e-7	-8.7813e-9	4.2105e-7	-8.7953e-9
0.50	3.4412e-6	-1.0871e-7	3.4564e-6	-1.0953e-7	3.3440e-6	-5.0043e-8	3.3586e-6	-5.0941e-8
0.75	1.1916e-5	-5.2837e-7	1.2043e-5	-5.3691e-7	1.1165e-5	-4.4063e-8	1.1288e-5	-5.2251e-8
1.00	2.9117e-5	-1.9203e-6	2.9895e-5	-1.9741e-6	2.6094e-5	3.9230e-7	2.6613e-5	3.5973e-7
1.25	5.8120e-5	-6.9004e-6	8.0762e-5	-7.3241e-6	4.9211e-5	1.0507e-6	5.1197e-5	9.8399e-7
1.50	1.0663e-4	-1.6962e-5	1.1246e-4	-1.8490e-5	8.4559e-5	6.5860e-6	8.8829e-5	6.9489e-6
1.75	1.7907e-4	-4.1475e-5	1.8988e-4	-4.6446e-5	1.3572e-4	2.2564e-5	1.4483e-4	2.4895e-5
2.00	2.7271e-4	-9.4756e-5	2.8733e-4	-1.0671e-4	2.1727e-4	6.0699e-5	2.3940e-4	6.6480e-5
2.25	3.6403e-4	-1.8365e-4	3.7900e-4	-1.9807e-4	3.6530e-4	1.1630e-4	4.1221e-4	1.1672e-4
2.50	4.4235e-4	-2.7320e-4	4.6903e-4	-2.8368e-4	6.0305e-4	1.3986e-4	6.7296e-4	1.2033e-4
2.75	5.5341e-4	-3.4771e-4	6.0446e-4	-3.6409e-4	8.9378e-4	1.1616e-5	9.8264e-4	4.8718e-5
3.00	7.1916e-4	-4.4225e-4	8.0052e-4	-4.7825e-4	1.2058e-3	-1.5358e-5	1.3161e-3	-8.4585e-5
3.25	9.3742e-4	-5.8981e-4	1.0489e-3	-6.5654e-4	1.5407e-3	-1.7361e-4	1.6763e-3	-2.7498e-4
3.50	1.1984e-3	-8.2000e-4	1.3455e-3	-9.3113e-4	1.8935e-3	-3.4303e-4	2.0691e-3	-4.9772e-4

TABLE 18. FORWARD AND BACKWARD SCATTERING AMPLITUDES
AT $T = 10°C$, $f = 8$ GHz, AND $\alpha = 15°$

| Raindrop Radius (mm) | Forward Scattering | | | | Backward Scattering | | | |
| | Vertical Polarization | | Horizontal Polarization | | Vertical Polarization | | Horizontal Polarization | |
	Real	Imaginary	Real	Imaginary	Real	Imaginary	Real	Imaginary
0.25	4.2398e-7	-1.0542e-8	4.2406e-7	-1.0546e-8	4.2097e-7	-8.7922e-9	4.2105e-7	-8.7960e-9
0.50	3.4522e-6	-1.0922e-7	3.4562e-6	-1.0944e-7	3.3550e-6	-5.0862e-8	3.3598e-6	-5.1111e-8
0.75	1.2007e-5	-5.3275e-7	1.2041e-5	-5.3504e-7	1.1257e-5	-5.3104e-8	1.1288e-5	-5.5443e-8
1.00	2.9720e-5	-1.9412e-6	2.9874e-5	-1.9596e-6	2.6501e-5	3.4235e-7	2.6575e-5	3.1316e-7
1.25	5.9852e-5	-7.1824e-6	6.0560e-5	-7.2962e-6	5.0813e-5	6.3575e-7	5.1345e-5	5.8490e-7
1.50	1.1038e-4	-1.7442e-5	1.1194e-4	-1.7852e-5	8.8156e-5	5.7861e-6	8.9300e-5	5.8490e-6
1.75	1.8638e-4	-4.2314e-5	1.8928e-4	-4.3848e-5	1.4394e-4	2.0868e-5	1.4593e-4	2.1461e-5
2.00	2.8597e-4	-9.6203e-5	2.8988e-4	-9.9029e-5	2.3829e-4	5.7227e-5	2.3877e-4	5.8713e-5
2.25	3.8638e-4	-1.8642e-4	3.9038e-4	-1.9029e-4	3.8829e-4	1.0938e-4	4.0092e-4	1.0938e-4
2.50	4.7810e-4	-2.7870e-4	4.8527e-4	-2.8151e-4	6.3969e-4	1.2668e-4	6.5849e-4	1.2115e-4
2.75	6.0757e-4	-3.5881e-4	6.2159e-4	-3.6321e-4	9.4970e-4	6.7587e-5	9.7357e-4	5.5554e-5
3.00	8.0098e-4	-4.6426e-4	8.2294e-4	-4.7398e-4	1.2881e-3	-5.7534e-5	1.3176e-3	-7.6937e-5
3.25	1.0538e-3	-6.3235e-4	1.0838e-3	-6.5047e-4	1.6563e-3	-2.4652e-4	1.6928e-3	-2.7502e-4
3.50	1.3017e-3	-8.9882e-4	1.4014e-3	-9.2911e-4	2.0532e-3	-4.6382e-4	2.0999e-3	-5.0755e-4

TABLE 19. FORWARD AND BACKWARD SCATTERING AMPLITUDES AT $T = 10°C$, $f = 11$ GHz, AND $\alpha = 90°$

| Raindrop Radius (mm) | Forward Scattering | | | | Backward Scattering | | | |
| | Vertical Polarization | | Horizontal Polarization | | Vertical Polarization | | Horizontal Polarization | |
	Real	Imaginary	Real	Imaginary	Real	Imaginary	Real	Imaginary
0.25	8.0070e-7	-2.8431e-8	8.0280e-7	-2.8585e-8	7.9195e-7	-2.1558e-8	7.9448e-7	-2.1701e-8
0.50	6.4843e-6	-3.2376e-7	6.6002e-6	-3.3310e-7	6.2027e-6	-8.5219e-8	6.3145e-6	-9.0696e-8
0.75	2.2317e-5	-1.7771e-6	2.3306e-5	-1.8890e-6	2.0185e-5	3.0198e-7	2.1099e-5	2.7907e-7
1.00	5.4111e-5	-7.2931e-6	5.8661e-5	-8.1152e-6	4.5557e-5	3.3189e-6	4.9585e-5	3.4348e-6
1.25	9.9432e-5	-2.1619e-5	1.1937e-4	-2.8813e-5	8.0429e-5	1.2955e-5	9.7366e-5	1.6499e-5
1.50	1.6760e-4	-6.1565e-5	2.0400e-4	-8.3615e-5	1.4273e-4	4.1856e-5	1.8974e-4	5.2589e-5
1.75	2.3302e-4	-1.3156e-4	2.8704e-4	-1.6702e-4	2.6069e-4	8.7055e-5	3.7220e-4	9.0404e-5
2.00	2.8823e-4	-2.0463e-4	3.9215e-4	-2.5177e-4	4.4596e-4	1.0723e-4	6.3889e-4	6.8905e-5
2.25	3.6085e-4	-2.7596e-4	5.5185e-4	-3.7258e-4	6.6059e-4	7.9959e-5	9.4547e-4	-2.3066e-5
2.50	4.5784e-4	-3.6394e-4	7.4780e-4	-5.6444e-4	8.8034e-4	2.3490e-5	1.2711e-3	-1.7010e-4
2.75	5.7273e-4	-4.4732e-4	9.6140e-4	-7.4432e-4	1.1042e-3	-4.2937e-5	1.6172e-3	-3.6794e-4
3.00	7.0275e-4	-6.2596e-4	1.1646e-3	-1.2282e-3	1.3387e-3	-1.2010e-4	1.9714e-3	-6.3260e-4
3.25	8.3820e-4	-8.1455e-4	1.3129e-3	-1.7165e-3	1.5748e-3	-2.1803e-4	2.2889e-3	-9.7700e-4
3.50	9.2872e-4	-1.0069e-3	1.3481e-3	-2.2684e-3	1.7419e-3	-3.1338e-4	2.4845e-3	-1.3694e-3

TABLE 20. FORWARD AND BACKWARD SCATTERING AMPLITUDES AT $T = 10°C$, $f = 11$ GHz, AND $\alpha = 75°$

| Raindrop Radius (mm) | Forward Scattering | | | | Backward Scattering | | | |
| | Vertical Polarization | | Horizontal Polarization | | Vertical Polarization | | Horizontal Polarization | |
	Real	Imaginary	Real	Imaginary	Real	Imaginary	Real	Imaginary
0.25	8.0086e-7	-2.8441e-8	8.0302e-7	-2.8585e-8	7.9211e-7	-2.1568e-8	7.9425e-7	-2.1697e-8
0.50	6.4919e-6	-3.2425e-7	6.6001e-6	-3.3297e-7	6.2104e-6	-8.5326e-8	6.3147e-6	-9.1364e-8
0.75	2.2381e-5	-1.7816e-6	2.3304e-5	-1.8859e-6	2.0250e-5	3.0336e-7	2.1103e-5	2.6829e-7
1.00	5.4399e-5	-7.3160e-6	5.8644e-5	-8.0831e-6	4.5859e-5	3.3319e-6	4.9618e-5	3.3568e-6
1.25	1.0074e-4	-2.2365e-5	1.1934e-4	-2.9098e-5	8.1662e-5	1.3142e-5	9.7554e-5	1.5813e-5
1.50	1.7049e-4	-6.2473e-5	2.0445e-4	-8.3079e-5	1.4568e-4	4.2752e-5	1.8997e-4	5.1135e-5
1.75	2.3878e-4	-1.3315e-4	2.8920e-4	-1.6631e-4	2.6693e-4	8.8497e-5	3.7202e-4	8.7604e-5
2.00	2.9877e-4	-2.0768e-4	3.9582e-4	-2.5183e-4	4.5809e-4	1.0861e-4	6.3916e-4	6.4104e-5
2.25	3.7859e-4	-2.8141e-4	5.5720e-4	-3.7244e-4	6.6840e-4	8.0150e-5	9.4750e-4	-3.2256e-5
2.50	4.8523e-4	-3.7676e-4	7.5753e-4	-5.6447e-4	9.1486e-4	1.8768e-5	1.2755e-3	-1.8823e-4
2.75	6.1106e-4	-5.0327e-4	9.7490e-4	-8.4594e-4	1.1548e-3	-5.8257e-5	1.6232e-3	-4.0119e-4
3.00	7.5071e-4	-6.6893e-4	1.1836e-3	-1.2327e-3	1.4060e-3	-1.5202e-4	1.9760e-3	-6.8677e-4
3.25	8.9234e-4	-8.8056e-4	1.3386e-3	-1.7249e-3	1.6584e-3	-2.7112e-4	2.2887e-3	-1.0561e-3
3.50	9.8653e-4	-1.1089e-3	1.3805e-3	-2.2916e-3	1.8493e-3	-3.7617e-4	2.4871e-3	-1.4695e-3

TABLE 21. FORWARD AND BACKWARD SCATTERING AMPLITUDES AT $T = 10°C$, $f = 11$ GHz, AND $\alpha = 60°$

| Raindrop Radius (mm) | Forward Scattering | | | | Backward Scattering | | | |
| | Vertical Polarization | | Horizontal Polarization | | Vertical Polarization | | Horizontal Polarization | |
	Real	Imaginary	Real	Imaginary	Real	Imaginary	Real	Imaginary
0.25	8.0128e-7	-2.8468e-8	8.0302e-7	-2.8583e-8	7.9253e-7	-2.1594e-8	7.9426e-7	-2.1700e-8
0.50	6.5128e-6	-3.2561e-7	6.5997e-6	-3.3262e-7	6.2314e-6	-8.6678e-8	6.3153e-6	-9.2228e-8
0.75	2.2555e-5	-1.7938e-6	2.3297e-5	-1.8770e-6	2.0428e-5	2.9111e-7	2.1111e-5	2.5266e-7
1.00	5.5184e-5	-7.3786e-6	5.8597e-5	-7.9952e-6	4.6671e-5	3.2679e-6	4.9693e-5	3.2256e-6
1.25	1.0421e-4	-2.3267e-5	1.1917e-4	-2.8695e-5	8.4997e-5	1.2830e-5	9.7817e-5	1.4501e-5
1.50	1.7825e-4	-6.3898e-5	2.0557e-4	-8.0490e-5	1.5360e-4	4.2283e-5	1.8948e-4	4.7793e-5
1.75	2.5429e-4	-1.3612e-4	2.9490e-4	-1.6284e-4	2.8322e-4	8.6752e-5	3.6843e-4	8.2984e-5
2.00	3.2738e-4	-2.1439e-4	4.0566e-4	-2.5002e-4	4.8873e-4	1.0304e-4	6.3510e-4	6.0549e-5
2.25	4.2716e-4	-2.9664e-4	5.7136e-4	-3.7026e-4	7.3521e-4	6.5627e-5	9.4816e-4	-3.7346e-5
2.50	5.6051e-4	-4.1021e-4	7.7963e-4	-5.6251e-4	9.9833e-4	-1.5246e-5	1.2850e-3	-2.0244e-4
2.75	7.1670e-4	-5.6981e-4	1.0102e-3	-8.4826e-4	1.2740e-3	-1.2794e-4	1.6420e-3	-4.3526e-4
3.00	8.8342e-4	-7.8480e-4	1.2321e-3	-1.2430e-3	1.5597e-3	-2.7496e-4	2.0007e-3	-7.5017e-4
3.25	1.0430e-3	-1.0594e-3	1.4018e-3	-1.7460e-3	1.8400e-3	-4.6215e-4	2.3165e-3	-1.1554e-3
3.50	1.1515e-3	-1.3749e-3	1.4643e-3	-2.3394e-3	2.0632e-3	-6.3853e-4	2.5274e-3	-1.6074e-3

TABLE 22. FORWARD AND BACKWARD SCATTERING AMPLITUDES AT $T = 10°C$, $f = 11$ GHz, AND $\alpha = 45°$

| Raindrop Radius (mm) | Forward Scattering | | | | Backward Scattering | | | |
| | Vertical Polarization | | Horizontal Polarization | | Vertical Polarization | | Horizontal Polarization | |
	Real	Imaginary	Real	Imaginary	Real	Imaginary	Real	Imaginary
0.25	8.0186e-7	-2.8504e-8	8.0302e-7	-2.8581e-8	7.9311e-7	-2.1632e-8	7.9426e-7	-2.1703e-8
0.50	6.5413e-6	-3.2746e-7	6.5992e-6	-3.3213e-7	6.2601e-6	-8.9062e-8	6.3160e-6	-9.3160e-8
0.75	2.2793e-5	-1.8105e-6	2.3288e-5	-1.8664e-6	2.0670e-5	2.6630e-7	2.1127e-5	2.3479e-7
1.00	5.6258e-5	-7.4641e-6	5.8533e-5	-7.8752e-6	4.7775e-5	3.1303e-6	4.9789e-5	3.0653e-6
1.25	1.0893e-4	-2.4210e-5	1.1893e-4	-2.7837e-5	8.9504e-5	1.1998e-5	9.8065e-5	1.2840e-5
1.50	1.8882e-4	-6.5584e-5	2.0706e-4	-7.6661e-5	1.6429e-4	4.0409e-5	1.8835e-4	4.3377e-5
1.75	2.7547e-4	-1.3987e-4	3.0261e-4	-1.5772e-4	3.0507e-4	8.1898e-5	3.6228e-4	7.7617e-5
2.00	3.6652e-4	-2.2319e-4	4.1893e-4	-2.4705e-4	5.2955e-4	9.1042e-5	6.2757e-4	5.8781e-5
2.25	4.9389e-4	-3.1727e-4	5.9062e-4	-3.6673e-4	8.0554e-4	3.8209e-5	9.4729e-4	-3.7943e-5
2.50	6.6423e-4	-4.5613e-4	8.1128e-4	-5.5890e-4	1.1080e-3	-7.3612e-5	1.2972e-3	-2.1103e-4
2.75	8.6265e-4	-6.6193e-4	1.0593e-3	-8.5020e-4	1.4290e-3	-2.4107e-4	1.6691e-3	-4.6544e-4
3.00	1.0671e-3	-9.4628e-4	1.3002e-3	-1.2562e-3	1.7558e-3	-4.6911e-4	2.0393e-3	-8.1417e-4
3.25	1.2518e-3	-1.3103e-3	1.4910e-3	-1.7750e-3	2.0647e-3	-7.6023e-4	2.3637e-3	-1.2618e-3
3.50	1.3794e-3	-1.7476e-3	1.5850e-3	-2.4030e-3	2.3157e-3	-1.0582e-3	2.5937e-3	-1.7629e-3

TABLE 23. FORWARD AND BACKWARD SCATTERING AMPLITUDES AT $T = 10°C$, $f = 11$ GHz, AND $\alpha = 30°$

| Raindrop Radius (mm) | Forward Scattering | | | | Backward Scattering | | | |
| | Vertical Polarization | | Horizontal Polarization | | Vertical Polarization | | Horizontal Polarization | |
	Real	Imaginary	Real	Imaginary	Real	Imaginary	Real	Imaginary
0.25	8.0243e-7	-2.8541e-8	8.0301e-7	-2.8579e-8	7.9369e-7	-2.1671e-8	7.9426e-7	-2.1706e-8
0.50	6.5696e-6	-3.2931e-7	6.5987e-6	-3.3164e-7	6.2888e-6	-9.1795e-8	6.3167e-6	-9.3997e-8
0.75	2.3032e-5	-1.8272e-6	2.3279e-5	-1.8551e-6	2.0912e-5	2.3622e-7	2.1140e-5	2.1822e-7
1.00	5.7332e-5	-7.5496e-6	5.8470e-5	-7.7552e-6	4.8876e-5	2.9597e-6	4.9882e-5	2.9139e-6
1.25	1.1365e-4	-2.5043e-5	1.1864e-4	-2.6860e-5	9.3961e-5	1.0906e-5	9.8243e-5	1.1223e-5
1.50	1.9940e-4	-6.7175e-5	2.0853e-4	-7.2720e-5	1.7486e-4	3.7802e-5	1.8694e-4	3.9014e-5
1.75	2.9669e-4	-1.4351e-4	3.1029e-4	-1.5245e-4	3.2664e-4	7.5540e-5	3.5539e-4	7.2713e-5
2.00	4.0580e-4	-2.3192e-4	4.3212e-4	-2.4389e-4	5.6974e-4	7.6254e-5	6.1891e-4	5.8592e-5
2.25	5.6109e-4	-3.3800e-4	6.0975e-4	-3.6291e-4	8.7457e-4	5.7326e-6	9.4536e-4	-3.5325e-5
2.50	7.6895e-4	-5.0258e-4	8.4297e-4	-5.5459e-4	1.2151e-3	-1.4044e-4	1.3090e-3	-2.1425e-4
2.75	1.0104e-3	-7.5570e-4	1.1092e-3	-8.5116e-4	1.5792e-3	-3.6788e-4	1.6972e-3	-4.8805e-4
3.00	1.2535e-3	-1.1116e-3	1.3704e-3	-1.2688e-3	1.9431e-3	-6.8458e-4	2.0805e-3	-8.6879e-4
3.25	1.4638e-3	-1.5687e-3	1.5835e-3	-1.8047e-3	2.2735e-3	-1.0900e-3	2.4152e-3	-1.3574e-3
3.50	1.6100e-3	-2.1338e-3	1.7115e-3	-2.4676e-3	2.5399e-3	-1.5290e-3	2.6652e-3	-1.9065e-3

TABLE 24. FORWARD AND BACKWARD SCATTERING AMPLITUDES AT $T = 10°C$, $f = 11$ GHz, AND $\alpha = 15°$

| Raindrop Radius (mm) | Forward Scattering | | | | Backward Scattering | | | |
| | Vertical Polarization | | Horizontal Polarization | | Vertical Polarization | | Horizontal Polarization | |
	Real	Imaginary	Real	Imaginary	Real	Imaginary	Real	Imaginary
0.25	8.0286e-7	-2.8567e-8	8.0301e-7	-2.8578e-8	7.9411e-7	-2.1699e-8	7.9427e-7	-2.1709e-8
0.50	6.5906e-6	-3.3066e-7	6.5984e-6	-3.3129e-7	6.3097e-6	-9.3962e-8	6.3172e-6	-9.4578e-8
0.75	2.3206e-5	-1.8394e-6	2.3273e-5	-1.8469e-6	2.1088e-5	2.1170e-7	2.1149e-5	2.0650e-7
1.00	5.8118e-5	-7.6122e-6	5.8423e-5	-7.6673e-6	4.9679e-5	2.8190e-6	4.9949e-5	2.8045e-6
1.25	1.1709e-4	-2.5618e-5	1.1843e-4	-2.6105e-5	9.7194e-5	9.9842e-6	9.8341e-5	1.0051e-5
1.50	2.0715e-4	-6.8310e-5	2.0960e-4	-6.9797e-5	1.8253e-4	3.5559e-5	1.8577e-4	3.5838e-5
1.75	3.1225e-4	-1.4615e-4	3.1590e-4	-1.4855e-4	3.4227e-4	7.0192e-5	3.5000e-4	6.9318e-5
2.00	4.3467e-4	-2.3830e-4	4.4174e-4	-2.4151e-4	5.9887e-4	6.4106e-5	6.1207e-4	5.9106e-5
2.25	6.1057e-4	-3.5327e-4	6.2367e-4	-3.5998e-4	9.2451e-4	-2.0513e-5	9.4346e-4	-3.2031e-5
2.50	8.4626e-4	-5.3697e-4	8.6619e-4	-5.5103e-4	1.2925e-3	-1.9366e-4	1.3175e-3	-2.1433e-4
2.75	1.1197e-3	-8.2543e-4	1.1463e-3	-8.5127e-4	1.6870e-3	-4.6792e-4	1.7183e-3	-5.0135e-4
3.00	1.3917e-3	-1.2351e-3	1.4231e-3	-1.2777e-3	2.0760e-3	-8.5391e-4	2.1120e-3	-9.0535e-4
3.25	1.6210e-3	-1.7629e-3	1.6531e-3	-1.8268e-3	2.4182e-3	-1.3493e-3	2.4548e-3	-1.4239e-3
3.50	1.7806e-3	-2.4255e-3	1.8075e-3	-2.5162e-3	2.6891e-3	-1.9022e-3	2.7201e-3	-2.0079e-3

TABLE 25. FORWARD AND BACKWARD SCATTERING AMPLITUDES
AT $T = 10°C$, $f = 14$ GHz, AND $\alpha = 90°$

Raindrop Radius (mm)	Forward Scattering				Backward Scattering			
	Vertical Polarization		Horizontal Polarization		Vertical Polarization		Horizontal Polarization	
	Real	Imaginary	Real	Imaginary	Real	Imaginary	Real	Imaginary
0.25	1.2986e-6	-6.0630e-8	1.3018e-5	-6.0943e-8	1.2800e-6	-4.2485e-8	1.2843e-6	-4.2783e-8
0.50	1.0598e-5	-7.5580e-7	1.0788e-5	-7.7686e-7	1.0013e-5	-1.1045e-7	1.0195e-5	-1.2004e-7
0.75	3.6765e-6	-4.5646e-6	3.8405e-5	-4.8440e-6	3.3656e-5	1.2461e-6	3.4170e-5	1.2187e-6
1.00	8.8291e-5	-1.9835e-5	9.5678e-5	-3.2000e-5	7.5616e-5	9.9970e-6	8.2702e-5	1.0379e-5
1.25	1.5364e-4	-5.6133e-5	1.8183e-4	-7.1958e-5	1.4257e-4	3.2566e-5	1.7826e-4	3.7522e-5
1.50	2.3140e-4	-1.2695e-4	2.8351e-4	-1.5730e-4	2.8190e-4	6.8141e-5	3.7500e-4	5.0971e-5
1.75	3.1364e-4	-2.0948e-4	4.2282e-4	-2.8929e-4	4.9034e-4	6.4544e-5	6.6433e-4	1.3190e-5
2.00	4.1946e-4	-3.1155e-4	6.1321e-4	-4.5397e-4	7.2885e-4	1.2344e-5	9.9865e-4	-1.2300e-4
2.25	5.4472e-4	-4.4958e-4	8.1972e-4	-7.4574e-4	9.7322e-4	-7.2311e-5	1.3450e-3	-3.4147e-4
2.50	6.8085e-4	-6.3153e-4	9.9740e-4	-1.1548e-3	1.2179e-3	-1.7970e-4	1.6683e-3	-6.3859e-4
2.75	8.1750e-4	-8.6158e-4	1.0911e-3	-1.6693e-3	1.4438e-3	-3.1076e-4	1.9135e-3	-1.0049e-3
3.00	9.2025e-4	-1.1339e-3	1.0613e-3	-2.2243e-3	1.6239e-3	-4.5825e-4	2.0160e-3	-1.3764e-3
3.25	9.9605e-4	-1.4275e-3	9.2797e-4	-2.7463e-3	1.7307e-3	-5.9758e-4	1.9697e-3	-1.6634e-3
3.50	1.0251e-3	-1.6677e-3	7.5708e-4	-3.1854e-3	1.7140e-3	-6.5823e-4	1.7989e-3	-1.7927e-3

TABLE 26. FORWARD AND BACKWARD SCATTERING AMPLITUDES
AT $T = 10°C$, $f = 14$ GHz, AND $\alpha = 75°$

Raindrop Radius (mm)	Forward Scattering				Backward Scattering			
	Vertical Polarization		Horizontal Polarization		Vertical Polarization		Horizontal Polarization	
	Real	Imaginary	Real	Imaginary	Real	Imaginary	Real	Imaginary
0.25	1.2989e-6	-6.0660e-8	1.3024e-6	-6.0961e-8	1.2803e-6	-4.2506e-8	1.2837e-6	-4.2768e-8
0.50	1.0610e-5	-7.5685e-7	1.0788e-5	-7.7650e-7	1.0025e-5	-1.1069e-7	1.0195e-5	-1.2239e-7
0.75	3.6871e-5	-4.5746e-6	3.8401e-5	-4.8353e-6	3.2767e-5	1.2463e-6	3.4178e-5	1.1943e-6
1.00	8.8777e-5	-1.9891e-5	9.5670e-5	-3.1911e-5	7.6141e-5	1.0016e-5	8.2759e-5	1.0195e-5
1.25	1.5589e-4	-5.7049e-5	1.8239e-4	-7.1846e-5	1.4484e-4	3.3730e-5	1.7915e-4	3.6755e-5
1.50	2.3650e-4	-1.2877e-4	2.8512e-4	-1.5718e-4	2.8746e-4	6.8380e-5	3.7509e-4	5.8316e-5
1.75	3.2388e-4	-2.1335e-4	4.2582e-4	-2.6933e-4	5.0277e-4	6.7587e-5	6.6522e-4	3.6538e-6
2.00	4.3762e-4	-3.2093e-4	6.1881e-4	-4.5419e-4	7.5246e-4	1.3149e-5	1.0027e-3	-1.3203e-4
2.25	5.7211e-4	-4.7009e-4	8.2957e-4	-7.4722e-4	1.0115e-3	-7.8088e-5	1.3502e-3	-3.6130e-4
2.50	7.1555e-4	-6.6970e-4	1.0126e-3	-1.1993e-3	1.2721e-3	-2.0013e-4	1.6737e-3	-6.7813e-4
2.75	8.4900e-4	-9.2274e-4	1.1130e-3	-1.6782e-3	1.5134e-3	-3.4864e-4	1.9168e-3	-1.0630e-3
3.00	9.5374e-4	-1.2200e-3	1.0916e-3	-2.2401e-3	1.7078e-3	-5.1570e-4	2.0188e-3	-1.4586e-3
3.25	1.0215e-3	-1.5378e-3	9.6847e-4	-2.7718e-3	1.8286e-3	-6.7198e-4	1.9709e-3	-1.7673e-3
3.50	1.0466e-3	-1.8051e-3	7.8308e-4	-3.2305e-3	1.8451e-3	-7.3885e-4	1.8031e-3	-1.9103e-3

TABLE 27. FORWARD AND BACKWARD SCATTERING AMPLITUDES
AT $T = 10°C$, $f = 14$ GHz, AND $\alpha = 60°$

Raindrop Radius (mm)	Forward Scattering				Backward Scattering			
	Vertical Polarization		Horizontal Polarization		Vertical Polarization		Horizontal Polarization	
	Real	Imaginary	Real	Imaginary	Real	Imaginary	Real	Imaginary
0.25	1.2996e-6	-6.0715e-8	1.3024e-6	-6.0957e-8	1.2810e-6	-4.2562e-8	1.2837e-6	-4.2776e-8
0.50	1.0644e-5	-7.5973e-7	1.0787e-5	-7.7553e-7	1.0060e-5	-1.1357e-7	1.0196e-5	-1.2441e-7
0.75	3.7160e-5	-4.6022e-6	3.8390e-5	-4.8110e-6	3.3064e-5	1.2206e-6	3.4199e-5	1.1558e-6
1.00	9.0104e-5	-2.0044e-5	9.5646e-5	-3.1668e-5	7.7539e-5	9.8570e-6	8.2861e-5	9.8675e-6
1.25	1.6197e-4	-5.8477e-5	1.8320e-4	-7.0394e-5	1.5098e-4	3.3569e-5	1.7889e-4	3.4799e-5
1.50	2.5032e-4	-1.3227e-4	2.8942e-4	-1.5517e-4	3.0194e-4	6.7054e-5	3.7279e-4	5.5691e-5
1.75	3.5190e-4	-2.2248e-4	4.3412e-4	-2.6768e-4	5.3351e-4	6.1577e-5	6.6406e-4	7.2927e-6
2.00	4.8744e-4	-3.3476e-4	6.3359e-4	-4.5262e-4	8.0867e-4	-7.2468e-6	1.0074e-3	-1.3866e-4
2.25	6.4760e-4	-5.2413e-4	8.5516e-4	-7.4880e-4	1.0994e-3	-1.3018e-4	1.3642e-3	-3.8169e-4
2.50	8.1172e-4	-7.7173e-4	1.0508e-3	-1.1691e-3	1.3896e-3	-3.0059e-4	1.6958e-3	-7.1866e-4
2.75	9.5333e-4	-1.0870e-3	1.1647e-3	-1.7007e-3	1.6525e-3	-5.1332e-4	1.9453e-3	-1.1393e-3
3.00	1.0497e-3	-1.4513e-3	1.1573e-3	-2.2814e-3	1.8566e-3	-7.4945e-4	2.0542e-3	-1.5743e-3
3.25	1.0968e-3	-1.8327e-3	1.0461e-3	-2.8391e-3	1.9810e-3	-9.7049e-4	2.0159e-3	-1.9334e-3
3.50	1.1015e-3	-2.1777e-3	8.6805e-4	-3.3433e-3	2.0239e-3	-1.0733e-3	1.8788e-3	-2.1319e-3

TABLE 28. FORWARD AND BACKWARD SCATTERING AMPLITUDES
AT $T = 10°C$, $f = 14$ GHz, AND $\alpha = 45°$

Raindrop Radius (mm)	Forward Scattering				Backward Scattering			
	Vertical Polarization		Horizontal Polarization		Vertical Polarization		Horizontal Polarization	
	Real	Imaginary	Real	Imaginary	Real	Imaginary	Real	Imaginary
0.25	1.3005e-6	-6.0790e-8	1.3024e-6	-6.0951e-8	1.2819e-6	-4.2640e-8	1.2838e-6	-4.2784e-8
0.50	1.0691e-5	-7.6368e-7	1.0786e-5	-7.7419e-7	1.0107e-5	-1.1862e-7	1.0198e-5	-1.2666e-7
0.75	3.7555e-5	-4.6398e-6	3.8375e-5	-4.7795e-6	3.3469e-5	1.1657e-6	3.4225e-5	1.1104e-6
1.00	9.1918e-5	-2.0254e-5	9.5614e-5	-2.1337e-5	7.9432e-5	9.5323e-6	8.2801e-5	9.4637e-6
1.25	1.7025e-4	-6.0158e-5	1.8441e-4	-6.8116e-5	1.5924e-4	3.2039e-5	1.7790e-4	3.2170e-5
1.50	2.6912e-4	-1.3670e-4	2.9524e-4	-1.5301e-4	3.2123e-4	6.2270e-5	3.6864e-4	5.2797e-5
1.75	3.9026e-4	-2.3464e-4	4.4529e-4	-2.6492e-4	5.7388e-4	4.7333e-5	6.6085e-4	6.6248e-6
2.00	5.5589e-4	-3.7720e-4	6.5386e-4	-4.4973e-4	8.8185e-4	-4.5436e-5	1.0128e-3	-1.4184e-4
2.25	7.5171e-4	-5.9854e-4	8.8068e-4	-7.5002e-4	1.2119e-3	-2.1657e-4	1.3836e-3	-3.9921e-4
2.50	9.4459e-4	-9.1341e-4	1.1042e-3	-1.1817e-3	1.5357e-3	-4.6308e-4	1.7292e-3	-7.6549e-4
2.75	1.0973e-3	-1.3168e-3	1.2376e-3	-1.7317e-3	1.8167e-3	-7.7488e-4	1.9917e-3	-1.2254e-3
3.00	1.1811e-3	-1.7769e-3	1.2489e-3	-2.3395e-3	2.0174e-3	-1.1185e-3	2.1148e-3	-1.7126e-3
3.25	1.1964e-3	-2.2808e-3	1.1552e-3	-2.9350e-3	2.1234e-3	-1.4421e-3	2.0938e-3	-2.1383e-3
3.50	1.1649e-3	-2.7069e-3	9.9041e-4	-3.5023e-3	2.1673e-3	-1.6428e-3	1.9908e-3	-2.4217e-3

TABLE 29. FORWARD AND BACKWARD SCATTERING AMPLITUDES
AT $T = 10°C$, $f = 14$ GHz, AND $\alpha = 30°$

Raindrop Radius (mm)	Forward Scattering				Backward Scattering			
	Vertical Polarization		Horizontal Polarization		Vertical Polarization		Horizontal Polarization	
	Real	Imaginary	Real	Imaginary	Real	Imaginary	Real	Imaginary
0.25	1.3014e-6	-6.0865e-8	1.3024e-6	-6.0945e-8	1.2828e-6	-4.2719e-8	1.2838e-6	-4.2792e-8
0.50	1.0738e-5	-7.6759e-7	1.0785e-5	-7.7288e-7	1.0154e-5	-1.2439e-7	1.0199e-5	-1.2872e-7
0.75	3.7949e-5	-4.6774e-6	3.8360e-5	-4.7473e-6	3.3873e-5	1.0998e-6	3.4250e-5	1.0673e-6
1.00	9.3733e-5	-2.0444e-5	9.5582e-5	-2.1005e-5	8.1316e-5	9.1374e-6	8.3088e-5	9.0733e-6
1.25	1.7852e-4	-6.1740e-5	1.8561e-4	-6.5724e-5	1.6736e-4	2.8766e-5	1.7670e-4	2.9567e-5
1.50	2.8794e-4	-1.4100e-4	3.0103e-4	-1.4867e-4	3.4014e-4	5.5772e-5	3.6389e-4	5.0301e-5
1.75	4.2879e-4	-2.4674e-4	4.5640e-4	-2.6193e-4	6.1343e-4	2.9499e-5	6.5676e-4	7.3735e-6
2.00	6.2496e-4	-4.0984e-4	6.7416e-4	-4.4641e-4	9.5274e-4	-9.0317e-5	1.0175e-3	-1.4192e-4
2.25	8.5691e-4	-6.7398e-4	9.2670e-4	-7.5056e-4	1.3197e-3	-3.1437e-4	1.4035e-3	-4.1176e-4
2.50	1.0791e-3	-1.0580e-3	1.1591e-3	-1.1938e-3	1.6724e-3	-6.4423e-4	1.7646e-3	-8.0488e-4
2.75	1.2429e-3	-1.5529e-3	1.3128e-3	-1.7633e-3	1.8628e-3	-1.0653e-3	2.0416e-3	-1.3046e-3
3.00	1.3125e-3	-2.1140e-3	1.3455e-3	-2.4000e-3	2.1467e-3	-1.5287e-3	2.1803e-3	-1.8444e-3
3.25	1.2930e-3	-2.6868e-3	1.2677e-3	-3.0357e-3	2.2157e-3	-1.8686e-3	2.1773e-3	-2.3400e-3
3.50	1.2145e-3	-3.2626e-3	1.1177e-3	-3.5698e-3	2.2304e-3	-2.2946e-3	2.1049e-3	-2.7161e-3

TABLE 30. FORWARD AND BACKWARD SCATTERING AMPLITUDES
AT $T = 10°C$, $f = 14$ GHz, AND $\alpha = 15°$

Raindrop Radius (mm)	Forward Scattering				Backward Scattering			
	Vertical Polarization		Horizontal Polarization		Vertical Polarization		Horizontal Polarization	
	Real	Imaginary	Real	Imaginary	Real	Imaginary	Real	Imaginary
0.25	1.3021e-6	-6.0919e-8	1.3024e-6	-6.0941e-8	1.2835e-6	-4.2778e-8	1.2838e-6	-4.2797e-8
0.50	1.0772e-5	-7.7047e-7	1.0784e-5	-7.7186e-7	1.0188e-5	-1.2895e-7	1.0203e-5	-1.3017e-7
0.75	3.8239e-5	-4.7050e-6	3.8349e-5	-4.7237e-6	3.4168e-5	1.0463e-6	3.4269e-5	1.0369e-6
1.00	9.5082e-5	-2.0617e-5	9.5558e-5	-2.0762e-5	8.2687e-5	8.8150e-6	8.3162e-5	8.7928e-6
1.25	1.8458e-4	-6.2867e-5	1.8648e-4	-6.3935e-5	1.7321e-4	2.7771e-5	1.7571e-4	2.7673e-5
1.50	3.0174e-4	-1.4411e-4	3.0525e-4	-1.4617e-4	3.5376e-4	5.0249e-5	3.6013e-4	4.8658e-5
1.75	4.5708e-4	-2.5960e-4	4.6451e-4	-2.5959e-4	6.6179e-4	-1.4797e-5	6.5538e-4	1.5852e-6
2.00	6.7580e-4	-4.3390e-4	6.8904e-4	-4.4379e-4	1.0035e-3	-1.2613e-4	1.0207e-3	-1.4061e-4
2.25	9.3462e-4	-7.2893e-4	9.5338e-4	-7.5059e-4	1.3902e-3	-3.1669e-4	1.4183e-3	-4.1884e-4
2.50	1.1787e-3	-1.1658e-3	1.2001e-3	-1.2025e-3	1.7676e-3	-7.8658e-4	1.7913e-3	-8.3129e-4
2.75	1.3506e-3	-1.7289e-3	1.3693e-3	-1.7868e-3	2.0603e-3	-1.2938e-3	2.0798e-3	-1.3601e-3
3.00	1.4088e-3	-2.3682e-3	1.4174e-3	-2.4458e-3	2.2242e-3	-1.8516e-3	2.2304e-3	-1.9398e-3
3.25	1.3594e-3	-3.0178e-3	1.3522e-3	-3.1126e-3	2.2554e-3	-2.3854e-3	2.3406e-3	-2.4892e-3
3.50	1.2417e-3	-3.6873e-3	1.2138e-3	-3.7983e-3	2.2303e-3	-2.8103e-3	2.1894e-3	-2.9371e-3

TABLE 31. FORWARD AND BACKWARD SCATTERING AMPLITUDES AT $T = 10°C$, $f = 19$ GHz, AND $\alpha = 90°$

| Raindrop Radius (mm) | Forward Scattering | | | | Backward Scattering | | | |
| | Vertical Polarization | | Horizontal Polarization | | Vertical Polarization | | Horizontal Polarization | |
	Real	Imaginary	Real	Imaginary	Real	Imaginary	Real	Imaginary
0.25	2.3954e-6	-1.5782e-7	2.4023e-6	-1.5865e-6	2.3497e-6	-1.0047e-7	2.3566e-6	-1.0115e-7
0.50	1.9763e-5	-2.1955e-6	2.0119e-5	-2.2550e-6	1.8437e-5	-1.0175e-7	1.8778e-5	-1.2677e-7
0.75	6.8413e-5	-1.4410e-5	7.1487e-5	-1.5277e-5	6.1653e-5	4.4759e-6	6.4656e-5	4.4009e-6
1.00	1.5424e-4	-5.8407e-5	1.6517e-4	-6.4541e-5	1.5593e-4	2.4287e-5	1.7399e-4	2.3251e-5
1.25	2.4592e-4	-1.3423e-4	2.9584e-4	-1.6575e-4	3.1222e-4	3.9407e-5	3.9217e-4	2.3776e-5
1.50	3.6804e-4	-2.5398e-4	4.7693e-4	-3.4212e-4	5.6266e-4	8.4639e-8	7.2167e-4	-7.9050e-5
1.75	5.0879e-4	-4.3001e-4	6.7514e-4	-6.5531e-4	8.3289e-4	-1.1005e-4	1.0683e-3	-3.1844e-4
2.00	6.4369e-4	-6.6885e-4	8.0676e-4	-1.1088e-3	1.0781e-3	-2.6443e-4	1.3388e-3	-6.5893e-4
2.25	7.5072e-4	-9.6044e-4	8.0562e-4	-1.6328e-3	1.2634e-3	-4.3821e-4	1.4604e-3	-1.0165e-3
2.50	8.1580e-4	-1.2785e-3	6.8720e-4	-1.2264e-3	1.3542e-3	-5.9645e-4	1.4145e-3	-1.2766e-3
2.75	8.4723e-4	-1.5936e-3	5.5642e-4	-2.5499e-3	1.3353e-3	-6.8389e-4	1.2606e-3	-1.3603e-3
3.00	8.8571e-4	-1.8867e-3	4.6782e-4	-2.9346e-3	1.2019e-3	-6.7872e-4	1.0206e-3	-1.2366e-3
3.25	9.5898e-4	-2.1762e-3	4.5681e-4	-3.3569e-3	9.6195e-4	-5.6258e-4	7.3525e-4	-9.0268e-4
3.50	1.1025e-3	-2.4014e-3	4.5021e-4	-3.8608e-3	5.5932e-4	-2.9454e-4	3.9669e-4	-3.3872e-4

TABLE 32. FORWARD AND BACKWARD SCATTERING AMPLITUDES AT $T = 10°C$, $f = 19$ GHz, AND $\alpha = 75°$

| Raindrop Radius (mm) | Forward Scattering | | | | Backward Scattering | | | |
| | Vertical Polarization | | Horizontal Polarization | | Vertical Polarization | | Horizontal Polarization | |
	Real	Imaginary	Real	Imaginary	Real	Imaginary	Real	Imaginary
0.25	2.3958e-6	-1.5787e-7	2.4023e-6	-1.5864e-6	2.3502e-6	-1.0052e-7	2.3566e-6	-1.0116e-7
0.50	1.9786e-5	-2.1983e-6	2.0118e-5	-2.2538e-6	1.8462e-5	-1.0252e-7	1.8779e-5	-1.3067e-7
0.75	6.8618e-5	-1.4441e-5	7.1486e-5	-1.5250e-5	6.1874e-5	4.4769e-6	6.4674e-5	4.3334e-6
1.00	1.5534e-4	-5.8909e-5	1.6743e-4	-6.4450e-5	1.5717e-4	2.3973e-5	1.7190e-4	2.2890e-5
1.25	2.5050e-4	-1.3649e-4	2.9708e-4	-1.6600e-4	3.1764e-4	4.2932e-5	3.9241e-4	2.3313e-5
1.50	3.7820e-4	-2.6006e-4	4.7998e-4	-3.4251e-4	5.7681e-4	5.1746e-6	7.2368e-4	-8.1217e-5
1.75	5.2595e-4	-4.4608e-4	6.8267e-4	-6.5675e-4	8.6074e-4	-1.0856e-4	1.0732e-3	-3.2713e-4
2.00	6.6480e-4	-7.0227e-4	8.1846e-4	-1.1136e-3	1.1213e-3	-2.7327e-4	1.3456e-3	-6.8032e-4
2.25	7.6868e-4	-1.0147e-3	8.2377e-4	-1.6430e-3	1.3218e-3	-4.5652e-4	1.4690e-3	-1.0544e-3
2.50	8.2446e-4	-1.3528e-3	7.1345e-4	-2.1446e-3	1.4289e-3	-6.2757e-4	1.4275e-3	-1.3322e-3
2.75	8.4957e-4	-1.6796e-3	5.7268e-4	-2.5756e-3	1.4275e-3	-7.2554e-4	1.2660e-3	-1.4311e-3
3.00	8.8099e-4	-1.9875e-3	4.8255e-4	-2.9688e-3	1.3230e-3	-7.1929e-4	1.0383e-3	-1.3200e-3
3.25	9.4940e-4	-2.2923e-3	4.6888e-4	-3.3972e-3	1.1232e-3	-5.9225e-4	7.8054e-4	-9.9269e-4
3.50	1.0848e-3	-2.5475e-3	4.6841e-4	-3.9088e-3	8.2534e-4	-2.6583e-4	5.0763e-4	-4.2062e-4

TABLE 33. FORWARD AND BACKWARD SCATTERING AMPLITUDES AT $T = 10°C$, $f = 19$ GHz, AND $\alpha = 60°$

| Raindrop Radius (mm) | Forward Scattering | | | | Backward Scattering | | | |
| | Vertical Polarization | | Horizontal Polarization | | Vertical Polarization | | Horizontal Polarization | |
	Real	Imaginary	Real	Imaginary	Real	Imaginary	Real	Imaginary
0.25	2.3971e-6	-1.5801e-7	2.4023e-6	-1.5863e-6	2.3515e-6	-1.0066e-7	2.3566e-6	-1.0118e-7
0.50	1.9850e-5	-2.2060e-6	2.0117e-5	-2.2506e-6	1.8527e-5	-1.1023e-7	1.8782e-5	-1.3647e-7
0.75	6.9176e-5	-1.4524e-5	7.1482e-5	-1.5174e-5	6.2463e-5	4.3923e-6	6.4711e-5	4.2218e-6
1.00	1.5800e-4	-5.9455e-5	1.6773e-4	-6.3910e-5	1.6005e-4	2.3392e-5	1.7190e-4	2.2147e-5
1.25	2.6302e-4	-1.4108e-4	3.0053e-4	-1.6488e-4	3.3119e-4	4.1918e-5	3.9123e-4	2.2325e-5
1.50	4.0604e-4	-2.7489e-4	4.8798e-4	-3.4148e-4	6.0918e-4	-3.5567e-6	7.2541e-4	-8.2606e-5
1.75	5.7330e-4	-4.8771e-4	6.9943e-4	-6.5811e-4	9.1965e-4	-1.4196e-4	1.0833e-3	-3.3636e-4
2.00	7.2354e-4	-7.9057e-4	8.4667e-4	-1.1237e-3	1.2035e-3	-3.5217e-4	1.3660e-3	-7.0981e-4
2.25	8.2010e-4	-1.1589e-3	8.6232e-4	-1.6685e-3	1.4159e-3	-5.9309e-4	1.4981e-3	-1.1145e-3
2.50	8.5356e-4	-1.5477e-3	7.5876e-4	-2.1910e-3	1.5281e-3	-8.1000e-4	1.4674e-3	-1.4303e-3
2.75	8.5299e-4	-1.9183e-3	6.1932e-4	-2.6468e-3	1.5389e-3	-9.4600e-4	1.3232e-3	-1.5743e-3
3.00	8.6228e-4	-2.2674e-3	5.2381e-4	-3.0644e-3	1.4639e-3	-9.6532e-4	1.1234e-3	-1.5140e-3
3.25	9.1341e-4	-2.6180e-3	5.0088e-4	-3.5114e-3	1.3165e-3	-8.5026e-4	9.0787e-4	-1.2408e-3
3.50	1.0273e-3	-2.9492e-3	4.9700e-4	-4.0456e-3	1.1566e-3	-5.0958e-4	7.1597e-4	-7.3254e-4

TABLE 34. FORWARD AND BACKWARD SCATTERING AMPLITUDES AT $T = 10°C$, $f = 19$ GHz, AND $\alpha = 45°$

| Raindrop Radius (mm) | Forward Scattering | | | | Backward Scattering | | | |
| | Vertical Polarization | | Horizontal Polarization | | Vertical Polarization | | Horizontal Polarization | |
	Real	Imaginary	Real	Imaginary	Real	Imaginary	Real	Imaginary
0.25	2.3988e-6	-1.5820e-7	2.4023e-6	-1.5861e-7	2.3532e-6	-1.0086e-7	2.3566e-6	-1.0121e-7
0.50	1.9937e-5	-2.2165e-6	2.0115e-5	-2.2462e-6	1.8616e-5	-1.2359e-7	1.8786e-5	-1.4314e-7
0.75	6.9939e-5	-1.4637e-5	7.1476e-5	-1.5070e-5	6.3258e-5	4.2328e-6	6.4756e-5	4.0875e-6
1.00	1.6164e-4	-6.0201e-5	1.6813e-4	-6.3172e-5	1.6393e-4	2.2317e-5	1.7182e-4	2.1272e-5
1.25	2.8012e-4	-1.4695e-4	3.0516e-4	-1.6287e-4	3.4885e-4	3.6562e-5	3.8870e-4	2.1299e-5
1.50	4.4419e-4	-2.9483e-4	4.9896e-4	-3.3946e-4	6.5038e-4	-2.4248e-5	7.2651e-4	-8.2569e-5
1.75	6.3844e-4	-5.4461e-4	7.2271e-4	-6.5911e-4	9.9225e-4	-2.0330e-4	1.0965e-3	-3.4405e-4
2.00	8.0446e-4	-9.1255e-4	8.8629e-4	-1.1369e-3	1.2988e-3	-4.8498e-4	1.3950e-3	-7.4186e-4
2.25	8.9034e-4	-1.3596e-3	9.1671e-4	-1.7035e-3	1.5119e-3	-8.1206e-4	1.5425e-3	-1.1862e-3
2.50	8.9093e-4	-1.8211e-3	8.2275e-4	-2.2561e-3	1.6103e-3	-1.1075e-3	1.5289e-3	-1.5545e-3
2.75	8.5066e-4	-2.2551e-3	6.8473e-4	-2.7484e-3	1.6126e-3	-1.3089e-3	1.4083e-3	-1.7662e-3
3.00	8.2256e-4	-2.6637e-3	5.7985e-4	-3.2026e-3	1.5498e-3	-1.3817e-3	1.2411e-3	-1.7891e-3
3.25	8.3993e-4	-3.0772e-3	5.3991e-4	-3.6781e-3	1.4435e-3	-1.3104e-3	1.0688e-3	-1.6148e-3
3.50	9.1079e-4	-3.5158e-3	5.2402e-4	-4.2484e-3	1.4025e-3	-1.0299e-3	9.4757e-4	-1.2421e-3

TABLE 35. FORWARD AND BACKWARD SCATTERING AMPLITUDES AT $T = 10°C$, $f = 19$ GHz, AND $\alpha = 30°$

| Raindrop Radius (mm) | Forward Scattering | | | | Backward Scattering | | | |
| | Vertical Polarization | | Horizontal Polarization | | Vertical Polarization | | Horizontal Polarization | |
	Real	Imaginary	Real	Imaginary	Real	Imaginary	Real	Imaginary
0.25	2.4005e-6	-1.5839e-7	2.4023e-6	-1.5859e-7	2.3549e-6	-1.0105e-7	2.3566e-6	-1.0123e-7
0.50	2.0024e-5	-2.2269e-6	2.0113e-5	-2.2418e-6	1.8705e-5	-1.3878e-7	1.8789e-5	-1.4935e-7
0.75	7.0702e-5	-1.4750e-5	7.1471e-5	-1.4967e-5	6.4049e-5	4.0447e-6	6.4797e-5	3.9599e-6
1.00	1.6528e-4	-6.0947e-5	1.6853e-4	-6.2433e-5	1.6778e-4	2.1058e-5	1.7171e-4	2.0452e-5
1.25	2.9723e-4	-1.5268e-4	3.0977e-4	-1.6066e-4	3.6584e-4	2.9043e-5	3.8566e-4	2.0563e-5
1.50	4.8299e-4	-3.1470e-4	5.0995e-4	-3.3713e-4	6.8947e-4	-4.9912e-5	7.2692e-4	-8.1268e-5
1.75	7.0406e-4	-6.0193e-4	7.4631e-4	-6.5961e-4	1.0595e-3	-2.7420e-4	1.1096e-3	-3.4900e-4
2.00	8.8610e-4	-1.0364e-3	9.2691e-4	-1.1498e-3	1.3824e-3	-6.3427e-4	1.4253e-3	-7.7014e-4
2.25	9.6053e-4	-1.5651e-3	9.7245e-4	-1.7392e-3	1.5846e-3	-1.0565e-3	1.5892e-3	-1.2544e-3
2.50	9.2550e-4	-2.1031e-3	8.8891e-4	-2.3238e-3	1.6523e-3	-1.4406e-3	1.5932e-3	-1.6778e-3
2.75	8.4001e-4	-2.6048e-3	7.5187e-4	-2.8554e-3	1.6252e-3	-1.7192e-3	1.4953e-3	-1.9636e-3
3.00	7.6564e-4	-3.0767e-3	6.3543e-4	-3.3500e-3	1.5494e-3	-1.8621e-3	1.3565e-3	-2.0829e-3
3.25	7.3648e-4	-3.5551e-3	5.7334e-4	-3.8581e-3	1.4555e-3	-1.8601e-3	1.2178e-3	-2.0306e-3
3.50	7.4827e-4	-4.1045e-3	5.3836e-4	-4.4712e-3	1.4365e-3	-1.7058e-3	1.1411e-3	-1.8361e-3

TABLE 36. FORWARD AND BACKWARD SCATTERING AMPLITUDES AT $T = 10°C$, $f = 19$ GHz, AND $\alpha = 15°$

| Raindrop Radius (mm) | Forward Scattering | | | | Backward Scattering | | | |
| | Vertical Polarization | | Horizontal Polarization | | Vertical Polarization | | Horizontal Polarization | |
	Real	Imaginary	Real	Imaginary	Real	Imaginary	Real	Imaginary
0.25	2.4018e-6	-1.5852e-7	2.4022e-6	-1.5858e-7	2.3562e-6	-1.0120e-7	2.3566e-6	-1.0125e-7
0.50	2.0088e-5	-2.2345e-6	2.0112e-5	-2.2386e-6	1.8792e-5	-1.5078e-7	1.8792e-5	-1.5374e-7
0.75	7.1260e-5	-1.4833e-5	7.1467e-5	-1.4891e-5	6.4625e-5	3.8934e-6	6.4825e-5	3.8686e-6
1.00	1.6795e-4	-6.1494e-5	1.6882e-4	-6.1893e-5	1.7055e-4	2.0047e-5	1.7160e-4	1.9870e-5
1.25	3.0977e-4	-1.5684e-4	3.1313e-4	-1.5898e-4	3.7792e-4	2.2605e-5	3.8321e-4	2.0189e-5
1.50	5.1062e-4	-3.2927e-4	5.1799e-4	-3.3530e-4	7.1702e-4	-7.0906e-5	7.2693e-4	-7.9682e-5
1.75	7.5241e-4	-6.4420e-4	7.6375e-4	-6.5974e-4	1.1062e-3	-3.3055e-4	1.1192e-3	-3.5136e-4
2.00	9.4634e-4	-1.1285e-3	9.5725e-4	-1.1590e-3	1.4376e-3	-7.5162e-4	1.4481e-3	-7.8932e-4
2.25	1.0119e-3	-1.7187e-3	1.0150e-3	-1.7658e-3	1.6255e-3	-1.1486e-3	1.6248e-3	-1.3035e-3
2.50	9.4899e-4	-2.3151e-3	9.3869e-4	-2.3749e-3	1.6611e-3	-1.7031e-3	1.6418e-3	-1.7691e-3
2.75	8.2679e-4	-2.8692e-3	8.0213e-4	-2.9372e-3	1.5998e-3	-2.0451e-3	1.5597e-3	-2.1133e-3
3.00	7.1255e-4	-3.3900e-3	6.7587e-4	-3.4640e-3	1.4985e-3	-2.2491e-3	1.4393e-3	-2.3112e-3
3.25	6.4062e-4	-3.9170e-3	5.9423e-4	-3.9987e-3	1.3935e-3	-2.3134e-3	1.3197e-3	-2.3623e-3
3.50	5.9847e-4	-4.5494e-3	5.3888e-4	-4.6477e-3	1.3672e-3	-2.2867e-3	1.2638e-3	-2.3253e-3

TABLE 37. FORWARD AND BACKWARD SCATTERING AMPLITUDES AT $T = 10°C$, $f = 24$ GHz, AND $\alpha = 90°$

Raindrop Radius (mm)	Forward Scattering				Backward Scattering			
	Vertical Polarization		Horizontal Polarization		Vertical Polarization		Horizontal Polarization	
	Real	Imaginary	Real	Imaginary	Real	Imaginary	Real	Imaginary
0.25	3.8250e-6	-3.2672e-7	3.8360e-6	-3.2841e-7	3.7370e-6	-1.9548e-7	3.7478e-6	-1.9693e-7
0.50	3.1827e-5	-4.9189e-6	3.2404e-5	-5.0517e-6	2.9586e-5	-8.9786e-8	3.0142e-5	-1.2300e-7
0.75	1.0805e-4	-3.2848e-5	1.1395e-4	-3.4826e-5	1.0340e-4	8.1815e-6	1.0868e-4	7.7467e-6
1.00	2.2933e-4	-1.1750e-4	2.4993e-4	-1.3011e-4	2.7551e-4	1.8744e-5	3.0316e-4	1.1715e-5
1.25	3.8642e-4	-2.4957e-4	4.3567e-4	-3.2797e-4	5.1001e-4	-2.5985e-5	6.2738e-4	-9.4989e-5
1.50	5.0680e-4	-4.8020e-4	6.1371e-4	-6.9931e-4	7.9173e-4	-1.7661e-4	9.5473e-4	-3.8020e-4
1.75	6.1008e-4	-7.8415e-4	6.5786e-4	-1.1954e-3	1.0013e-3	-3.7679e-4	1.1248e-3	-7.4301e-4
2.00	6.7631e-4	-1.1174e-3	5.6152e-4	-1.6815e-3	1.0942e-3	-5.5955e-4	1.1027e-3	-1.0139e-3
2.25	7.0466e-4	-1.4372e-3	4.2761e-4	-2.0908e-3	1.0520e-3	-6.4640e-4	9.3853e-4	-1.0816e-3
2.50	7.4419e-4	-1.7472e-3	3.9106e-4	-2.4788e-3	8.9068e-4	-5.9616e-4	7.2482e-4	-9.1611e-4
2.75	8.4339e-4	-2.0637e-3	4.1367e-4	-2.8432e-3	6.0858e-4	-3.9875e-4	4.9360e-4	-4.9923e-4
3.00	9.9607e-4	-2.4434e-3	4.3672e-4	-3.5492e-3	3.1750e-4	-3.9016e-5	3.1982e-4	1.4316e-4
3.25	1.1573e-3	-2.9208e-3	3.7963e-4	-4.2830e-3	-1.8912e-4	4.4793e-4	3.4790e-5	8.9621e-4
3.50	1.3444e-3	-3.3641e-3	1.1738e-4	-4.9495e-3	-5.8903e-4	9.7837e-4	1.2770e-4	1.5773e-3

TABLE 38. FORWARD AND BACKWARD SCATTERING AMPLITUDES AT $T = 10°C$, $f = 24$ GHz, AND $\alpha = 75°$

Raindrop Radius (mm)	Forward Scattering				Backward Scattering			
	Vertical Polarization		Horizontal Polarization		Vertical Polarization		Horizontal Polarization	
	Real	Imaginary	Real	Imaginary	Real	Imaginary	Real	Imaginary
0.25	3.8257e-6	-3.2682e-7	3.8360e-6	-3.2836e-7	3.7397e-6	-1.9586e-7	3.7478e-6	-1.9686e-7
0.50	3.1865e-5	-4.9250e-6	3.2404e-5	-5.0490e-6	2.9628e-5	-7.1802e-8	3.0144e-5	-1.1132e-7
0.75	1.0839e-4	-3.2924e-5	1.1298e-4	-3.4770e-5	1.0378e-4	8.1690e-6	1.0871e-4	7.6060e-6
1.00	2.3100e-4	-1.1810e-4	2.5024e-4	-1.2986e-4	2.7754e-4	1.8530e-5	3.0324e-4	1.0861e-5
1.25	3.6391e-4	-2.5516e-4	4.3800e-4	-3.2848e-4	5.2188e-4	-1.9315e-5	6.2846e-4	-9.4080e-5
1.50	5.1907e-4	-4.9649e-4	6.1941e-4	-7.0124e-4	8.1773e-4	-1.7158e-4	9.6061e-4	-3.8485e-4
1.75	6.3026e-4	-8.1732e-4	6.6882e-4	-1.2160e-3	1.0430e-3	-3.7864e-4	1.1340e-3	-7.5807e-4
2.00	6.7955e-4	-1.1681e-3	5.7918e-4	-1.6940e-3	1.1540e-3	-5.6443e-4	1.1182e-3	-1.0441e-3
2.25	6.9639e-4	-1.5030e-3	4.5000e-4	-2.1118e-3	1.1376e-3	-6.5800e-4	9.6817e-4	-1.1266e-3
2.50	7.3318e-4	-1.8198e-3	3.9878e-4	-2.5036e-3	1.0050e-3	-6.0874e-4	7.5100e-4	-9.6843e-4
2.75	8.2087e-4	-2.1503e-3	4.1945e-4	-2.9715e-3	7.6904e-4	-3.9799e-4	5.1023e-4	-5.5595e-4
3.00	9.7234e-4	-2.5486e-3	4.5115e-4	-3.5800e-3	5.4693e-4	-1.9723e-5	3.3127e-4	8.9786e-5
3.25	1.1303e-3	-3.0404e-3	3.9857e-4	-4.2963e-3	1.2564e-4	9.0228e-4	2.7535e-4	8.0447e-4
3.50	1.2942e-3	-3.5069e-3	1.8215e-4	-4.9963e-3	-2.0536e-4	1.0912e-3	3.7108e-4	1.5447e-3

TABLE 39. FORWARD AND BACKWARD SCATTERING AMPLITUDES AT $T = 10°C$, $f = 24$ GHz, AND $\alpha = 60°$

Raindrop Radius (mm)	Forward Scattering				Backward Scattering			
	Vertical Polarization		Horizontal Polarization		Vertical Polarization		Horizontal Polarization	
	Real	Imaginary	Real	Imaginary	Real	Imaginary	Real	Imaginary
0.25	3.8277e-6	-3.2710e-7	3.8360e-6	-3.2836e-7	3.7397e-6	-1.9586e-7	3.7478e-6	-1.9690e-7
0.50	3.1969e-5	-4.9419e-6	3.2402e-5	-5.0415e-6	2.9734e-5	-8.8795e-8	3.0150e-5	-1.4397e-7
0.75	1.0933e-4	-3.3133e-5	1.1301e-4	-3.4618e-5	1.0480e-4	7.9325e-6	1.0875e-4	7.3831e-6
1.00	2.3560e-4	-1.1974e-4	2.5110e-4	-1.2920e-4	2.8264e-4	1.5799e-5	3.0324e-4	9.7956e-6
1.25	3.8445e-4	-2.6869e-4	4.4402e-4	-3.2783e-4	5.4707e-4	-2.5448e-5	3.5123e-4	-9.4643e-5
1.50	5.5307e-4	-5.3847e-4	6.3359e-4	-7.0381e-4	8.6577e-4	-2.0209e-4	9.7110e-4	-3.9128e-4
1.75	6.6253e-4	-9.0432e-4	6.9261e-4	-1.2147e-3	1.1074e-3	-4.5144e-4	1.1561e-3	-7.8550e-4
2.00	6.9208e-4	-1.2994e-3	6.0840e-4	-1.7249e-3	1.2256e-3	-6.7675e-4	1.1503e-3	-1.1021e-3
2.25	6.8401e-4	-1.6707e-3	4.8473e-4	-2.2401e-3	1.2260e-3	-8.0108e-4	1.0178e-3	-1.1226e-3
2.50	6.9968e-4	-2.0198e-3	4.2111e-4	-2.5724e-3	1.1311e-3	-7.7472e-4	8.2793e-4	-1.1081e-3
2.75	7.5555e-4	-2.3895e-3	4.3608e-4	-3.0513e-3	9.5060e-4	-5.7519e-4	6.2068e-4	-7.1636e-4
3.00	9.0366e-4	-2.8314e-3	4.6614e-4	-3.6632e-3	7.4262e-4	-1.9343e-4	4.9975e-4	-1.4307e-4
3.25	1.0427e-3	-3.3702e-3	4.2387e-4	-4.3685e-3	5.3332e-4	3.4366e-4	5.2165e-4	5.9308e-4
3.50	1.1754e-3	-3.8971e-3	2.4517e-4	-5.1227e-3	3.9146e-4	9.8675e-4	7.0786e-4	1.3168e-3

TABLE 40. FORWARD AND BACKWARD SCATTERING AMPLITUDES AT $T = 10°C$, $f = 24$ GHz, AND $\alpha = 45°$

Raindrop Radius (mm)	Forward Scattering				Backward Scattering			
	Vertical Polarization		Horizontal Polarization		Vertical Polarization		Horizontal Polarization	
	Real	Imaginary	Real	Imaginary	Real	Imaginary	Real	Imaginary
0.25	3.8304e-6	-3.2748e-7	3.8359e-6	-3.2832e-7	3.7425e-6	-1.9625e-7	3.7479e-6	-1.9696e-7
0.50	3.2112e-5	-4.9649e-6	3.2400e-5	-5.0313e-6	2.9881e-5	-1.1777e-7	3.0158e-5	-1.5076e-7
0.75	1.1062e-4	-3.3419e-5	1.1307e-4	-3.4409e-5	1.0617e-4	7.5650e-6	1.0880e-4	7.1180e-6
1.00	2.4187e-4	-1.2198e-4	2.5221e-4	-1.2829e-4	2.8941e-4	1.1814e-5	3.0306e-4	8.6832e-6
1.25	4.1257e-4	-2.8680e-4	4.5233e-4	-3.2636e-4	5.7799e-4	-4.2706e-5	6.3238e-4	-9.3717e-5
1.50	5.9977e-4	-5.9586e-4	6.5342e-4	-7.0690e-4	9.2082e-4	-2.8088e-4	9.8463e-4	-3.9738e-4
1.75	7.0685e-4	-1.0241e-3	7.2620e-4	-1.2325e-3	1.1703e-3	-5.7803e-4	1.1880e-3	-8.1763e-4
2.00	7.0827e-4	-1.4815e-3	6.4993e-4	-1.7677e-3	1.2785e-3	-8.7262e-4	1.1962e-3	-1.1769e-3
2.25	6.8360e-4	-1.9018e-3	5.2536e-4	-2.2349e-3	1.2759e-3	-1.0680e-3	1.0894e-3	-1.1539e-3
2.50	6.8030e-4	-2.3003e-3	4.5132e-4	-2.6715e-3	1.2035e-3	-1.0695e-3	9.2842e-4	-1.3115e-3
2.75	6.9091e-4	-2.7317e-3	4.5092e-4	-3.1668e-3	1.0872e-3	-9.0413e-4	7.7309e-4	-1.0372e-3
3.00	7.6648e-4	-3.2270e-3	4.7792e-4	-3.7839e-3	9.6545e-4	-5.5175e-4	6.9099e-4	-5.3334e-4
3.25	8.9009e-4	-3.8314e-3	4.5418e-4	-4.5186e-3	8.8903e-4	-3.8888e-5	7.5801e-4	1.2742e-4
3.50	9.8896e-4	-4.4543e-3	3.1264e-4	-5.3043e-3	9.7766e-4	9.7703e-4	1.0000e-3	8.0321e-4

TABLE 41. FORWARD AND BACKWARD SCATTERING AMPLITUDES AT $T = 10°C$, $f = 24$ GHz, AND $\alpha = 30°$

Raindrop Radius (mm)	Forward Scattering				Backward Scattering			
	Vertical Polarization		Horizontal Polarization		Vertical Polarization		Horizontal Polarization	
	Real	Imaginary	Real	Imaginary	Real	Imaginary	Real	Imaginary
0.25	3.8323e-6	-3.2776e-7	3.8359e-6	-3.2828e-7	3.7453e-6	-1.9666e-7	3.7480e-6	-1.9701e-7
0.50	3.2254e-5	-4.9878e-6	3.2398e-5	-5.0211e-6	3.0027e-5	-1.5091e-7	3.0168e-5	-1.7261e-7
0.75	1.1191e-4	-3.3705e-5	1.1313e-4	-3.4200e-5	1.0752e-4	7.1177e-6	1.0893e-4	6.8083e-6
1.00	2.4815e-4	-1.2433e-4	2.5333e-4	-1.2738e-4	2.9603e-4	1.0477e-5	3.0346e-4	7.7144e-6
1.25	4.4074e-4	-3.0477e-4	4.6085e-4	-3.2462e-4	6.0646e-4	-6.4740e-5	6.3287e-4	-9.2127e-5
1.50	6.4675e-4	-6.5302e-4	6.7357e-4	-7.0874e-4	9.8875e-4	-1.2938e-4	9.9781e-4	-4.0168e-4
1.75	7.5142e-4	-1.1453e-3	7.6076e-4	-1.2003e-3	1.2160e-3	-7.2120e-4	1.2166e-3	-8.4759e-4
2.00	7.2344e-4	-1.6672e-3	6.9302e-4	-1.8116e-3	1.2989e-3	-1.0904e-3	1.2433e-3	-1.2511e-3
2.25	6.3923e-4	-2.1431e-3	5.6735e-4	-2.3102e-3	1.2723e-3	-1.3279e-3	1.1553e-3	-1.4696e-3
2.50	5.8300e-4	-2.5897e-3	4.8101e-4	-2.7767e-3	1.1969e-3	-1.3997e-3	1.0253e-3	-1.5308e-3
2.75	5.8057e-4	-3.0690e-3	4.6194e-4	-3.2914e-3	1.1087e-3	-1.2961e-3	9.0427e-4	-1.3604e-3
3.00	6.4136e-4	-3.6337e-3	4.7658e-4	-3.9132e-3	1.0422e-3	-1.0057e-3	8.4666e-4	-9.9695e-4
3.25	6.9784e-4	-4.3056e-3	4.6822e-4	-4.6530e-3	1.0583e-3	-5.4793e-4	9.2258e-4	-4.5514e-4
3.50	7.0553e-4	-5.0474e-3	3.5037e-4	-5.4939e-3	1.2708e-3	-4.1803e-5	1.1557e-3	1.0471e-4

TABLE 42. FORWARD AND BACKWARD SCATTERING AMPLITUDES AT $T = 10°C$, $f = 24$ GHz, AND $\alpha = 15°$

Raindrop Radius (mm)	Forward Scattering				Backward Scattering			
	Vertical Polarization		Horizontal Polarization		Vertical Polarization		Horizontal Polarization	
	Real	Imaginary	Real	Imaginary	Real	Imaginary	Real	Imaginary
0.25	3.8352e-6	-3.2814e-7	3.8359e-6	-3.2825e-7	3.7473e-6	-1.9695e-7	3.7480e-6	-1.9705e-7
0.50	3.2358e-5	-5.0047e-6	3.2397e-5	-5.0136e-6	3.0133e-5	-1.7826e-7	3.0170e-5	-1.8245e-7
0.75	1.1285e-4	-3.3915e-5	1.1318e-4	-3.4047e-5	1.0850e-4	6.7618e-6	1.0885e-4	6.6905e-6
1.00	2.5276e-4	-1.2587e-4	2.5415e-4	-1.2672e-4	3.0082e-4	7.8295e-6	3.0264e-4	7.0576e-6
1.25	4.6140e-4	-3.1789e-4	4.6674e-4	-3.2322e-4	6.2603e-4	-8.2907e-5	6.3296e-4	-9.0563e-5
1.50	6.8131e-4	-6.9517e-4	6.8849e-4	-7.1016e-4	1.0002e-3	-3.8384e-4	1.0074e-3	-4.0390e-4
1.75	7.8420e-4	-1.2349e-3	7.8864e-4	-1.2631e-3	1.2408e-3	-8.3366e-4	1.2396e-3	-8.4844e-4
2.00	7.3390e-4	-1.8055e-3	7.2551e-4	-1.8448e-3	1.2964e-3	-1.2612e-3	1.2789e-3	-1.3057e-3
2.25	6.1076e-4	-2.3324e-3	5.8966e-4	-2.3674e-3	1.2401e-3	-1.5470e-3	1.2038e-3	-1.5454e-3
2.50	5.3072e-4	-2.8074e-3	5.0247e-4	-2.8378e-3	1.1472e-3	-1.6650e-3	1.0946e-3	-1.7021e-3
2.75	5.0196e-4	-3.3287e-3	4.6669e-4	-3.3885e-3	1.0558e-3	-1.6151e-3	9.9243e-4	-1.6350e-3
3.00	5.1700e-4	-3.9388e-3	4.7173e-4	-4.0139e-3	1.0043e-3	-1.3839e-3	9.3980e-4	-1.3805e-3
3.25	5.1310e-4	-4.6620e-3	4.6777e-4	-4.7562e-3	1.0412e-3	-9.4884e-4	9.9771e-4	-9.5656e-4
3.50	4.7471e-4	-5.5132e-3	3.7802e-4	-5.6300e-3	1.2353e-3	-5.8006e-4	1.1745e-3	-5.2774e-4

TABLE 43. FORWARD AND BACKWARD SCATTERING AMPLITUDES
AT $T = 10°C$, $f = 28$ GHz, AND $\alpha = 90°$

Raindrop Radius (mm)	Forward Scattering				Backward Scattering			
	Vertical Polarization		Horizontal Polarization		Vertical Polarization		Horizontal Polarization	
	Real	Imaginary	Real	Imaginary	Real	Imaginary	Real	Imaginary
0.25	5.2077e-6	-5.2704e-7	5.2227e-6	-5.2974e-7	5.0727e-6	-3.0492e-7	5.0874e-6	-3.0695e-7
0.50	4.3560e-5	-8.3548e-6	4.4353e-5	-8.5818e-6	4.0582e-5	-1.3289e-7	4.1358e-5	-2.2666e-7
0.75	1.4435e-4	-5.4846e-5	1.4874e-4	-5.8373e-5	1.4709e-4	8.7473e-6	1.5720e-4	6.9854e-6
1.00	2.9622e-4	-1.8523e-4	3.2353e-4	-2.0822e-4	3.8629e-4	-1.4684e-5	4.2302e-4	-3.2720e-5
1.25	4.3623e-4	-3.9001e-4	5.1289e-4	-5.3183e-4	6.4331e-4	-1.3269e-4	7.6173e-4	-2.6479e-4
1.50	5.5007e-4	-7.1113e-4	5.7055e-4	-1.0163e-3	8.6524e-4	-3.5177e-4	9.4951e-4	-6.2826e-4
1.75	5.9417e-4	-1.0581e-3	4.7481e-4	-1.4871e-3	9.4410e-4	-5.4122e-4	9.2111e-4	-8.8605e-4
2.00	6.1680e-4	-1.3796e-3	3.5640e-4	-1.8828e-3	8.7207e-4	-6.0955e-4	7.4906e-4	-9.1656e-4
2.25	6.7194e-4	-1.6987e-3	3.5337e-4	-2.2869e-3	6.7335e-4	-5.0089e-4	5.3280e-4	-6.8350e-4
2.50	7.9780e-4	-2.0576e-3	3.9069e-4	-2.8092e-3	5.5983e-4	-2.1188e-4	2.8601e-4	-1.7603e-4
2.75	9.5817e-4	-2.5137e-3	3.6600e-4	-3.4799e-3	-1.1628e-5	2.5515e-4	1.3442e-4	5.2975e-4
3.00	1.0872e-3	-3.0656e-3	2.1650e-4	-4.1906e-3	-3.4857e-4	8.1853e-4	1.3781e-4	1.2153e-3
3.25	1.1444e-3	-3.6659e-3	6.9963e-5	-4.8716e-3	-5.9886e-4	1.3132e-3	1.6913e-4	1.6666e-3
3.50	1.2232e-3	-4.1694e-3	-1.0144e-4	-5.5060e-3	-7.8453e-4	1.5579e-3	1.6423e-4	1.7296e-3

TABLE 44. FORWARD AND BACKWARD SCATTERING AMPLITUDES
AT $T = 10°C$, $f = 28$ GHz, AND $\alpha = 75°$

Raindrop Radius (mm)	Forward Scattering				Backward Scattering			
	Vertical Polarization		Horizontal Polarization		Vertical Polarization		Horizontal Polarization	
	Real	Imaginary	Real	Imaginary	Real	Imaginary	Real	Imaginary
0.25	5.2087e-6	-5.2720e-7	5.2226e-6	-5.2972e-7	5.0737e-6	-3.0497e-7	5.0874e-6	-3.0700e-7
0.50	4.3612e-5	-8.3654e-6	4.4352e-5	-8.5645e-6	4.0639e-5	-1.3685e-7	4.1361e-5	-2.4003e-7
0.75	1.4493e-4	-5.5290e-5	1.5110e-4	-5.8458e-5	1.4776e-4	8.4055e-6	1.5492e-4	6.9317e-6
1.00	2.9853e-4	-1.8652e-4	3.2403e-4	-2.0797e-4	3.8926e-4	-1.5337e-5	4.2315e-4	-3.3987e-5
1.25	4.4460e-4	-4.0052e-4	5.1646e-4	-5.3302e-4	6.6198e-4	-1.2457e-4	7.6633e-4	-2.6487e-4
1.50	5.5792e-4	-7.3587e-4	5.7871e-4	-1.0206e-3	9.0083e-4	-3.4685e-4	9.5950e-4	-6.3580e-4
1.75	5.9419e-4	-1.0982e-3	4.8914e-4	-1.4974e-3	9.9694e-4	-5.4016e-4	9.3813e-4	-9.0779e-4
2.00	6.0544e-4	-1.4340e-3	3.8193e-4	-1.9009e-3	9.5581e-4	-6.0726e-4	7.8358e-4	-9.4955e-4
2.25	6.5773e-4	-1.7578e-3	3.5768e-4	-2.3070e-3	7.9038e-4	-5.0095e-4	5.6489e-4	-7.2169e-4
2.50	7.7677e-4	-2.1298e-3	3.9812e-4	-2.8314e-3	5.2719e-4	-2.0130e-4	3.4837e-4	-2.1563e-4
2.75	9.2959e-4	-2.6008e-3	3.8425e-4	-3.5047e-3	2.1816e-4	2.8457e-4	2.4520e-4	4.9543e-4
3.00	1.0516e-3	-3.1696e-3	2.5645e-4	-4.2250e-3	-5.7044e-5	8.7276e-4	3.0336e-4	1.1959e-3
3.25	1.1197e-3	-3.7802e-3	8.9962e-5	-4.9130e-3	-2.5118e-4	1.4135e-3	4.2636e-4	1.6678e-3
3.50	1.2026e-3	-4.3160e-3	-7.8473e-5	-5.5628e-3	-4.3793e-4	1.7305e-3	4.6390e-4	1.7930e-3

TABLE 45. FORWARD AND BACKWARD SCATTERING AMPLITUDES
AT $T = 10°C$, $f = 28$ GHz, AND $\alpha = 60°$

Raindrop Radius (mm)	Forward Scattering				Backward Scattering			
	Vertical Polarization		Horizontal Polarization		Vertical Polarization		Horizontal Polarization	
	Real	Imaginary	Real	Imaginary	Real	Imaginary	Real	Imaginary
0.25	5.2114e-6	-5.2764e-7	5.2226e-6	-5.2967e-7	5.0765e-6	-3.0542e-7	5.0875e-6	-3.0708e-7
0.50	4.3757e-5	-8.3943e-6	4.4352e-5	-8.5645e-5	4.0790e-5	-1.6615e-7	4.1370e-5	-2.6087e-7
0.75	1.4626e-4	-5.5695e-5	1.5123e-4	-5.8242e-5	1.4922e-4	7.9846e-6	1.5496e-4	6.6035e-6
1.00	3.0487e-4	-1.9004e-4	3.2546e-4	-2.0730e-4	3.9647e-4	-1.8985e-4	4.2346e-4	-3.5371e-5
1.25	4.6773e-4	-4.2705e-4	5.2540e-4	-5.3386e-4	6.9536e-4	-1.4008e-4	7.7272e-4	-2.6563e-4
1.50	5.8019e-4	-8.0015e-4	5.9636e-4	-1.0297e-3	9.5063e-4	-3.9584e-4	9.7724e-4	-6.5093e-4
1.75	5.9729e-4	-1.2002e-3	5.1109e-4	-1.5223e-3	1.0582e-3	-6.2406e-4	9.6677e-4	-9.5000e-4
2.00	5.8487e-4	-1.5666e-3	4.0185e-4	-1.9433e-3	1.0368e-3	-7.1815e-4	8.2884e-4	-1.0267e-3
2.25	6.1684e-4	-1.9197e-3	3.7070e-4	-2.3628e-3	9.1717e-4	-6.3136e-4	6.3968e-4	-8.3999e-4
2.50	7.1783e-4	-2.3246e-3	4.0599e-4	-2.8920e-3	7.2826e-4	-3.4225e-4	6.6758e-4	-3.7768e-4
2.75	8.5247e-4	-2.8324e-3	4.0191e-4	-3.5690e-3	5.2137e-4	1.4259e-4	4.1844e-4	3.0070e-4
3.00	9.6247e-4	-3.4386e-3	2.9427e-4	-4.3075e-3	5.3985e-4	7.4389e-4	5.4083e-4	1.0043e-3
3.25	1.0317e-3	-4.0969e-3	1.1451e-4	-5.0279e-3	2.6503e-4	1.3280e-3	7.4160e-4	1.5322e-3
3.50	1.1189e-3	-4.7143e-3	-1.9895e-5	-5.7226e-3	1.6371e-4	1.7590e-3	8.7153e-4	1.7822e-3

TABLE 46. FORWARD AND BACKWARD SCATTERING AMPLITUDES
AT $T = 10°C$, $f = 28$ GHz, AND $\alpha = 45°$

Raindrop Radius (mm)	Forward Scattering				Backward Scattering			
	Vertical Polarization		Horizontal Polarization		Vertical Polarization		Horizontal Polarization	
	Real	Imaginary	Real	Imaginary	Real	Imaginary	Real	Imaginary
0.25	5.2151e-6	-5.2825e-7	5.2226e-6	-5.2960e-7	5.0802e-6	-3.0605e-7	5.0876e-6	-3.0717e-7
0.50	4.3954e-5	-8.4337e-6	4.4351e-5	-8.5472e-6	4.0996e-5	-2.1547e-7	4.1381e-5	-2.8536e-7
0.75	1.4809e-4	-5.6249e-5	1.5140e-4	-5.7947e-5	1.5118e-4	7.2586e-6	1.5499e-4	6.2253e-6
1.00	3.1353e-4	-1.9485e-4	3.2728e-4	-2.0636e-4	4.0587e-4	-2.4957e-5	4.2367e-4	-3.6679e-5
1.25	4.9945e-4	-4.6265e-4	5.3786e-4	-5.3427e-4	7.3290e-4	-1.7491e-4	7.7993e-4	-2.6594e-4
1.50	6.1090e-4	-8.8800e-4	6.2128e-4	-1.0417e-3	9.9682e-4	-4.8639e-4	1.0004e-3	-6.6948e-4
1.75	6.0137e-4	-1.3407e-3	5.4248e-4	-1.5565e-3	1.0961e-3	-7.7168e-4	1.0055e-3	-1.0057e-3
2.00	5.5520e-4	-1.7506e-3	4.3028e-4	-2.0030e-3	1.0769e-3	-9.1228e-4	8.8878e-4	-1.1349e-3
2.25	5.5655e-4	-2.1461e-3	3.8799e-4	-2.4431e-3	9.8865e-4	-8.6567e-4	7.3254e-4	-1.0173e-3
2.50	6.2757e-4	-2.5982e-3	4.1280e-4	-2.9799e-3	8.6703e-4	-6.1225e-4	6.0184e-4	-6.3904e-4
2.75	7.3026e-4	-3.1600e-3	4.1910e-4	-3.6611e-3	7.6404e-4	-1.5788e-4	5.9022e-4	-3.8171e-5
3.00	8.1033e-4	-3.8229e-3	3.3781e-4	-4.4232e-3	7.3519e-4	4.2767e-4	7.5605e-4	6.3651e-4
3.25	8.5777e-4	-4.5470e-3	2.0282e-4	-5.1902e-3	7.8500e-4	1.0308e-3	1.0322e-3	1.2113e-3
3.50	9.1953e-4	-5.2709e-3	4.1891e-5	-5.9555e-3	8.7530e-4	1.5188e-3	1.2820e-3	1.5818e-3

TABLE 47. FORWARD AND BACKWARD SCATTERING AMPLITUDES
AT $T = 10°C$, $f = 28$ GHz, AND $\alpha = 30°$

Raindrop Radius (mm)	Forward Scattering				Backward Scattering			
	Vertical Polarization		Horizontal Polarization		Vertical Polarization		Horizontal Polarization	
	Real	Imaginary	Real	Imaginary	Real	Imaginary	Real	Imaginary
0.25	5.2188e-6	-5.2685e-7	5.2226e-6	-5.2953e-7	5.0840e-6	-3.0670e-7	5.0877e-6	-3.0726e-7
0.50	4.4151e-5	-8.4732e-6	4.4350e-5	-8.5299e-6	4.1200e-5	-2.7083e-7	4.1392e-5	-3.0837e-7
0.75	1.4991e-4	-5.6803e-5	1.5157e-4	-5.7652e-5	1.5311e-4	6.4347e-6	1.5501e-4	5.8748e-6
1.00	3.2221e-4	-1.9966e-4	3.2909e-4	-2.0542e-4	4.1498e-4	-3.1573e-5	4.2380e-4	-3.7744e-5
1.25	5.3127e-4	-4.9849e-4	5.5047e-4	-5.3430e-4	7.6498e-4	-2.1703e-4	7.8649e-4	-2.6535e-4
1.50	6.4187e-4	-9.7619e-4	6.4689e-4	-1.0533e-3	1.0280e-3	-5.9010e-4	1.0237e-3	-6.8659e-4
1.75	6.0529e-4	-1.4829e-3	5.7516e-4	-1.5913e-3	1.1032e-3	-9.3821e-4	1.0447e-3	-1.0613e-3
2.00	5.2378e-4	-1.9384e-3	4.5988e-4	-2.0653e-3	1.0645e-3	-1.1310e-3	9.4797e-4	-1.2477e-3
2.25	4.9111e-4	-2.3790e-3	4.0455e-4	-2.5283e-3	9.8118e-4	-1.1399e-3	8.1990e-4	-1.2111e-3
2.50	5.2663e-4	-2.8822e-3	4.1629e-4	-3.0747e-3	8.9373e-4	-9.2942e-4	7.1644e-4	-3.3875e-4
2.75	5.8819e-4	-3.5026e-3	4.2734e-4	-3.7586e-3	8.5897e-4	-5.2405e-4	7.1822e-4	-4.4858e-4
3.00	6.2092e-4	-4.2302e-3	3.7060e-4	-4.5423e-3	9.3452e-4	2.4330e-5	8.9137e-4	1.5951e-4
3.25	6.1383e-4	-5.0233e-3	2.5298e-4	-5.3586e-3	1.1258e-3	6.1276e-4	1.2091e-3	7.4293e-4
3.50	5.8922e-4	-5.8555e-3	7.8857e-5	-6.2090e-3	1.3864e-3	1.0802e-3	1.5392e-3	1.1824e-3

TABLE 48. FORWARD AND BACKWARD SCATTERING AMPLITUDES
AT $T = 10°C$, $f = 28$ GHz, AND $\alpha = 15°$

Raindrop Radius (mm)	Forward Scattering				Backward Scattering			
	Vertical Polarization		Horizontal Polarization		Vertical Polarization		Horizontal Polarization	
	Real	Imaginary	Real	Imaginary	Real	Imaginary	Real	Imaginary
0.25	5.2215e-6	-5.2930e-7	5.2226e-6	-5.2948e-7	5.0867e-6	-3.0717e-7	5.0877e-6	-3.0732e-7
0.50	4.4296e-5	-8.5020e-6	4.4349e-5	-8.5173e-6	4.1348e-5	-3.1423e-7	4.1400e-5	-3.2473e-7
0.75	1.5125e-4	-5.7208e-5	1.5169e-4	-5.7436e-5	1.5451e-4	5.7848e-6	1.5502e-4	5.6275e-6
1.00	3.2857e-4	-2.0319e-4	3.3042e-4	-2.0474e-4	4.2151e-4	-3.6728e-5	4.2386e-4	-3.8434e-5
1.25	5.5461e-4	-5.2453e-4	5.5976e-4	-5.3415e-4	7.8570e-4	-2.5093e-4	7.9109e-4	-2.6535e-4
1.50	6.5471e-4	-1.0410e-3	6.6603e-4	-1.0617e-3	1.0433e-3	-6.7170e-4	1.0410e-3	-6.9837e-4
1.75	6.0807e-4	-1.5880e-3	5.9986e-4	-1.6172e-3	1.0923e-3	-1.0683e-3	1.0741e-3	-1.1022e-3
2.00	4.9970e-4	-2.0783e-3	4.8230e-4	-2.1124e-3	1.0269e-3	-1.3017e-3	9.9142e-4	-1.3336e-3
2.25	4.3993e-4	-2.5539e-3	4.1628e-4	-2.5940e-3	9.3108e-4	-1.3426e-3	8.8146e-4	-1.3635e-3
2.50	4.4579e-4	-3.0966e-3	4.1563e-4	-3.1486e-3	8.4724e-4	-1.1815e-3	7.9089e-4	-1.1825e-3
2.75	4.7173e-4	-3.7641e-3	4.2766e-4	-3.8338e-3	8.3459e-4	-8.1896e-4	7.8591e-4	-7.9440e-4
3.00	4.5789e-4	-4.5459e-3	3.8808e-4	-4.6321e-3	9.6080e-4	-9.0412e-4	9.3905e-4	-2.5974e-4
3.25	3.8579e-4	-5.3927e-3	2.8209e-4	-5.4857e-3	1.2435e-3	2.5798e-4	1.2572e-3	3.0359e-4
3.50	2.4039e-4	-6.3110e-3	8.7258e-5	-6.4087e-3	1.5703e-3	7.1018e-4	1.5986e-3	7.6138e-4

TABLE 49. FORWARD AND BACKWARD SCATTERING AMPLITUDES AT $T = 10°C$, $f = 30$ GHz, AND $\alpha = 90°$

| Raindrop Radius (mm) | Forward Scattering | | | | Backward Scattering | | | |
| | Vertical Polarization | | Horizontal Polarization | | Vertical Polarization | | Horizontal Polarization | |
	Real	Imaginary	Real	Imaginary	Real	Imaginary	Real	Imaginary
0.25	5.9785e-6	-6.5257e-7	5.9957e-6	-6.5591e-7	5.8150e-6	-3.7242e-7	5.8319e-6	-3.7505e-7
0.50	5.0110e-5	-1.0591e-5	5.1024e-5	-1.0880e-5	4.6802e-5	-2.4303e-7	4.7705e-5	-3.6603e-7
0.75	1.6381e-4	-6.8818e-5	1.6843e-4	-7.3359e-5	1.7233e-4	6.9677e-6	1.8455e-4	4.2618e-6
1.00	3.2953e-4	-2.2898e-4	3.5918e-4	-2.5947e-4	4.4118e-4	-4.3525e-5	4.8108e-4	-6.9313e-5
1.25	4.6222e-4	-4.7384e-4	5.2181e-4	-6.4776e-4	6.8869e-4	-1.9840e-4	7.9179e-4	-3.6095e-4
1.50	5.4312e-4	-8.2323e-4	5.0829e-4	-1.1427e-3	8.5714e-4	-4.2821e-4	8.8968e-4	-7.0955e-4
1.75	5.6418e-4	-1.1665e-3	3.8868e-4	-1.5728e-3	8.6408e-4	-5.7560e-4	7.9055e-4	-8.7306e-4
2.00	6.0101e-4	-1.4786e-3	3.0550e-4	-1.9543e-3	7.1956e-4	-5.6078e-4	5.7470e-4	-7.7065e-4
2.25	6.9265e-4	-1.8244e-3	3.5723e-4	-2.4186e-3	4.5954e-4	-3.3771e-4	3.5692e-4	-4.3895e-4
2.50	8.4468e-4	-2.2520e-3	3.7051e-4	-3.0372e-3	1.1157e-4	7.6613e-5	1.6844e-4	2.3049e-4
2.75	9.8223e-4	-2.7881e-3	2.6001e-4	-3.7449e-3	-2.8877e-4	6.3194e-4	1.7779e-4	9.6023e-4
3.00	1.0467e-3	-3.3883e-3	1.0993e-4	-4.4305e-3	-4.8661e-4	1.1622e-3	1.6233e-4	1.4824e-3
3.25	1.0861e-3	-3.9777e-3	-1.9002e-4	-5.1092e-3	-6.2984e-4	1.4962e-3	1.8263e-4	1.6416e-3
3.50	1.1898e-3	-4.4873e-3	-1.6048e-4	-5.8227e-4	-7.2264e-4	1.4525e-3	4.2207e-5	1.3542e-3

TABLE 50. FORWARD AND BACKWARD SCATTERING AMPLITUDES AT $T = 10°C$, $f = 30$ GHz, AND $\alpha = 75°$

| Raindrop Radius (mm) | Forward Scattering | | | | Backward Scattering | | | |
| | Vertical Polarization | | Horizontal Polarization | | Vertical Polarization | | Horizontal Polarization | |
	Real	Imaginary	Real	Imaginary	Real	Imaginary	Real	Imaginary
0.25	5.9797e-6	-6.5277e-7	5.9957e-6	-6.5589e-7	5.8162e-6	-3.7262e-7	5.8319e-6	-3.7510e-7
0.50	5.0171e-5	-1.0604e-5	5.1024e-5	-1.0874e-5	4.6869e-5	-2.4844e-7	4.7709e-5	-3.8261e-7
0.75	1.6450e-4	-6.9445e-5	1.7155e-4	-7.3505e-5	1.7312e-4	6.4673e-6	1.8153e-4	4.2318e-6
1.00	3.3211e-4	-2.3077e-4	3.5980e-4	-2.5923e-4	4.4464e-4	-4.4532e-5	4.8124e-4	-7.0829e-5
1.25	4.6998e-4	-4.8713e-4	5.2611e-4	-6.4953e-4	7.0148e-4	-1.8988e-4	7.9798e-4	-3.6142e-4
1.50	5.4731e-4	-8.5079e-4	5.1756e-4	-1.1485e-3	8.9756e-4	-4.2255e-4	9.0210e-4	-7.1856e-4
1.75	5.5885e-4	-1.2076e-3	4.0538e-4	-1.5852e-3	9.2763e-4	-5.7108e-4	8.1343e-4	-8.9407e-4
2.00	5.8323e-4	-1.5345e-3	3.3812e-4	-1.9749e-3	8.1965e-4	-5.5127e-4	6.2490e-4	-8.0424e-4
2.25	6.7474e-4	-1.8812e-3	3.5992e-4	-2.4374e-3	5.9813e-4	-3.3771e-4	4.0320e-4	-4.2294e-4
2.50	8.1923e-4	-2.3228e-3	3.8223e-4	-3.0576e-3	3.0704e-4	9.8898e-5	2.4879e-4	2.1910e-4
2.75	9.5004e-4	-2.8733e-3	2.8958e-4	-3.7719e-3	7.3356e-5	6.7152e-4	2.6127e-4	9.3947e-4
3.00	1.0225e-3	-3.4827e-3	1.2682e-4	-4.4643e-3	-1.7417e-4	1.2398e-3	4.6127e-4	1.4784e-3
3.25	1.0683e-3	-4.0959e-3	7.4745e-5	-5.1529e-3	-3.0009e-4	1.6225e-3	4.4367e-4	1.6769e-3
3.50	1.1729e-3	-4.6446e-3	-1.3420e-4	-5.8778e-3	-4.6771e-4	1.6620e-3	2.9910e-4	1.4763e-3

TABLE 51. FORWARD AND BACKWARD SCATTERING AMPLITUDES AT $T = 10°C$, $f = 30$ GHz, AND $\alpha = 60°$

| Raindrop Radius (mm) | Forward Scattering | | | | Backward Scattering | | | |
| | Vertical Polarization | | Horizontal Polarization | | Vertical Polarization | | Horizontal Polarization | |
	Real	Imaginary	Real	Imaginary	Real	Imaginary	Real	Imaginary
0.25	5.9828e-6	-6.5582e-7	5.9957e-6	-6.5332e-7	5.8193e-6	-3.7317e-7	5.8320e-6	-3.7520e-7
0.50	5.0338e-5	-1.0641e-5	5.1024e-5	-1.0858e-5	4.7046e-5	-2.8612e-7	4.7719e-5	-4.0855e-7
0.75	1.6605e-4	-6.9997e-5	1.7173e-4	-7.3261e-5	1.7485e-4	5.8921e-6	1.8158e-4	3.8492e-6
1.00	3.3920e-4	-2.3569e-4	3.6160e-4	-2.5858e-4	4.5283e-4	-4.9581e-5	4.8184e-4	-7.2439e-5
1.25	4.9158e-4	-5.2094e-4	5.3651e-4	-6.5178e-4	7.4676e-4	-2.1099e-4	8.0708e-4	-3.6364e-4
1.50	5.6000e-4	-9.2177e-4	5.3538e-4	-1.1616e-3	9.4612e-4	-4.7690e-4	9.2270e-4	-7.3876e-4
1.75	5.4931e-4	-1.3105e-3	4.2433e-4	-1.6145e-3	9.8961e-4	-6.5458e-4	8.4604e-4	-9.4315e-4
2.00	5.5159e-4	-1.6643e-3	3.5216e-4	-2.0193e-3	9.1508e-4	-6.5792e-4	6.7886e-4	-8.8969e-4
2.25	6.2383e-4	-2.0413e-3	3.6909e-4	-2.4899e-3	7.5355e-4	-4.5430e-4	4.9123e-4	-5.4998e-4
2.50	7.5038e-4	-2.5123e-3	3.9278e-4	-3.1115e-3	5.5214e-4	-3.5501e-5	3.8598e-4	5.4254e-5
2.75	8.6776e-4	-3.0956e-3	3.1795e-4	-3.8374e-3	3.7807e-4	5.4181e-4	5.5443e-4	7.6442e-4
3.00	9.3976e-4	-3.7457e-3	1.7097e-4	-4.5582e-3	2.7356e-4	1.1396e-3	6.4117e-4	1.3435e-3
3.25	9.9393e-4	-4.4211e-3	5.0255e-5	-5.2760e-3	2.1392e-4	1.6015e-3	7.8507e-4	1.6426e-3
3.50	1.1003e-3	-5.0682e-3	-7.0611e-5	-6.0338e-3	6.5640e-5	1.8200e-3	7.2434e-4	1.6185e-3

TABLE 52. FORWARD AND BACKWARD SCATTERING AMPLITUDES AT $T = 10°C$, $f = 30$ GHz, AND $\alpha = 45°$

| Raindrop Radius (mm) | Forward Scattering | | | | Backward Scattering | | | |
| | Vertical Polarization | | Horizontal Polarization | | Vertical Polarization | | Horizontal Polarization | |
	Real	Imaginary	Real	Imaginary	Real	Imaginary	Real	Imaginary
0.25	5.9870e-6	-6.5406e-7	5.9956e-6	-6.5573e-7	5.8237e-6	-3.7393e-7	5.8321e-6	-3.7532e-7
0.50	5.0567e-5	-1.0692e-5	5.1024e-5	-1.0836e-5	4.7285e-5	-3.4910e-7	4.7733e-5	-4.3908e-7
0.75	1.6818e-4	-7.0751e-5	1.7197e-4	-7.2927e-5	1.7715e-4	4.9199e-6	1.8162e-4	3.4165e-6
1.00	3.4888e-4	-2.4240e-4	3.6383e-4	-2.5767e-4	4.6339e-4	-5.7706e-5	4.8241e-4	-7.3928e-5
1.25	5.2125e-4	-5.6666e-4	5.5110e-4	-6.5410e-4	7.8423e-4	-2.5584e-4	8.1782e-4	-3.6601e-4
1.50	5.7763e-4	-1.0187e-3	5.6071e-4	-1.1791e-3	9.9381e-4	-5.7698e-4	9.4956e-4	-7.6485e-4
1.75	5.3626e-4	-1.4519e-3	4.5169e-4	-1.6552e-3	1.0210e-3	-8.0309e-4	8.8905e-4	-1.0103e-3
2.00	5.0707e-4	-1.8448e-3	3.7209e-4	-2.0858e-3	9.6321e-4	-8.4730e-4	7.4715e-4	-1.0141e-3
2.25	5.5012e-4	-2.2636e-3	3.7693e-4	-2.5653e-3	8.5015e-4	-6.8253e-4	5.9648e-4	-7.4945e-4
2.50	6.6449e-4	-2.7815e-3	4.0275e-4	-3.1895e-3	7.3359e-4	-2.9797e-4	5.2684e-4	-2.2403e-4
2.75	7.3444e-4	-3.4160e-3	3.5049e-4	-3.9303e-3	6.7612e-4	2.5591e-4	6.3113e-4	4.4161e-4
3.00	7.8456e-4	-4.1246e-3	2.2429e-4	-4.6913e-3	7.0340e-4	8.6068e-4	8.7800e-4	1.0487e-3
3.25	8.2278e-4	-4.8763e-3	1.0595e-4	-5.4539e-3	7.7711e-4	1.3874e-3	1.1290e-3	1.4589e-3
3.50	9.0780e-4	-5.6450e-3	-1.2731e-5	-6.2644e-3	8.0342e-4	1.7363e-3	1.2276e-3	1.6242e-3

TABLE 53. FORWARD AND BACKWARD SCATTERING AMPLITUDES AT $T = 10°C$, $f = 30$ GHz, AND $\alpha = 30°$

| Raindrop Radius (mm) | Forward Scattering | | | | Backward Scattering | | | |
| | Vertical Polarization | | Horizontal Polarization | | Vertical Polarization | | Horizontal Polarization | |
	Real	Imaginary	Real	Imaginary	Real	Imaginary	Real	Imaginary
0.25	5.9913e-6	-6.5481e-7	5.9956e-6	-6.5564e-7	5.8280e-6	-3.7474e-7	5.8322e-6	-3.7543e-7
0.50	5.0795e-5	-1.0742e-5	5.1024e-5	-1.0815e-5	4.7522e-5	-4.1956e-7	4.7746e-5	-4.6776e-7
0.75	1.7032e-4	-7.1505e-5	1.7221e-4	-7.2594e-5	1.7941e-4	3.8257e-6	1.8163e-4	3.0195e-6
1.00	3.5858e-4	-2.4912e-4	3.6607e-4	-2.5676e-4	4.7353e-4	-6.8627e-5	4.8291e-4	-7.5122e-5
1.25	5.5104e-4	-6.1218e-4	5.6594e-4	-6.5600e-4	8.1406e-4	-3.0916e-4	8.2794e-4	-3.6743e-4
1.50	5.9559e-4	-1.1160e-3	5.8689e-4	-1.1964e-3	1.0017e-3	-6.9110e-4	9.7643e-4	-7.8992e-4
1.75	5.2318e-4	-1.5948e-3	4.8027e-4	-1.6968e-3	1.0142e-3	-9.7030e-4	9.3192e-4	-1.0788e-3
2.00	4.6118e-4	-2.0293e-3	3.9269e-4	-2.1486e-3	9.4663e-4	-1.0615e-3	8.1272e-4	-1.1471e-3
2.25	4.7168e-4	-2.4940e-3	3.8375e-4	-2.6463e-3	8.5407e-4	-9.4289e-4	6.8981e-4	-9.7303e-4
2.50	5.3139e-4	-3.0645e-3	4.0698e-4	-3.2731e-3	7.8813e-4	-6.0412e-4	6.3747e-4	-5.5281e-4
2.75	5.7577e-4	-3.7590e-3	3.7482e-4	-4.0272e-3	8.1782e-4	-8.7665e-5	7.4640e-4	3.5365e-5
3.00	5.7492e-4	-4.5323e-3	2.6896e-4	-4.8304e-3	9.6975e-4	5.0071e-4	1.0202e-3	6.3702e-4
3.25	5.5581e-4	-5.3497e-3	1.4752e-4	-5.6441e-3	1.2027e-3	1.0461e-3	1.3632e-3	1.1220e-3
3.50	5.5503e-4	-6.2222e-3	4.8636e-6	-6.5189e-3	1.4210e-3	1.4215e-3	1.6092e-3	1.4308e-3

TABLE 54. FORWARD AND BACKWARD SCATTERING AMPLITUDES AT $T = 10°C$, $f = 30$ GHz, AND $\alpha = 15°$

| Raindrop Radius (mm) | Forward Scattering | | | | Backward Scattering | | | |
| | Vertical Polarization | | Horizontal Polarization | | Vertical Polarization | | Horizontal Polarization | |
	Real	Imaginary	Real	Imaginary	Real	Imaginary	Real	Imaginary
0.25	5.9944e-6	-6.5535e-7	5.9956e-6	-6.5556e-7	5.8311e-6	-3.7533e-7	5.8322e-6	-3.7551e-7
0.50	5.0963e-5	-1.0779e-5	5.1024e-5	-1.0799e-5	4.7695e-5	-4.7471e-7	4.7755e-5	-4.8816e-7
0.75	1.7188e-4	-7.2058e-5	1.7239e-4	-7.2349e-5	1.8104e-4	2.9664e-6	1.8163e-4	2.7411e-6
1.00	3.6569e-4	-2.5405e-4	3.6770e-4	-2.5610e-4	4.8076e-4	-7.3545e-5	4.8325e-4	-7.5886e-5
1.25	5.7292e-4	-6.4543e-4	5.7691e-4	-6.5719e-4	8.3204e-4	-3.5172e-4	8.3522e-4	-3.6786e-4
1.50	6.0894e-4	-1.1874e-3	6.0656e-4	-1.2090e-3	1.0048e-3	-7.8051e-4	9.9649e-4	-8.0778e-4
1.75	5.1365e-4	-1.7006e-3	5.0203e-4	-1.7279e-3	9.8887e-4	-1.1002e-3	9.6378e-4	-1.1300e-3
2.00	4.2676e-4	-2.1671e-3	4.0822e-4	-2.1992e-3	9.0082e-4	-1.2270e-3	8.5993e-4	-1.2500e-3
2.25	4.1126e-4	-2.6680e-3	3.8744e-4	-2.7091e-3	8.0421e-4	-1.1452e-3	7.5296e-4	-1.1520e-3
2.50	4.4028e-4	-3.2812e-3	4.0650e-4	-3.3381e-3	7.5111e-4	-8.4288e-4	7.0137e-4	-8.2525e-4
2.75	4.4326e-4	-4.0270e-3	3.8769e-4	-4.1013e-3	8.2117e-4	-3.5585e-4	7.9218e-4	-3.1516e-4
3.00	3.8312e-4	-4.8529e-3	2.9573e-4	-4.9361e-3	1.0535e-3	2.1242e-4	1.0597e-3	2.5981e-4
3.25	2.8875e-4	-5.7116e-3	1.6848e-4	-5.7919e-3	1.4062e-3	7.4366e-4	1.4463e-3	7.7476e-4
3.50	1.5530e-4	-6.6462e-3	-1.3593e-5	-6.7230e-3	1.7151e-3	1.1363e-3	1.7610e-3	1.1637e-3

TABLE 55. FORWARD AND BACKWARD SCATTERING AMPLITUDES AT $T = 10°C$, $f = 33$ GHz, AND $\alpha = 90°$

Raindrop Radius (mm)	Forward Scattering Vertical Polarization Real	Imaginary	Horizontal Polarization Real	Imaginary	Backward Scattering Vertical Polarization Real	Imaginary	Horizontal Polarization Real	Imaginary
0.25	7.2339e-6	-8.7641e-7	7.2546e-6	-8.8089e-7	7.0205e-6	-4.9193e-7	7.0408e-6	-4.9542e-7
0.50	6.0770e-5	-1.4707e-5	6.1880e-5	-1.5112e-5	5.7061e-5	-5.7906e-7	5.8175e-5	-7.6133e-7
0.75	1.9423e-4	-9.4018e-5	1.9890e-4	-1.0052e-4	2.1375e-4	4.8230e-7	2.2954e-4	-4.2761e-6
1.00	3.7384e-4	-3.0827e-4	4.0379e-4	-3.5249e-4	5.1544e-4	-1.0199e-4	5.5654e-4	-1.4163e-4
1.25	4.7720e-4	-6.0471e-4	4.9344e-4	-8.1526e-4	7.2114e-4	-2.9850e-4	7.8434e-4	-4.9336e-4
1.50	5.0968e-4	-9.6856e-4	4.0278e-4	-1.2787e-3	9.7731e-4	-5.0695e-4	7.6329e-4	-7.5992e-4
1.75	5.2749e-4	-1.2953e-3	3.0031e-4	-1.6639e-3	7.0582e-4	-5.5870e-4	5.9285e-4	-7.6348e-4
2.00	6.0080e-4	-1.6329e-3	3.2281e-4	-2.0925e-3	4.8099e-4	-3.8959e-4	3.8179e-4	-4.7270e-4
2.25	7.4387e-4	-2.0507e-3	3.4934e-4	-2.6774e-3	1.5662e-4	-1.7607e-5	1.7847e-4	1.1231e-4
2.50	8.7612e-4	-2.5900e-3	2.5937e-4	-3.3740e-3	-1.6529e-4	5.5253e-4	1.2879e-4	8.1147e-4
2.75	9.3235e-4	-3.1951e-3	1.1291e-4	-4.0571e-3	-4.0034e-4	1.0907e-3	1.6730e-4	1.3381e-3
3.00	9.6547e-4	-3.7869e-3	-8.1828e-6	-4.7362e-3	-5.2528e-4	1.4088e-3	1.8314e-4	1.4845e-3
3.25	1.0422e-3	-4.3873e-3	-9.7052e-5	-5.5251e-3	-5.7773e-4	1.3548e-3	1.9667e-5	1.1912e-3
3.50	1.1941e-3	-4.9787e-3	-3.1696e-4	-6.3520e-3	-6.0973e-4	8.4021e-4	-4.1381e-4	5.2893e-4

TABLE 56. FORWARD AND BACKWARD SCATTERING AMPLITUDES AT $T = 10°C$, $f = 33$ GHz, AND $\alpha = 75°$

Raindrop Radius (mm)	Forward Scattering Vertical Polarization Real	Imaginary	Horizontal Polarization Real	Imaginary	Backward Scattering Vertical Polarization Real	Imaginary	Horizontal Polarization Real	Imaginary
0.25	7.2353e-6	-8.7668e-7	7.2546e-6	-8.8086e-7	7.0219e-6	-4.9219e-7	7.0408e-6	-4.9550e-7
0.50	6.0845e-5	-1.4726e-5	6.1881e-5	-1.5104e-5	5.7145e-5	-5.8748e-7	5.8181e-5	-7.8363e-7
0.75	1.9507e-4	-9.5030e-5	2.0347e-4	-1.0081e-4	2.1476e-4	-3.6015e-7	2.2512e-4	-4.2349e-6
1.00	3.7666e-4	-3.1108e-4	4.0490e-4	-3.5232e-4	5.1957e-4	-1.0365e-4	5.5702e-4	-1.4358e-4
1.25	4.8271e-4	-6.2159e-4	4.9900e-4	-8.1794e-4	7.4935e-4	-2.8919e-4	7.9328e-4	-4.9470e-4
1.50	5.0817e-4	-9.9845e-4	4.1392e-4	-1.2867e-3	8.4627e-4	-4.9891e-4	7.8036e-4	-7.7078e-4
1.75	5.1499e-4	-1.3378e-3	3.2275e-4	-1.6790e-3	7.8615e-4	-5.4796e-4	6.2859e-4	-7.8575e-4
2.00	5.8471e-4	-1.6784e-3	3.2482e-4	-2.1079e-3	5.9844e-4	-3.8176e-4	4.1676e-4	-4.9844e-4
2.25	7.2055e-4	-2.1068e-3	3.5759e-4	-2.6941e-3	3.2671e-4	1.3973e-5	2.4428e-4	8.6973e-5
2.50	8.4691e-4	-2.6370e-3	2.8332e-4	-3.3956e-3	6.2370e-5	5.8227e-4	2.3846e-4	7.9485e-4
2.75	9.1074e-4	-3.2709e-3	1.2710e-4	-4.0849e-3	-1.2241e-4	1.1533e-3	3.5117e-4	1.3366e-3
3.00	9.5034e-4	-3.8857e-3	8.8715e-6	-4.7729e-3	-2.3379e-4	1.5184e-3	4.0688e-4	1.5204e-3
3.25	1.0265e-3	-4.5220e-3	-6.2682e-5	-5.5691e-3	-3.2721e-4	1.5318e-3	2.4739e-4	1.2924e-3
3.50	1.1683e-3	-5.1549e-3	-2.5061e-4	-6.4138e-3	-5.4161e-4	1.1175e-3	-2.5265e-4	7.4686e-4

TABLE 57. FORWARD AND BACKWARD SCATTERING AMPLITUDES AT $T = 10°C$, $f = 33$ GHz, AND $\alpha = 60°$

Raindrop Radius (mm)	Forward Scattering Vertical Polarization Real	Imaginary	Horizontal Polarization Real	Imaginary	Backward Scattering Vertical Polarization Real	Imaginary	Horizontal Polarization Real	Imaginary
0.25	7.2391e-6	-8.7741e-7	7.2546e-6	-8.8077e-7	7.0257e-6	-4.9293e-7	7.0409e-6	-4.9563e-7
0.50	6.1050e-5	-1.4778e-5	6.1884e-5	-1.5082e-5	5.7364e-5	-6.4128e-7	5.8194e-5	-8.1855e-7
0.75	1.9699e-4	-9.5885e-5	2.0375e-4	-1.0053e-4	2.1692e-4	-1.2501e-6	2.2519e-4	-4.7013e-6
1.00	3.8435e-4	-3.1859e-4	4.0708e-4	-3.5178e-4	5.2882e-4	-1.1136e-4	5.5795e-4	-1.4565e-4
1.25	4.9834e-4	-6.6500e-4	5.1119e-4	-8.2295e-4	7.8675e-4	-3.1792e-4	8.0648e-4	-5.0027e-4
1.50	5.0646e-4	-1.0734e-3	4.3014e-4	-1.3052e-3	8.9505e-4	-5.5628e-4	8.0471e-4	-7.9839e-4
1.75	4.9085e-4	-1.4377e-3	3.3598e-4	-1.7122e-3	8.6010e-4	-6.2893e-4	6.6839e-4	-8.4412e-4
2.00	5.4036e-4	-1.8500e-3	3.3169e-4	-2.1504e-3	7.2364e-4	-4.8386e-4	4.8506e-4	-5.9484e-4
2.25	6.5815e-4	-2.2571e-3	3.6447e-4	-2.7380e-3	5.3117e-4	-1.0392e-4	3.5425e-4	-4.7600e-5
2.50	7.2226e-4	-2.8339e-3	3.0577e-4	-3.4480e-3	3.6204e-4	4.5866e-4	3.9693e-4	6.4651e-4
2.75	8.3759e-4	-3.4837e-3	1.6468e-4	-4.1626e-3	2.6406e-4	1.0527e-3	5.7174e-4	1.2238e-3
3.00	8.8598e-4	-4.1578e-3	5.1662e-5	-4.8766e-3	2.0949e-4	1.4951e-3	7.0015e-4	1.5047e-3
3.25	9.6535e-4	-4.8741e-3	-1.6100e-5	-5.6852e-3	1.1684e-4	1.6495e-3	5.9927e-4	1.4389e-3
3.50	1.1006e-3	-5.6121e-3	-1.6135e-4	-6.5679e-3	-1.7634e-4	1.5102e-3	1.4819e-4	1.1096e-3

TABLE 58. FORWARD AND BACKWARD SCATTERING AMPLITUDES AT $T = 10°C$, $f = 33$ GHz, AND $\alpha = 45°$

Raindrop Radius (mm)	Forward Scattering Vertical Polarization Real	Imaginary	Horizontal Polarization Real	Imaginary	Backward Scattering Vertical Polarization Real	Imaginary	Horizontal Polarization Real	Imaginary
0.25	7.2442e-6	-8.7840e-7	7.2546e-6	-8.8064e-7	7.0309e-6	-4.9397e-7	7.0411e-6	-4.9579e-7
0.50	6.1331e-5	-1.4850e-5	6.1887e-5	-1.5053e-5	5.7659e-5	-7.3024e-7	5.8212e-5	-8.5965e-7
0.75	1.9961e-4	-9.7054e-5	2.0413e-4	-1.0015e-4	2.1977e-4	-2.7176e-6	2.2525e-4	-5.2132e-6
1.00	3.9488e-4	-3.2889e-4	4.1005e-4	-3.5104e-4	5.4044e-4	-1.2346e-4	5.5927e-4	-1.4759e-4
1.25	5.1993e-4	-7.2378e-4	5.2837e-4	-8.2917e-4	8.2002e-4	-3.7642e-4	8.2247e-4	-5.0753e-4
1.50	5.0471e-4	-1.1758e-3	4.5351e-4	-1.3303e-3	9.2201e-4	-6.6241e-4	8.3586e-4	-8.3600e-4
1.75	4.5863e-4	-1.5756e-3	3.5527e-4	-1.7589e-3	8.9248e-4	-7.7494e-4	7.1835e-4	-9.2809e-4
2.00	4.7954e-4	-1.9777e-3	3.4079e-4	-2.2115e-3	7.9245e-4	-6.6909e-4	5.6511e-4	-7.4353e-4
2.25	5.6835e-4	-2.4723e-3	3.7074e-4	-2.8017e-3	6.7239e-4	-3.2662e-4	4.6875e-4	-2.7136e-4
2.50	6.5573e-4	-3.0928e-3	3.3232e-4	-3.5231e-3	6.0344e-4	2.0854e-4	5.4028e-4	3.7786e-4
2.75	7.0178e-4	-3.7959e-3	2.1083e-4	-4.2746e-3	6.2183e-4	8.0662e-4	7.6749e-4	9.8116e-4
3.00	7.3571e-4	-4.5419e-3	9.9465e-5	-5.0285e-3	6.8549e-4	1.3154e-3	9.9547e-4	1.3730e-3
3.25	7.9605e-4	-5.3504e-3	3.7341e-5	-5.8589e-3	7.0185e-4	1.6207e-3	1.0475e-3	1.4964e-3
3.50	9.1128e-4	-6.2263e-3	-7.7651e-5	-6.7890e-3	5.4361e-4	1.7168e-3	7.8255e-4	1.4082e-3

TABLE 59. FORWARD AND BACKWARD SCATTERING AMPLITUDES AT $T = 10°C$, $f = 33$ GHz, AND $\alpha = 30°$

Raindrop Radius (mm)	Forward Scattering Vertical Polarization Real	Imaginary	Horizontal Polarization Real	Imaginary	Backward Scattering Vertical Polarization Real	Imaginary	Horizontal Polarization Real	Imaginary
0.25	7.2494e-6	-8.7940e-7	7.2546e-6	-8.8052e-7	7.0362e-6	-4.9503e-7	7.0412e-6	-4.9595e-7
0.50	6.1611e-5	-1.4922e-5	6.1890e-5	-1.5024e-5	5.7952e-5	-8.2926e-7	5.8228e-5	-8.9829e-7
0.75	2.0223e-4	-9.8221e-5	2.0449e-4	-9.9771e-5	2.2254e-4	-4.3516e-6	2.2527e-4	-5.6737e-6
1.00	4.0543e-4	-3.3921e-4	4.1303e-4	-3.5030e-4	5.5138e-4	-1.3661e-4	5.6056e-4	-1.4917e-4
1.25	5.4178e-4	-7.8227e-4	5.4596e-4	-8.3500e-4	8.4133e-4	-4.4486e-4	8.3786e-4	-5.1395e-4
1.50	5.0366e-4	-1.2783e-3	4.7792e-4	-1.3556e-3	9.2130e-4	-7.8269e-4	8.6673e-4	-8.7355e-4
1.75	4.2740e-4	-1.7154e-3	3.7572e-4	-1.8072e-3	8.7460e-4	-9.3783e-4	7.6663e-4	-1.0163e-3
2.00	4.1863e-4	-2.1583e-3	3.4947e-4	-2.2765e-3	7.8306e-4	-8.7453e-4	6.3782e-4	-9.0771e-4
2.25	4.7431e-4	-2.7014e-3	3.7527e-4	-2.8708e-3	7.0150e-4	-5.7476e-4	5.5859e-4	-5.3135e-4
2.50	5.2157e-4	-3.3761e-3	3.5340e-4	-3.6028e-3	7.0652e-4	-7.1889e-5	6.3319e-4	4.5651e-5
2.75	5.1914e-4	-4.1390e-3	2.5057e-4	-4.3933e-3	8.3762e-4	5.1446e-4	8.8303e-4	6.4717e-4
3.00	4.9832e-4	-4.9454e-3	1.3447e-4	-5.1938e-3	1.0477e-3	1.0499e-3	1.1983e-3	1.1206e-3
3.25	5.0309e-4	-5.8137e-3	6.0930e-5	-6.0493e-3	1.2388e-3	1.4386e-3	1.4276e-3	1.3981e-3
3.50	5.4104e-4	-6.7961e-3	-4.9927e-5	-7.0229e-3	1.2822e-3	1.6283e-3	1.4063e-3	1.5153e-3

TABLE 60. FORWARD AND BACKWARD SCATTERING AMPLITUDES AT $T = 10°C$, $f = 33$ GHz, AND $\alpha = 15°$

Raindrop Radius (mm)	Forward Scattering Vertical Polarization Real	Imaginary	Horizontal Polarization Real	Imaginary	Backward Scattering Vertical Polarization Real	Imaginary	Horizontal Polarization Real	Imaginary
0.25	7.2531e-6	-8.8013e-7	7.2545e-6	-8.8043e-7	7.0400e-6	-4.9581e-7	7.0413e-6	-4.9606e-7
0.50	6.1817e-5	-1.4977e-5	6.1892e-5	-1.5002e-5	5.8166e-5	-9.0655e-7	5.8239e-5	-9.2577e-7
0.75	2.0416e-4	-9.9076e-5	2.0476e-4	-9.9491e-5	2.2455e-4	-5.6265e-6	2.2527e-4	-5.9933e-6
1.00	4.1317e-4	-3.4678e-4	4.1521e-4	-3.4975e-4	5.5906e-4	-1.4674e-4	5.6148e-4	-1.5019e-4
1.25	5.5793e-4	-8.2494e-4	5.5904e-4	-8.3907e-4	8.5089e-4	-4.9898e-4	8.4910e-4	-5.1806e-4
1.50	5.0335e-4	-1.3536e-3	4.9643e-4	-1.3743e-3	9.0647e-4	-8.7615e-4	8.8972e-4	-9.0108e-4
1.75	4.0526e-4	-1.8191e-3	3.9142e-4	-1.8437e-3	8.3465e-4	-1.0626e-3	8.0180e-4	-1.0836e-3
2.00	3.7412e-4	-2.2947e-3	3.5564e-4	-2.3266e-3	7.3279e-4	-1.0300e-3	6.8786e-4	-1.0306e-3
2.25	4.0275e-4	-2.8783e-3	3.7616e-4	-2.9247e-3	6.5868e-4	-7.6021e-4	6.1247e-4	-7.4453e-4
2.50	4.1202e-4	-3.6013e-3	3.6572e-4	-3.6646e-3	6.9810e-4	-2.7723e-4	6.7040e-4	-2.3763e-4
2.75	3.5211e-4	-4.4136e-3	2.7528e-4	-4.4851e-3	9.0673e-4	2.9726e-4	9.1405e-4	3.4408e-4
3.00	2.5887e-4	-5.2564e-3	1.5138e-4	-5.3243e-3	1.2332e-3	8.2766e-4	1.2737e-3	8.5748e-4
3.25	1.8977e-4	-6.1422e-3	5.7050e-5	-6.2012e-3	1.5708e-3	1.2292e-3	1.6256e-3	1.2246e-3
3.50	9.8335e-5	-7.1152e-3	-8.4071e-5	-7.1987e-3	1.7345e-3	1.4963e-3	1.7737e-3	1.4893e-3
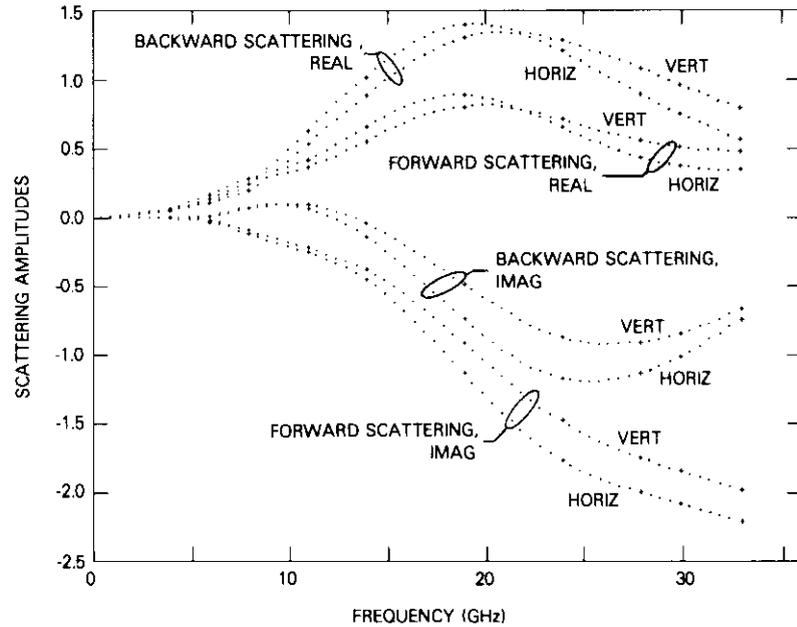
Figure 2. *Scattering Amplitudes for a Raindrop of 2 mm Radius at 10°C Propagating at a 45° Angle*

Acknowledgments

References

[1] T. Oguchi, "Attenuation and Phase Rotation of Radio Waves Due to Rain: Calculations at 19.3 and 34.8 GHz," *Radio Science*, Vol.8, No. 1, 1973, pp. 31-38.

[2] T. Oguchi, "Scattering Properties of Pruppacher-Pitter Form Raindrops and Cross-Polarization Due to Rain: Calculations at 11, 13, 19.3 and 34.8 GHz," *Radio Science*, Vol. 12, 1977, pp. 41-51.

[3] B. G. Evans, N. K. Uzunoglu, and A. R. Holt, "Two New Approaches to the Calculation of Rain-Induced Attenuation and Cross Polarization," *Proceedings of URSI, Commission F*, LaBaule, France, 1977, pp. 175-179.

[4] D. J. Fang, "Attenuation and Phase Shift of Microwaves Due to Canted Raindrops," *COMSAT Technical Review*, Vol. 5, No. 2, Spring 1975, pp. 135-156.

[5] J. A. Morrison and M. J. Cross, "Scattering of a Plane Electromagnetic Wave by Axisymmetric Raindrops," *Bell System Technical Journal*, Vol. 53, No. 6, 1974, pp. 955-1019.

[6] K. K. Mei, "Unimoment Method of Solving Antenna and Scattering Problems," *IEEE Transactions on Antennas and Propagation*, AP-22, November 1974, pp. 760-766.

[7] S. K. Chang and K. K. Mei, "Application of the Unimoment Method to Electromagnetic Scattering of Dielectric Cylinders," *IEEE Transactions on Antennas and Propagation*, AP-24, January 1976, pp. 35-42.

[8] H. R. Pruppacher and R. L. Pitter, "A Semi-Empirical Determination of the Shape of Cloud and Raindrops," *Journal of Atmospheric Science*, Vol. 28, No. 1, 1971, pp. 86-94.

[9] P. S. Ray, "Broad Complex Refractive Indices of Ice and Water," *Applied Optics*, Vol. 11, 1972, pp. 1836-1844.

Appendix A.   A summary of the basic approach and essential equation for the evaluation of FSA and BSA

The unimoment method solves the raindrop scattering problem by using two imaginary spheres to separate space into three regions as shown in Figure A-1. Region I is inside the interior tangent sphere, region III is exterior to the exterior tangent sphere, and region II is between the two spheres and contains the raindrop exterior surface. The unimoment method solves the raindrop scattering problem by matching the spherical harmonic potentials at the spherical boundaries as well as at the actual raindrop boundary. Since the geometry is symmetrical with respect to the azimuthal angle ϕ, all the electromagnetic field quantities in a spherical coordinate system (r, θ, ϕ) can be decomposed into summations of azimuthal modes

$$E(r, \theta, \phi) = \sum_{m=-M}^{M} e_m(r, \theta) \, e^{im\phi} \tag{A-1a}$$

$$H(r, \theta, \phi) = \sum_{m=-M}^{M} h_m(r, \theta) \, e^{im\phi} \quad . \tag{A-1b}$$

Furthermore, in the homogeneous region (I) and bounded space region (II), the azimuthal mode field, e_m and h_m, can be represented in terms of the following standard radial TE and TM potential spherical harmonic expansions:

$$e_m^{\tau}(r, \theta) = \sqrt{\mu_r} \sum_{\substack{n=|m| \\ n\neq0}}^{N_m^{\tau}} [a_{m,n}^{\tau}\alpha_{m,n}^{\tau}(r, \theta) + b_{m,n}^{\tau}\beta_{m,n}^{\tau}(r, \theta)] \tag{A-2a}$$

INCIDENT
WAVEFRONT

RAINDROP AXIS OF
SYMMETRY

BOUNDARY OF
PRUPPACHER &
PITTER RAINDROP

IMAGINARY
SPHERICAL
BOUNDARIES
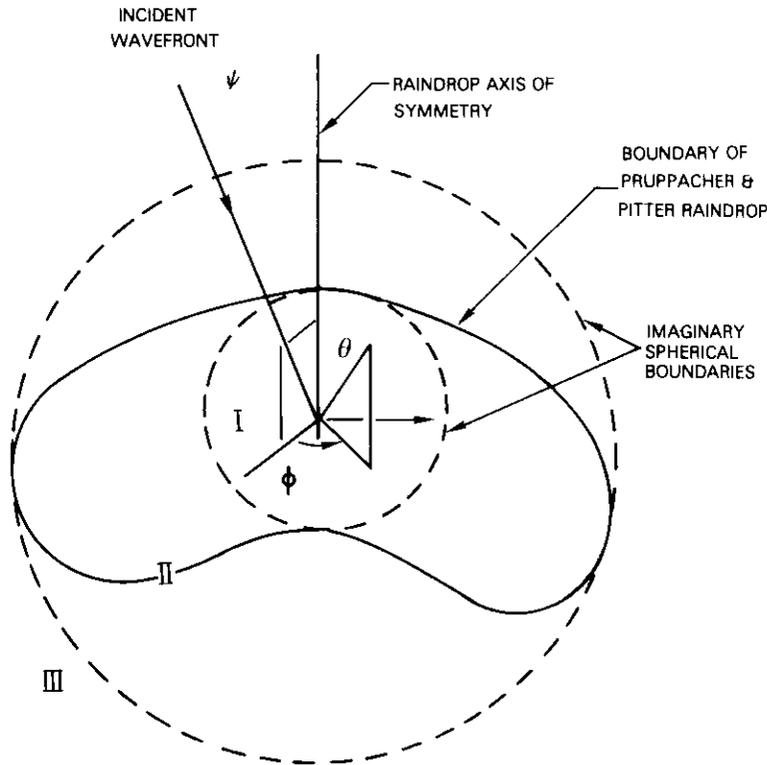
Figure A-1. *Region Boundaries for the Unimoment Method*

$$h_m^{\tau}(r, \theta) = \sqrt{\epsilon_r} \sum_{\substack{n=|m| \\ n\neq0}}^{N_m^{\tau}} [a_{m,n}^{\tau}\alpha_{m,n}^{\tau}(r, \theta) - b_{m,n}^{\tau}\alpha_{m,n}^{\tau}(r, \theta)] \tag{A-2b}$$

where τ is region I or region II; μ_r and ϵ_r are the relative permeability and dielectric constant, respectively; and $a_{m,n}^{\tau}$ and $b_{m,n}^{\tau}$ will be determined by numerical calculations; and N_m, m is sufficiently large to provide adequate accuracy. The radial TE and TM fields are given in terms of spherical harmonics as

$$\alpha_{m,n}^{\tau}(r, \theta) = - \frac{B_n^{\tau}(Kr)}{Kr} \frac{\partial P_n^m(\cos \theta)}{\partial \theta} \tag{A-3a}$$

$$\beta_{m,n}^{\tau}(r, \theta) = \frac{m}{Kr} \frac{\partial B_n^{\tau}(Kr)}{\partial(Kr)} \frac{P_n^m(\cos \theta)}{\sin \theta} \tag{A-3b}$$

$$K = \sqrt{\epsilon_r\mu_r}\frac{\omega}{c} \tag{A-3c}$$

where ω is the radian frequency, c is the velocity of the light, $P_n^m(.)$ is the associated Lengendre polynomials, and $B_n^{\tau}(.)$ is the Riccati spherical Bessel function. The field in region III is simply

$$e_m^{\mathrm{III}}(r, \theta) = e_m^i(r, \theta) + \sum_{\substack{n=|m \\ n\neq0}}^{N_m^{\mathrm{III}}} [a_{m,n}^{\mathrm{III}}\alpha_{m,n}^{\mathrm{III}}(r, \theta) + b_{m,n}^{\mathrm{III}}\beta_{m,n}^{\mathrm{III}}(r, \theta)] \tag{A-4a}$$

$$h_m^{\mathrm{III}}(r, \theta) = h_m^i(r, \theta) + \sum_{\substack{n=|m \\ n\neq0}}^{N_m^{\mathrm{III}}} [a_{m,n}^{\mathrm{III}}\beta_{m,n}^{\mathrm{III}}(r, \theta) - b_{m,n}^{\mathrm{III}}\alpha_{m,n}^{\mathrm{III}}(r, \theta)] \tag{A-4b}$$

where e_m^i and h_m^i are the incident plane wave electric and magnetic fields decomposed into azimuthal modes in accordance with equation (A-1).

The solutions at the two spherical boundaries are then numerically matched based upon the following assumption:

$$(\nabla^2 + K^2)\begin{bmatrix} e_m^{\tau} \\ h_m^{\tau} \end{bmatrix} e^{im\phi} \cong 0 \tag{A-5}$$

i.e., the TE and TM potentials at any given boundary point locally satisfy Hemholtz equations for $\tau =$ I, II, or III. Therefore, the solution of equation (A-5) at a given boundary point can be written as

$$\begin{bmatrix} e_m^T \\ h_m^T \end{bmatrix} = \begin{bmatrix} E_m^T(r, \theta) \\ H_m^T(r, \theta) \end{bmatrix} e^{-j\omega/c[L_m(r,\theta,\phi)+m\phi]} \qquad \text{(A-6)}$$

where E_m and H_m are real valued functions, and the phase term is derived from the eikonal, L_m. The value of L_m can be determined by considering the magnitude of the local propagation vector. The solution for the scattering field coefficient then proceeds by using the method of moments, which yields a family of linear equations in $a_{m,n}^T$ and $b_{m,n}^T$. The unknown coefficients may be determined by inverting the equation matrix. A detailed description will be available in two forthcoming documents [A-1], [A-2].

References

[A-1] K. K. Mei, C. Yeh, and D. J. Fang, "Microwave Scattering Amplitudes for Raindrops," in preparation.
[A-2] D. J. Fang, "Microwave Scattering Amplitudes for Raindrops," COMSAT Technical Memorandum, CL-13-78, May 1978.

Appendix B.   A comparison with the results of Oguchi

After publishing several classic papers on scattering by spheroidal raindrops [B-1], Oguchi recently published calculations [B-2] using the more realistic raindrop profiles given by Pruppacher and Pitter [B-3], which are also employed in this paper. Oguchi's results at 11, 13, 19.3, and 34.8 GHz will be compared with those presented in this paper. Table B-1 lists the FSAS at 11 and 19.3 GHz for three different equivolumic raindrop radii: 0.25, 1.50, and 3.25 mm. For comparison, raindrop temperatures of 20°, which was also assumed by Oguchi, and 10°, are included.

The two sets of numbers are in fairly good agreement. Minor differences in magnitude are caused by the use of two different numerical methods in the calculations. Also, Oguchi calculated the dielectric constants using the traditional Debye equation while the more precise Ray's equation was employed in this paper. The two equations can produce noticeably different FSAS as indicated previously by Morrison and Cross [B-4]. Furthermore, the effect of temperature can also be recognized.

TABLE B-1. COMPARISON OF THE FSAs GENERATED BY THE UNIMOMENT METHOD AND BY OGUCHI'S POINT-MATCHING METHOD

f (GHz)	a (mm)	T (°C)	Vertical Polarization		Horizontal Polarization	
			Unimoment Method	Point-Matching Method	Unimoment Method	Point-Matching Method
11	0.25	20	$8.025 \times 10^{-7} - j2.184 \times 10^{-8}$	$8.043 \times 10^{-7} - j2.283 \times 10^{-8}$	$8.046 \times 10^{-7} - j2.195 \times 10^{-8}$	$8.065 \times 10^{-7} - j2.294 \times 10^{-8}$
		10	$8.007 \times 10^{-7} - j2.843 \times 10^{-8}$	—*	$8.028 \times 10^{-7} - j2.858 \times 10^{-8}$	—*
	1.50	20	$1.739 \times 10^{-4} - j7.656 \times 10^{-6}$	$1.765 \times 10^{-4} - j8.283 \times 10^{-6}$	$2.056 \times 10^{-4} - j1.042 \times 10^{-4}$	$2.036 \times 10^{-4} - j1.029 \times 10^{-4}$
		10	$1.676 \times 10^{-4} - j6.156 \times 10^{-6}$	—*	$2.040 \times 10^{-4} - j8.361 \times 10^{-6}$	—*
	3.25	20	$8.185 \times 10^{-4} - j7.915 \times 10^{-4}$	$8.220 \times 10^{-4} - j7.955 \times 10^{-4}$	$1.296 \times 10^{-3} - j1.680 \times 10^{-3}$	$1.302 \times 10^{-3} - j1.683 \times 10^{-3}$
		10	$8.382 \times 10^{-4} - j8.145 \times 10^{-4}$	—*	$1.313 \times 10^{-3} - j1.716 \times 10^{-3}$	—*
19.3	0.25	20	$2.489 \times 10^{-6} - j1.355 \times 10^{-7}$	$2.493 \times 10^{-6} - j1.408 \times 10^{-7}$	$2.496 \times 10^{-6} - j1.361 \times 10^{-7}$	$2.500 \times 10^{-6} - j1.415 \times 10^{-7}$
		10	$2.397 \times 10^{-6} - j1.580 \times 10^{-7}$	—*	$2.402 \times 10^{-6} - j1.588 \times 10^{-7}$	—*
	1.50	20	$3.488 \times 10^{-4} - j2.571 \times 10^{-4}$	$3.744 \times 10^{-4} - j2.704 \times 10^{-4}$	$4.627 \times 10^{-4} - j3.472 \times 10^{-4}$	$4.703 \times 10^{-4} - j3.477 \times 10^{-4}$
		10	$3.684 \times 10^{-4} - j2.541 \times 10^{-4}$	—*	$4.769 \times 10^{-4} - j3.420 \times 10^{-4}$	—*
	3.25	20	$9.160 \times 10^{-4} - j2.144 \times 10^{-3}$	$9.30 \times 10^{-4} - j2.144 \times 10^{-3}$	$4.466 \times 10^{-4} - j3.342 \times 10^{-3}$	$4.500 \times 10^{-4} - j3.344 \times 10^{-3}$
		10	$9.290 \times 10^{-4} - j2.178 \times 10^{-3}$	—*	$4.506 \times 10^{-4} - j3.864 \times 10^{-3}$	—*

*Not available.

References

[B-1] T. Oguchi, "Attenuation and Phase Rotation of Radio Waves Due to Rain: Calculations at 19.3 and 34.8 GHz," *Radio Science*, Vol. 8, No. 1, 1973, pp. 31–38.

[B-2] T. Oguchi, "Scattering Properties of Pruppacher-Pitter Form Raindrops and Cross-Polarization Due to Rain: Calculations at 11, 13, 19.3 and 34.8 GHz," *Radio Science*, Vol. 12, 1977, pp. 41–51.

[B-3] H. R. Pruppacher and R. L. Pitter, "A Semi-Empirical Determination of the Shape of Cloud and Raindrops," *Journal of Atmospheric Science*, Vol. 28, No. 1, 1971, pp. 86–94.

[B-4] J. A. Morrison and M. J. Cross, "Scattering of a Plane Electromagnetic Wave by Axisymmetric Raindrops," *Bell System Technical Journal*, Vol. 53, No. 6, 1974, pp. 955–1019.

Appendix C. Evaluation of attenuation and phase shift from FSA

The method for evaluating attenuation ($A^{h,v}$ in deg/km) has been documented [C-1]. Only the essential equations are presented herein:

$$K^{h,v} = K_0 + \frac{2\pi}{k_0} \int_0^\infty FSA^{h,v}(a)\ N(R, a)\ da \tag{C-1}$$

$$A^{h,v} = 8.686 \times Im(K^{h,v}) \tag{C-2}$$

$$\phi^{h,v} = \frac{180}{\pi} \times Re(K^{h,v}) \tag{C-3}$$

where superscripts h and v refer to horizontal and vertical polarizations, respectively; K is the equivalent plane wave number; K_0 is the free space wave number; FSAS can be obtained from Table B-1; and N is the drop size distribution (m^{-3} cm^{-1}) for a given rain rate, $R(mm/hr)$, and equivolumic spherical raindrop radius, a(cm).

For example, with the Marshall and Palmer drop size distribution [C-2],

$$N(R, a) = 8 \times 10^{-4} \exp\left\{-3.67 \frac{a}{0.089R^{2.2}}\right\} \tag{C-4}$$

$K^{h,v}$ can be evaluated either by direct integration of equation (C-1) or by converting the integration into equivalent summations. Since the forward scattering amplitudes have been tabulated in terms of discrete values of a, the summation method is used. Final results of $A^{h,v}$ and $\phi^{h,v}$ for the terrestrial propagation case (propagation angle = 90°) at 19.3 GHz and 10°C are shown in Table C-1 as well as the equivalent values generated from Oguchi's data [C-3].

TABLE C-1. VALUES OF $A^{v,h}$ AND $\phi^{v,h}$ DERIVED FROM EQUATIONS (C-1) TO (C-4)

Rain Rate	Vertical Polarization*		Horizontal Polarization*	
(mm/hr)	A^v(dB/km)	ϕ^v(deg/km)	A^h(dB/km)	ϕ^h(deg/km)
0.25	0.016 (0.0118)	0.413 (0.72)	0.0175 (0.0122)	0.441 (0.73)
1.25	0.096 (0.075)	1.610 (2.80)	0.113 (0.081)	2.050 (2.89)
2.50	0.196 (0.167)	2.780 (5.01)	0.241 (0.182)	4.000 (5.23)
12.50	0.911 (0.997)	9.030 (18.95)	1.220 (1.148)	17.20 (20.41)
25.00	1.660 (2.079)	14.40 (33.32)	2.280 (2.478)	29.90 (36.48)
50.00	2.890 (4.258)	22.20 (58.44)	4.070 (5.279)	49.30 (65.02)
100.00	4.790 (8.523)	33.30 (102.97)	6.880 (11.075)	76.70 (116.02)
150.00	6.300 (12.720)	41.50 (144.28)	9.140 (16.990)	97.00 (163.08)

*Values in parentheses are the equivalent values generated using Oguchi's coefficients.

Although these two sets of values agree in trends and very roughly in magnitudes, there is a difference in detail, which can be attributed to the factors summarized in Table C-2. The difference in numerical methods also contributes to the final results (Appendix B). In terms of the other three parameters, the choices made in the present paper are believed to be more realistic. In particular, raindrops at 20°C are extremely rare, and drop size measurements [C-4] indicate that the Marshall-Palmer distribution is more accurate.

TABLE C-2. DIFFERENCES BETWEEN THE TWO METHODS OF CALCULATING SCATTERING AMPLITUDES

Parameter	Present Calculations of Scattering Amplitudes	Oguchi's Calculations of Scattering Amplitudes
Numerical Method	Unimoment	Point Matching
Dielectric Constant	Ray's equation	Debye equation
Temperature of Drop	10°C	20°C
Drop Size Distribution	Marshall-Palmer	Laws-Parsons

References

[C-1] T. Oguchi, "Attenuation and Phase Rotation of Radio Waves Due to Rain: Calculations at 19.3 and 34.8 GHz," *Radio Science*, Vol. 8, No. 1, 1973, pp. 31–38.

[C-2] J. S. Marshall and W. Palmer, "The Distribution of Raindrops with Size," *Journal of Meteorology*, Vol. 5, 1948, pp. 165–166.

[C-3] T. Oguchi, "Scattering Properties of Pruppacher-Pitter Form Raindrops and Cross-Polarization Due to Rain: Calculations at 11, 13, 19.3 and 34.8 GHz," *Radio Science*, Vol. 12, 1977, pp. 41–51.

[C-4] D. Atlas, R. C. Srivastava, and R. S. Sekhon, "Doppler Radar Characteristics of Precipitation at Vertical Incidence," Report 22, Laboratory for Atmospheric Probing, University of Chicago, 1971.

Dickson J. Fang received his B.S.E.E. in 1962 from Taiwan University, Taipei, China, and his M.S.E.E. and Ph.D. from Stanford University in 1964 and 1967. From 1967 to 1974, he was a radio physicist at Stanford Research Institute, and authored 17 papers on wave propagations, radio auroras, and ionospheric irregularities. While on leave from Stanford (1969–1970), he was a visiting professor at Taiwan University, where he published a graduate textbook on electromagnetic theory and five articles on the college education system. He joined COMSAT *in 1974. As Assistant Manager of the Propagations Studies Department, he is currently responsible for research on microwave transmissions for satellite-earth communications applications.*

Frank J. Lee received a B.S. in electrophysics from the National Chiao-tung University in Taiwan in 1970 and an M.S. in Computer Science from the University of Virginia in 1973. He currently is a D.Sc. candidate at the George Washington University.

From 1973 to 1976, he was a Research Assistant at George Washington University. In 1976, he joined COMSAT *Laboratories as a member of the technical staff in the Engineering Applications Department of the Computer Center.*

CTR Note

INTELSAT V 14-GHz tunnel diode noise figure study *

R. C. MOTT

(Manuscript received: June 27, 1978)

Introduction

Tunnel diode amplifiers (TDAS) have been used in the 6-GHz band as low-noise front ends in communications satellites for many years. In 1977, COMSAT Laboratories conducted a 14-GHz tunnel diode noise figure study to demonstrate the attainable front-end noise figure of the INTELSAT V satellite receiver. For this study, a 14-GHz microstrip TDA exhibiting state-of-the-art performance was developed to test INTELSAT V space-qualifiable tunnel diodes.

The 14-GHz microstrip TDA computer-aided design achieves a close match between predicted and measured amplifier noise figure and gain. A computer-aided stability analysis of the TDA circuit defines the circulator voltage standing-wave ratio (VSWR) requirement for TDA unconditional stability. Amplifier circulators have been selected to meet this stability criterion.

Richard Mott is a member of the Circuit Design Department of the Microwave Laboratory, COMSAT Laboratories.

14-GHz microstrip TDA design

The design approach is similar to that used for the COMSAT-designed ATS-F 4-GHz TDA [1] and DOMSAT simulator 4- and 6-GHz TDAS [2]. Circuit design considerations included stable operation independent of tunnel diode bias voltage level, noise figure minimization using low-loss circuitry, and circuit reproducibility.

Microstrip circuit realization was selected for its ruggedness, reproducibility, short production time, low cost, and ease of component mounting and circuit tuning. Amorphous fused-silica substrate material was selected for its almost nondispersive characteristics, low and accurate dielectric constant, and low-loss characteristics [3]. The entire microstrip TDA circuit is fabricated on a 25.4-mm x 8.84-mm piece of 0.381-mm-thick substrate material.

The space-qualifiable cylindrically packaged tunnel diode, manufactured by Aertech Industries, Inc., is shunt-mounted through the microstrip substrate to minimize in-band resistance. The TDA circuit parameters are therefore dictated by the tunnel diode's in-band admittance.

Figures 1 and 2 show the computer-modeled microstrip TDA equivalent circuit and microstrip pattern, respectively. The basic microstrip circuit elements of this (negative resistance) reflection amplifier consist of in-band admittance transformation and broad-banding gain control circuitry, and out-of-band conductance-adding stability-control circuitry. Redundant shunt-attached circuitry achieves the design-required high characteristic admittances using microstrip lines with realizable characteristic admittances. [At 14 GHz, a practical lower limit for characteristic impedance of a short (less than 45°) microstrip line length on 0.381-mm fused-silica is approximately 35Ω.]

The TDA circuit description begins at the diode port. The diode's in-band admittance is determined from the factory-specified equivalent circuit parameters [4] of Figure 1, in which the diode is assumed to be biased for low-noise operation [5]. The characteristic impedance of the approximately one-quarter-wavelength transmission line impedance transformer, which connects the tunnel diode port to the broad-banding port, is determined by the required TDA gain, the biased tunnel diode's in-band negative conductance, and the circulator's characteristic admittance expressed by

$$g_o = \frac{Y_o + G_D}{Y_o - G_D} \qquad (1)$$
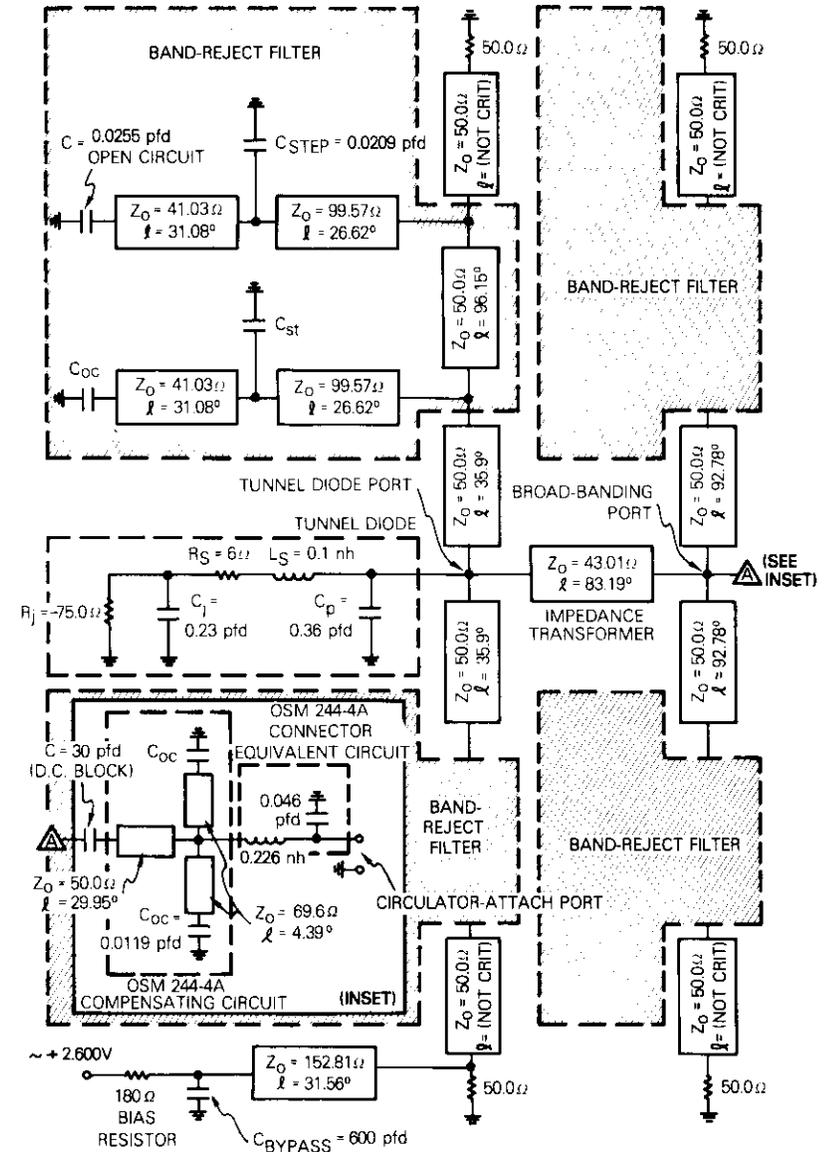
Figure 1. COMSAT *14-GHz TDA Equivalent Circuit*
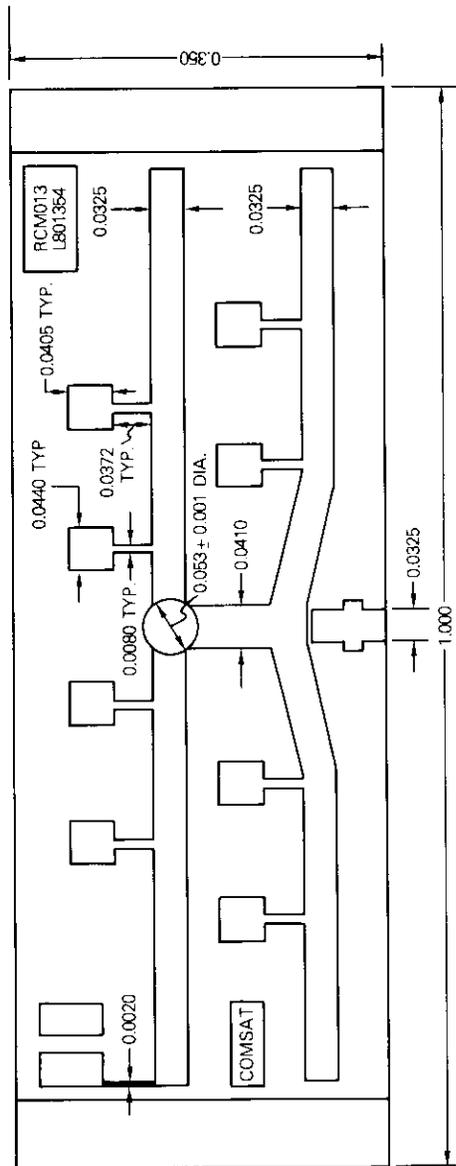
and

$$Y_T = \sqrt{Y_o Y_c} \qquad (2)$$

where Y_o = in-band admittance presented to tunnel diode

   g_o = band center voltage gain

   $-G_D$ = tunnel diode's in-band negative conductance

   Y_T = $\lambda/4$ transformer characteristic admittance

   Y_c = circulator characteristic admittance.

Two-section, wideband, maximally flat bandstop filters [6]-[8] provide in-band short-circuit terminations for the two 50Ω transmission lines attached to the diode port. The inductive susceptance of these 50Ω lines shunt resonates the tunnel diode's in-band capacitive susceptance.

Because of the semi-lumped element circuit realization for the bandstop filters, no harmonic stopband occurs within the tunnel diode's active frequency range whose upper limit is its ~33-GHz resistive cutoff frequency. This filtering scheme terminates the diode with a positive conductance out-of-band, which is a necessary condition for stability [5]. Two broad-banding resonant 50Ω circuits are shunt-attached to the broad-banding port. Each resonant circuit consists of a quarter-wavelength 50Ω line short-circuit terminated with a 2-section maximally flat bandstop filter described above. This terminating scheme provides more out-of-band stability-aiding positive conductance at the diode. A beam-lead 30-pF DC blocking capacitor protects the TDA from externally attached microwave circuits and connects the broad-banding port to a distributed-element compensating circuit. This circuit compensates for the impedance mismatch introduced by the OSM-244-4A microstrip launcher-to-coaxial line transition connector, which is simulated in Figure 1 by the lumped elements [9].

The DC bias circuit, which consists of an RC low-pass filter and a high-impedance line, is connected to one of the bandstop filter's 50Ω terminations. Resistive film on the high-impedance line isolates the RF from the bias circuit.

A microwave circuit analysis computer program "HEAVY DUTY" [10], which was used extensively for the TDA circuit design, is based on the cascaded S-parameter matrix concept and permits the use of lossy microstrip transmission lines. In-band gain response is fine tuned by computer

Figure 2. TDA Microstrip Pattern

modeling the described microstrip TDA circuit with slight length adjustments of impedance transformer and broad-banding lines.

The tunnel diode, mounted through an ultrasonically drilled hole in the fused-silica substrate, is attached to the microstrip circuit with wedge-bonded gold ribbon. Chip component circuit elements are silver-epoxied to the substrate. Final tuning to accommodate small variations in the assumed set of tunnel diode parameters is accomplished with gold ribbon squares which are clear-epoxied to the circuit.

TDA stability analysis

A Nyquist stability analysis of the tunnel diode was performed as a function of negative junction resistance. The $Z(\omega)$ impedance plot generated by this analysis is shown in Figure 3. This set of curves indicates that the diode's complex frequency impedance function has two zeros in the right half plane when the junction resistance absolute value is less than or equal to 72Ω. That is, in this junction resistance range, the diode's complex frequency impedance function is equal to zero at two distinct complex frequencies, each having a positive-real part:

$$Z(\alpha + j\omega) = 0 \quad , \quad \alpha > 0 \quad . \tag{3}$$

At these two complex frequencies, the transient current will increase exponentially with time, resulting in short-circuit instability:

$$I = I_o \, e^{(\alpha + j\omega)t} \quad , \quad \alpha > 0 \quad . \tag{4}$$

The inflection point (point of minimum negative junction resistance) occurs at about -66Ω; therefore, the diode is short-circuit unstable in this bias range [5]. Since the Nyquist analysis of the TDA circuit does not consider the circulator load effect on the amplifier's stability, an absolute junction plane stability analysis was performed. Figure 4 shows the circuit used for this stability analysis, which revealed instabilities at the diode junction as a function of the amplifier microstrip circuit and the circulator load.

The circuit was modeled while the circulator load magnitude was varied from 0.0 to 0.999 and the phase from 0° to 360°. For some magnitudes, the phase increment was as fine as 10°. A -66Ω diode negative resistance was used to simulate the most critical stability conditions. For each circulator load analyzed, a frequency sweep was performed, generally from
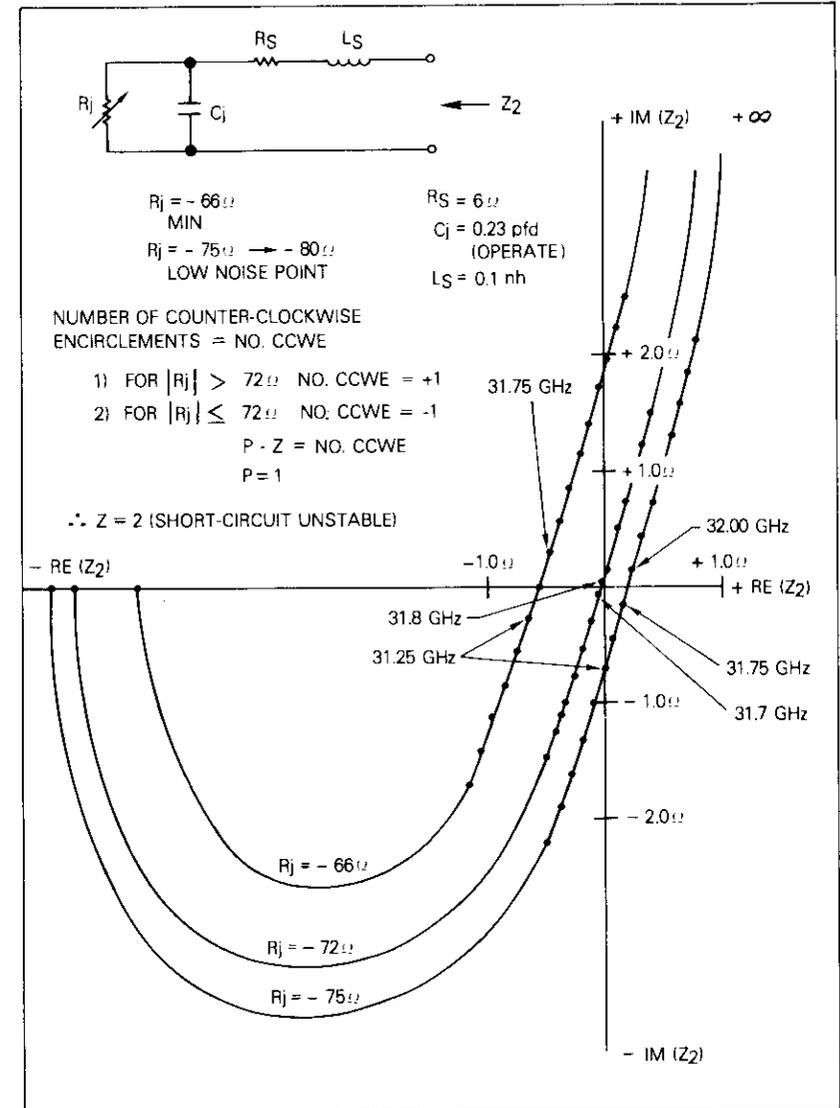
Figure 3. INTELSAT V *14-GHz Tunnel Diode Nyquist Stability Test for Short-Circuit Stability as a Function of Negative Junction Resistance* [*The presence of right-half plane zeros* (Z) *in the impedance function implies short-circuit instability.*]
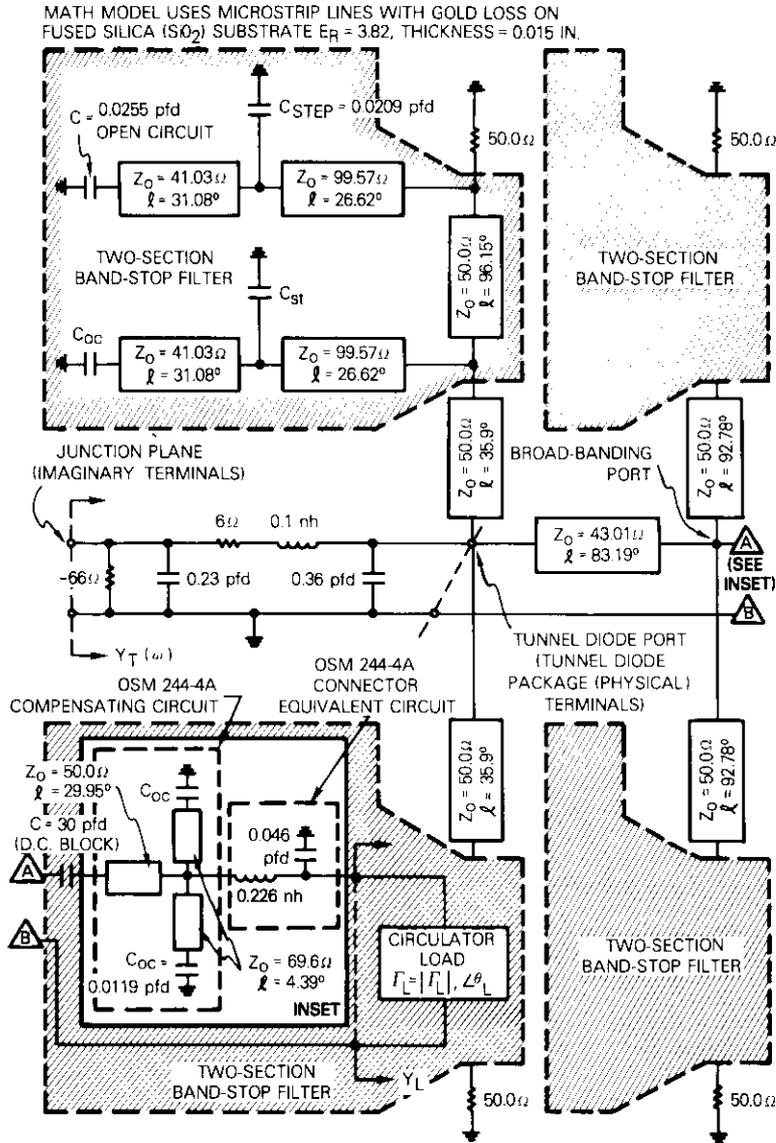
Figure 4. COMSAT *14-GHz TDA Circuit Definition for Absolute Junction Plane Stability Test [numerical analysis of $Y_T(\omega)$]*

0.01 to 34.00 GHz (above the resistive cutoff frequency F_{Ro}). An instability was considered present at any frequency for which the junction plane admittance $Y_T(\omega)$ of Figure 4 was a pure negative conductance. Figure 5 tabulates these instability frequencies as a function of circulator reflection coefficient $|\Gamma|$. Table 1 is a partial list of these specific frequencies and their particular circulator load conditions of magnitude and phase. It should be noted that the circuit is stable even for some phase angles of a particular forbidden circulator load magnitude.

The analysis reveals that the circuit is unconditionally stable with a circulator load of any phase angle and a VSWR of 1.33:1.0 or better in-band (14.00 to 14.50 GHz), and with a VSWR of 19.0:1.0 or better for all frequencies outside of the band (12.75 to 16.26 GHz). Therefore, the requirement of unconditional stability does not impose a difficult VSWR requirement on the circulator's TDA port; amplifier circulators were easily selected to meet the stability criterion of Figure 5.
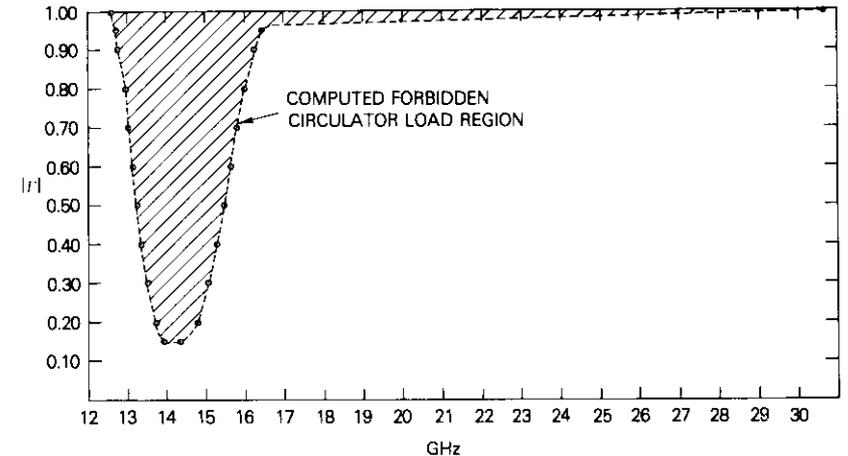

Figure 5. *Stability Analysis of* COMSAT *TDA Circuit Using Microstrip Line Modeling with Gold-Line Loss Included and Tunnel Diode Inflection-Point Junction Negative Resistance*

TDA gain analysis

The TDA circuit (Figure 1) has been computer modeled to produce the 12.7-dB gain specified in the original INTELSAT V* satellite front-end

---

*The INTELSAT V satellite is being fabricated by Ford Aerospace and Communications Corp.

TABLE 1. FORBIDDEN CIRCULATOR LOAD CONDITIONS

Circuit Reflection Coefficient $\|\Gamma\|$	Phase $R_t = -66\Omega$ (deg)	Frequency of Instability (GHz)
0.0	0*	None
0.1	0	None
0.1	15	None
0.1	345	None
0.1	330	None
0.1	300	None
0.1	285	None
0.1	315	None
0.1	270	None
0.1	255	None
0.1	240	None
0.1	225	None
0.1	210	None
0.1	195	None
0.1	180	None
0.1	165	None
0.1	150	None
0.1	135	None
0.1	120	None
0.1	105	None
0.1	85	None
0.1	60	None
0.1	45	None
0.1	30	None
0.12	300	None
0.12	330	None
0.12	0	None
0.12	30	None
0.12	270	None
0.12	240	None
0.12	210	None
0.12	180	None
0.12	150	None
0.13	300	None
0.13	330	None
0.13	0	None
0.13	30	None

TABLE 1. FORBIDDEN CIRCULATOR LOAD CONDITIONS (Continued)

Circuit Reflection Coefficient $\|\Gamma\|$	Phase $R_t = -66\Omega$ (deg)	Frequency of Instability (GHz)
0.14	300	None
0.14	270	None
0.14	280	None
0.14	240	None
0.14	330	None
0.14	310	None
0.15	300	14.25
0.15	330	14.355
0.15	0	None
0.15	270	14.05
0.15	240	13.9255
0.15	210	None
0.2	0	14.55
0.2	15	14.65
0.2	30	~14.655
0.2	45	14.755
0.2	60	14.8065
0.2	75	None
0.2	90	None
0.2	105	None
0.2	120	None
0.2	135	None
0.2	150	None
0.2	165	None
0.2	180	None
0.2	195	13.735
0.2	210	13.75
0.2	230	13.85
0.2	260	13.95
0.2	290	14.15
0.2	300	14.25

*Stable for all phases.

design. Figure 6 compares this computer simulation with a measured TDA gain response. It should be noted that the maximum deviation between the measured and calculated in-band gain is 0.40 dB. Figure 7 is a photograph of a tuned TDA microstrip circuit.
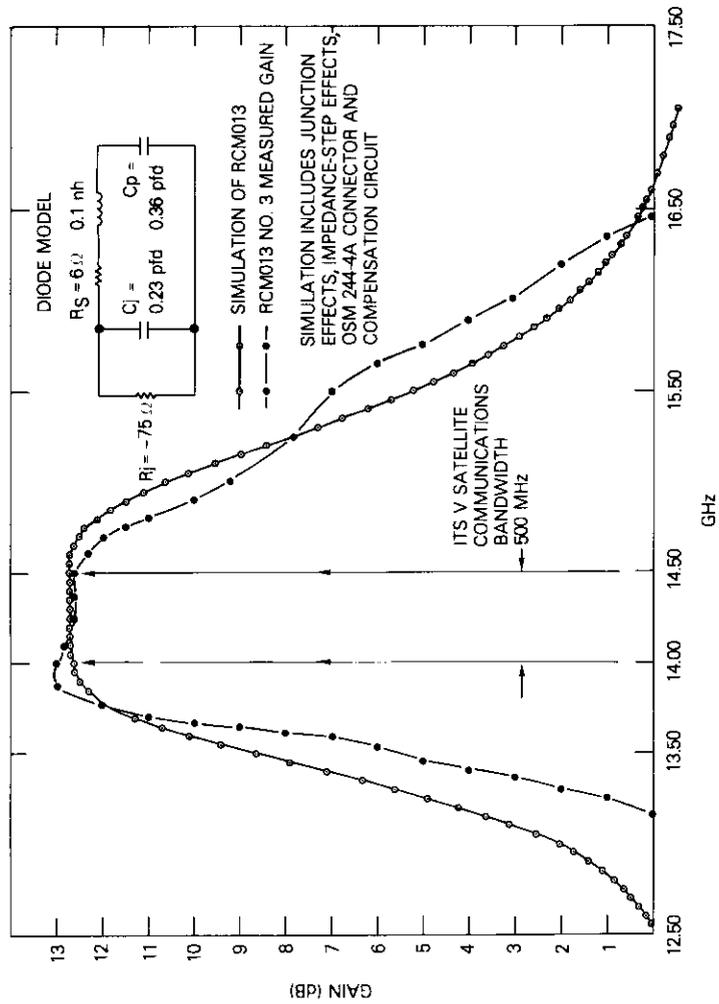
Figure 6. *Comparison of Measured and Simulated Gain of* COMSAT *14-GHz TDA Circuit for 12.70-dB Gain Specification*

Figure 8 compares simulated and measured wideband gain responses of the TDA biased at 14-dB gain, while Figure 9 shows the amplifier's in-band gain response as a function of bias voltage. It should be noted that in Figure 9 the gain for 2.600-V bias is 14.30 ± 0.10 dB across the 14.00- to 14.50-GHz band. The TDA is stable for all bias voltages as shown in Figure 10, in which the inflection-point gain maximum is reached at 2.200 V. Figure 11 shows this TDA's predicted and measured noise figure and measured gain across the band for a bias of 2.600 V.
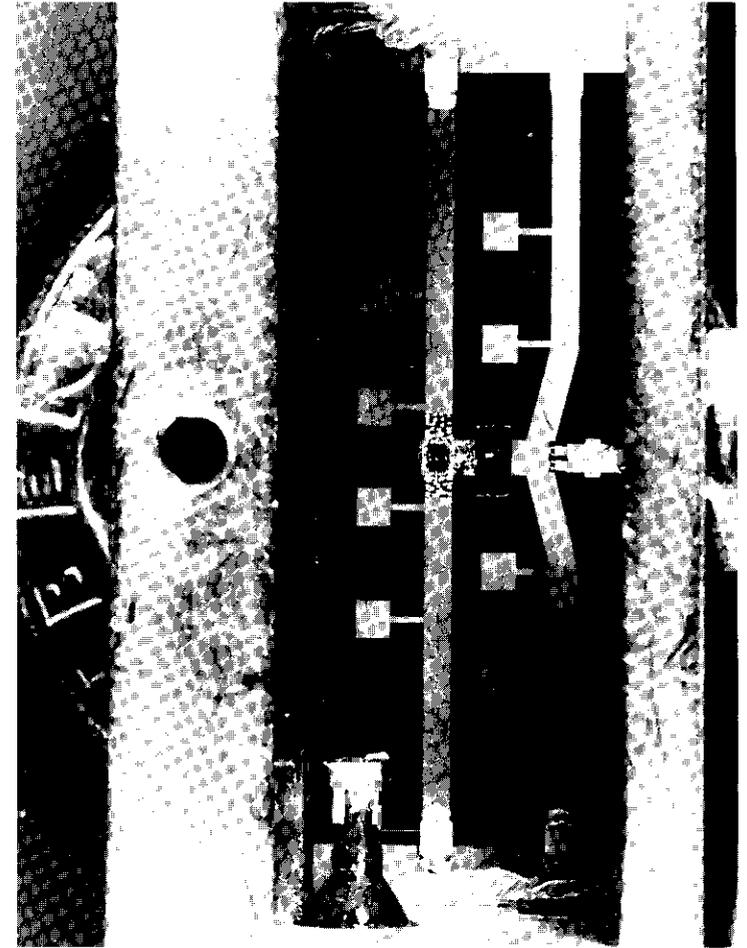
Figure 7. *Tuned* COMSAT *14-GHz TDA*
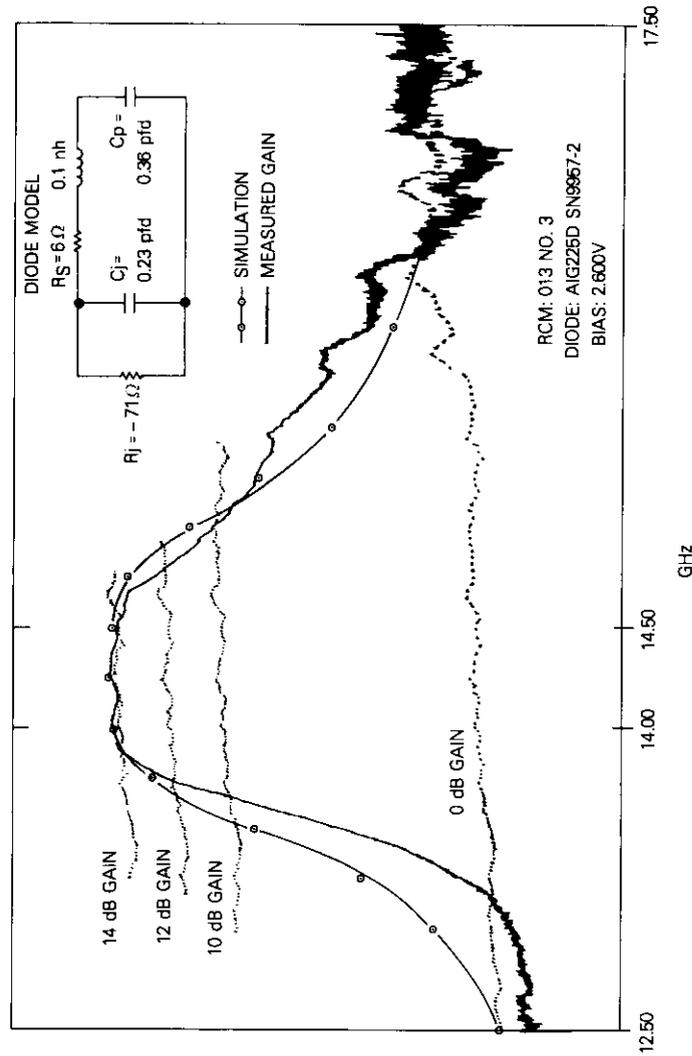
Figure 8. *Comparison of Measured and Simulated Gain of* COMSAT *14-GHz TDA Circuit for 14.20-dB Gain Specification*
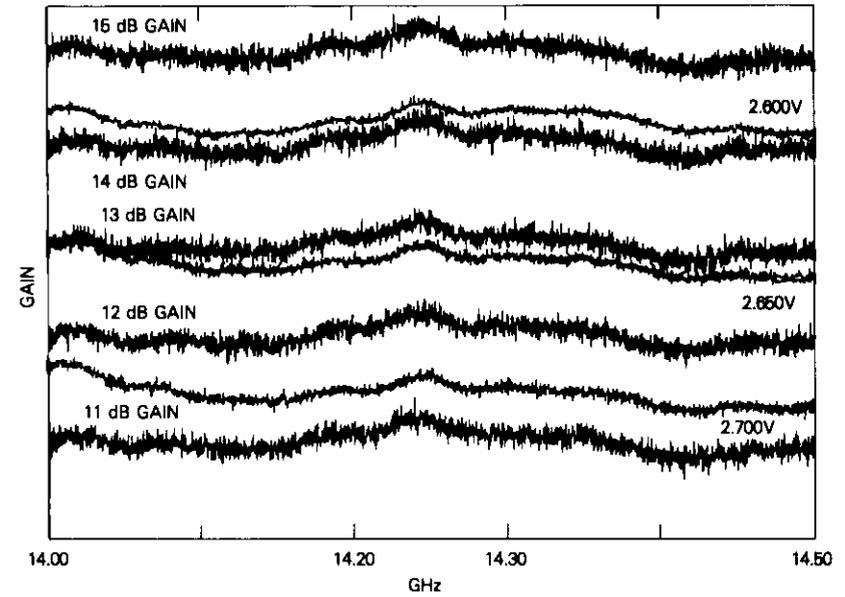
Figure 9. *14-GHz TDA Variation (in-band) as a Function of Bias Voltage*
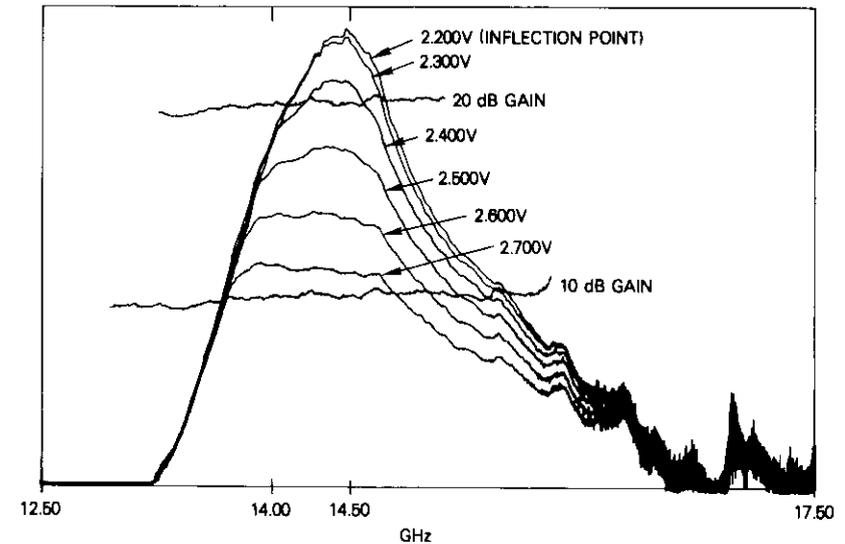
Figure 10. *14-GHz TDA Gain Variation (wideband) as a Function of Bias Voltage*

TDA: RCM013 NO. 3
DIODE NOISE FIGURE: 5.38 dB
BIAS: +2.600V
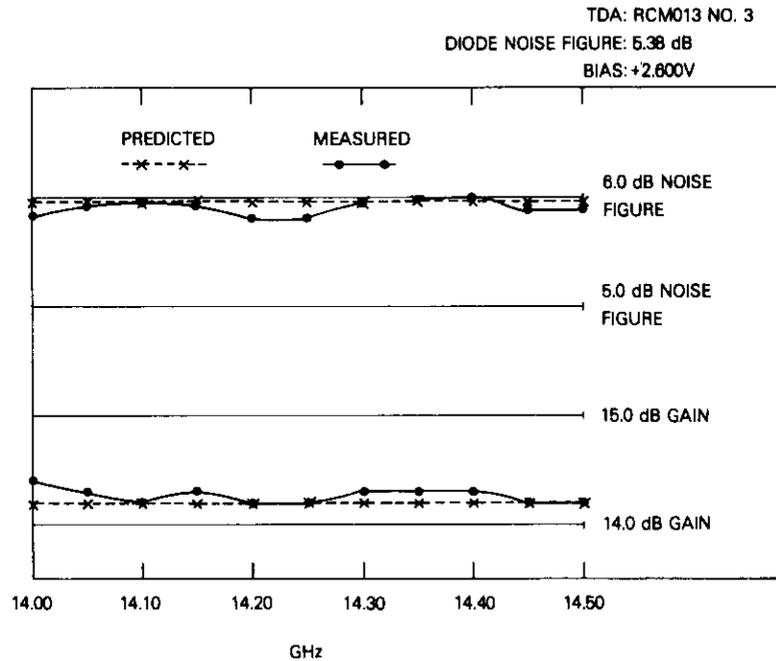
Figure 11. *14-GHz Microstrip TDA Predicted and Measured Noise Figure and Gain*

TDAs fabricated to this design are stable (oscillation-free) for all bias voltages and exhibit only one gain maximum, which further indicates stability. A spectrum analyzer search up to 40 GHz at various bias levels revealed no TDA oscillations.

TDA noise figure analysis

Five quartz-microstrip 14-GHz TDAs have been measured for noise figure across the 14.00- to 14.50-GHz design bandwidth. These TDAS use either INTELSAT V specified tunnel diodes purchased from Aertech with 5.10-dB maximum noise figures, or similarly specified tunnel diodes supplied by Aertech with out-of-specification noise figures (greater than 5.10 dB).

The TDA noise figure table (Table 2) details the contributions from separate elements of the TDA and the measured noise figure for each TDA analyzed. Generally, excellent correlation exists between estimated and measured TDA noise figure.

(*Continued*)

TABLE 2. 14-GHz QUARTZ MICROSTRIP TDA NOISE FIGURES AND TUNNEL DIODE PARAMETERS

TDA Number	1	2	3	4	5
Aertech Tunnel Diode Number	AIX 296 SN 9715-12	AIX 295 SN 8728-6	AIX 296 SN 61-17	AIG 225D SN 9957-2	AIG 225D SN 635-7
Tunnel Diode (Aertech Calculated) Noise Figure	5.10 dB	5.10 dB	5.07 dB	5.38 dB	5.83 dB
Calculated Insertion Loss of 12.7 mm of 50Ω Microstrip Circuitry at 14.25 GHz	0.10 dB	0.10 dB	0.10 dB	0.10 dB	0.10 dB
Estimated Mixed-Impedance Microstrip Junction Loss	0.10 dB	0.10 dB	0.10 dB	0.10 dB	0.10 dB
Estimated SMA-Type Connector/Launcher Loss	0.10 dB	0.10 dB	0.10 dB	0.10 dB	0.10 dB
Circulator Input Path Loss (Measured)	0.40 dB	0.20 dB	0.40 dB	0.20 dB	0.20 dB
Estimated TDA Noise Figure	5.80 dB	5.60 dB	5.77 dB	5.88 dB	6.33 dB
Automatic Noise Figure Setup Measured TDA Noise Figure (14.00–14.50 GHz)	5.80 ± 0.05 dB	5.63 ± 0.05 dB	5.80 ± 0.05 dB	5.96 ± 0.02 dB	6.25 + 0.01 − 0.00 dB
"Y-Factor" Noise Figure Setup Measured TDA Noise Figure (14.00–14.50 GHz)				5.90 ± 0.12 dB	

noise figures is less than 0.20 dB for TDA 4.

All TDAS were measured with an A.I.L. "automatic" noise figure measurement setup using a 14-GHz diode noise generator. In addition, TDA 4 has been measured with a "Y factor" noise figure measurement setup using an Argon gas tube 14-GHz noise generator. The correlation between these two noise figure measurement techniques is within 0.20 dB. Table 2 gives the factory's measured parameters supplied with each diode.

Conclusions

A broadband 14-GHz microstrip TDA has been designed and successfully fabricated. A good match has been achieved between the computer-simulated and measured gain responses. This stable, oscillation-free TDA design has produced measured gain and noise figures of 14.30 ± 0.10 dB and 5.60 ± 0.05 dB, respectively, across the 14.00- to 14.50-GHz band using a 5.10-dB noise figure tunnel diode. The TDA microstrip circuit loss contribution to noise figure is estimated at 0.30 dB. This estimation and measured input-path circulator loss have been used to accurately predict measured TDA noise figures. Generally, when mounted to a good-quality 4-port circulator, this TDA circuit produces an amplifier noise figure which is 0.50 dB higher than that of the incorporated tunnel diode.

Acknowledgments

References

[1] R. E. Stegens, "Design of a Narrow-Band MIC Tunnel-Diode Amplifier and Mating Circulator for the ATS-F Propagation Experiment," COMSAT Technical Memorandum CL-21-73, July 9, 1973.

[2] R. C. Mott and M. Wachs, "Design and Performance of Satellite Communications Simulator for Domestic Applications," COMSAT Technical Memorandum CL-53-72, October 20, 1972.

[3] M. V. Schneider, "Microstrip Lines for Microwave Integrated Circuits," *Bell System Technical Journal*, May–June, 1969, pp. 1435–1441.

[4] Aertech Industries, *Microwave Components and Diodes*, 1975, pp. 139–141.

[5] H. Watson, *Microwave Semiconductor Devices and Their Circuit Application*, New York: McGraw-Hill, 1969.

[6] G. L. Mathaei, L. Young, and E. M. T. Jones, *Microwave Filters, Impedance-Matching Networks, and Coupling Structures*, New York: McGraw-Hill, 1964.

[7] P. Silvester and P. Benedek, "Equivalent Capacitances of Microstrip Open Circuits," *IEEE Transactions on Microwave Theory and Techniques*, MTT-20, No. 8, August 1972, pp. 511–516.

[8] R. C. Mott, "A Design Procedure for Microstrip Wideband Maximally Flat Bandstop Filters," Private Communication (Unpublished Paper).

[9] J. Wight et al., "Equivalent Circuits of Microstrip Impedance Discontinuities and Launchers," *IEEE Transactions on Microwave Theory and Techniques*, MTT-22, No. 1, January 1974, pp. 48–52.

[10] W. H. Childs, "HEAVY DUTY—A Microwave Circuit Analysis Computer Program," Private Communication.